

# **Molecules, Macromolecules, and Supramolecules Incorporating Gold Nanoparticles and their Applications in Catalysis, and Photobiology**

Dissertation

Zur Erlangung des akademischen Grades einer Doktorin der  
Naturwissenschaften (Dr.rer.nat.)

in der Bayreuth Graduiertenschule für Mathematik und Natur-  
wissenschaften (BayNAT)

der Universität Bayreuth

vorlegt von

Chen Liang

aus China

Bayreuth 2021

Die vorliegende Arbeit wurde in der Zeit von Mai 2017 bis Mai 2021 am Lehrstuhl Makromolekulare Chemie II der Universität Bayreuth unter Betreuung von Herrn Professor Dr. Andreas Greiner angefertigt.

Vollständiger Abdruck der von der Bayreuther Graduiertenschule für Mathematik und Naturwissenschaften (BayNAT) der Universität Bayreuth genehmigten Dissertation zur Erlangung des akademischen Grades einer Doktorin der Naturwissenschaften (Dr. rer. nat.).

Dissertation eingereicht am: 06.07.2021

Zulassung durch das Leitungsgremium: 14.07.2021

Wissenschaftliches Kolloquium: 30.11.2021

Amtierender Direktor: Prof. Dr. Hans Keppler

Prüfungsausschuss:

Prof. Dr. Andreas Greiner (Gutachter)

Prof. Dr. Hans-Werner Schmidt (Gutachter)

Prof. Dr. Andreas Möglich (Vorsitz)

Prof. Dr. Anna Schenk

(Weiterer Gutachter: Prof. Dr. Michael Buchmeiser)

天行健，君子以自強不息。

地勢坤，君子以厚德載物。

-- 《易經》

*"The heavens are in motion ceaselessly,  
the enlightened exert themselves constantly.*

*While the earth is supportive and natural,  
only the virtuous can bear the utmost."*

*Book of Changes*

# Content

1. Introduction.....	1
2. Theoretical Background.....	3
2.1 Gold nanoparticles (AuNP).....	3
2.1.1 Properties of AuNP .....	3
2.1.2 The concept of colloid stability .....	5
2.1.3 Synthesis of AuNP .....	6
2.2 Surface modification strategies for the AuNP.....	12
2.2.1 Surface modification with polymer.....	12
2.2.2 Conjugation strategies for AuNP .....	14
2.3 Self-assembly of AuNP .....	17
2.4 The catalytic applications of AuNP.....	21
2.5 Electrospinning.....	26
2.6 Wet-laid process.....	29
2.7 Fabrication of sponge .....	31
2.8 Self-assembly of BTA.....	33
3. Aim and Concept.....	37
4. Results and Discussions.....	39
4.1 Size-dependent AuNP catalytic behavior in 4-nitrophenol reduction .....	39
4.1.1 Preparation of the Ct@AuNP and PVP@AuNP .....	40
4.1.2 Characterization of the Ct@AuNP and PVP@AuNP .....	41
4.1.3 Catalytic study of Ct@AuNP and PVP@AuNP for 4-nitrophenol reduction.....	47
4.1.4 Conclusion .....	65
4.2 Stable mesoscale nonwovens of electrospun polyacrylonitrile and interpenetrating supramolecular 1,3,5-Benzenetrisamide fibers as efficient carrier for gold nanoparticles .....	66
4.2.1 Fabrication of the composite nonwoven.....	67

4.2.2	Characterization of the composite nonwovens.....	72
4.2.3	<i>In situ</i> formation of the AuNP within a composite nonwoven.....	83
4.2.4	Catalytic study of the AuNP-immobilized composite nonwoven.....	83
4.2.5	Conclusion.....	88
4.3	Multifunctional sponge combining the network of supramolecular nanofibers and short electrospun fibers.....	90
4.3.1	Fabrication of BTA-sponge.....	91
4.3.2	Characterization of the BTA-sponge.....	94
4.3.3	<i>In situ</i> formation of the AuNP within the BTA-sponge.....	101
4.3.4	Filtration of the AuNP.....	112
4.3.5	Catalytic reduction of 4-nitrophenol in batch system.....	119
4.3.6	Catalytic reduction of 4-nitrophenol in continuous flow system.....	124
4.3.7	Conclusion.....	129
4.4	Photobiologically directed assembly of gold nanoparticles.....	131
4.4.1	Introduction of the LOV protein.....	131
4.4.2	Concept and preparation of LOV protein conjugated AuNP.....	131
4.4.3	Characterization of LOV protein conjugated AuNP.....	134
4.4.4	Characterization of assembly of the LOV protein conjugated AuNP.....	136
4.4.5	Conclusion.....	142
5.	Summary.....	144
6.	Zusammenfassung.....	146
7.	Outlook.....	149
8.	Materials and Experimental Methods.....	151
8.1	Materials.....	151
8.2	Material characterization.....	152
8.3	Experimental procedures.....	158
9.	List of Abbreviations and Symbols.....	168

10. Appendix.....	170
11. Acknowledgements .....	176
12. List of Publications.....	178
13. Reference .....	179
14. (Eidesstattliche) Versicherungen und Erklärungen.....	197

# 1 Introduction

Gold is one of the most ancient and important metals for mankind. It is still the key to world finance as a traded metal.<sup>1</sup> The extraction of gold originated in the 5<sup>th</sup> millennium B.C. near Varna (Bulgaria), and gold production of 10 tons per year was achieved in Egypt around 1200 – 1300 B.C.<sup>2</sup> Until now it has been estimated that nearly 161,000 tons of gold have been mined during the history of man. The discovery of gold nanoparticles (AuNP) was historically closely related to the exploitation of gold ruby glass. The Lycurgus cup at the British Museum in London, as the milestone of the history of gold ruby glass from the 4<sup>th</sup> century AD, opened the door to the journey of AuNP.<sup>1, 3, 4</sup>

AuNP<sup>2</sup>, among nanoparticles (NP) of various noble metals are the oldest and have been the most extensively studied in the past few years in many research fields, such as catalysis,<sup>5</sup> biology,<sup>6-8</sup> electronics<sup>9, 10</sup>, and photonics.<sup>2, 11-13</sup> In comparison with bulk materials or small molecules, NP present unique physical and chemical properties due to their high chemical and physical stabilities and large surface area.<sup>2</sup> Meanwhile, NP have attracted extensive attention in the field of biotechnology because of their biocompatibility, low toxicity, photothermal effect, and easy functionalization with organic and biological molecules. Moreover, the size and shape dependent properties of AuNP also show great potential in nanoscience and nanotechnology applications. In the past years, AuNP conjugated to small molecules, macromolecules and supramolecules have been widely investigated, to expand their applications and to improve their usability and accessibility.<sup>14-16</sup> This work aims at studying and developing AuNP conjugates and assessing their applications in the areas of catalysis, separation and photobiology.

This thesis focuses, firstly, on the fundamental study of AuNP catalysts and the influencing factors of their catalytic performances. The major aim is to provide novel insights into the design of excellent gold catalysts for future applications. The thesis will also describe the design of efficient support for the AuNP. To achieve these goals, the understanding of the intrinsic nature of AuNP and their catalytic mechanisms are crucial. Furthermore, the exploration of new knowledge of how AuNP interact with their

carriers also plays an important role in developing novel catalytic carriers, which can be potentially used in the industry.

To design the carrier for the AuNP, electrospinning as a versatile method to create diverse platforms for AuNP should be introduced here. Using the technique of electrospinning has rapidly been increased and developed tremendously and utilized in numerous fields, such as catalysis,<sup>17</sup> energy harvesting,<sup>18</sup> biological application,<sup>19</sup> stimuli-responsive material,<sup>20</sup> air and water purification since the beginning of the 2000s.<sup>21</sup> In this thesis, novel materials (two-dimensional (2D) materials and three-dimensional (3D) materials) as the support for AuNP are developed via electrospinning along with other polymer processing techniques, such as wet-laid, self-assembly supramolecule and sponge fabrication. The major aims of the development of effective support for AuNP are to: 1) develop novel types of support differing from previous literatures; 2) improve the catalytic activities of the AuNP; 3) reduce leaching of the AuNP during catalytic reaction processes and 4) explore their applications, such as the filtration of the NP.

In addition, self-assembly of AuNP is also covered in this thesis, which has been a hot topic in the past decade that has attracted huge attention. The assembly of the NP can generally be triggered by various ligands<sup>22-24</sup> and under diverse conditions.<sup>25-29</sup> Light-responsive self-assembly of AuNP has great potential in the field of biology. In comparison with the other types of stimuli, light leads to a non-destructive method that can also be widely used in biological environments, providing more possibilities. This thesis work further develops this concept by combining photobiology and material science, to realize the photobiological directing assembly of AuNP under the control of light.

Fundamental knowledge of AuNP and their various applications will be introduced in detail in the next chapter. Moreover, the fabrication methods, such as electrospinning, wet-laid process, sponges and the self-assembly of benzene-1,3,5-tricarboxamide (BTA) nanofibers will also be reviewed in this thesis, as they are closely related to the work undertaken.

## 2 Theoretical Background

### 2.1 Gold nanoparticles (AuNP)

#### 2.1.1 Properties of AuNP

The AuNP in aqueous solution present a wide range of colors, such as brown, orange, red, and purple. An example is given in Figure 2.1, which shows the characteristic smooth color transition of AuNP from dark red to violet with increasing sizes from 30 to 90 nm.<sup>30</sup> A set of ultraviolet-visible (UV-Vis) spectra showing the corresponding maximal absorbance increase from 519 to 569 nm for typical spherical AuNP is included in Figure 2.2.<sup>31</sup> These two pieces of information can be combined to give a clear picture of the relationship between absorbance peak and particle size (Figure 2.3). The absorption band is a so-called surface plasmon band governed by the collective oscillation of the conduction electrons. The electromagnetic field of the incident light wave induces the formation of an electron gas that deviates from what is known as the surface plasma oscillation. A schematic display of the generation of a surface plasmon oscillation is presented in Figure 2.4. The surface plasmon resonance effect as one of the most important physical properties of AuNP is dependent on the morphology and chemical environments of AuNP, such as size, shape, inter-particle interaction, dielectric properties, solvent, surface ligand, core charge, temperature and physiology.<sup>32, 33</sup> This property of AuNP has led to numerous applications in bioimaging.<sup>32, 34</sup>

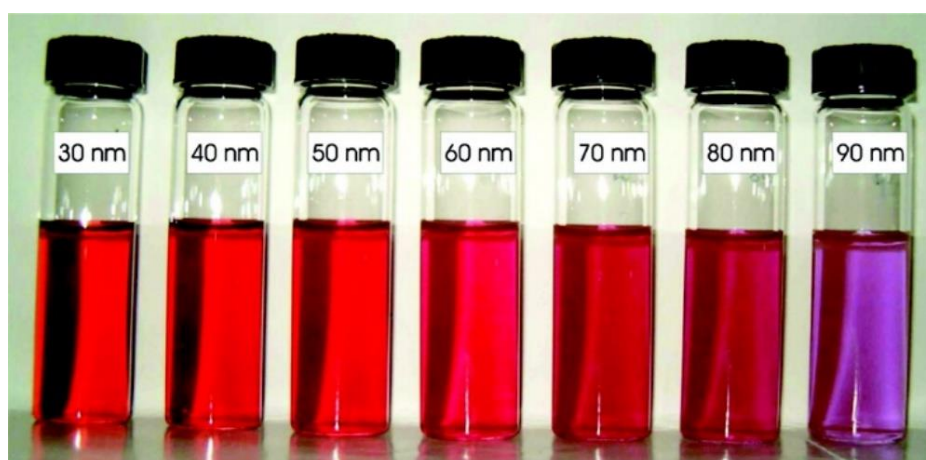


**Figure 2.1.** Colloidal AuNP of different sizes show different colors.<sup>30</sup> Reprinted from reference 30 with permission.

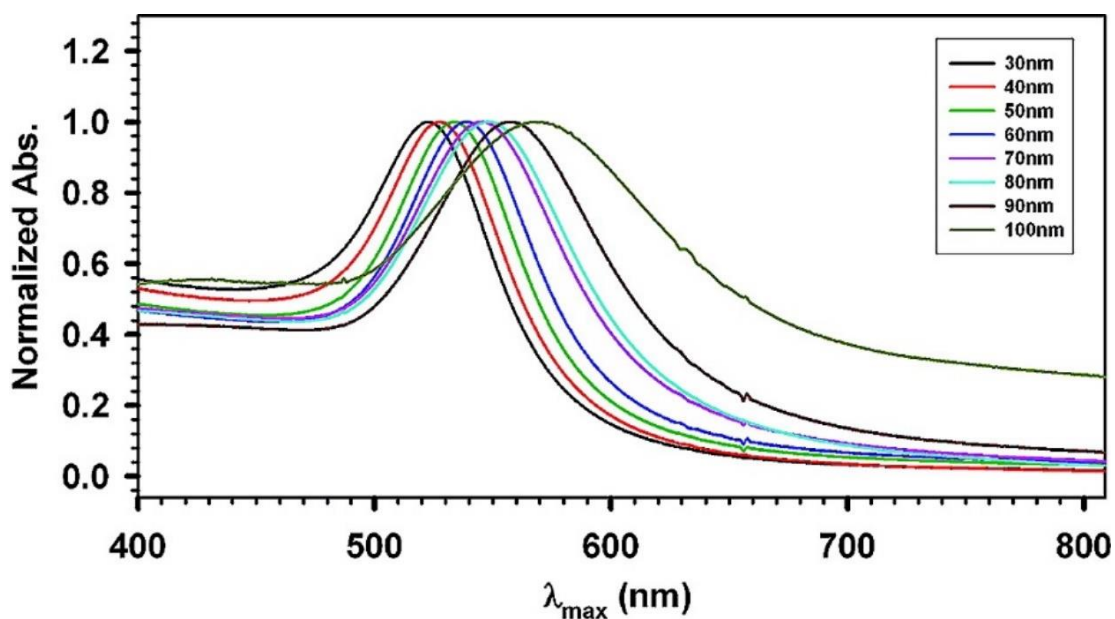


**Figure 2.2.** UV-Vis absorption spectra of colloidal solutions of AuNP of different sizes.<sup>30</sup> Reprinted from reference 30 with permission.

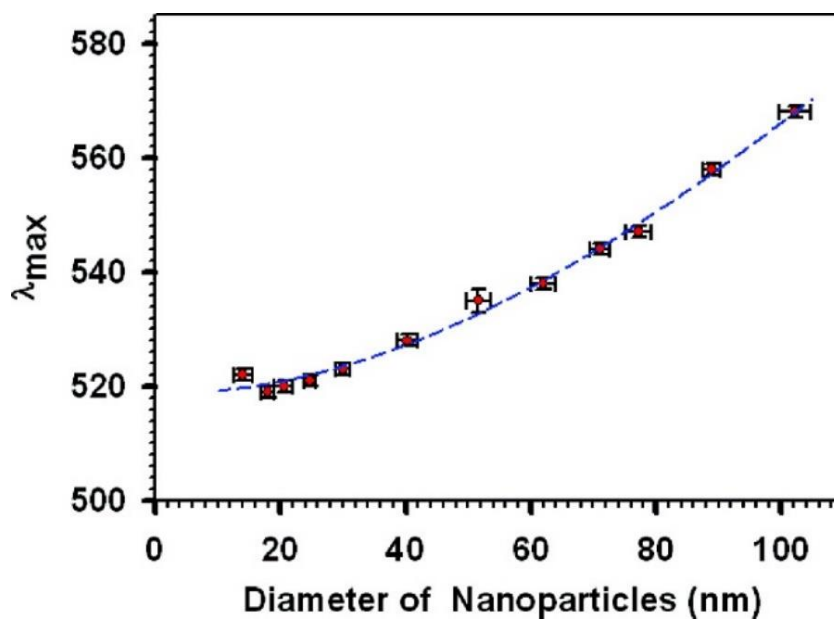


**Figure 2.3.** Correlation between surface plasmon resonance band  $\lambda_{max}$  and the NP size.<sup>30</sup> Reprinted from reference 30 with permission.

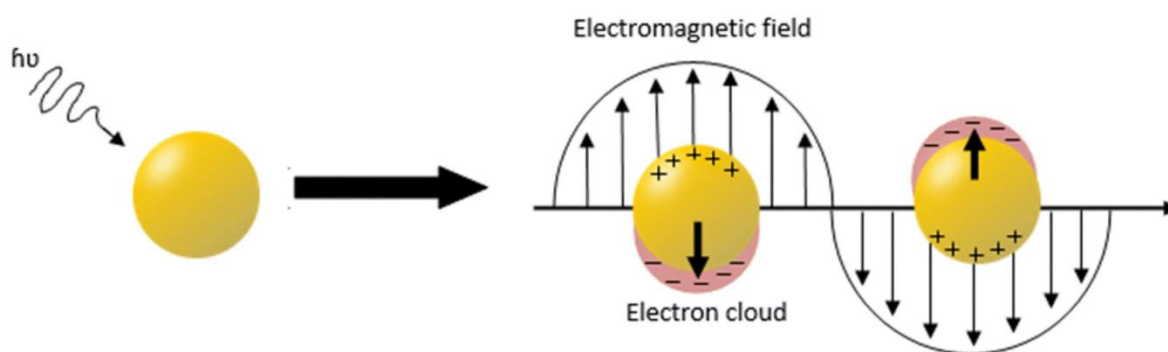


**Figure 2.4.** Schematic representation of conduction electron oscillation across the NP in the incident light electromagnetic field.<sup>35</sup> Reprinted from reference 35 with permission.

### 2.1.2 The concept of colloid stability

The stability of AuNP in suspensions plays an important role in nanomaterials. The AuNP lose their functionality after aggregation or settling down. Hence, extensive efforts have been devoted to retaining the stability of AuNP in the suspension. The NP is prone to reversible agglomeration or irreversible aggregation in suspension because of the attractive force composed of the Van der Waals, electrostatic or magnetic forces. On the contrary, the electrostatic and steric stabilization as the repulsive force prevents the NP from aggregation, agglomeration, and undergoing coalescent processes.<sup>36</sup>

The DLVO theory was developed 70 years ago by two Russian (Derjaguin and Landau) and two Dutch scientists (Verwey and Overbeek) as the theory to explain colloid stability. In this theory, the total force between two NP is the addition of the attractive Van der Waals ( $\phi_{vdw}$ ) and repulsive electrostatic interactions regarded as the electric double layer ( $\phi_{electrostatic}$ ), as well as the hydration ( $\phi_{hydration}$ ) and osmotic forces ( $\phi_{osmotic}$ ) (shown in Equation 2.1 and Figure 2.5).

$$(\phi_h) = (\phi_{vdw}) + (\phi_{electrostatic}) + (\phi_{hydration}) + (\phi_{osmotic}) \quad \text{Equation 2.1}$$

Various parameters generally affect the stability of NP, such as chemical composition, size,<sup>37</sup> surface charge, shape and ion concentration.<sup>38-41</sup> The size of the NP has a great influence on its stability. Stability generally increases with the increasing size of the NP.<sup>42, 43</sup> The attractive Van der Waal force is not dependent on the ion concentration. However, the repulsive force is entirely dependent on the ion concentration. Therefore, a higher ion concentration leads to a lower repulsive force.<sup>36</sup> In addition, the shape of

a NP influences the aggregation in a wide range of electrolyte conditions, which was studied by the Navid B. Saleh Group. The poly-acrylic acid capped AuNP and gold nanorods were selected as representatives. In this work, the gold nanospheres showed a higher aggregation tendency than the gold nanorods. The gold nanorod has higher stability originating from the steric repulsion of poly-acrylic acid coatings (shown in Figure 2.6). Functionalization and modification of NP can provide steric and hydration repulsions to increase their stability in the high ionic strength media.

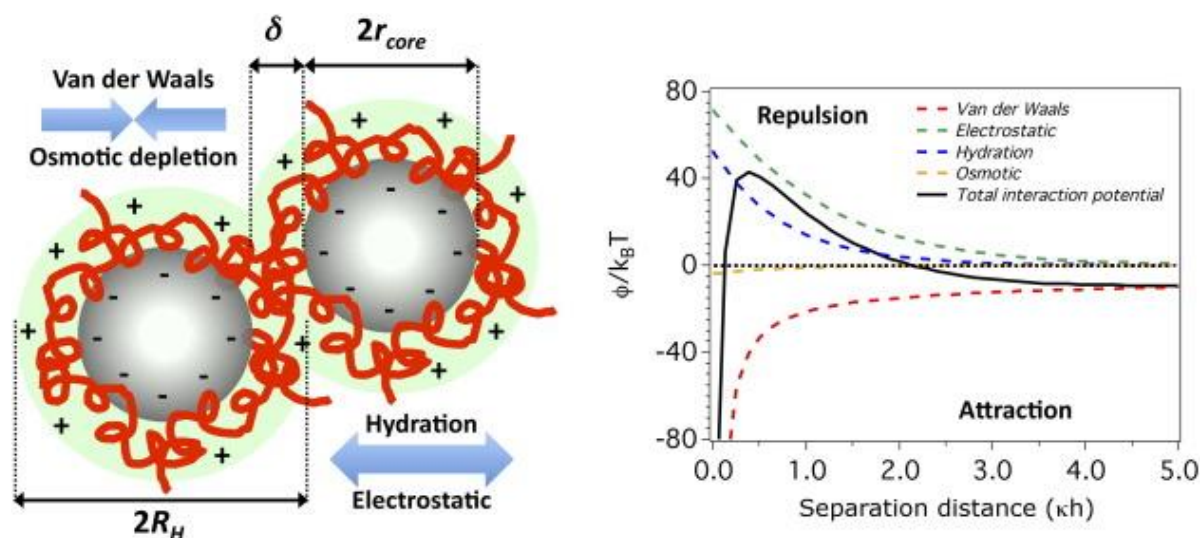


**Figure 2.5.** Interactions between core-shell NP: Parameters employed for DLVO calculations: two NP having the same core radius  $r_{core}$  and the same polymer shell thickness  $\delta$ ,  $R_H = r_{core} + \delta$  can be seen as the core-shell radius. Traditional forces for the colloid interactions (electrostatic, VdW) together with the other structural contributions (hydration and osmotic) that take place when particles are suspended in fluid media. Reprinted from reference 44 with permission.<sup>44</sup>

### 2.1.3 Synthesis of AuNP

The first scientific report about the synthesis of AuNP was made in 1857 by Michael Faraday; the “beautiful ruby fluid” of “fine nanoparticles” was obtained from the reduction of gold chloride by phosphorous, using carbon disulfide as a stabilizer.<sup>45</sup> Countless efforts have thereafter explored the preparation of monodispersed AuNP with controlled sizes and shapes over the years. The synthetic method of creating AuNP can generally be divided into three main classes: physical, chemical and biological procedures.<sup>46, 47</sup> Chemical methods can be further divided into two major approaches. One approach focuses on the investigation of reductive reagents, such

as borohydrides, citric acids and oxalic acids. The gold ion ( $\text{Au}^{3+}$ ) can, firstly, be reduced into  $\text{Au}^{1+}$ , before it is further converted into  $\text{Au}^0$ . The other main approach of chemical synthesis is the formation of AuNP using stabilization agents, such as trisodium citrate, sulfur ligands, polymers or surfactant. Aggregation of the AuNP can be avoided in this approach by enhancing the repulsive force between the AuNP. Meanwhile, the stabilizing reagents can also be regarded as the reduction agents.<sup>46, 48</sup>

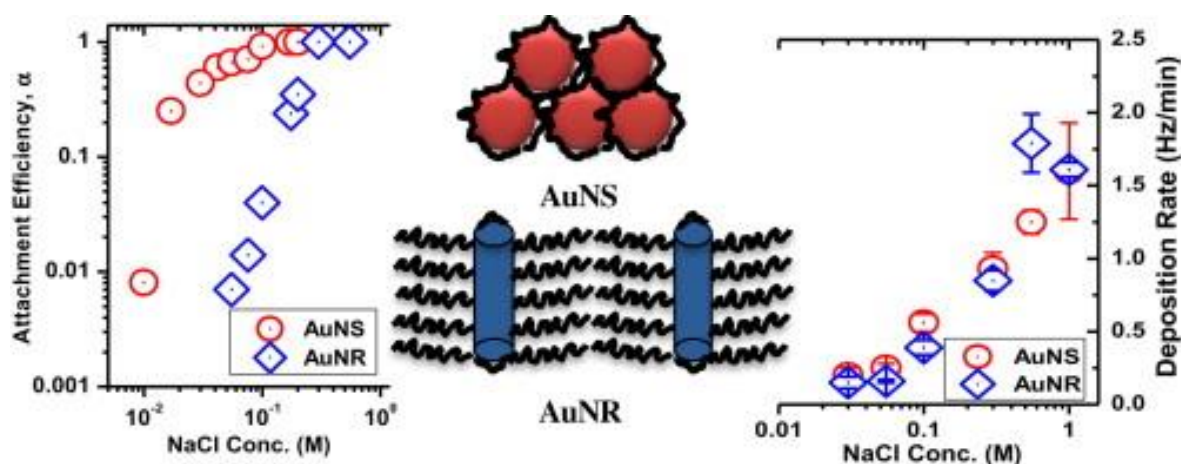


**Figure 2.6.** The effect of AuNP shape on the deposition and aggregation performance.

<sup>37</sup> Graphical abstract reprinted from reference 37 with permission.

### 2.1.3.1 The Turkevich-Frens method

The synthesis of AuNP based on the reduction of  $\text{HAuCl}_4$  using citrate as the reductive and stabilizing reagent under boiling temperature was first introduced by Turkevich in 1951.<sup>43</sup> Spherical AuNP with a size distribution from 10 to 20 nm can be obtained by this method. The Turkevich method was then modified by Frens in 1973 to obtain AuNP with diameters from 15 to 150 nm by controlling the ratio between sodium citrate and gold acid.<sup>49</sup> The Turkevich-Frens method was later verified and has been studied by many research groups in the past decades.<sup>46, 50-52</sup> It has remained popular and frequently used till now because of its facile synthetic conditions, well controlled size, and easy preparation, modification and functionalization.<sup>47, 53</sup> Ji et al.<sup>54</sup> demonstrated that the size and morphology of AuNP was strongly affected by the variation of the  $\text{Na}_3\text{Ct}/\text{HAuCl}_4$  ratio from 0.7:1 to 28:1 (Figure 2.7), if the auric acid concentration was fixed at 0.25 mM. When the ratio of  $\text{Na}_3\text{Ct}/\text{HAuCl}_4$  is smaller than 3.5:1, which covers most of the  $\text{Na}_3\text{Ct}/\text{HAuCl}_4$  ratios in the Frens method, the final size of AuNP will decrease with the increasing concentration of sodium citrate. However, a further

increase of the  $\text{Na}_3\text{Ct}/\text{HAuCl}_4$  concentration ratio from 3.5:1 to 28 induced an increase of the size of the AuNP and leveled off. Their work proved that sodium citrate as a weak base can change the pH of solutions in the traditional Frens method by varying its concentrations. Consequently, the reactivity of the gold complexes is changed and the growth mechanism and final size distribution are affected.

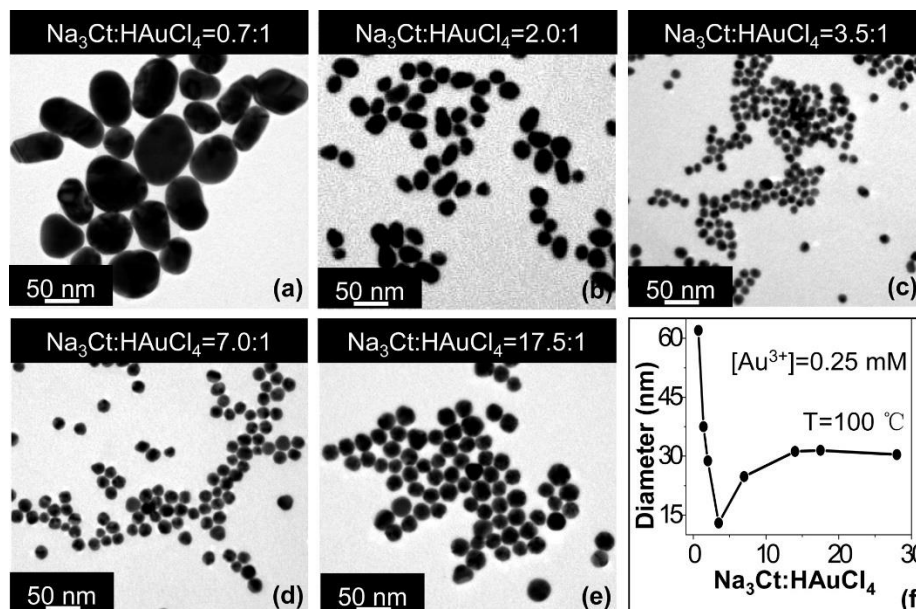


**Figure 2.7.** Transmission electron microscopy (TEM) images (a - e) and summary (f) of gold nanocrystals average sizes. The NP were synthesized using different  $\text{Na}_3\text{Ct}/\text{HAuCl}_4$  precursor ratios, which are labeled in each image. All nanocrystals were grown with an initial  $\text{HAuCl}_4$  concentration of 0.25 mM in boiling water.<sup>54</sup> Reprinted from reference 54 with permission.

The growth of particles follows one of the two pathways shown in Figure 2.8. Under low pH (3.7-6.5), the intermediate  $[\text{AuCl}_3(\text{OH})]^-$  goes through nucleation within 10 s, followed by the fast and random attachment to polycrystalline nanowires and intraparticle ripening of the nanowires, which finally lead to particle formation. If the pH is higher than 6.5, namely 6.5–7.7, the formation of AuNP follows the common nucleation-growth route: Reduction through  $[\text{AuCl}_2(\text{OH})]_2^-$  and  $[\text{AuCl}(\text{OH})]_3^-$  with about 60 s nucleation, followed by diffusion-controlled growth.

In addition, numerous efforts have been made by many research groups to understand the nucleation and growth processes of the particles.<sup>55-60</sup> Ji et al.<sup>58</sup> presented a reliable deduction that the formation of AuNP was completed following a four-step procedure.

(Figure 2.9) The initial step is the rapid formation of small nuclei (particle radius around 2 nm), consuming 20% of the initial gold salt within 60 s with 45% polydispersity. The small nuclei undergo Ostwald ripening<sup>61</sup> or coalescence<sup>62</sup> to generate particles of around 4 nm radius with 20% polydispersity in 20 min. Self-sharpening diffusional growth through the reduction of the gold precursor occurs during the 25–50 min period. This long-time diffusion-controlled growth is due to the limited concentration of gold metal in the solution. The final step is said to be autocatalytic reduction by consumption of the remaining gold salt in the solution with polydispersity decreased to 10%.

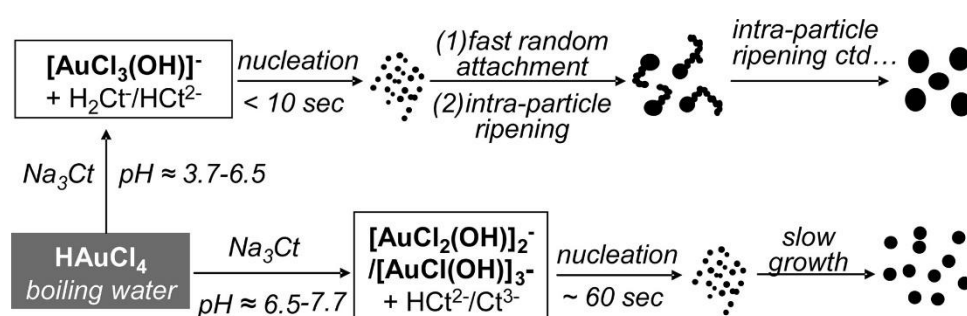


**Figure 2.8.** Illustration of two reaction pathways for the gold nanocrystal synthesis via citrate reduction.<sup>54</sup> Reprinted from reference 54 with permission.

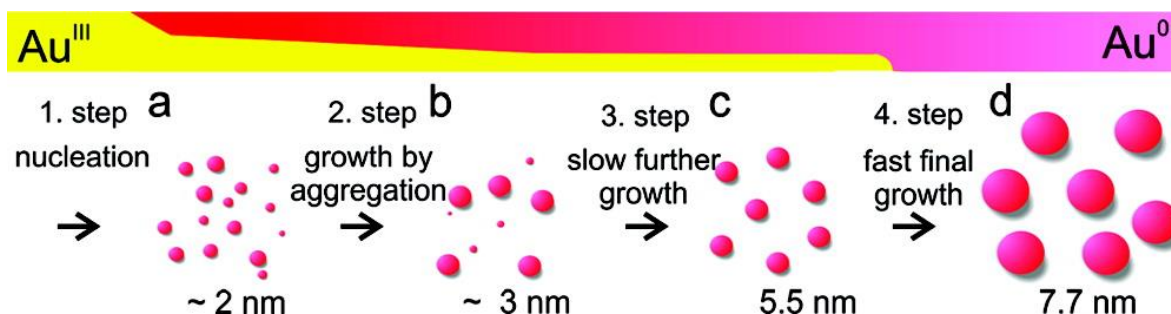


**Figure 2.9.** Schematic illustration of the AuNP formation process deduced.<sup>58</sup> Reprinted from reference 58 with permission.

### 2.1.3.2 The Brust–Schiffrin method

Another widely used synthetic method of creating small AuNP is the two-phase Brust–Schiffrin method, which was first published by Brust and Schiffrin in 1994, to prepare the thiolate functionalized AuNP in an *in situ* condition.<sup>63</sup> Since then, extensive efforts have been made to elucidate the mechanism of AuNP formation via the Brust–Schiffrin method.<sup>64</sup> One widely accepted hypothesis developed by Tong’s group<sup>65</sup> states that gold precursors are transferred from aqueous solution to a toluene phase and generate

a tetraoctylammonium (TOA) metal (I) halide complex  $[\text{TOA}][\text{AuX}_2]$  by using TOA as the phase transfer reagent. The metal ion precursor was then converted into  $[\text{TOA}][\text{Au}(\text{I})\text{X}_2]$ -AuNP in the presence of thiol. The metal ions are converted into naked metal by the addition of sodium borohydride ( $\text{NaBH}_4$ ) and the diffusion of the ligand through the TOA shell, and the Au-S forms on the water/organic solvent interface in the presence of a ligand. (Figure 2.10) This method shows several advantages, such as facile synthetic conditions, and AuNP being thermally stable and stable in air without aggregation and decomposition. The AuNP synthesized have also a low dispersity, controllable size (2–5 nm) and normal cuboctahedral and icosahedral shapes, while facile surface modification by ligand substitution is possible.<sup>46, 64</sup>

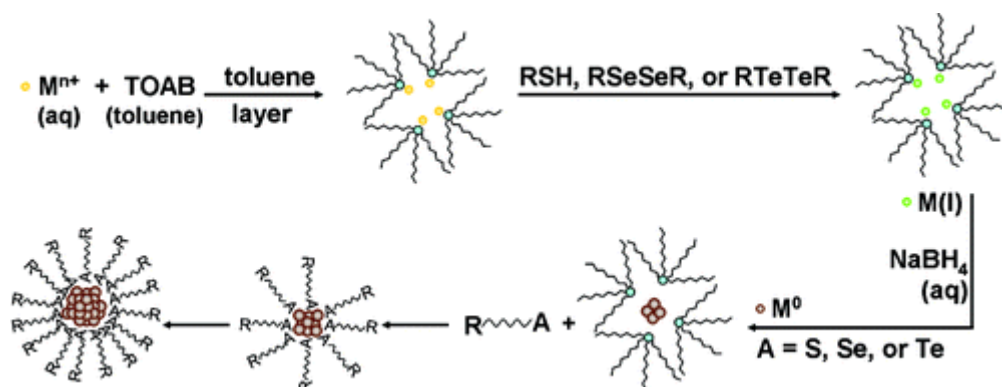


**Figure 2.10.** Mechanism of the synthesis of chalcogenate-protected metal NP via the Brust-Schiffrin Method.<sup>65</sup> Reprinted from reference 65 with permission.

### 2.1.3.3 The Seed growth method

Another widely adopted synthetic method of creating AuNP in the past has been the seed growth method.<sup>66</sup> It becomes more and more difficult to control the size and shape of the AuNP with increasing size using the traditional method. Compared with the *in situ* method, the seed-growth method offers better control of the size and shape of the AuNP, extending the attainable size and morphology of AuNP. To date, monodisperse AuNP up to 300 nm have been synthesized,<sup>66, 67</sup> of which many have been reported by Natan and co-workers. To obtain AuNP up to 100 nm, the gold nano seed is prepared by the reduction of gold acid with  $\text{NaBH}_4$  in the presence of citrate as a capping ligand. It was then added to the growth solution, which contains citrate or hydroxylamine<sup>68</sup> as a reductant.<sup>69</sup> Although this method can indeed enlarge the size distribution of AuNP, rod shape particles are also produced. Bastús et.al.<sup>66</sup> reported

an improved method, which enabled the preparation of monodisperse citrate-stabilized AuNP up to 200 nm in size with narrow size distribution (Figure 2.11). The successful kinetic control of the growth process was achieved via adjusting the temperature, the ratio between the gold precursor to the seed concentration, and the pH. The final citrate-capped AuNP (Ct@AuNP) can be easily modified by other ligands and lead to various application possibilities.

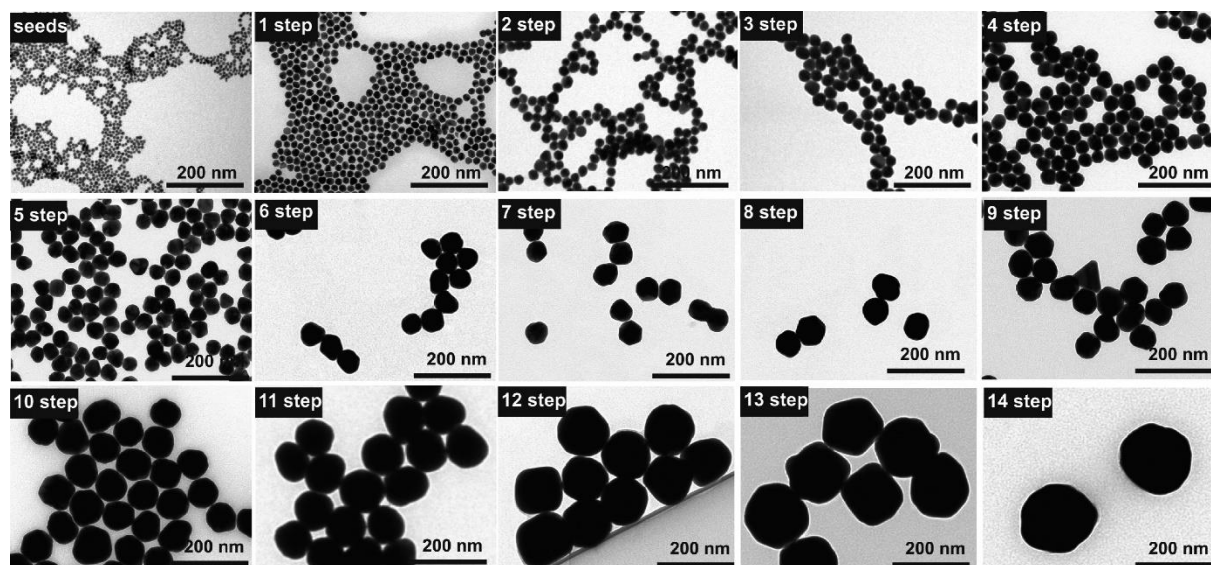


**Figure 2.11.** Seed growth with seed solution dilution. Transmission electron microscopy images of Au seed particles and those obtained after different growth steps. An increase of particle size from  $8.4 \pm 1.0$  to  $180.5 \pm 10.7$  nm and a decrease of concentration from  $\sim 3 \times 10^{12}$  to  $\sim 5 \times 10^9$  NP / mL can be observed.<sup>66</sup> Reprinted from reference 66 with permission.

#### 2.1.3.4 Other methods

Methods such as  $\gamma$ -irradiation, microwave irradiation, the sonochemical method, UV radiation, laser ablation, the thermolytic and photochemical process are regarded as physical procedures. Meanwhile, the synthesis of AuNP via biological methods related to the concept of “green chemistry” has also emerged and been well developed in the past few years. Different plant extracts,<sup>70</sup> plant-based compounds and derivatives, amino acid, fungi, algae, enzymes, flavonoid, microbes,<sup>71</sup> and proteins have been demonstrated to act as reductive agents and stabilizers.<sup>46</sup> Different types of AuNP have also been synthesized.<sup>72</sup>

## 2.2 Surface modification strategies for the AuNP

The functionalization of AuNP can be achieved by conjugation with different functionalized materials, such as surfactants, small molecules, supramolecular polymers, proteins, peptides, DNAs, RNAs and oligonucleotides.<sup>3, 73</sup>

### 2.2.1 Surface modification with polymer

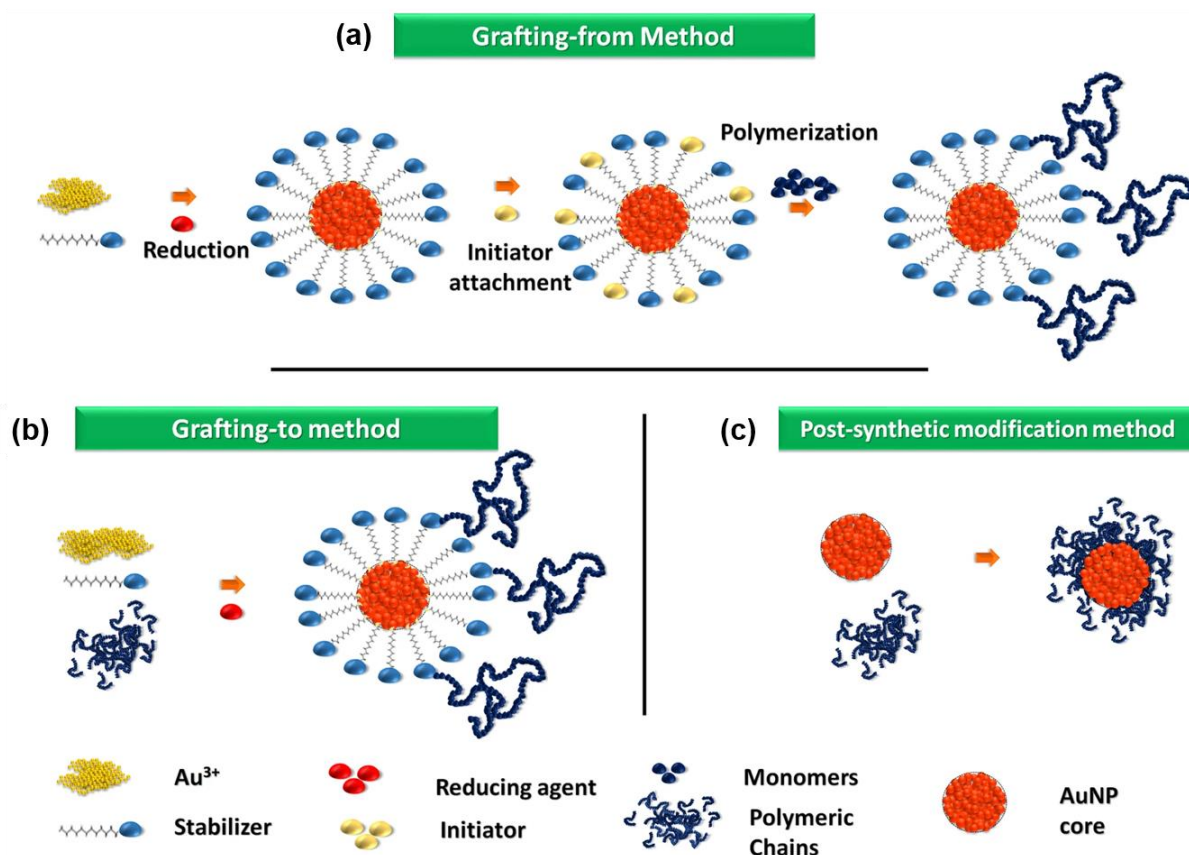


**Figure 2.12.** Three techniques for polymer-stabilized AuNP synthesis: (a) grafting-from, (b) grafting-to and (c) post-synthetic modification.<sup>74</sup> Reprinted from reference 74 with permission.

The first production of polymer stabilized AuNP was documented in 1781 by Helcher and polysaccharide was used.<sup>74, 75</sup> The polymer functionalized NP can generally be obtained by three main strategies: The grafting from approach, grafting to method and post-synthetic modification method (Figure 2.12). The grafting from approach was carried out by attaching the small initiators to the AuNP, followed by the growth of the polymer chain from scaffolds. This method includes living radical polymerization<sup>76</sup> and surface-confined atom-transfer radical polymerization.<sup>77</sup> This method provides various

advantages, such as good control of the molecular weight of polymers related to the thickness of the brush, designed architectures of the polymers, and good control of the density of the polymer grafting to the surface by fixing and varying the initiators on the surface of the AuNP. In addition, it also promotes the uniform distribution of polymer films on the surface of various solids.

The “Grafting to” method is a one-pot synthesis method normally performed with sulfur containing polymers, which contain functional groups such as dithioester, trithioester, thiol, thioether and disulfide, at the end or in the middle of the polymer. It should be noted that the sulfur functional group can be attached only on one side of the terminal, and the other side is capped with sulfur-free functional groups. Thus, the preparation of polymer by reversible addition–fragmentation chain-transfer using chain transfer reagents containing sulfur atoms will provide a facile way to undergo the grafting to method.<sup>78</sup> This method has advantages such as a simplified synthetic procedure and purification steps, high stability over years even in the solid state, and possible functionalization with various polymers.

The post-synthetic modification method is defined as the synthesis of AuNP is carried out through the traditional methods and was modified with polymers by using the ligand exchange method. It processes either NP or the polymer matrix that are well controlled. At the same time, the incorporation method of the NP with a polymer matrix affects the material properties, such as catalytic activity, conductivity, and optical properties.

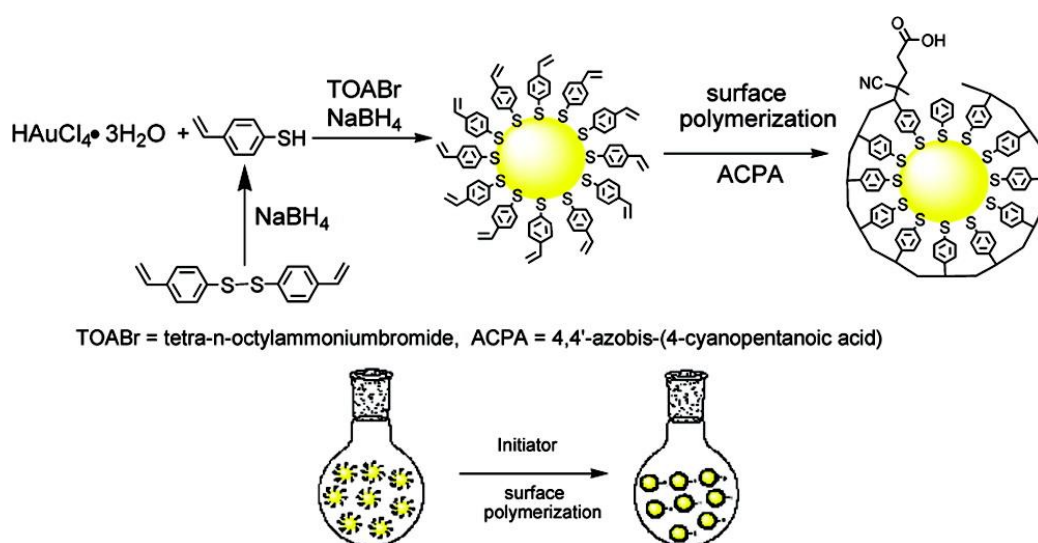


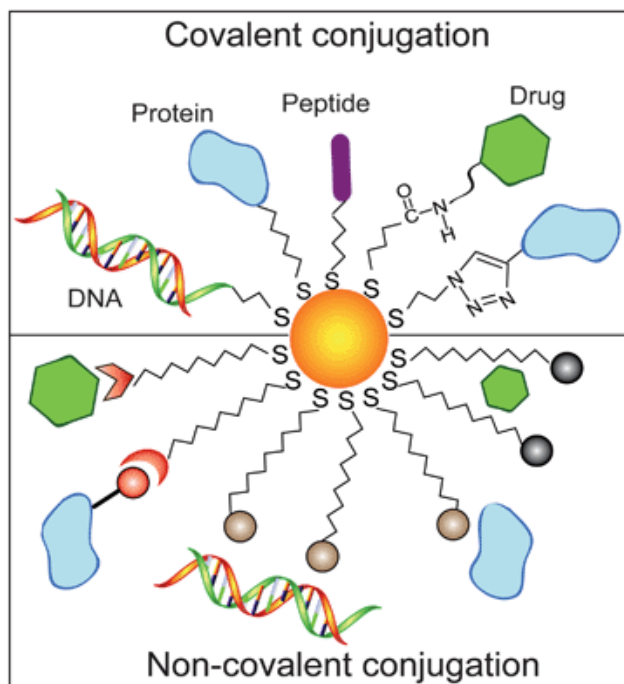
**Figure 2.13.** Schematic description of the graft around method to produce monofunctionalized AuNP.<sup>79</sup> Reprinted from reference 79 with permission.

Besides these above-mentioned methods, our group introduced for the first time a “graft around method”. The concept of the “graft around method” is depicted in Figure 2.13. A layer of the 4-vinyl-thiophenol moieties was firstly immobilized on the surface of the AuNP via traditional Brust–Schriffrin method, followed by free radical polymerization of the vinyl groups within the single AuNP using 4,4'-azobis-(4-cyanopentanoic acid) as the initiator. Remarkably, the decomposition of the initiator should be slower than the surface polymerization. This graft around method provides foundation to realize the precise stoichiometric control of the functionality on the surface of the AuNP.<sup>79</sup>

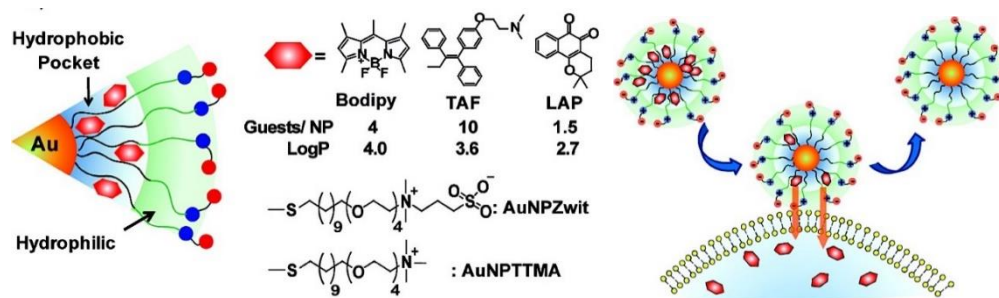
### 2.2.2 Conjugation strategies for AuNP

The labile citrates, thiols and amine ligands can be easily obtained by chemical synthesis. However, the Ct@AuNP is not stable over a range of buffer conditions, which limits their bio-application of AuNP.<sup>73, 80-82</sup> The AuNP should be modified by undergoing ligand exchange reaction to replace the original ligand by others.<sup>83</sup> Place ligand exchange provides AuNP with the possibility of binding to the secondary organic molecules or biomolecules on the surface.<sup>84</sup> Thus, AuNP can present a great potential in biotechnological and biomedical applications.<sup>85</sup> The procedure of ligand exchange is relatively simple: The AuNP is mixed with free ligands, and the incoming ligands gradually replace the initial ligands on the surface of the AuNP. In this way, place ligand exchange offers the chance for AuNP to attach to ligands that cannot be bound during the synthetic procedure.<sup>86</sup>

The AuNP conjugates can be obtained by both non-covalent and covalent methods. (Figure 2.14) The non-covalent methods depend mainly on the ionic attraction between the negatively charged gold and positively charged incoming conjugates, the hydrophobic interaction between the conjugates and the gold surface and dative binding between conjugates and the gold-conducting electrons.<sup>87, 88</sup> The non-covalent method has been widely used in drug delivery and biosensing applications. Figure 2.15 describes the drug delivery by the incorporation of drugs into AuNP via the hydrophobic entrapment method. It has the potential to prevent the reduced efficiency of drug release caused by the attachment of the drug to AuNP via covalent binding and the intracellular process of the prodrug.

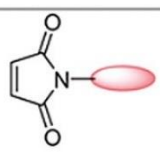
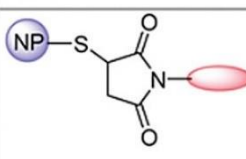
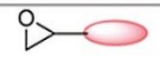
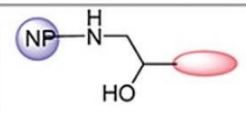
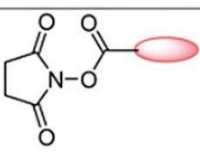
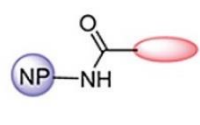
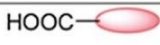
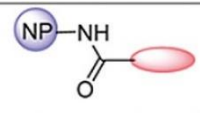
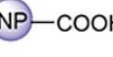
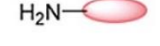
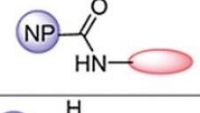
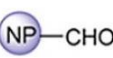
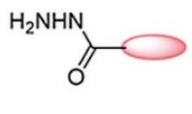
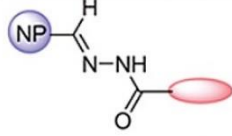
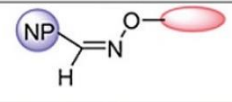
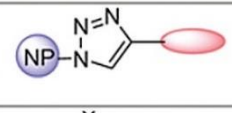
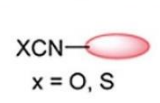
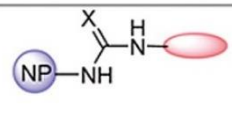
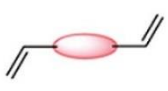
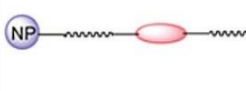
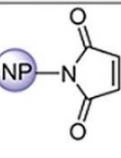
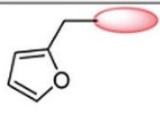
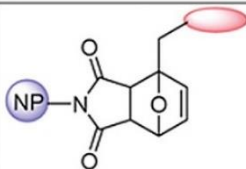


**Figure 2.14.** AuNP conjugation approaches through covalent and non-covalent conjugation.<sup>31</sup> Reprinted from reference 31 with permission.



**Figure 2.15.** Drugs entrapped inside the hydrophobic layer of AuNP.<sup>85</sup> Reprinted from reference 85 with permission.

**Table 2.1** NP functionalization chemistry via covalent bonding.<sup>88</sup> Reprinted from reference 88 with permission.

Ligand	Substrate	Ligand Attached to Substrate	Reaction
			Michael Addition
			Epoxide Opening
			Amidation
			Amide Bond Formation
			Amide Bond Formation
			Imine Formation
			Imine Formation
			Click Chemistry
			Addition of Amine to Cyanates
			Cross Methathesis
			Diels-Alder Reaction

The conjugation of AuNP can also be achieved by covalent attachment to surface ligands. The conjugation of the biomolecules (proteins, DNAs, carbohydrates, lipids, antibodies) depends strongly on the surface modification. Table 2.1 has listed many of the chemistries which can be used for the functionalization of AuNP. The modification of AuNP can be implemented by various chemical reactions, such as Michael addition, epoxide opening, amidation, amide bond formation, imine formation, click reaction, addition of amine to cyanates, cross metathesis and Diels-Alder reaction. The covalent conjugations always take place between free molecules and the pre-grafted thiolate ligands on the surface of AuNP.

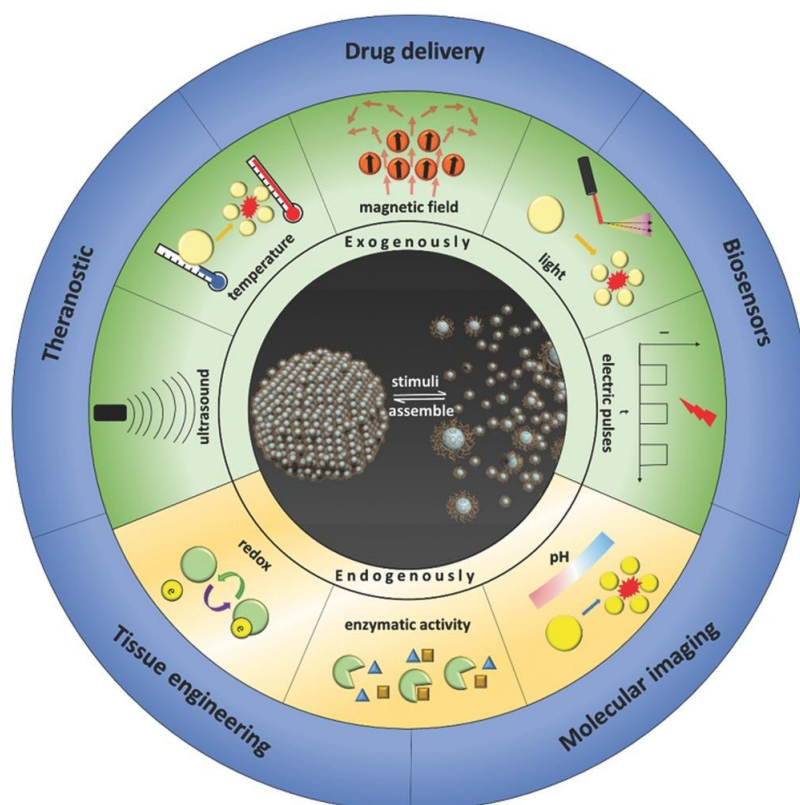


**Figure 2.16.** Schematic illustration of the stimuli-responsive NP assemblies that can be used in a variety of biomedical applications.<sup>89</sup> Reprinted from reference 89 with permission.

### 2.3 Self-assembly of AuNP

Countless efforts have been made to develop smart materials with highly organized self-assembly structures for many years. The self-assembly of NP presents innovative physical and chemical properties differing from those of the single dispersed NP and the bulk aggregates. Remarkably, dynamic and controlled self-assembly of NP at

nanoscale possess great potential in many applications, including optoelectronic devices,<sup>90</sup> sensors,<sup>91</sup> switchable catalysts<sup>92</sup> and biomedicine.<sup>93</sup> The construction of smart materials is still confronted with the challenge of achieving stimuli reversible self-assembly of NP.<sup>94</sup> The NP generally undergoes self-assembly into high-order superstructure via various interactions, such as hydrogen bonding, electrostatic,  $\pi$ - $\pi$ , coordination, host-guest, dipole-dipole and van der Waals.<sup>95</sup>

The precisely controlled self-assembly of NP can be achieved by the incorporation of moieties in the conjugates of the NP. These particular moieties, for example, can respond to external stimuli (e.g., solvent, acid/base, metal ions, pH, light, magnetism, electricity, temperature, and redox)<sup>94</sup> (Figure 2.16). They present diverse biomedical applications, such as drug delivery, biosensors, molecule imaging and tissue engineering.

Among the stimuli mentioned previously, light offers many advantages in realizing the well-controlled self-assembly of NP. It has the following unique features: 1) the stimuli exerted can be initiated and removed rapidly on demand; 2) the procedure is noninvasive; 3) it offers precise temporal and spatial control at a precise location; 4) different wavelengths can be used; and 5) good control of the organized, three-dimensional suprastructures is possible.

The most popular moieties currently employed in response to light for the control of the self-assembly of NP are azobenzene, stilbene, and spiropyran.<sup>95-97</sup> Azobenzene (1,2-diphenyldiazene) has been widely investigated in light-controlled self-assembly of AuNP owing to its reversible isomerization. The trans-cis isomerization process leads to a big change in the structure of the molecule, significantly decreasing the distance between the two substituents from  $\sim 9$  to  $6.5 \text{ \AA}$ . (Figure 2.17) The thermodynamically more stable trans isomer of azobenzene is converted to cis isomer under UV light ( $\lambda = 365 \text{ nm}$ ). However, the cis isomer reverts spontaneously to the trans form once the UV light is switched off. Although this thermal re-isomerization is slow, the reversing process can be achieved in picoseconds with the help of external heating or exposure to visible light ( $\lambda = 430 \text{ nm}$ ). It should also be noted that the sample presents a photostationary state consisting of up to 90% cis isomer and trans isomer under UV light. The cis isomer constantly relaxes into trans form because of thermostability.<sup>98</sup> The incorporation of azobenzene with the AuNP triggers the aggregation of AuNP

under UV light.<sup>97, 99</sup> (Figure 2.17) The cause is the attractive dipole-dipole force between the cis isomers on the surface of the AuNP, after they enter the close proximity of each other due to Brownian motion. It has also been suggested that the dipole moment of the cis isomer leads to the instability of the NP in nonpolar solvents.<sup>100</sup> The resulting NP aggregates are metastable, and recover in the dark within hours or days.

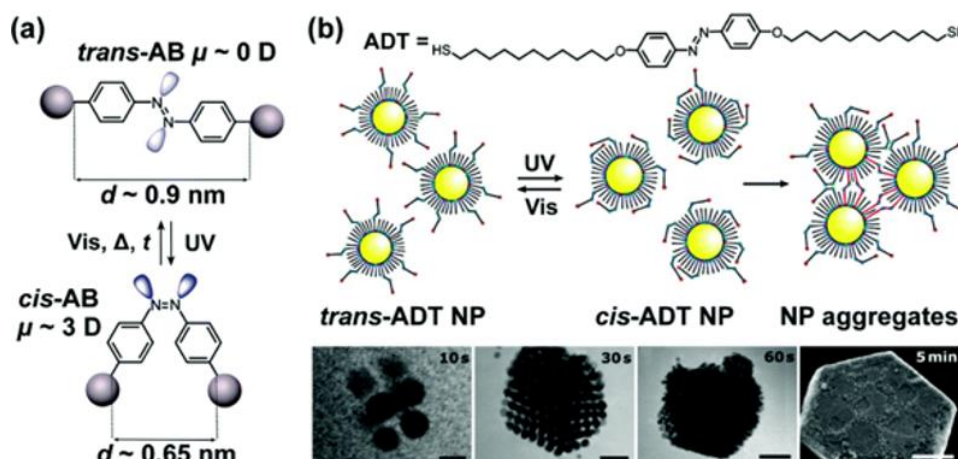


**Figure 2.17.** Light-controlled dynamic self-assembly that is based on azobenzene switches. (a) An azobenzene switch in *trans* and *cis* (top and bottom) conformations. The *cis* form possesses a dipole moment of  $\sim 3$  D. (b) Schemes of nanoparticles that are covered by azobenzene-terminated ligands and interacting *via* light-induced dipoles (when the azobenzenes are in its *cis* form). The electron-microscopy images show the crystals formed by the particles.<sup>99</sup> Reprinted from reference 99 with permission.

Another major type of light-responsive compound is spiropyran.<sup>96</sup> As a photo-switchable molecule, its structural isomerization can be triggered by light. The incorporation of spiropyran molecules with polymer, biomacromolecules and inorganic particles to create dynamic materials that are responsive to light has been widely studied in the past few years. The spiropyran molecule consists of an indoline and a chromene building block, which are spatially perpendicular to each other via a spiro junction. Conversion to the open-ring isomer (merocyanine) can be triggered by UV illumination. (Figure 2.18) It undergoes a cleavage of the  $C_{\text{spiro}}\text{-O}$  bond that gives rise to a *cis* form of the merocyanine and, finally, transforms into the *trans*-merocyanine because of the rotation around the central C-C bonds. Merocyanine has higher basicity

than spiropyran and its protonation can generate MCH<sup>+</sup>. The corresponding pK<sub>a</sub> is 2.25 due to the formation of the 2-hydroxy-4-nitrophenyl building block. Thus, these property differences between spiropyran and merocyanine make the reversible isomerization achievable by altering the pH. Spiropyran can be converted to merocyanine in the presence of an acid due to the affinity of the ring-open form to the proton. (Figure 2.18)

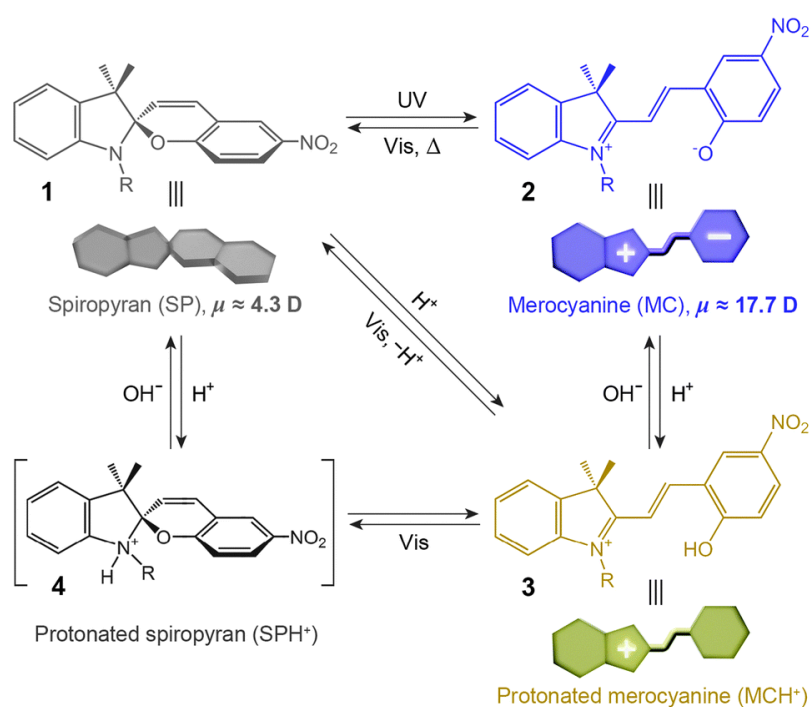


**Figure 2.18.** Spiropyran isomerization: the conversion from the closed-ring isomer of spiropyran to the open-ring isomer (Merocyanine).<sup>96</sup> Reprinted from reference 96 with permission.

The dynamic conversion between the opened and closed spiropyran constructions responsive to orthogonal stimuli facilitates their applications in light-controlled self-assembly of AuNP.<sup>101, 102</sup> (Figure 2.19) The reversible non-photoresponsive AuNP, for example, can be triggered by light in photo-responsive media containing light-switchable spiropyran molecules. Spiropyran molecules can release and attract protons (H<sup>+</sup>), thus, they can influence the stability of the AuNP modified by pH-sensitive capping ligands. The concept and process of the self-assembly of the AuNP are illustrated in Figure 2.19. It will be described briefly that the AuNP modified with ligand consisting of COOH functional group at the end and, at the same time, the dispersion

contains photoswitchable protonated merocyanine (MCH<sup>+</sup>) molecule. The acidity of the aqueous media increases when exposed to blue light, and can induce the disassembly of the AuNP. By contrast, the assembly of AuNP takes place spontaneously in the dark.

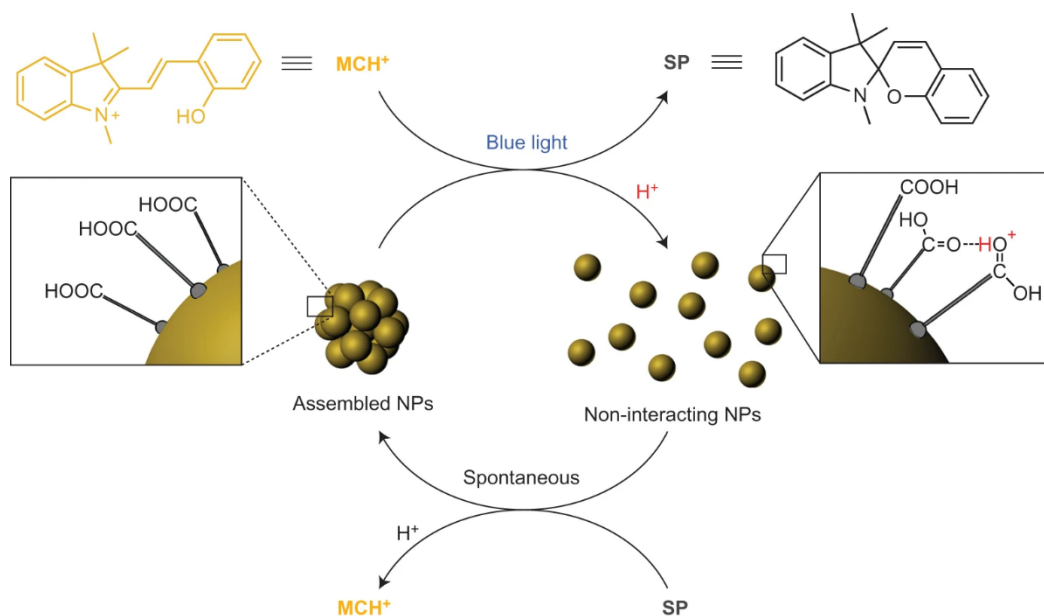


**Figure 2.19.** Blue light-triggered AuNP self-assembly in the presence of the photoswitchable spiropyran molecule and the AuNP having COOH functional group at the end.<sup>26</sup> Reprinted from reference 26 with permission.

## 2.4 The catalytic applications of AuNP

Noble metal NP have received a lot of attention in the field of catalysis since the last century due to their high surface to volume ratios. The NP present excellent catalytic activities and selectivity in comparison with a traditional catalyst. However, the catalytic properties of NP remained unexploited for a very long time. The AuNP, for example, was considered an inert catalyst to chemical reactions, until Haruta et al. reported CO oxidation at a low temperature in the presence of a metal oxide supported AuNP as a catalyst in 1987. This breakthrough opened the door to the application of AuNP<sup>103</sup> in the field of catalysis, and a lot of significant progress has been made in the past few decades.<sup>104</sup>

The AuNP has become the catalyst of choice for many reactions, such as CO oxidation, hydrogenation, coupling reaction, epoxidation reactions, oxidation of alcohols and selective oxidation of alkanes.<sup>5, 105, 106</sup> Two of the targets of this thesis work is to study

the influence of the surface of AuNP on the catalytic reaction and to design novel and reliable supports for AuNP and evaluate the corresponding catalytic activity.

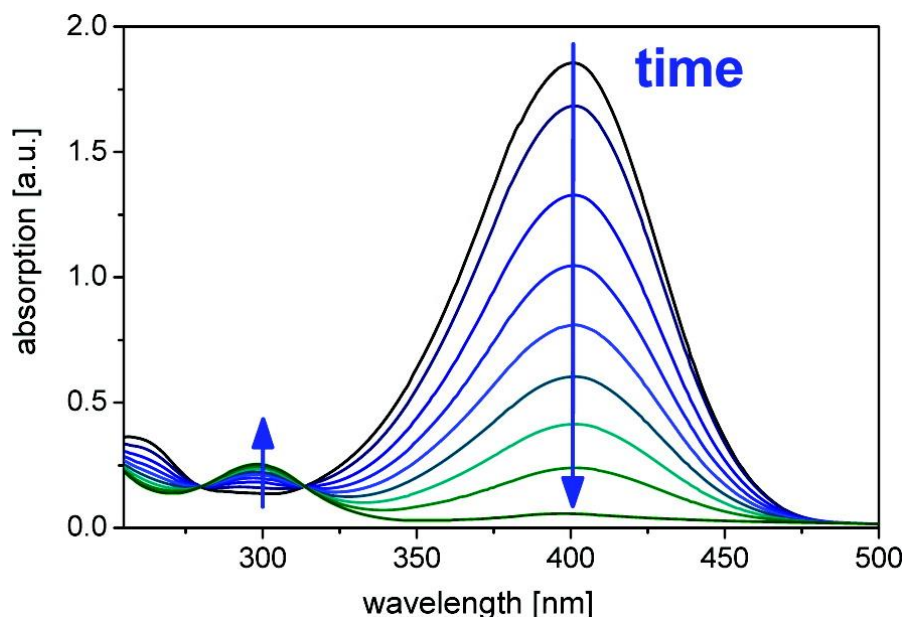


**Figure 2.20.** The UV-Vis absorption spectra of the reduction of nitrophenol by sodium borohydride. The main 400 nm peak from nitrophenolate ions shows an decreasing height (blue arrow) with reaction time, whereas another peak (aminophenol) is slowly emerging at 300 nm. The two isosbestic points can be observed at 280 and 314 nm.<sup>107</sup> Reprinted from reference 107 with permission.

Therefore, only 4-nitrophenol reduction as the model reaction is selected to determine the catalytic behavior of AuNP in aqueous media in this work.<sup>108</sup> The catalytic reaction can be monitored using UV-Vis spectroscopy (Figure 2.20). Details about the mechanism and the parameters affecting the reaction will be introduced in the following part. The earliest attempt to employ this reaction to test the activity of a catalyst was reported by Pal and co-workers in 2001.<sup>109</sup> The main benefit of using this reaction is its facile catalytic conditions without any side products. In addition, the reaction can be quantitatively monitored using UV-Vis spectroscopy. This reaction also accords to the concept of green chemistry, as 4-nitrophenol is one of the major toxic pollutants in industry, agriculture and wastewater. The nitro group in the aromatic ring enhances its chemical stability, hence, the decomposition of the 4-nitrophenol becomes very difficult via simple chemical and biological degradation. However, by employing the catalytic reaction it can be converted to a commercially important product, namely 4-aminophenol. The

latter is an important intermediate for the production of analgesic and anti-pyretic drugs, such as acetanilide and paracetamol.<sup>110</sup>

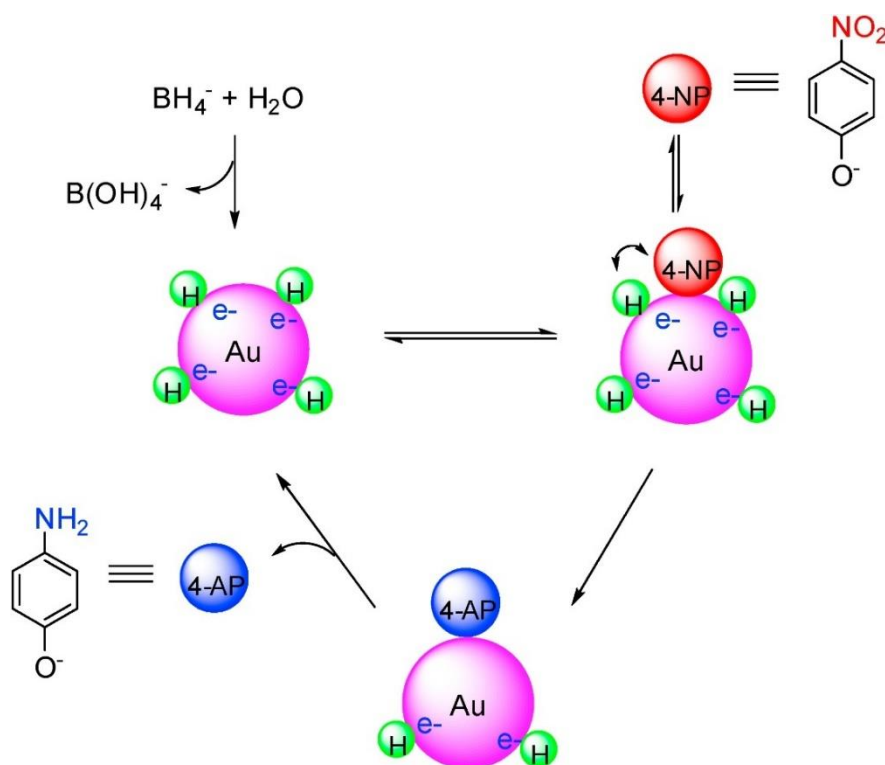


**Figure 2.21.** Langmuir-Hinshelwood mechanism model for the nano-gold catalyzed reduction of 4-NP to 4-AP in the presence of NaBH<sub>4</sub>.<sup>108</sup> Reprinted from reference 108 with permission.

The nitrophenol reduction on the surface of AuNP using sodium borohydride as the reductant undergoes a Langmuir-Hinshelwood mechanism.<sup>111, 112</sup> (Figure 2.21) In the first step, the 4-NP and the borohydride ions are adsorbed onto the surface of AuNP along with the hydrolysis of the NaBH<sub>4</sub>. Borohydride ions then transfer a surface-hydrogen species onto the surface of the AuNP. The adsorption of nitrophenol and the generation of the hydrogen species are reversible, which can be understood in terms of a Langmuir isotherm. It can be assumed that the adsorption and desorption of both reagents on the surface are reversible and rapid. Furthermore, the diffusion of the reactant to the surface of the AuNP can be regarded as very fast. Thus, some research groups have suggested that the reduction of nitrophenol adsorbed on the surface of AuNP by the hydrogen species is the rate-determining step of the catalytic reaction. The desorption step of the catalytic cycle is also fast and cannot be counted in the kinetic determining step. Meanwhile, the evaluation of the rate constant can be carried

out according to the Langmuir-Hinshelwood model. By using the latter model, the apparent kinetic constant rate constant,  $k_{app}$ , is proportional to the total surface,  $S$ , of all the AuNP. The kinetic constants  $k_{app}$  and  $k_1$  can be described by the following Equation 2.2.

$$\frac{dc_{Nip}}{dt} = -k_{app} \cdot c_{Nip} = -k_1 \cdot S \cdot c_{Nip} \quad \text{Equation 2.2}$$

The Langmuir-Hinshelwood model implies that

$$\frac{dc_{Nip}}{dt} = -k S \theta_{Nip} \theta_{BH_4} \quad \text{Equation 2.3}$$

Where  $\theta_{Nip}$  and  $\theta_{BH_4}$  describe the surface coverage of the NP by nitrophenol and borohydride, respectively, and  $k$  is the rate constant of the surface reaction. This Equation 2.3 implies that  $S\theta_{Nip}$  is proportional to the number of nitrophenol molecules adsorbed in the system and  $\theta_{BH_4}$  describes the probability of finding a hydrogen specie in the vicinity of a nitrophenol molecule. As an assumption in the Langmuir-Hinshelwood mechanism, the total number of molecules absorbed on the surface of the AuNP does not affect the concentration of the species given in the solution. Therefore, the change of the concentration of the solution is undetectable because of the adsorption of the small molecules on the surface of the AuNP.

The induction time, for many cases, (Figure 2.22) can be measured during the reaction using AuNP as the catalyst. It is a time interval at the beginning of the catalytic reaction where the decay of the peak at 400 nm is not apparent over time by adding the AuNP catalyst. Although the 4-nitrophenol reduction has been widely studied in the past few decades, the exact mechanism of the catalytic reaction is still contentious. Initially, Pal described the induction time as a time for re-reduction of the surface of the AuNP, and the induction time vanished under the nitrogen gas condition. Some other literature points out that the induction time is the time for the diffusion of the reactants onto the surface of the AuNP.<sup>113-115</sup> However, Ballauff and co-workers demonstrated that the induction period is not initiated by the diffusion of the reactants to the catalyst based on the evaluation of the Damköhler number. The work of Nereitina and coworkers recently revealed that the content of the dissolved oxygen within the aqueous solution plays an important role in the determination of the induction time.

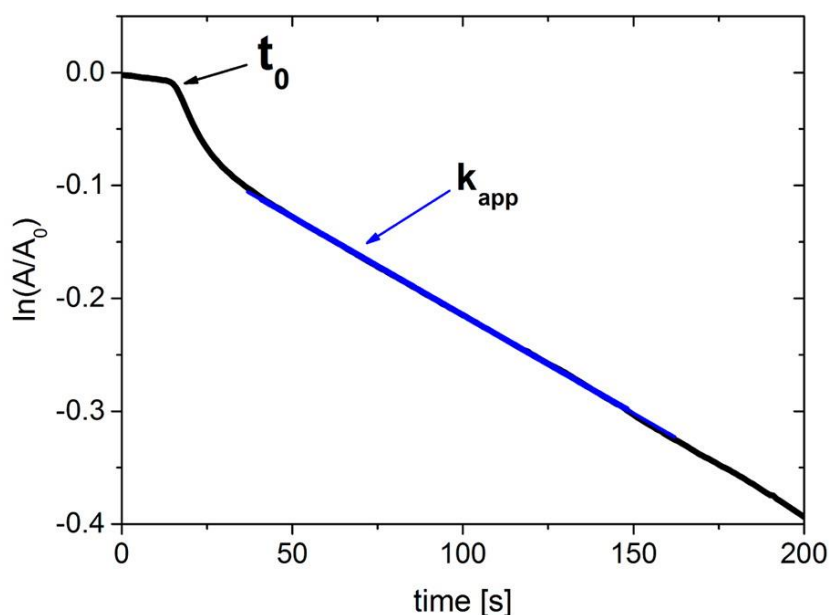


**Figure 2.22.** Typical time dependence of the 4-nitrophenolate ion absorption at 400 nm. The linear section is displayed by the blue portion of the line, from which  $k_{app}$  is taken. The induction period  $t_0$  is marked with the black arrow, which is 20 s in this case.<sup>115</sup> Reprinted from reference 115 with permission.

According to previous kinetic studies, several parameters of AuNP are considered as key factors determining the activity of AuNP, such as size, shape,<sup>116</sup> crystallinity,<sup>117</sup> ligand packing, hydrophobicity, catalyst-reactant interactions, porosities of the nanocomposites.<sup>118</sup> The catalytic reaction is also affected by the reaction conditions, such as irradiation, dissolved oxygen and pH.

In addition to the factors mentioned above, aggregation of the AuNP during the reaction also affects the catalytic activity dramatically. High surface areas of AuNP result in high surface energy of the AuNP, which gives rise to their instability, and leads to the aggregation of the AuNP during the catalytic reaction and reduces their catalytic activity. Hence, the support is essential to ensure the long-term stability of AuNP and the development of novel supports for them to prevent their aggregation and leaching has become a hot topic in NP research. To date, AuNP immobilized on different supports catalyzing 4-nitrophenol reduction have been widely reported in the literature. The support of AuNP can generally be categorized into 1) small molecules, such as citrate and cetyltrimethylammonium bromide;<sup>118, 119</sup> 2) polymer and dendrimer such as poly (ethylene glycol), polyvinylpyrrolidone, polyaniline, polyethyleneimine and polyvinyl alcohol. 3) biological molecules and natural extract, such as peptide and protein; 4)

carbon materials, such as carbon dot and carbon nanotube; 5) oxide metal or composites of two or three oxides, such as  $\text{TiO}_2$ ,  $\text{Al}_2\text{O}_3$ ,  $\text{Fe}_3\text{O}_4$ ; 6) metal and covalent organic frameworks; and 7) silicon. Especially polymer nanocomposites, such as porous polymer, polymer film and membrane, hydrogel, aerogel, sponge and nonwoven offer numerous possibilities as support.<sup>119</sup>

## 2.5 Electrospinning

The history of electrospinning dates back to 1600 and its concept was initially introduced by William Gibert. Thereafter, electrospinning had been gradually developed over several centuries. Remarkably, the production of fibers was recorded by Charles V.Boys in 1887 through drawing from a viscous liquid with the help of an external electric field. Dramatically significant developments have been realized in the past few decades (Figure 2.23). In 2009, more than 1500 papers were published on the topic of electrospinning. To date, electrospinning as a simple and easily controlled technique has been commonly used in scientific research and industrial production. The electrospinning process enables the fabrication of fibers with a diameter ranging from several micrometers down to a nanometer or even below.

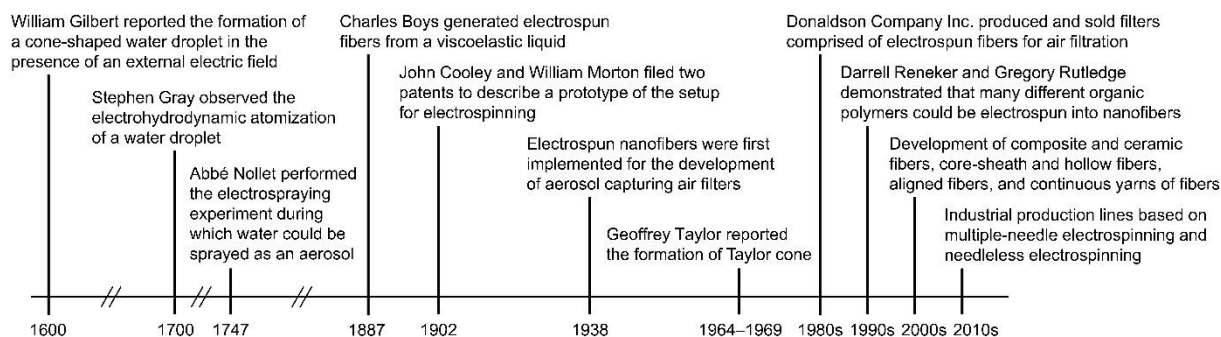


**Figure 2.23.** A summary of the history of the electrospinning technique. (The contribution from Anton Formhals, who issued at least 22 patents starting from 1931 until 1944 about electrospinning, is missing).<sup>120</sup> Reprinted from reference 120 with permission.

The materials for electrospinning are normally natural and synthetic polymers dissolved in solution or melt. Until now more than 100 different polymers have been employed in electrospinning. In addition, small molecules can also be directly investigated in electrospinning, if a stable electrified jet can be obtained by the formation of the chain entanglement, such as amphiphiles and cyclodextrin derivatives.

Even colloidal particles and the composites obtained by combining the sol-gel chemistry have also been widely studied for electrospinning.

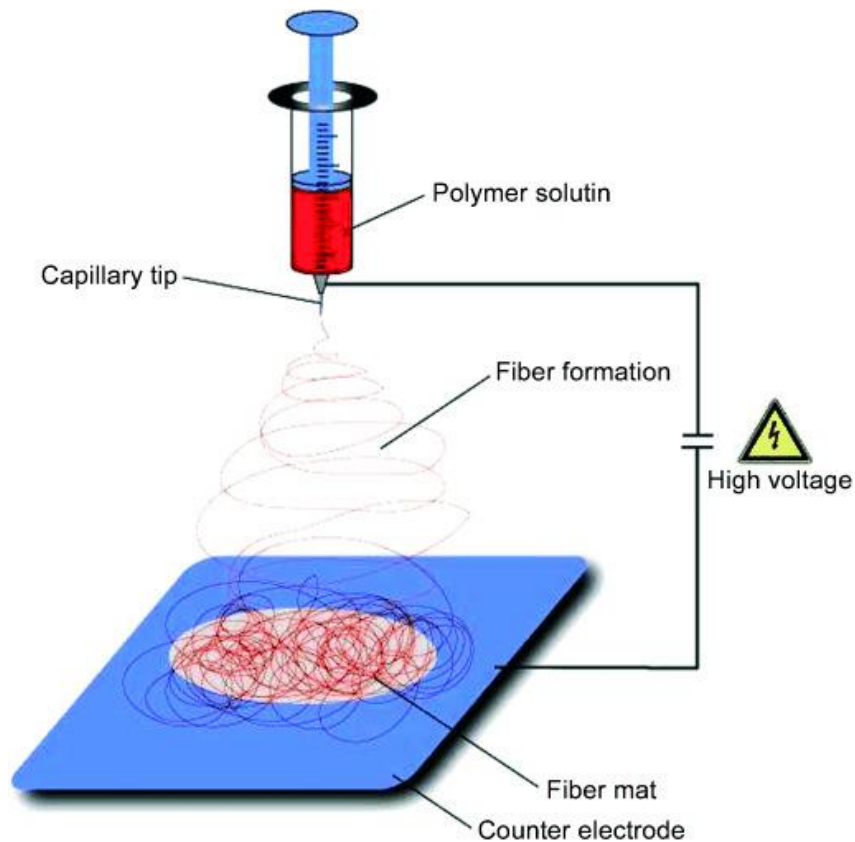


**Figure 2.24.** A laboratory setup for an electrospinning experiment. The electrode was arranged perpendicularly.<sup>121</sup> Reprinted from reference 121 with permission.

Figure 2.24 describes the basic setup for electrospinning. It consists of three main parts: A high-voltage power supply, spinneret (normally hypodermic needle equipped with a blunt tip) with a syringe pump and a conductive collector (metal screen plate, rotator, etc.). The electrospun solution is normally held in a syringe and a constant flow rate is applied and controlled by the syringe pump. During the electrospinning process, a pendant droplet of the polymer solution at the nozzle of the spinneret is extruded and held because of the surface tension. An external high voltage is then exerted to the spinneret connected to a syringe containing a polymer solution and the charges are built on the surface of the droplet. Once the electric field is increased to a critical value, the charge repulsion reaches a level that is strong enough to overcome the surface tension. As a result, the liquid drop will be elongated and deformed into a so-called “Taylor cone” shape and the fine charge jet of the fluid is ejected from the tip of

the Taylor cone and moves towards the grounded collector. Figure 2.25 describes the 3D trajectory of the jet that is caused by many instabilities. The initial trajectory of the jet presents a nearly straight line at a certain distance from the spinneret, then the jet bends into a whipping path. The jet undergoes an unstable and whipping process before reaching the collector, thus, the jet is stretched long and thinly. Meanwhile, the solvent begins to evaporate immediately after the jet is formed. In the end, the jet is solidified and the fibers formed are deposited on the collector.<sup>121-125</sup>

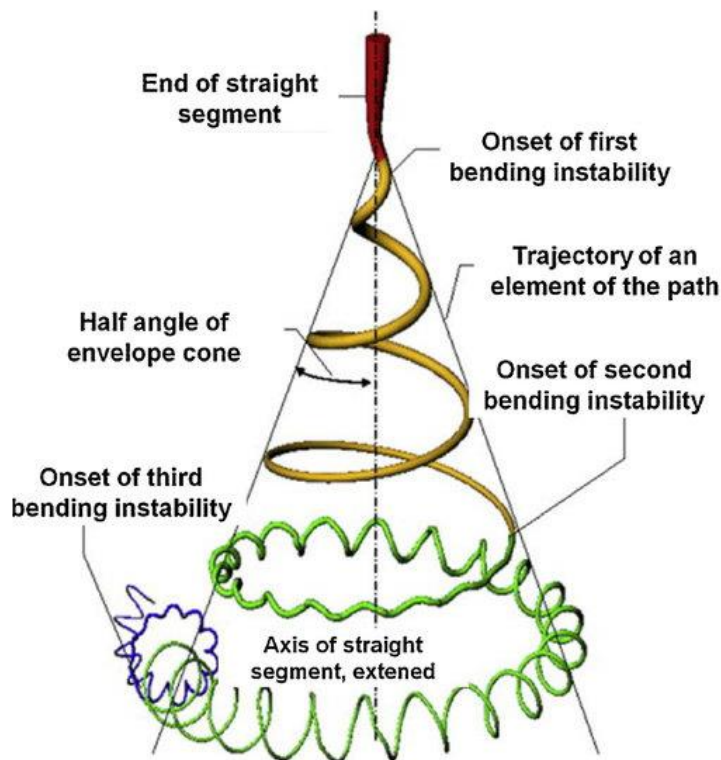


**Figure 2.25.** Schematic illustration displaying the path of an electrospun jet. Reprinted from reference 126 with permission.<sup>126</sup>

Many parameters have influences on the morphology and the diameter of the fibers, such as the intrinsic properties of the polymer solution: Structure, molecule weight and molecular weight distribution, melting point, glass-transition temperature, solubility of the polymer, polymer concentration, viscoelasticity, surface tension and electronic conductivity. The processing parameters and the ambient conditions also have an impact, for example, the voltage applied, flow rate of the polymer solution, the working distance between the spinneret and the collector, the temperature and the humidity.

Nowadays, electrospinning has been applied in various fields, such as shape memory, self-cleaning and healing. Sensing applications have been developed depending on its stimuli responsive properties. Electrospinning has also been widely adopted in diverse filtration applications (air filtration, water treatment), benefiting from the large surface-to-volume ratio, high porosity and high flux with effective adsorption. It has also been tested in the fields of catalysis, energy harvesting, photonics and electronics due to the large surface area, high porosity and high stability features. Furthermore, the electrospun nanofibers have high potential in bio-applications, such as drug delivery, scaffolds in tissue engineering, biomedical and wound healing.<sup>121</sup>

It is not the aim of this thesis to introduce every aspect of the applications of electrospinning in detail. Therefore, only the incorporation of NP into the electrospun nanofibers and their corresponding catalytic applications are highlighted. There are generally several major strategies to incorporate the NP inside the electrospun nanofibers or on their surface: Incorporation of the NP directly during the electrospinning, pretreatment of the as-spun nanofibers, surface deposition of NP on the surface of the electrospun fibers, *in situ* synthesis and hydrothermal treatment. The simplest preparation method of NP-decorated fibers is immersing the as-spun fibers in the NP solution. The NP can adsorb on the fiber surface by electrostatic force, hydrogen bonding or chemical binding. They can be attached on the surface via the *in situ* reduction method. The electrospun nonwoven is immersed in the precursor solution and the precursor of the NP is stabilized on the surface of the nonwoven. With the help of reductive agents, the NP forms on the surface. This method can yield a uniform distribution of NP on the surface of nanofibers.

## **2.6 Wet-laid process**

The fabrication of wet-laid nonwovens is derived from the paper-making technology. Wet-laid nonwoven differs from wet-laid papers, and is defined by EDANA as nonwoven if more than 50% by mass of its fibrous content is made up of fibers (excluding chemically-digested vegetable fibers) with a length to diameter ratio greater than 300, or more than 30% fiber content for materials with a density less than 0.4 g/cm<sup>3</sup>.<sup>127</sup> The manufacturing of the nonwovens via the wet-laid process requires a large amount of solvent in order to obtain homogenous dispersion of fibers. The preparation of wet-laid nonwoven can be achieved by the following steps: Stable dispersion of the fibers in

solution, formation of a web on a fine mesh screen via filtration and bonding of the fibers within the web.<sup>128</sup> The polyacrylonitrile (PAN)/ poly( $\epsilon$ -caprolactone) (PCL)/ silver nanowire (AgNW) nonwovens, for example, were prepared via the wet-laid process and are illustrated in Figure 2.26. It should be noted that the preparation of the uniformed distribution of fibers in the solution in advance plays a crucial role in the fabrication of homogenous wet-laid nonwovens.<sup>129</sup> The fabrication of nonwovens via the wet-laid process generally has several advantages over the other procedures, such as the viability of the pore size of the nonwovens, flexibility of the blending of different kinds of fibers and other materials, low energy consumption, easy large-scale fabrications and higher industrial application potential.<sup>129</sup> In addition, one or more layers of membrane materials, woven materials, plastic or metal materials can be used as supporters. Consequently, the properties and the application range of the wet-laid nonwoven can be broadened.<sup>129</sup> The wet-laid nonwovens have a great potential in fields such as battery separation,<sup>130</sup> filtration, high-temperature insulation, fire protection and medical wipes. Among them, glass fiber, the most common reinforcement material in the composites market, has been widely fabricated and studied regarding usage in the wet-laid process. The homogenous dispersion of glass fibers in aqueous solution always require the addition of a surfactant, to overcome the intrinsic hydrophobicity of the fibers.<sup>131</sup> Polypropylene, polyethylene polyester, aramid, carbon, and regenerated cellulose fibers have also been widely used in wet-laid nonwoven manufacture.<sup>132-134</sup>

Previous work in our group also provided a new perspective on the preparation of nanofiber nonwovens. (Figure 2.27) It was demonstrated that they can be prepared by the combination of the electrospinning technique and the wet-laid process. Wet-laid nonwovens can be obtained by filtrating the dispersion of the shot cut electrospun fibers on the filtration substrates. The product provided similar properties in aerosol filtration compared with nonwovens obtained by the electrospinning. This method can provide advantages such as the controlled thickness and large-scale fabrication (Figure 2.27). In addition, the nonwovens can also be mixed with other materials, such as inorganic NP, polymers, supramolecules, and surfactants.

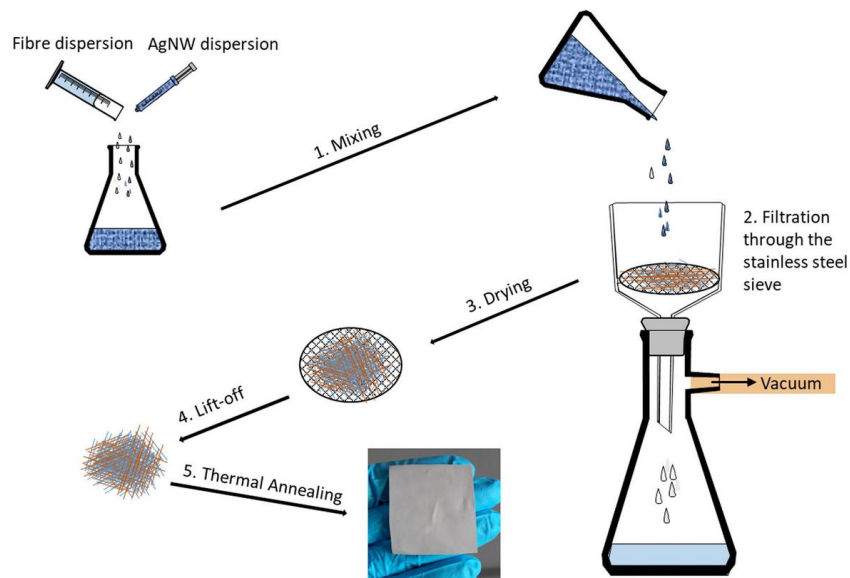


**Figure 2.26.** Preparation procedure of PAN/PCL/AgNW nonwovens via the wet-laid process and the nonwoven morphology.<sup>135</sup> Reprinted from reference 135 with permission.

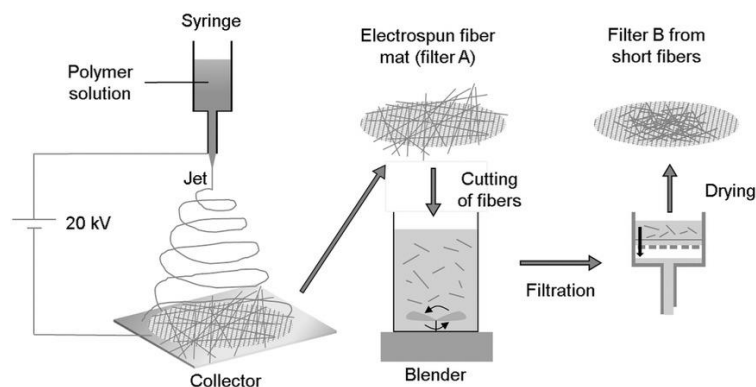


**Figure 2.27.** Schematic displaying of the preparation of nonwoven to be used in filtration applications by electrospinning directly (A) and by short nanofiber filtration from suspension (B).<sup>136</sup> Reprinted from reference 136 with permission.

## 2.7 Fabrication of sponge

The 3D materials such as cork, wood, bamboo and corals, as can be found in nature, consist of cellular structures. The latter comprise either open or closed cell forms or both. Numerous efforts have been made to design synthetic 3D materials. Two representative materials used in industry and daily life currently are polystyrene and polyurethane foams, each with a closed cellular structure (Figure 2.28). Another main type

of material containing a cellular structure is aerogel. However, the definition of the aerogel is still controversial. This type of material typically has extremely high porosities and large surface to volume ratios. The aerogel is defined by the Union of Pure and Applied Chemistry as a “microporous solid in which the dispersed phase is a gas”. There is currently no clear definition of aerogels and sponges which can distinguish them. This is an aspect regarding sponges that will also be introduced in the following part.

The 3D composite materials with multistage pore structures have become a hot research topic recently and been extensively studied worldwide. As a family of 3D porous materials consisting of open cellular structures (Figure 2.28), investigation of sponges based on short electrospun fibers was initiated by the Ding research group and our group simultaneously. Thereafter, this technique opened the door to the preparation of 3D interconnected networks presenting open porous structures with electrospinning. Many potential applications of this novel type of sponge have also emerged. The 3D structure of sponges typically consists of large pores with a diameter up to a hundred micrometers and small pores with a diameter of several nanometers. Sponges can provide excellent reversibility, elasticity and toughness, ultralow density with excellent porosity (up to 99.99%), large specific surface area, ultralow thermal conductivity and a large capacity of fluid uptake.<sup>137, 138</sup> Moreover, the properties of the sponges can be easily adjusted by varying the composites, solvent, density, shape and the processing steps of creating the sponges to satisfy different needs. The preparation of sponges, for example, with ultralight and soft properties via self-assembly of the short fibers was first reported by our group. (Figure 2.29)

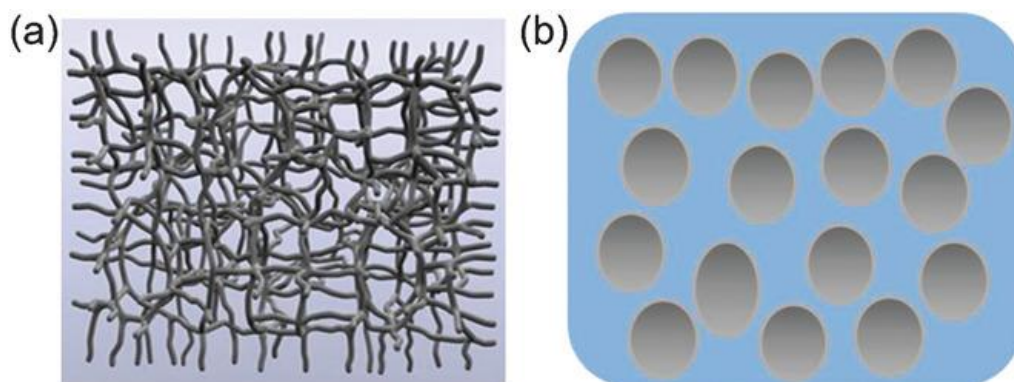


**Figure 2.28.** (a) open and (b) closed cellular structures. Pores are represented by gray spots.<sup>139</sup> Reprinted from reference 139 with permission.

The processing procedure involves the nonwoven being cut into short nanofibers, which are regarded as the one-dimensional building block and freeze-drying of the homogeneous dispersion of those fibers. The mechanically stable 3D structure can be obtained by chemical or physical crosslinking, such as chemical annealing, photo-crosslinking and thermal annealing of the entangled fibers.

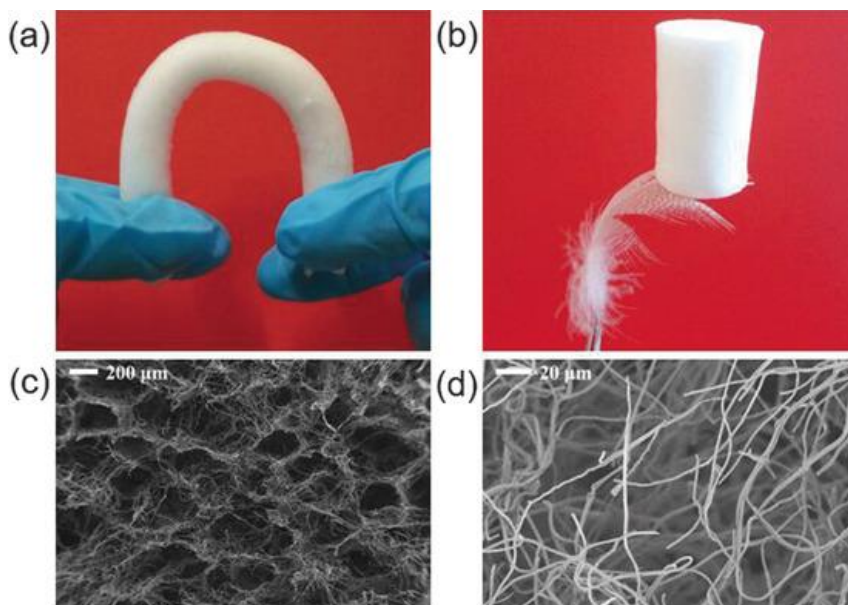


**Figure 2.29.** An ultra-light sponge that is composed of short electrospun fibers. (a) The mechanical flexibility of the sponges is demonstrated. (b) The sponge is placed on a feather. (c) and (d) SEM images showing pore morphology of the sponge at different magnifications.<sup>142</sup> Reprinted from reference 142 with permission.

The sponges can be used in a wide range of applications, such as a catalyst carrier, tissue engineering, insulation materials, sound absorption, electronics, energy harvesting, oil-water separation, electricity conduction and an actuator.

## 2.8 Self-assembly of BTA

Benzene-1,3,5-tricarboxamide<sup>140</sup>, is an interesting and well-studied supramolecular building block.<sup>141</sup> It was first documented in 1915 by Curtius,<sup>142</sup> and has been widely adopted to date.<sup>143</sup> The basic structure of BTA contains three N-centered or three C=O-centered amides bonded to a benzene ring (Figure 2.30). The formation of supramolecules can be achieved by threefold hydrogen bonding between the amides and results in one dimensional stacks with a helical character under certain conditions (Figure 2.31), which were driven by the mechanism of the cooperative self-assembly.<sup>144-</sup>

<sup>147</sup> Many deviations of the position of R-groups on the BTA structures have been documented in the last decade, such as alkyl, aryl, pyridyl, bipyridyl, porphyrinyl and triphenyl. The solvent, processing conditions, variant of the amide units and their concentration all play important roles in the self-assembly process and have an impact on the properties and suitable applications of the BTA molecules. The BTAs, for example, containing long alkyl chain present liquid crystalline properties. They can be used to obtain different functional materials depending on the variation of the side chain (R). Such examples include hydrogels, organogelators, metallo gels, porous organic materials, microcapsules and MRI contrast agents.<sup>148</sup> (Figure 2.32)

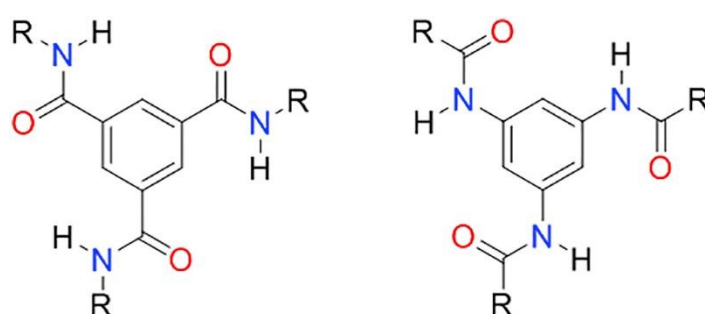


**Figure 2.30.** General structures of C=O (left) and N-centred (right) benzene-1,3,5-tricarboxamide (BTA) molecules.<sup>149</sup> Reprinted from reference 149 with permission.

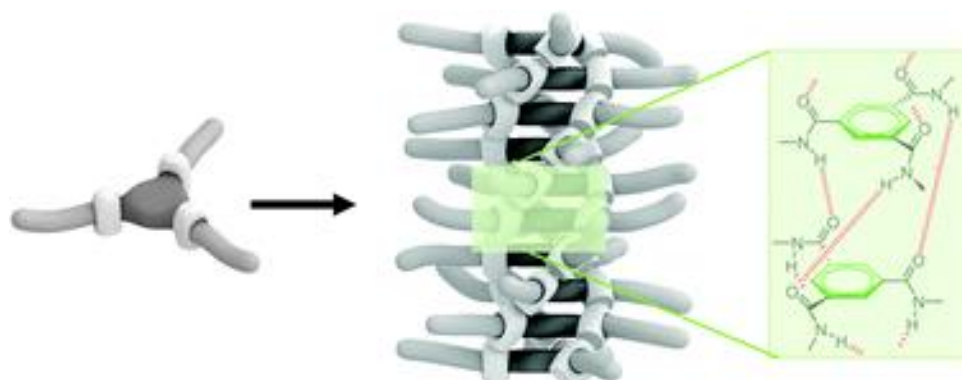


**Figure 2.31.** Schematic representation of benzene-1,3,5-tricarboxamide self-assembly into helical one-dimensional aggregates, which are stabilized by threefold intermolecular H-bonding.<sup>150</sup> Reprinted from reference 150 with permission.

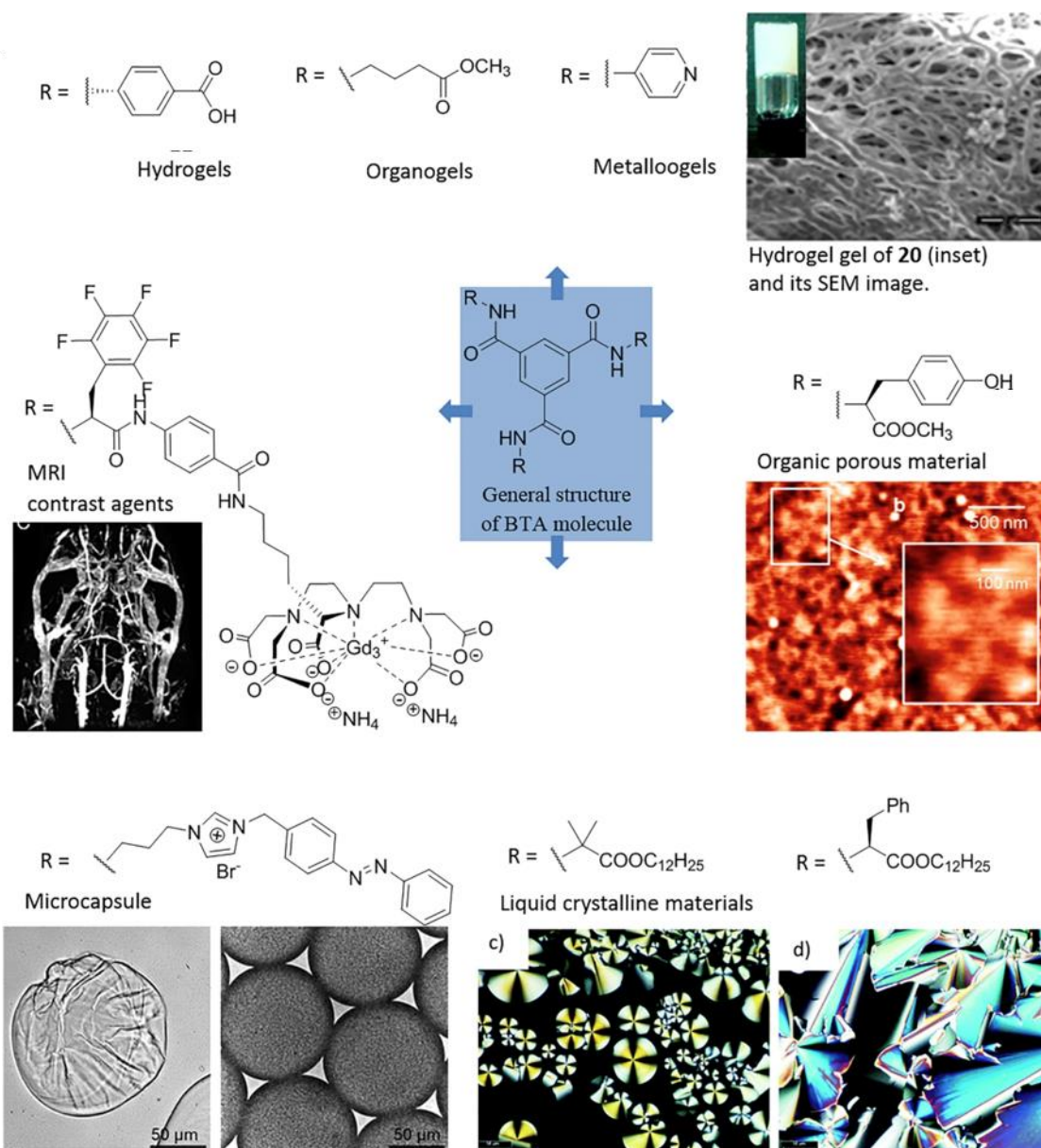


**Figure 2.32.** A generalized view of BTA molecules possessing different substituents that are found in various applications in different research fields.<sup>149</sup> Adapted from reference 149 with permission.

The fabrication of nanofibers has been attracting increasing attention in the past few years. Extensive research has been conducted as nanofibers possess the following advantages: (1) Facile fabrication conditions; (2) large-scale fabrication; (3) controlled responsivity with temperature, pH and other parameters; (4) reversibility and (5) outstanding mechanical properties. Thus, the supramolecular-based nanofibers show great potential in filter media, drug delivery and release, selective cell migration and adsorbent and catalyst support.<sup>151</sup> The self-assembly of BTA molecules into nanofibers

are normally carried out by a bottom-up method.<sup>151-155</sup> The Schmidt group, for example, described (Figure 2.33) that the formation of nanofibers can be achieved inside nonwoven. This procedure can be performed by immersing the nonwoven in the supramolecule solution at a high temperature, which ensures that the supramolecular motifs are totally dissolved. After the nonwoven was dragged out and evaporation of the solvent, the self-assembly nanofibers formed within the nonwoven.

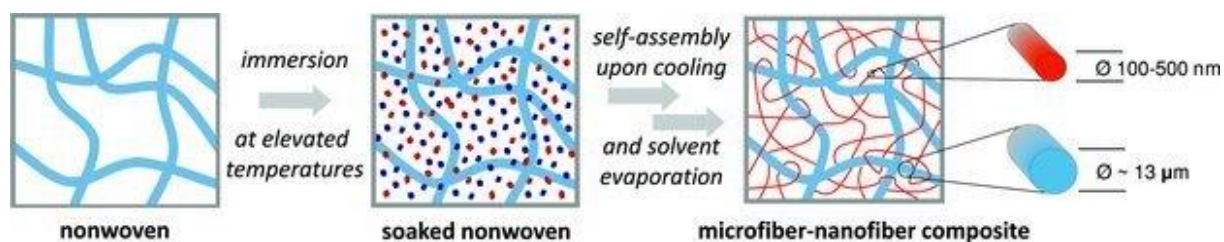


**Figure 2.33.** schematic representation of the in-situ supramolecular nanofiber formation by self-assembly, which yields microfiber-nanofiber composites. Blue fibers: nonwoven scaffold; red fibers: supramolecular nanofibers; blue dots: solvent; red dots: dissolved supramolecular building units.<sup>155</sup> Reprinted from reference 155 with permission.

### 3 Aim and Concept

Despite the fact that AuNP have been widely studied in the past few years because of their high potential in the field of catalysis and biology, vast areas still remain unexplored. This thesis focuses on the study and designing of AuNP conjugates for catalytic and photobiological applications. Firstly, efforts were devoted to figuring out the influence of the size of AuNP on the catalytic reactions. The work is continued by a study of the design of excellent carriers for AuNP. Furthermore, investigation into the photobiological directed assembly of AuNP has been performed and is presented in the thesis. The thesis is accordingly divided into four parts in which more details about the respective work are described and discussed.

1. A consensus in this research field is that smaller AuNP present higher catalytic activities than the bigger particles as they possess higher surface areas. However, very few researchers have studied the influence of the size of AuNP on the nitrophenol reductive reaction when the total surface of AuNP is kept the same. It is reasonable to predict that the total surface area is not the only dominating factor affecting the catalytic behavior. Hence, the aim of this part of the work is to shed more light on this scientific question, offering novel insights into the understanding of the catalytic reaction and making contributions to figuring out how to improve the catalyst activity.

2. In order to build on the first work mentioned previously, applications of AuNP catalysts were further investigated after the fundamental study. Despite the fact that various types of AuNP carriers have been developed in the past years, the design of novel carriers to stabilize AuNP with high catalytic activities without aggregation and leaching still remains a challenging task. New composites combining electrospun nonwoven with functionalized self-assembly nanofibers to stabilize the AuNP were studied in this project work. The ultimate goal is to yield high catalytic activity, reusability without leaching and aggregation even with extremely small AuNP with this framework.

3. It is well-known that the nonwoven bears some intrinsic drawbacks, for example, low porosity and long-term stability in the separation of the metal NP which hinder the efficient utilization of a wide variety of AuNP in the carrier and the efficiency of the separation of the AuNP. Inspired by the previous work, sponge was evaluated as it has higher surface to volume ratio than nonwoven. To the best of our knowledge, this is

the first time that sponge containing self-assembly nanofibers and short electrospun fibers have been developed. Thus, the primary aim of this project work is to develop mechanically stable sponge-type material containing the functionalized self-assembly nanofibers and electrospun fibers and study its properties. Based on the findings, exploration of their application potential in catalysis and filtration have also been performed.

4. It has already been demonstrated by several research groups that photoreceptor proteins undergo molecular responses to light under mild reaction conditions. In order to pioneer this property in material science, one project was done attempting to utilize and conjugate the light-induced homodimerization of light-oxygen-voltage (LOV) photoreceptors with AuNP. The assembly of AuNP can be achieved through the light-responsive photoreceptor. The ultimate goal of this work is to establish a new concept for reaction control from biology to macromolecular chemistry and extend the application scope of AuNP conjugated with genetically encoded light-responsive proteins.

## 4 Results and Discussion

### 4.1 Size-dependent AuNP catalytic behavior in 4-nitrophenol reduction

This work aims to study the influence of the size of the AuNP on their catalytic behavior. The nitrophenol reduction, which has been frequently studied in the past decades, was selected as the model reaction for this purpose. Previous studies have proven that the size, shape, chemical composition and ligand on the surface of the AuNP all have significant influences on their catalytic activities. However, the studies on the effects of the size of the AuNP on its catalytic behavior were normally based on the same amount of gold.<sup>156, 157</sup> To the best of our knowledge, only very a few studies have investigated the effect of the size of the AuNP on the condition that the total surface area of the AuNP was kept the same in the colloidal solution.<sup>158, 159</sup> Therefore, in this work, we adopted this precondition and AuNP of different sizes were investigated in nitrophenol reduction, to determine the apparent reaction rates of the nitrophenol reduction with AuNP catalysts. The AuNP with citrate and PVP capping ligand of different sizes were prepared and characterized, to study the effect of the average diameter of the AuNP on the catalytic reactivity.

**Table 4.1.1.** The preparation and the characterization of the AuNP of different sizes.

	Volume of citrate 1 wt% ( $\mu\text{L}$ )	$\lambda^{[b]}$ (nm)	TEM <sup>[c]</sup> (nm)	DLS <sup>[d]</sup> (nm)	Zeta Potential <sup>[d]</sup> (mV)
1	3750 <sup>[a]</sup>	518	9.8 $\pm$ 0.9	14 $\pm$ 1.6	-33.5 $\pm$ 3.5
2	650	519	16.9 $\pm$ 1.4	18.8 $\pm$ 0.4	-36.2 $\pm$ 1.7
3	438	520	19.6 $\pm$ 1.8	22.5 $\pm$ 1.2	-38.5 $\pm$ 0.4
4	375	526	35.2 $\pm$ 8.3	36.3 $\pm$ 0.3	-44.5 $\pm$ 4.6
5	313	528	42.1 $\pm$ 7.8	41.0 $\pm$ 0.1	-32.4 $\pm$ 0.5
6	250	538	58.1 $\pm$ 7.7	52.9 $\pm$ 0.4	-30.0 $\pm$ 0.7

[a] The concentration of  $\text{HAuCl}_4$  is  $1.0 \cdot 10^{-3}$  M.

[b]  $\lambda$  represents the wavelength where the maximal UV-Vis absorption of the Ct@AuNP colloidal dispersion appears.

[c] The average diameter of the AuNP was determined by TEM with at least 100 AuNP counted.

[d] The error was estimated error for the mean value. (Three measurements were taken into account)

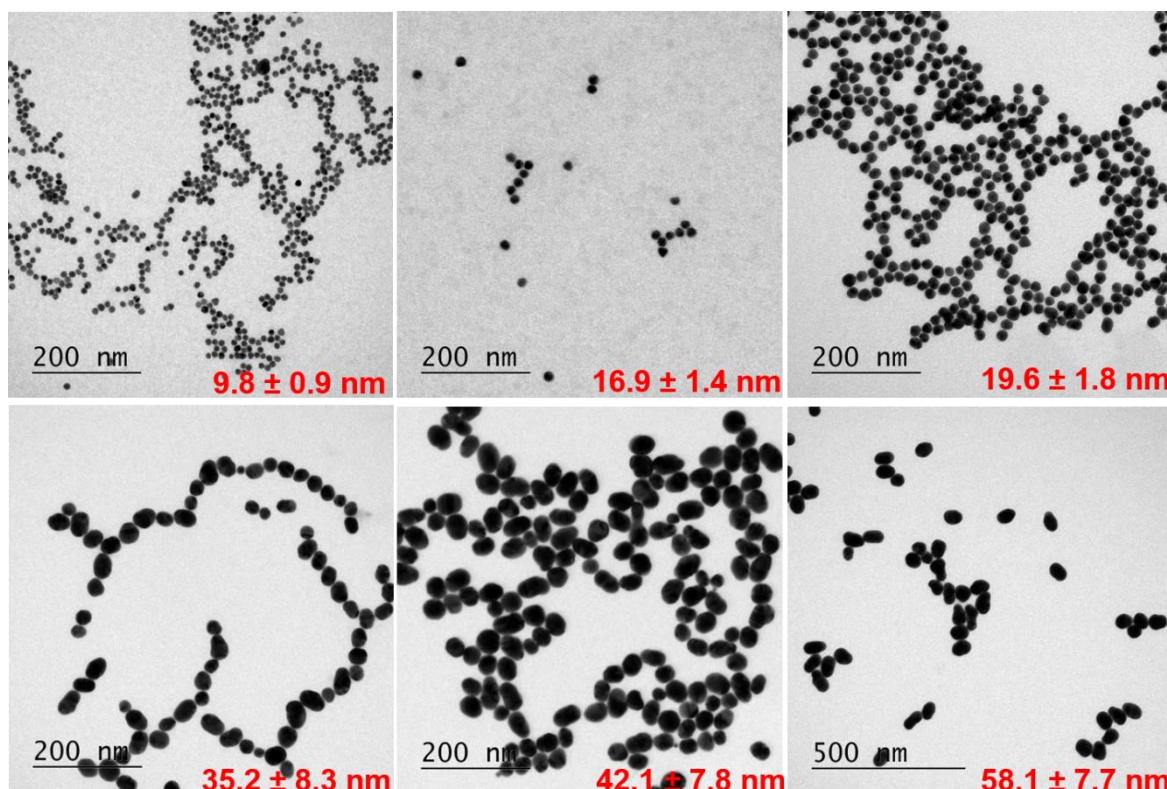


**Figure 4.1.1.** TEM images of the Ct@AuNP ranged from 10 - 58 nm prepared using the Frens method with some modifications.<sup>160</sup> Adaption from reference 160 with permission.

#### 4.1.1 Preparation of the Ct@AuNP and PVP@AuNP

The preparation of the AuNP of different sizes followed the traditional Frens method with small modifications. The AuNP of different sizes (10 – 58 nm) were synthesized by varying the ratio between the trisodium citrate and the chloroauric acid ( $\text{HAuCl}_4$ ), while the concentration of the  $\text{HAuCl}_4$  was fixed at  $0.25 \cdot 10^{-4}$  M for all the procedures except the synthesis of the 10 nm AuNP (Table 4.1). The concentration of the  $\text{HAuCl}_4$  was particularly tuned to  $1.0 \cdot 10^{-3}$  M for the preparation of the 10 nm AuNP. As is widely

known, the ligand on the surface of the AuNP also affects its catalytic performance. Thus, the synthetic method used to prepare the AuNP in this study can effectively eliminate the influence of the ligand on the catalytic behavior of the AuNP of different sizes. In addition, an excessive amount of trisodium citrate was employed in the synthetic procedure to exclude the influence of the residual  $\text{HAuCl}_4$  on the catalytic reaction.

#### 4.1.2 Characterization of the Ct@AuNP and PVP@AuNP

The results indicated that the size of the Ct@AuNP presented a decrease with an increase of the ratio between trisodium citrate and  $\text{HAuCl}_4$ , which can be observed via transmission electron microscopy (Figure 4.1.1). The size distribution of the Ct@AuNP was shown in Figure 4.1.2.

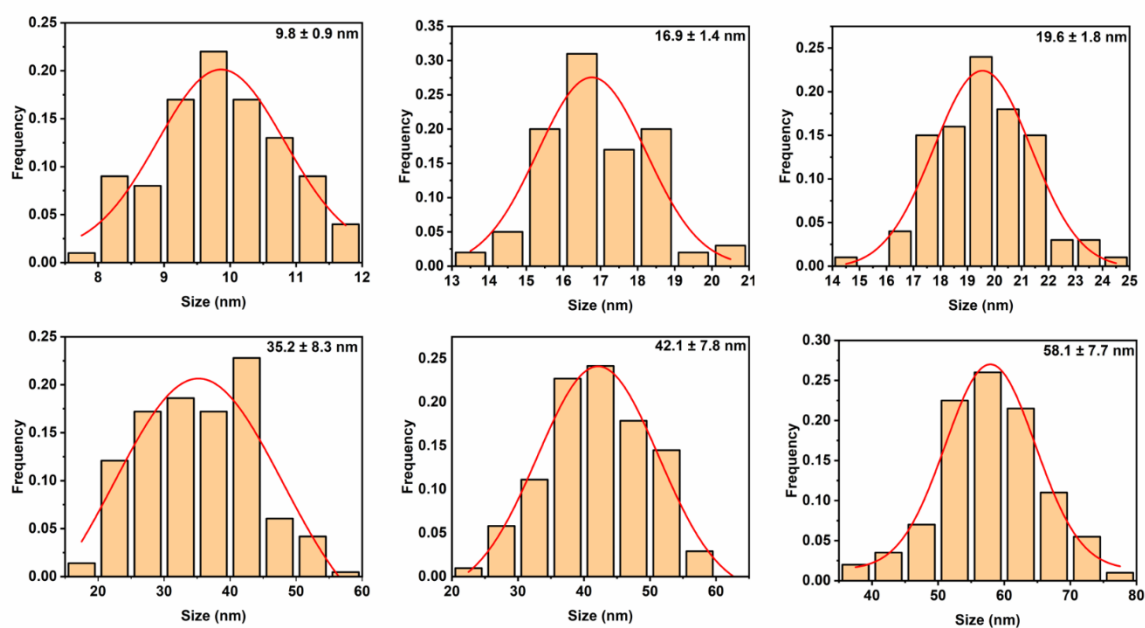


**Figure 4.1.2.** Size distribution of Ct@AuNP ranged from 10 to 58 nm prepared using the Frens method with some modifications.<sup>160</sup> Adaption from reference 160 with permission.

Furthermore, the red shift of the maximal absorption (Table 4.1.1) in the UV-Vis spectra indicates an increase of the size of the Ct@AuNP. The size distribution of the Ct@AuNP characterized by dynamic light scattering (DLS) is also in good agreement with the transmission electron microscopy (TEM) results (also see Table 4.1.1). The  $\zeta$  potentials of the Ct@AuNP of different sizes are in the range of -30 to -44.5 mV, which was contributed by the negative charge of the citrate on the surface of the AuNP (Table

4.1.1). The 10–58 nm PVP@AuNP was prepared by the ligand exchange method in aqueous solution under an ambient condition from the corresponding Ct@AuNP. The evaluation results of the morphology and the size distribution of the PVP@AuNP shown in Figure 4.1.3 imply that the PVP@AuNP has kept the same morphology and size distribution as the corresponding AuNP. These series of the PVP@AuNP investigated in the later catalytic application can effectively avoid the influence of unreacted gold and citrate ligand on the catalytic behavior of the AuNP. The UV-Vis analysis and  $\zeta$  potentials analysis were carried out to verify the successful ligand exchange. It presents a slight red shift of the maximal absorption in the UV-Vis spectra of the AuNP after the ligand exchange. The reason might be that PVP has a higher molecular weight than the citrate molecule. Moreover, the  $\zeta$  potentials of the PVP@AuNP of different sizes are in the range of -25.4 to -37.5 mV, due to the interaction of the PVP molecules with the surface of the AuNP. The  $\zeta$  potentials of the PVP@AuNP present a slight decrease in comparison to Ct@AuNP with the same size (Table 4.1.2). This is generally in a good agreement with what has been reported in the literature.<sup>161</sup> In addition, another piece of solid evidence proving the successful ligand exchange of the Ct@AuNP and PVP@AuNP comes from the examination of the stability of the colloidal dispersion by adding a large amount of sodium chloride, which could initiate the aggregation of the Ct@AuNP.<sup>162</sup> Nevertheless, the PVP@AuNP will present good stability under the same condition. Hence, the significant red shift of the UV-Vis absorption spectra can be observed with the Ct@AuNP of different sizes after the investigation of 0.3 M sodium chloride (Figure 4.1.4), whereas the UV-Vis spectra of the PVP@AuNP of different sizes remained the same before and after the addition of a same amount of sodium chloride (Figure 4.1.5).

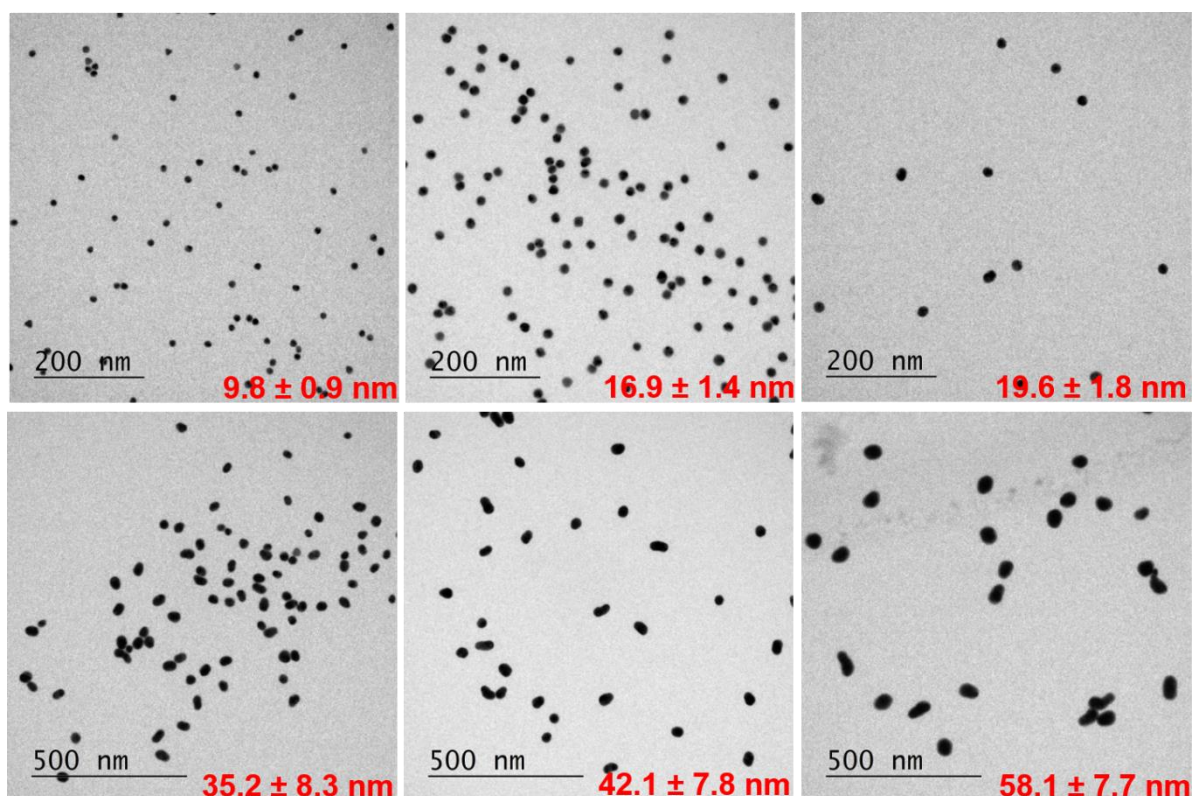


**Figure 4.1.3.** TEM images of the PVP@AuNP ranged from 10 - 58 nm prepared by ligand exchange method from Ct@AuNP.<sup>160</sup> Adaption from reference 160 with permission.

**Table 4.1.2.** Experimental details of the preparation of the PVP@AuNP and their characterizations.

Entry	Size (nm)	$\lambda^{[a]}$ (nm)	$\lambda^{[b]}$ (nm)	Zeta Potential <sup>[c]</sup> (mV)
1	$9.8 \pm 0.9$	521	520	$-29.7 \pm 1.5$
2	$16.9 \pm 1.4$	520	520	$-27.1 \pm 0.9$
3	$19.6 \pm 1.8$	523	523	$-37.5 \pm 2.4$
4	$35.2 \pm 8.3$	528	528	$-25.4 \pm 0.21$
5	$42.1 \pm 7.8$	530	530	$-29.4 \pm 0.2$
6	$58.1 \pm 7.7$	539	539	$-27.7 \pm 1.2$

[a] The wavelength where the maximal UV-Vis absorption peak of the PVP@AuNP colloidal dispersion is.

[b] The wavelength where the maximal UV-Vis absorption peak of the PVP@AuNP colloidal dispersion after the addition of 1 mL 0.3 M NaCl aqueous solution.

[c] The error was estimated error for the mean value. (Three measurements were taken into account.)

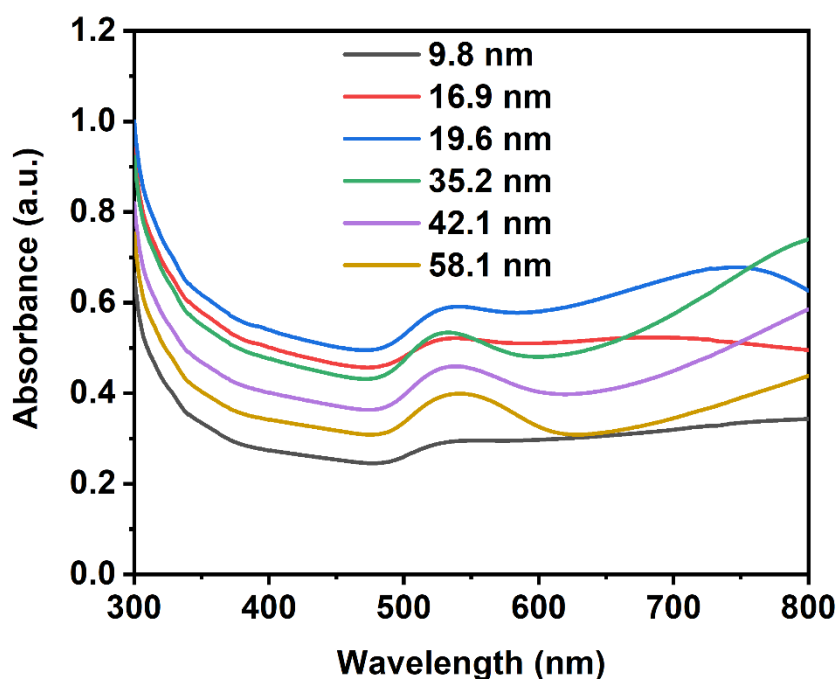


**Figure 4.1.4.** UV-Vis spectra of the colloidal Ct@AuNP of different sizes after the addition of the 1 mL 0.3 M sodium chloride aqueous solution.<sup>160</sup> Adaption from reference 160 with permission.

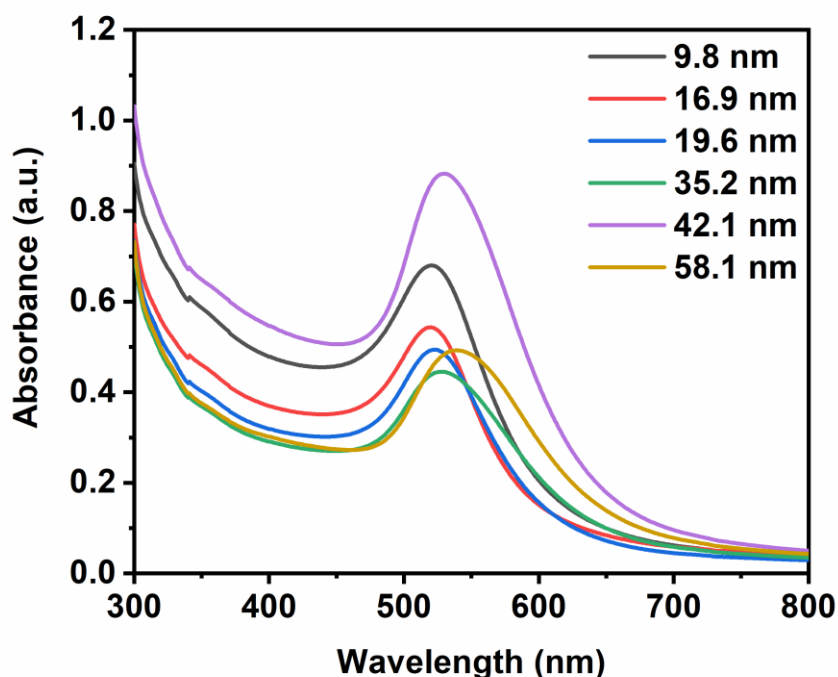


**Figure 4.1.5.** UV-Vis spectra of the colloidal PVP@AuNP of different sizes after the addition 1 mL 0.3 M sodium chloride aqueous solution.<sup>160</sup> Adaption from reference 160 with permission.

In our work, the evaluation of the total surface area of the AuNP plays an important role in comparing the apparent catalytic reaction rates of the AuNP of different sizes. The following equations were used for the calculation of the total surface area and deducing how the total surface area can be kept the same (Figure 4.1.6). This work is based on the assumption that both the small and the big AuNP match the spherical model and were investigated in the catalytic solution with the equal total areas. However, the shape of the AuNP will deviate on average from the spherical shape with an increasing size. Thus, the small-angle x-ray scattering (SAXS) as a volume-sensitive technique was performed to evaluate the average size of the AuNP (Figure 4.1.7). Herein, a concentrated 10 nm PVP@AuNP and a diluted 42 nm AuNP were selected to be measured. The experimental data of both colloidal dispersions can be modeled by a spherical NP with a Gaussian distribution. Herein, the radius of the small NP (10 nm PVP@AuNP evaluated by TEM) was determined by SAXS and has a value of  $5.6 \pm 0.5$  nm, and the radius of the big NP (42 nm PVP@AuNP by TEM) was determined by SAXS to be  $15.8 \pm 2.4$  nm. Hence, the assumption of the spherical

model of AuNP is adequate enough for the calculation of total surface area (Figure 4.1.6).

$S_{total1} = S_{total2}$	S: surface area
$N_1 4\pi r_1^2 = N_2 4\pi r_2^2$	$N_1$ : the number of the AuNP-1
$N_1 \pi d_1^2 = N_2 \pi d_2^2$	$N_2$ : the number of the AuNP-2
$m_1 = N_1 \rho v_1$	$r_1$ : the radius of the AuNP-1
$m_2 = N_2 \rho v_2$	$r_2$ : the radius of the AuNP-2
If $m_1$ is known	$d_1$ : the diameter of the AuNP-1
$m_2 = m_1 \frac{d_2}{d_1}$	$d_2$ : the diameter of the AuNP-2
	$v_1$ : the volume of single AuNP-1
	$v_2$ : the volume of the AuNP-2

**Figure 4.1.6.** The procedure for the calculation of total surface areas of the AuNP investigated in the catalytic reaction.

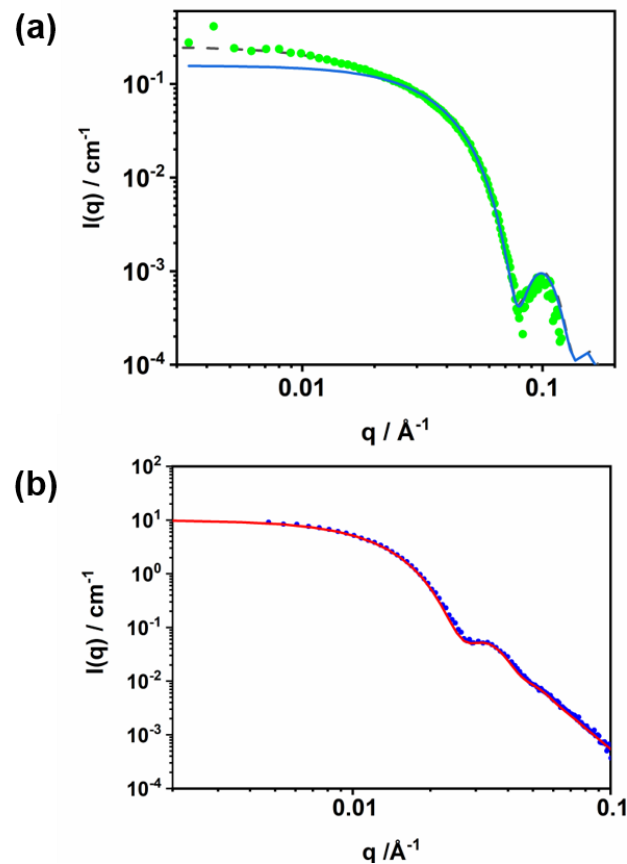


**Figure 4.1.7.** (a) PVP@AuNP dispersion measured by small angle X-ray scattering (SAXS). a, 10 nm AuNP in main text with average diameters  $d_{TEM} = 9.8 \pm 0.9$  nm; b,

42 nm AuNP in main text with average diameters  $d_{\text{TEM}} = 42.1 \pm 7.8$  nm. The polydisperse non-interacting hard spheres model was used to fit the experimental data (symbols) in SAXS with a Gaussian distribution and Radius  $R$  (solid lines, index SAXS). For the small and bigger AuNP, the results are  $R_{\text{SAXS}} = 5.6 \pm 0.5$  nm and  $R_{\text{SAXS}} = 15.8 \pm 2.4$  nm, respectively. The error in SAXS stands for the standard deviation of the Gaussian particle distribution. What should be noted here is that the Au core strongly dominates the scattering intensity  $I(q)$ , as the contrast of the stabilizing PVP ligand is low (excess electron densities: ca.  $4300 \text{ nm}^{-3}$  for Au, ca.  $330 \text{ nm}^{-3}$  for PVP). In another word, the particle size determined corresponds largely to the core size. (b) This simple model can be used to describe the diluted dispersion of the 42nm AuNP very well. For the small AuNPs derivations are noticed at low  $q$ , which might be explained by inter-particle interactions. As this dispersion has a much higher concentration and the likelihood of inter-particle interactions are higher, the stick hard spheres model<sup>163</sup> is used to describe the data more accurately (dashed lines in Figure 4.1.7a). This model has the inter-particle structure factor of a hard sphere fluid included, together with a narrow attractive potential well.

The interaction potential  $U(r)$  is given by  $U(r) = \begin{cases} \infty, & r < 2R \\ 0, & > 2R + \Delta \\ -U_0, & \text{between} \end{cases}$ , where  $\Delta$  is the width

of the square well and  $U_0$  the depth in units of  $kT$  ( $k$  Boltzmann constant,  $T$  temperature). The interaction strength is described by the stickiness  $\varepsilon$  and the perturbation parameter  $\tau$  which are connected to  $U_0$  by  $\varepsilon = \frac{\exp(\frac{U_0}{kT})}{12\tau}$  and  $\tau = \frac{\Delta}{2R+\Delta}$ . The calculation shown in Figure 4.1.7a (dashed line) is done with  $d_{\text{SAXS}} = 11.2 \pm 1.0$  nm (Gaussian distribution),  $\varepsilon = 0.05$  and  $\tau = 0.1$ .<sup>160</sup> Adaption from reference 160 with permission.

### 4.1.3 Catalytic Study of Ct@AuNP and PVP@AuNP for 4-nitrophenol reduction

In this study, the 4-nitrophenol reduction was chosen as the model reaction, because it can easily be tracked by UV-Vis under ambient conditions without any side product. Furthermore, this model reduction has been widely studied in the previous literature, which can be of great help in the evaluation of the reaction process. This work

highlights the influence of the size of the AuNP on the 4-nitrophenol reduction if the total surface area of the AuNP was kept the same. Consequently, the procedure displayed in Figure 4.1.6 was applied to calculate the total surface area of the AuNP employed in the nitrophenol reduction. The amount of gold applied to the reduction of 4-nitrophenol is proportional to the diameter of the AuNP (Figure 4.1.6), which is determined by inductively coupled plasma optical emission spectroscopy (ICP-OES). The amounts of the Ct@AuNP and PVP@ AuNP investigated in the catalytic reaction are summarized in Table 4.1.3. The total surface areas of the AuNP in the catalytic system were kept the same by tuning the amount of the AuNP used.

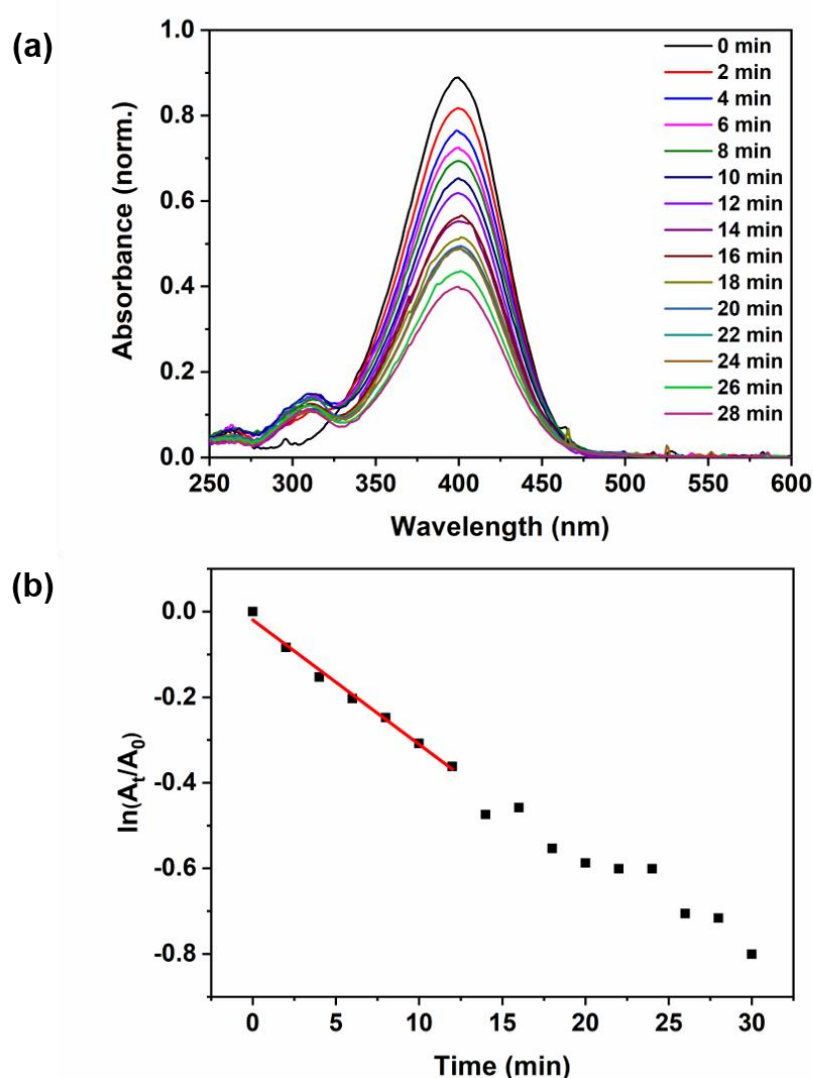


**Figure 4.1.8.** (a) The change of the maximal absorption in the UV-Vis spectra of the reduction of nitrophenol by sodium borohydride over time using 10 nm Ct@AuNP as the catalyst. (b) The first-order linear fitting of the nitrophenol reduction, and the

apparent reaction rate constant ( $k_{app}$ ) obtained from the linear fit.<sup>160</sup> Adaption from reference 160 with permission.

The reduction of 4-nitrophenol was performed in the presence of an excessive amount of freshly prepared sodium borohydride as the reducing agent under ambient conditions. After the addition of NaBH<sub>4</sub> to the catalytic solution, 4-nitrophenol was converted to the corresponding 4-nitrophenolate, and the UV absorption peak of 4-nitrophenol shifted from 317 to 400 nm. The colour of the solution changed from light to dark yellow. The reaction could not be initiated without the addition of a AuNP catalyst into the catalytic solution. A significant decrease of the peak at 400 nm indicated that 4-aminophenol was formed, accompanied by the occurrence of the peak around 300 nm. Since the amount of sodium borohydride is more excessive than that of 4-nitrophenol, 4-aminophenol, as the product, can be prevented from oxidation during the reaction. Figure 4.1.8a presents the UV-Vis spectra of the reductive procedure over time using 10 nm Ct@AuNP. The conversion of the reaction can be determined from the ratio between the concentration of 4-nitrophenolate at time t to its initial concentration. Alternatively, it can be described by the absorption ratio ( $A_{4-NP}/A_{4-NP(0)}$ ). The reaction can be assumed as pseudo-first-order by employing an excessive amount of sodium borohydride in the reaction. Thus, the reaction rate is regarded to be only independent on the concentration of 4-nitrophenol. The apparent catalytic rate constant of the 4-nitrophenol reduction by sodium borohydride in the presence of the AuNP can be described by the following equation 4.1.1. Accordingly, the apparent catalytic rate constant  $k_{app}$  was determined as the slope of the linear correlation of  $\ln(A/A_0)$  over time t. (Figure 4.1.8b)

$$-\ln \frac{C_t}{C_0} = -\ln \frac{A_t}{A_0} = kt \quad \text{Equation 4.1.1}$$

$k$  stands for the apparent reaction rate constant, and  $t$  represents the reaction time.  $C_t$  is the concentration of 4-nitrophenolate at time  $t$  and  $C_0$  is the initial concentration of 4-nitrophenol.  $A_t$  represents the corresponding absorbance peak of nitrophenolate in the UV-Vis spectra at time  $t$ .  $A_0$  is the initial absorbance peak of 4-nitrophenolate after the addition of the catalyst.

It should be noted that the average diameter value of the AuNP investigated in equations (Figure 4.1.6) can exit an estimated error to reliably evaluate the rate

constant  $k$ . Thus, the catalytic reaction, for the larger AuNP, was performed in two different ways. Namely, one is based on the total surface areas obtained from the diameter determined by TEM (this  $k$  value is defined as  $k_{TEM}$ ), the other utilized the total surface areas obtained from the diameter determined by SAXS (this  $k$  value is defined as  $k_{SAXS}$ ).

**Table 4.1.3.** Rate constant values ( $k_{TEM}$ ) observed employing citrate and PVP@AuNP catalysts of different sizes and the mass of gold in the AuNP colloidal solution used in the catalytic reaction.

Size (nm)	$m^{[a]}$ ( $\mu\text{g}$ )	$k_{TEM}^{[b]}$ ( $\text{min}^{-1}$ )	$k_{TEM}^{[c]}$ ( $\text{min}^{-1}$ )
$9.8 \pm 0.9$	0.26	$0.03 \pm 0.006$	$0.052 \pm 0.016$
$16.9 \pm 1.4$	0.44	$0.054 \pm 0.017$	$0.063 \pm 0.005$
$19.6 \pm 1.8$	0.51	$0.063 \pm 0.006$	$0.081 \pm 0.019$
$35.2 \pm 8.3$	0.92	$0.083 \pm 0.010$	$0.088 \pm 0.006$
$42.1 \pm 7.8$	1.10	$0.092 \pm 0.008$	$0.097 \pm 0.006$
$58.1 \pm 7.7$	1.53	0.10	$0.11 \pm 0.022$

[a] The mass of gold was determined by ICP-OES.

[b] Ct@AuNP was investigated in the catalytic reaction.

[c] PVP@AuNP was investigated in the catalytic reaction.

The AuNP of six different sizes with a citrate or PVP ligand were investigated in the 4-nitrophenol reduction under the same conditions. The effect of the AuNP particle size was studied by tuning the amounts of Ct@AuNP and PVP@AuNP of different sizes to keep the AuNP total surface area constant. Figure 4.1.9 displays the plot of the  $\ln(A/A_0)$  of the reaction catalyzed by Ct@AuNP of different sizes over time, and the apparent reaction rate constant can be estimated as the slope of the linear correction of  $\ln(A/A_0)$  over time (results were summarized in Table 4.1.3). Herein, the highest catalytic

reaction rate constant was achieved by using 58 nm Ct@AuNP as the catalyst ( $k_{\text{TEM}} = 0.10 \text{ min}^{-1}$ ). On the contrary, 10 nm Ct@AuNP presented the lowest apparent reaction rate constant for the 4-nitrophenol reduction ( $k_{\text{TEM}} = 0.03 \text{ min}^{-1}$ ). These results indicated that the apparent reaction rate constant of 4-nitrophenol gradually increased with the increasing size of the Ct@AuNP (Figure 4.1.10) if the total surface area of the AuNP of different sizes was kept the same. The Ct@AuNP of larger diameters presented better catalytic performance than those of smaller diameters.

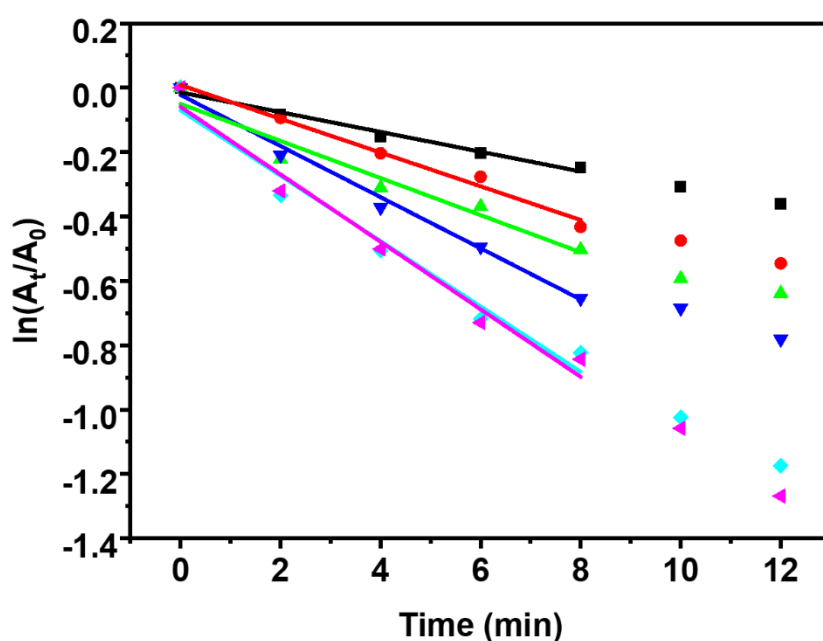


**Figure 4.1.9.** First-order linear fitting of the  $\ln(A_t/A_0)$  over time of 4-nitrophenol reduction by investigating Ct@AuNP ranging from 10 to 58 nm.<sup>160</sup> Adaption from reference 160 with permission.

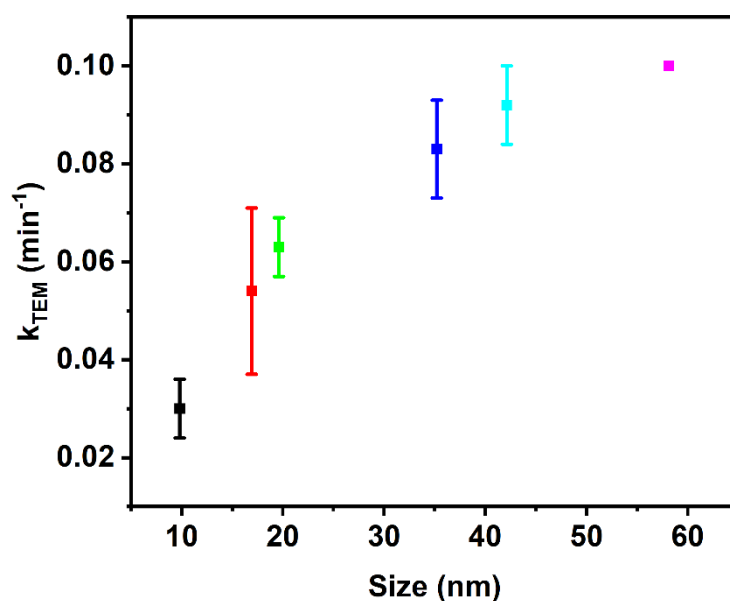


**Figure 4.1.10.** The apparent rate constants ( $k_{TEM}$ ) with standard deviations of the 4-nitrophenol reduction reaction by investigating Ct@AuNP of different sizes (10 to 58 nm).<sup>160</sup> Adaption from reference 160 with permission.

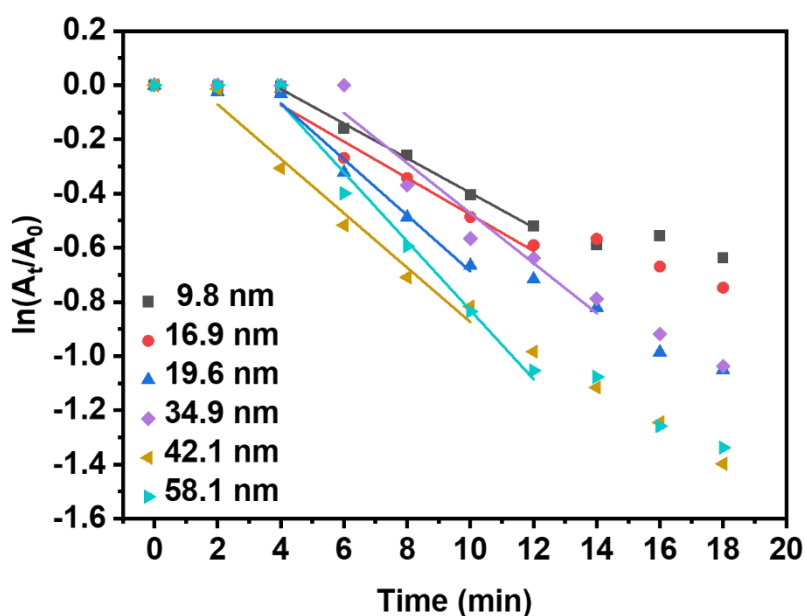


**Figure 4.1.11.** First-order linear fitting of the  $\ln(A_t/A_0)$  over time of 4-nitrophenol reduction by investigating PVP@AuNP ranged from 10 to 58 nm.<sup>160</sup> Adaption from reference 160 with permission.

The PVP@AuNP was prepared via place ligand exchange method from the original Ct@AuNP in aqueous dispersion to exclude the influence of the ligand and unreacted gold on the catalytic behavior of the AuNP catalyst. The dispersion of the PVP@AuNP was then investigated in 4-nitrophenol reduction under exactly the same conditions as the Ct@AuNP catalyst. The 4-nitrophenol reduction reaction catalyzed by PVP@AuNP ranging from 10 to 42 nm has a characteristic induction period during which no reaction takes place (Figure 4.1.11). The apparent reaction rate constant can be evaluated by linear fitting of the  $\ln(A/A_0)$  of the reaction catalyzed by 10 to 58 nm PVP@AuNP versus time. After the induction time, the apparent reaction rate constant presents an increasing trend with an increasing size of the AuNP (Table 4.1.3 and Figure 4.1.12). The highest  $k_{TEM}$  value ( $0.11 \text{ min}^{-1}$ ) was reached by investigating 58 nm PVP@AuNP as the catalyst, while the lowest  $k_{TEM}$  value ( $0.052 \text{ min}^{-1}$ ) was obtained by using the 10 nm PVP@AuNP as the catalyst. The total surface area of the PVP@AuNP for all the catalytic reactions was kept the same by varying the amount of gold used in the reaction. The results indicated that a bigger PVP@AuNP presented higher catalytic activities than a smaller one in the range of 10 to 58 nm (Figure 4.1.12). Thus, the PVP@AuNP as the catalyst has a similar tendency to that of Ct@AuNP. The apparent reaction rate constant presented an increase with the increasing size of Ct@AuNP and PVP@AuNP.

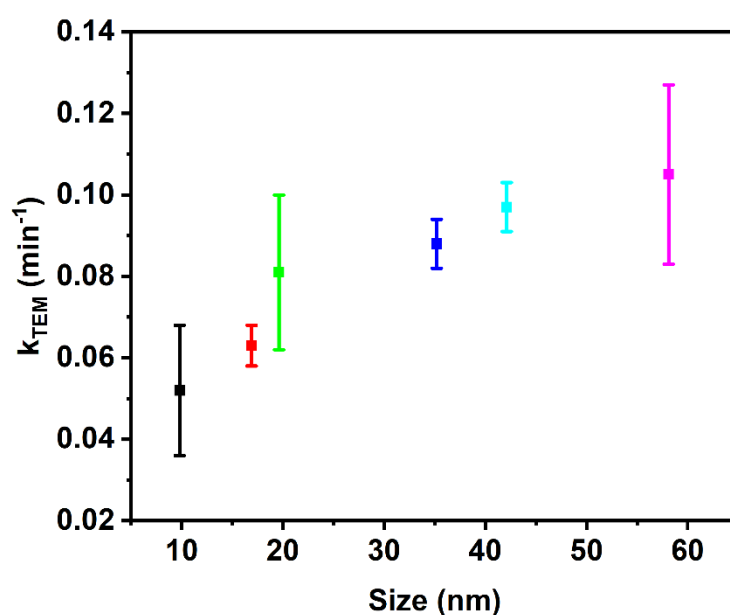


**Figure 4.1.12.** The apparent rate constants ( $k_{TEM}$ ) with standard deviations of the 4-nitrophenol reduction reaction by investigating PVP@AuNP of different sizes (10 to 58 nm).<sup>160</sup> Adaption from reference 160 with permission.

**Table 4.1.4.** Rate constant values observed by investigating Ct@AuNP and PVP@AuNP as the catalysts with size evaluation by SAXS.

<b>Size<sup>[a]</sup></b> <b>(nm)</b>	<b>m<sup>[b]</sup></b> <b>(<math>\mu</math>g)</b>	<b><math>k_{SAXS}</math><sup>[c]</sup></b> <b>(min<sup>-1</sup>)</b>	<b><math>k_{SAXS}</math><sup>[d]</sup></b> <b>(min<sup>-1</sup>)</b>
31.6 nm	0.83	0.073 $\pm$ 0.009	0.081 $\pm$ 0.002

[a] The size (diameter) of PVP@AuNP was determined by SAXS measurement.

[b] The mass of gold was determined by ICP-OES.

[c] Ct@AuNP were investigated in the catalytic reaction.

[d] PVP@AuNP were investigated in the catalytic reaction.

As has been discussed before, the catalytic reaction was carried out in another way, namely, with the total surface area calculated based on the diameter determined by SAXS. The apparent reaction rate constant was evaluated by the aforementioned method. The  $k_{SAXS}$  value reached 0.073  $\pm$  0.009 min<sup>-1</sup> for the 32 nm Ct@AuNP (determined by SAXS) and 0.081  $\pm$  0.009 min<sup>-1</sup> for the corresponding PVP@AuNP (Table 4.1.4). Therefore, the catalytic reaction rate achieved using bigger AuNP is higher than that from using the smaller AuNP. It can be deduced that the value of  $k_{SAXS}$  is in the same range as the  $k_{TEM}$ . It can be concluded that the spherical model is suitable for inserting the equation for calculating the total surface area (Figure 4.1.6), to obtain an average value of the catalytic reaction rate constant.

The effect of the surface area has been very well studied and reported in many published articles. The surface area is generally regarded as the dominating factor of the catalytic activity. The AuNP with higher total surface areas in the system present higher catalytic activity, thus, leading to a higher catalytic reaction rate. The total surface area was kept constant for all AuNP of different sizes in this work. The results indicated that the catalytic reaction rate does not only depend on the surface area but also on the size of the particles. The bigger AuNP offers higher catalytic activity than

the smaller ones when the total surface area is kept the same. Three different plausible causes to explain these results are discussed in the following part: the defect on the surface of the AuNP (crystalline structure of the surface of the AuNP), the diffusion of the reactants to the catalytic surface, and the ligand density on the surface of the AuNP.

The high resolution of TEM was performed to investigate how the catalytic behavior of the AuNP is influenced by their surface morphology. (Figure 4.1.13) Herein, the 10 and 42 nm Ct@AuNP were selected as the representatives to study their crystal structures. The selected area diffraction (SAED) patterns of both 10 and 42 nm Ct@AuNP present the characteristic polycrystalline features (Figure 4.1.14 and 4.1.15). However, apparent differences can still be observed among individual Ct@AuNP (Figure 4.1.13). In detail, there is either single crystalline or polycrystalline structure for 10 nm Ct@AuNP (Figure 4.1.13 b and d). The 42 nm Ct@AuNP contains a polycrystalline structure proven by the HR-TEM (Figure 4.1.13f). In addition, amorphous regions seem to be contained within the surface of the AuNP. However, previous studies have already proven that the AuNP normally can form crystalline structures. Therefore, it can be assumed that the amorphous regions (Figure 4.1.13f) were contributed by the different crystallographic planes. Figure 4.1.13f also indicated that 42 nm Ct@AuNP has more defects between the different crystalline domains. Defects of this type might be the twin boundary, grain boundary, edge dislocation, screw dislocation, stepped surface, kink or island.<sup>164</sup> In summary, the bigger AuNP are expected to contain more defects than the smaller AuNP as a result of the synthetic method.

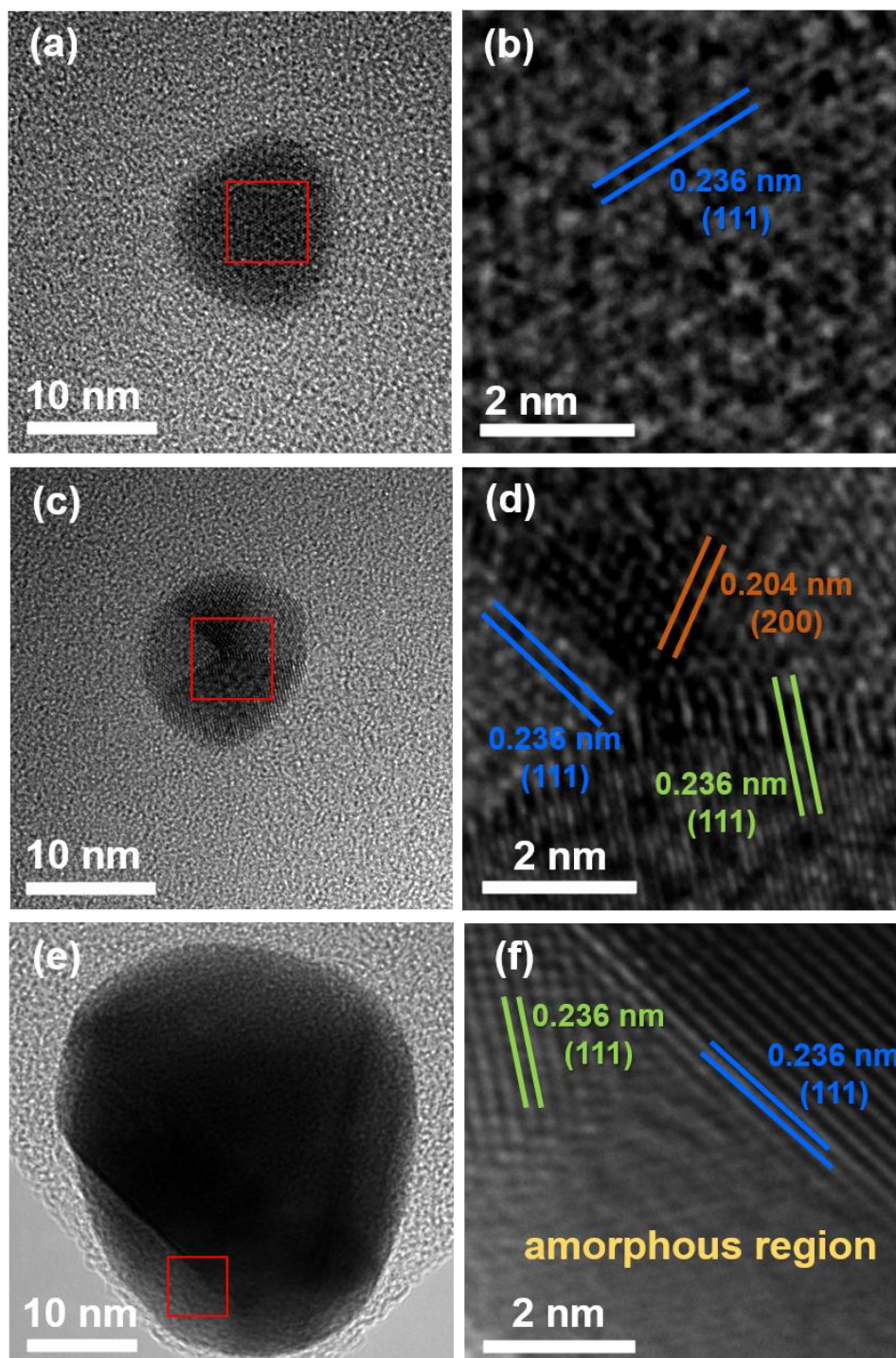


**Figure 4.1.13.** (a) TEM image of the 10 nm Ct@AuNP with a single crystalline structure. (b) HR-TEM image of the 10 nm Ct@AuNP. (c) HR-TEM image of the 10 nm Ct@AuNP containing a polycrystalline structure. (d) HR-TEM image of the 10 nm Ct@AuNP with a polycrystalline structure. (e) TEM image of the 42 nm Ct@AuNP (f) HR-TEM image of the 42 nm Ct@AuNP with polycrystalline and amorphous structures.<sup>160</sup> Adaption from reference 160 with permission.

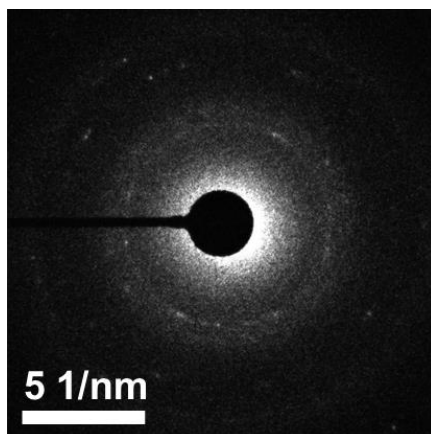


**Figure 4.1.14.** SAED patterns of 10 nm Ct@AuNP.<sup>160</sup> Adaption from reference 160 with permission.

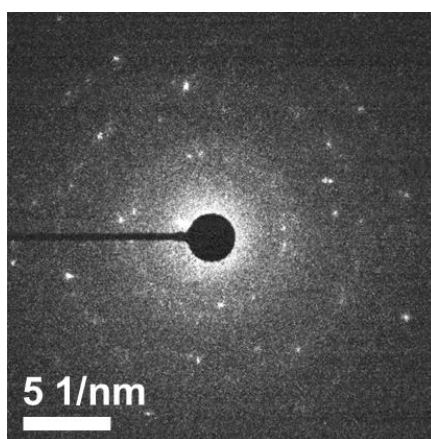


**Figure 4.1.15.** SAED patterns of 42 nm Ct@AuNP.<sup>160</sup> Adaption from reference 160 with permission.

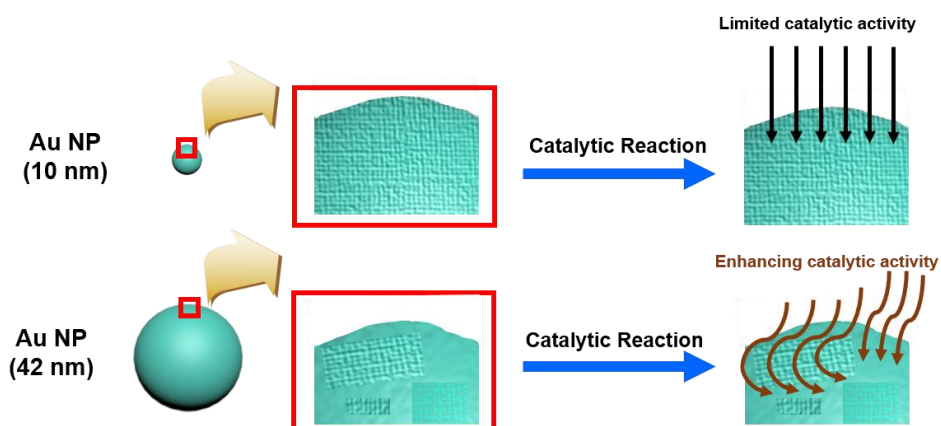


**Figure 4.1.16.** Illustration of the plausible mechanism of 42 nm AuNP processing higher catalytic activity than 10 nm AuNP.<sup>160</sup> Adaption from reference 160 with permission.

The 10 nm and 42 nm AuNP that are different in their crystallinity degrees might be the core factor influencing their catalytic performance in the nitrophenol reduction. An illustration (Figure 4.1.16) will yield the hypothesis to explain the influence of the defects on the catalytic behavior of the AuNP of 10 and 42 nm in detail. It was described that the 10 nm AuNP contains both single crystalline and polycrystalline structures. By contrast, the 42 nm AuNP possesses a polycrystalline and distortional structure. These types of structures indicated that the bigger NP has more defects than the smaller one. A lot of literature has already suggested that the defects on the surface of the NP can ease the association and dissociation of the reagents on the surface of the NP, and can also facilitate the attachment of the active species of the catalytic reactions onto the surface of the NP.<sup>165-167</sup> In addition, it can also be assumed that the defects on the surface of the AuNP are inclined to leach gold atoms to the catalytic solution, which can be useful for catalyzing the nitrophenol reduction. Hence, the defects of the bigger AuNP can be the key factor leading to the higher catalytic activity than the smaller AuNP.

The simulation work was solely done by Gabriel Sitaru and is described here for the sake of the complementment of this thesis.

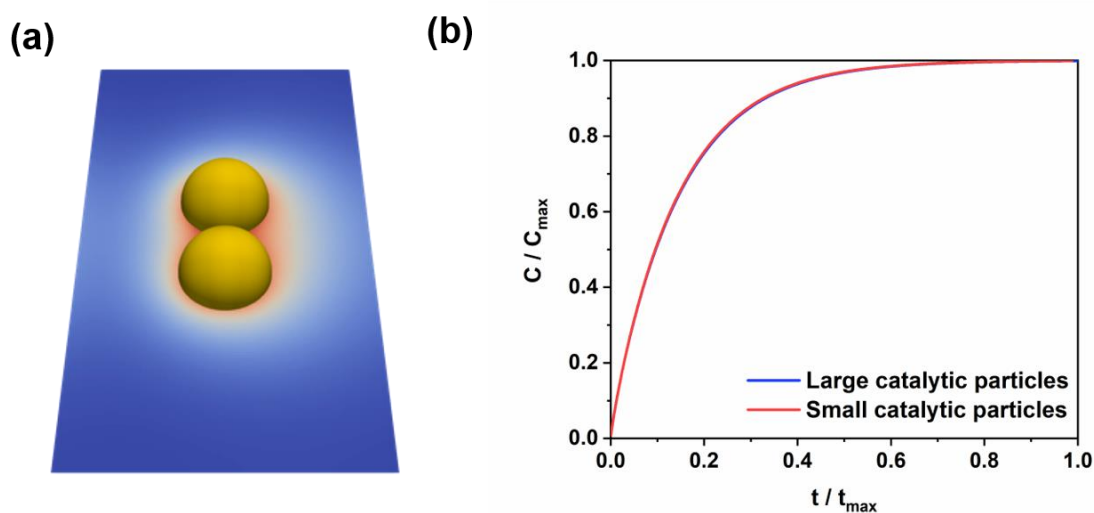


**Figure 4.1.17.** (a) Illustration of the product species concentrations for the scenario of small spheres at  $\frac{t}{t_{max}} = 0.01$ . Low and high concentrations are represented by blue and red lines, respectively. (b) In contrast to the experimental findings, It is suggested by our diffusion-reaction model that very similar catalytic activities are exhibited by

small and large particles. Thus, surface-modified diffusion is not an possible explanation for the experimental findings.<sup>160</sup> Adaption from reference 160 with permission.

Another reason why larger NP possess higher catalytic activity might be that the reactant diffusion in the vicinity of the surface of AuNP is modified. The time that a molecule stays close to the surface of AuNP is extended. To verify if this assumption stands, a computational algorithm was employed, together with a Lattice-Boltzmann scheme, in order to solve with the convection-diffusion-equation (see Methods). To perform this simulation, either one big or two small AuNP are set to be contained in a periodic box, and the box is surrounded by reactant species A (nitrophenol) solution with a homogenous concentration initially. NaBH<sub>4</sub> investigated is in excessive amount in comparison with nitrophenol, just like in the experiment. Therefore, a first-order reaction from nitrophenol (A) to aminophenol (B) was set to occur whenever the reactant reaches the close territory of the AuNP. Either one large or two small NP that are placed in a periodic box was compared with two simulation scenarios. The selection of the radius of NP yielded the same total surface area for both cases. Figure 4.1.17a displays a snapshot of the latter simulation.

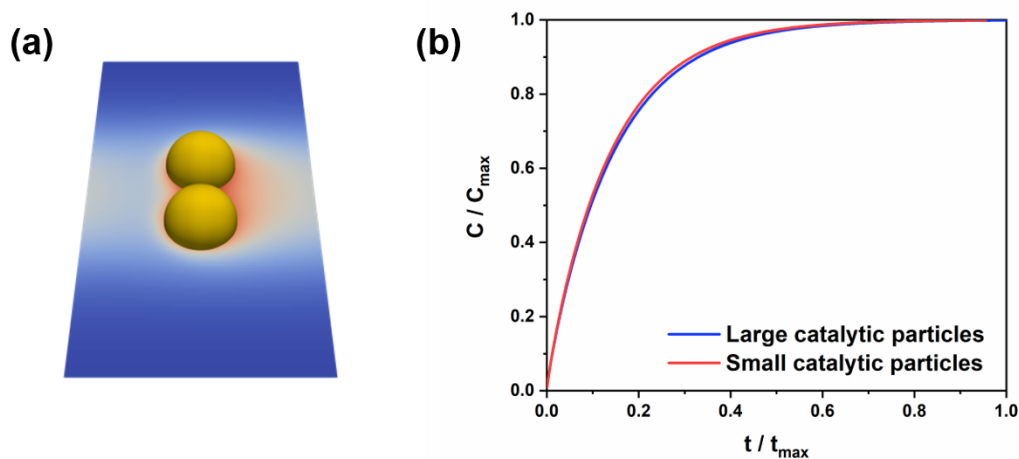


**Figure 4.1.18.** (a) Illustration of the product concentration if hydrodynamic advection is included (flow direction from left to right) in addition to reaction and diffusion. (b) However, the resulting catalytic activity is virtually not influenced.<sup>160</sup> Adaption from reference 160 with permission.

The reaction progress was illustrated in Figure 4.1.17b for both scenarios. In the simulation, the reaction rate showed no dependency on the size of AuNP, which is clearly the opposite to the experimental findings. An additional hydrodynamic flow in the experiment that corresponds to stirring applied did not have any influence on the results, which is shown in Figure 4.1.18. Further study was performed to study whether the surface of AuNP has an influence on the diffusion coefficients of the reactant molecules or not. What is known from literature is that molecule diffusion can be slowed down by an increasing hydrodynamic resistance and an anisotropy is induced in the system. This means perpendicular diffusion to the surface is more obstructed in comparison with lateral diffusion. Therefore, a particle model (see Methods) taking into consideration the anisotropic surface-modified diffusion was adopted to evaluate this effect.<sup>168, 169</sup> However, it can be seen in Figure 4.1.19 that the effects on the overall reaction efficiency are practically no different for the small and large NP. As a conclusion of this theoretical study, reactant diffusion modified by the surface near the NP cannot be the cause of the experimentally observed enhanced catalytic performance of the larger AuNP.

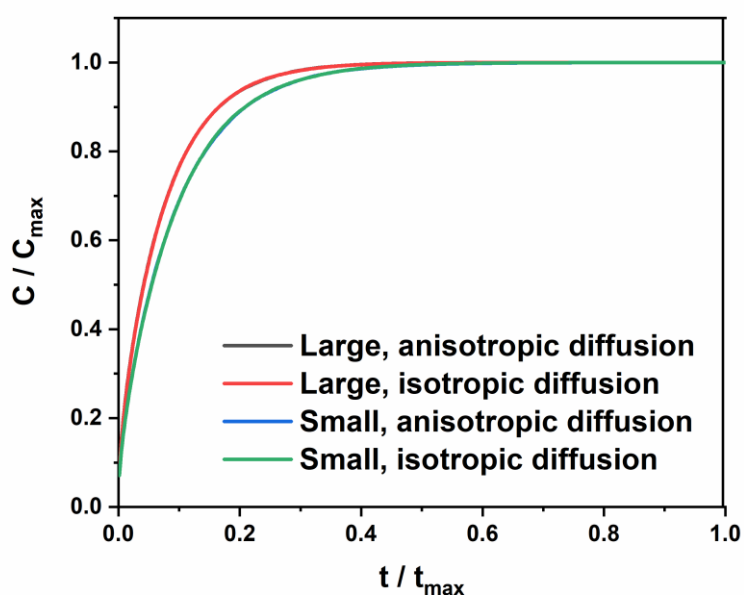


**Figure 4.1.19.** Reaction progress in the simple particle model with isotropic, homogeneous diffusion (red and blue curves), and reaction progress in a more complex particle model that has the anisotropic, non-homogeneous surface-modified

diffusion coefficients (cyan and brown curves) accounted for. In all cases, the reaction progress is very similar. Thus, the conclusion in the main text that even a complex surface-modified diffusion scenario is not a possible explanation for the enhanced catalytic activity experimentally observed for the large particles is underlined.<sup>160</sup> Adaption from reference 160 with permission.

### Methods: Lattice-Boltzmann

For the reactant ( $c_A$ ) and product ( $c_B$ ) concentrations, the time- and space-dependent convection-diffusion-reaction (CDR) equations were solved as follows:

$$\frac{\partial c_A(\vec{x}, t)}{\partial t} = D\Delta c_A(\vec{x}, t) - \vec{U}(\vec{x}) \cdot \nabla c_A(\vec{x}, t) - kc_A(\vec{x}, t)\delta(\vec{x})$$

$$\frac{\partial c_B(\vec{x}, t)}{\partial t} = D\Delta c_B(\vec{x}, t) - \vec{U}(\vec{x}) \cdot \nabla c_B(\vec{x}, t) + kc_B(\vec{x}, t)\delta(\vec{x})$$

$D$  stands for the diffusion coefficient;  $\vec{U}(\vec{x})$  represents the external convection velocity; and  $k$  is the rate constant of the reaction. The symbol  $\delta(\vec{x})$  indicates that it is only possible for the reaction to take place on the nanoparticle surfaces. Using a Lattice-Boltzmann method together with a single relaxation time, the CDR equations are solved. The grid has a size of 180x100x100 nodes. The large sphere owns a radius of 21 grid nodes while the small one has 15 grid nodes as radius. The reaction rate  $k$  is set to be 0.1 in simulation units.

The outer velocity is assumed to be constant temporally for the simulations, including external flow shown in Figure 4.1.18. The outer velocity is acquired using the free software package ESPResSo and from a separate Lattice-Boltzmann simulation of the Navier-Stokes equations. The Péclet number  $Pe$  is set to be 27, which represents the ratio between advection and diffusion.

### Methods: Particle Model

To account for the anisotropic diffusion illustrated in Figure 4.1.19, 2D simulations based on particle were performed. A set of 25000 point particles were used and labeled A initially. They represented the reactant species that were placed randomly in a periodic box that has a size of 160x160 simulation units. With a constant step size of 0.1, each reactant particle follows a random walk. The walk are set to be in an

unexpected direction that represents normal, isotropic diffusion with a diffusion coefficient  $D$ . Whenever a reactant particle hits the catalytic nanoparticle surface, a first-order A to B reaction takes place with a fixed probability. The large and small nanoparticles have a radius of 30 and 25 simulation units, respectively. Within a corona of 1 around the nanoparticles, the diffusion is anisotropic: lateral diffusion is slowed down mildly with setting  $D_{\parallel}$  at  $0.5D$ , while perpendicular diffusion to the nanoparticle surface is set to have a  $D_{\perp}$  of  $0.5D$  that corresponds to being more strongly slowed down. These choices is approximately corresponding to the well-known anisotropic diffusion to near-flat surfaces.

This is the end of the simulation.

Furthermore, the effect of the ligand density on the surface of the AuNP has also been studied for this reaction. For this purpose, the number of ligands on the surface of the AuNP can be evaluated according to the literature.<sup>170</sup> The study was carried out on the ligand density of the 10 nm 11-mercaptoundecanoic-capped AuNP (MUA@AuNP) and 42 nm MUA@AuNP. MUA@AuNP can be synthesized via the ligand exchange method (details can be found in the experimental part). It is worth pointing out here that the MUA ligand was firstly dissolved in an aqueous solution with the help of NaOH before the Ct@AuNP was slowly added in a dropwise fashion. Regarding the amount of ligand in the MUA@AuNP, the MUA@AuNP should be firstly dissolved in aqua regia overnight to reduce the influence of the AuNP on the accuracy of the nuclear magnetic resonance (NMR) spectroscopy, as the NMR peak can be broadened with the presence of the AuNP in the dispersion. Regarding the evaluation of the amount of the ligand in the solution with NMR, ACN can be selected as the reference, which does not give any peak overlapping with the peak from MUA (Figure 4.1.21a). A five-point calibration curve can then be drawn by plotting the integration ratio of the characteristic peak coming from MUA and from ACN against the concentration of the MUA in the aqueous solution (Figure 4.1.20). The results were summarized in Table 4.1.5. The amounts of gold in the solutions of the 10 and 42 nm@AuNP are determined to be 0.105 and 0.0454 mg, respectively, with the help of the ICP-OES measurement. At the same time, the ratios of the MUA/ACN of the corresponding 10 nm MUA@AuNP and 42 nm MUA@AuNP digested solution are 0.72 and 0.82, respectively. Based on the calibration curve, the mol of the ligand can be deduced to be  $0.378 \times 10^{-4}$  mmol and

0.426\*10<sup>-4</sup> mmol in the solutions of the digested 10 nm MUA@AuNP and the digested 42 nm MUA@AuNP, respectively. Furthermore, the number of ligands in the solution are also documented in Table 4.1.5. In addition, the total surface area of the AuNP can be calculated based on the equation shown in Figure 4.1.6. The ligand densities of the AuNP of the 10 nm and 42 nm MUA@AuNP are 6.9/ nm<sup>2</sup> and 7.5/ nm<sup>2</sup>, respectively (Table 4.1.5). This is an indication that if the total surface of the AuNP of different sizes are kept the same, the particles should have the same ligand density on the surface. Finally, the ligand density on the surface of the AuNP can be ruled out as a main factor which influences the catalytic activity in this work.

**Table 4.1.5.** Parameters of the MUA@AuNP of different diameters for the calculation of ligand density.

Ct@AuNP <sup>[a]</sup> (nm)	m <sub>Au</sub> <sup>[b]</sup> (mg)	Ratio of MUA/ACN <sup>[c]</sup>	The mol of ligand*10 <sup>-4</sup> (mmol) <sup>[d]</sup>	The number of ligands in solution	The total surface area of the AuNP in solution	Ligand (nm <sup>2</sup> )
10	0.105	0.72	0.378	2.27*10 <sup>16</sup>	3.3*10 <sup>15</sup>	6.9
42	0.454	0.82	0.426	2.56*10 <sup>16</sup>	3.4*10 <sup>15</sup>	7.5

[a] The size of MUA@AuNP was obtained by TEM and at least 100 NP were counted to evaluate the size of the MUA@AuNP.

[b] The amount of Au in the dispersion of the 10 and 42 nm MUA@AuNP for <sup>1</sup>H-NMR spectroscopy was evaluated with the help of ICP-OES.

[c] The ratio of the protons of the particular peak of MUA ligand against ACN.

[d] The concentration of ligands can be calculated from a five-point curve, which is plotted in Figure 4.1.20.

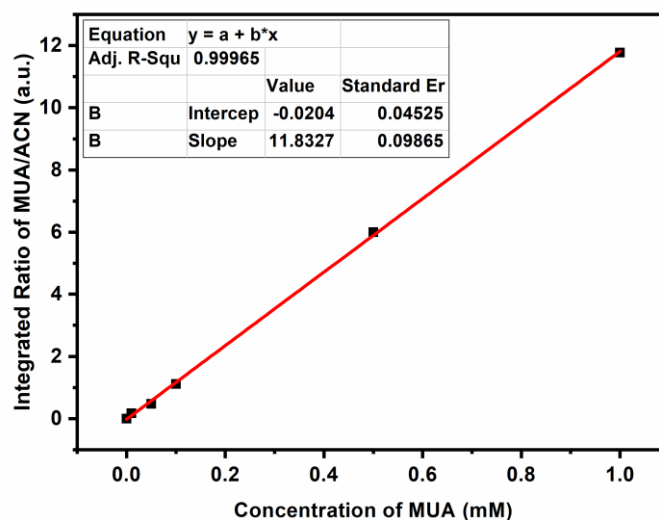


**Figure 4.1.20.** Representative calibration curve for the determination of the concentration of MUA ligands by plotting the integrated ratio of the characteristic protons from MUA and those of ACN versus the MUA concentration.<sup>160</sup> Adaption from reference 160 with permission.

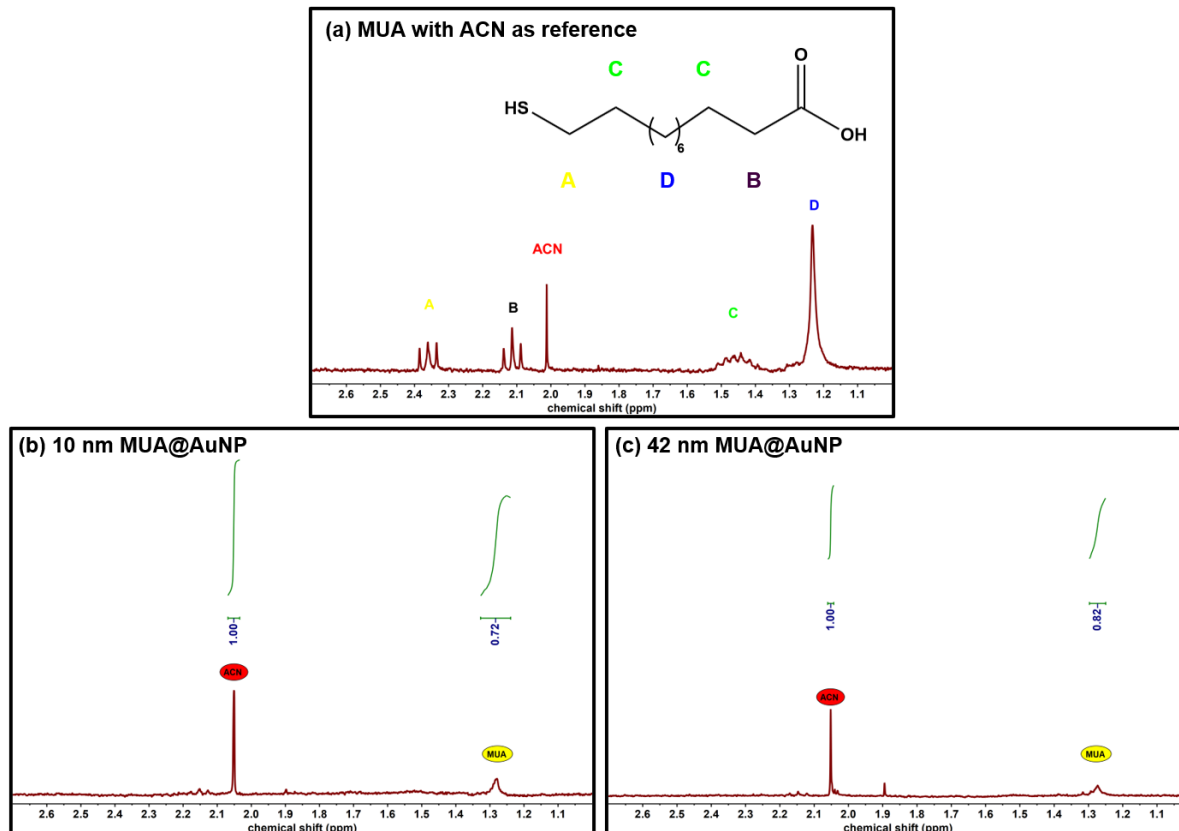


**Figure 4.1.21.** (a) <sup>1</sup>H-NMR spectrum of MUA dissolved in D<sub>2</sub>O by investigating ACN

as the reference. (b)  $^1\text{H-NMR}$  spectrum of MUA originating from the solution of 10 nm of MUA@AuNP in  $\text{D}_2\text{O}$  by investigating ACN as the reference. (c)  $^1\text{H-NMR}$  spectrum of MUA originating from the solution of 42 nm of MUA@AuNP in  $\text{D}_2\text{O}$  by investigating ACN as reference. <sup>160</sup> Adaption from reference 160 with permission.

#### **4.1.4 Conclusion**

In this work, 10 nm to 58 nm Ct@AuNP were synthesized by the traditional Frens method and the corresponding PVP@AuNP were prepared by the ligand exchange method. The nitrophenol reduction reaction was selected as the model reaction to study the catalytic performances of the AuNP. The amount of AuNP investigated was varied during the catalytic experiments in order to have the same total surface area for all the AuNP invested in the catalytic reactions. The results showed that the apparent catalytic reaction rate constant presented an increasing tendency with an increase of the average size of the AuNP when the total surface area of the AuNP is kept the same. To explore the reason behind this observation, the differences in crystalline structure of the AuNP of different sizes, the diffusion of the reactant to the active sites of the AuNP and the ligand density of the AuNP were thoroughly studied. The results indicated that the large NP most likely own more defects than the smaller NP, and this might be the crucial factor resulting in their higher catalytic activities in the 4-nitrophenol reduction. At the same time, the effect of ligand density and the diffusion of the reactant to the active site of the AuNP were ruled out.

## 4.2 Stable mesoscale nonwovens of electrospun polyacrylonitrile and interpenetrating supramolecular 1,3,5-Benzenetrisamide fibers as efficient carrier for gold nanoparticles

### I. Preparation of fiber dispersions

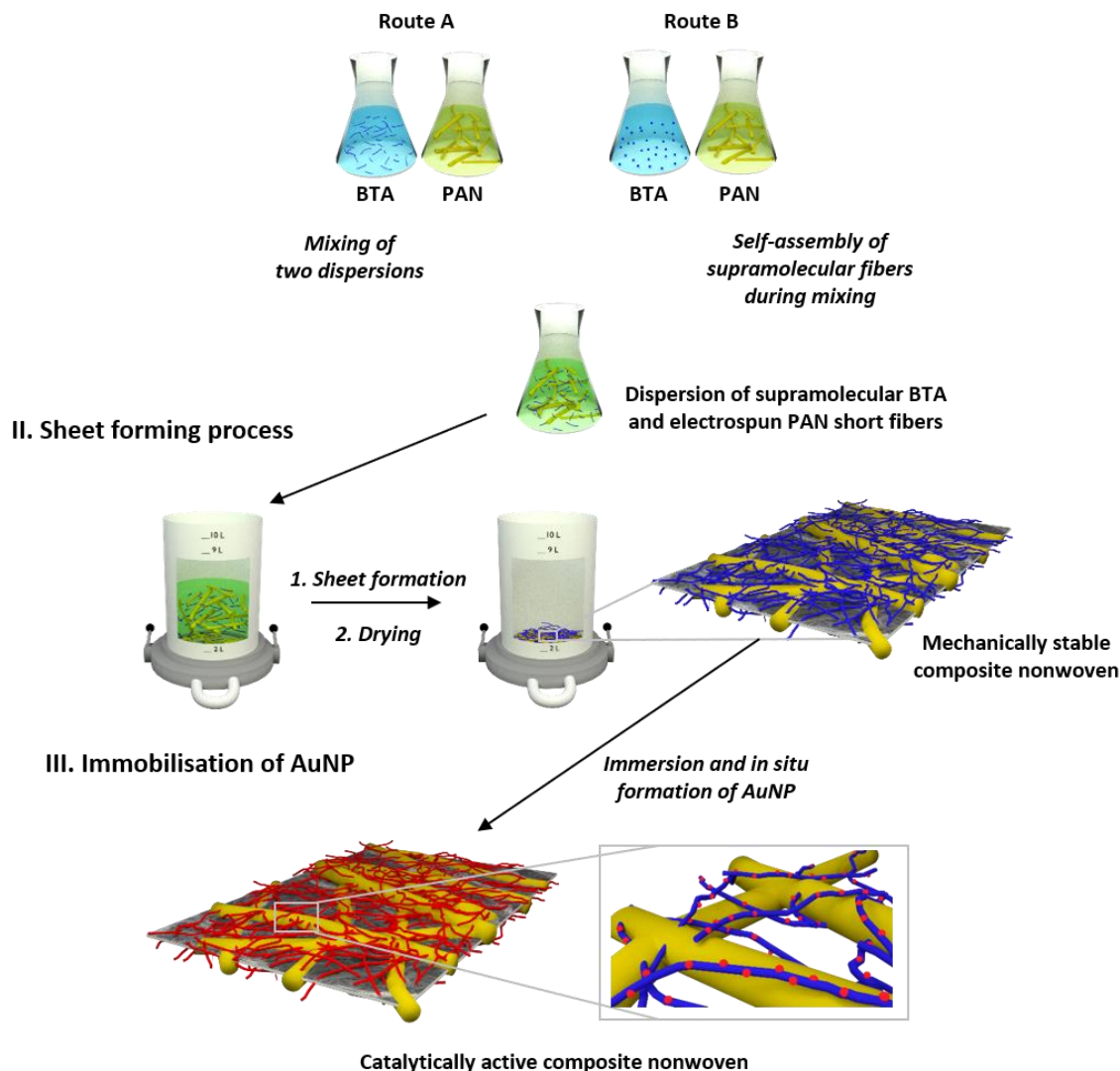


**Figure 4.2.1.** Schematic illustration of the fabrication process of the composite nonwoven from electrospun short PAN fibers (yellow fibers) and the supramolecular terpyridine-functionalized BTA nanofibers (blue fibers) via wet-laid technique. There are two different ways that can be used for the fabrication of the nonwoven, namely, route A, direct mixing of the dispersion of BTA nanofibers and the dispersion of short PAN fibers; route B, mixing BTA solution with short PAN fibers. The composite nonwoven can be obtained by the wet-laid process, and the AuNP immobilized

nonwoven can then be produced by the *in situ* formation method.<sup>171</sup> Adaption from reference 171 with permission.

The aggregation of AuNP during immobilization on the supports and leaching of the AuNP during the catalytic reaction are of great concern during the preparation of the AuNP catalyst. Many groups have already made efforts to develop new catalysts to prevent the aggregation of the AuNP and the leaching of the AuNP from the catalyst, as well as to improve the catalytic efficiency. In this work, we prepared a new nonwoven composite combining the electrospun short polyacrylonitrile (PAN) fibers and the supramolecular terpyridine-functionalized benzene-1,3,5-tricarboxamide (BTA) nanofibers via wet-laid technique. Owing to the entanglement of the BTA nanofibers and the short PAN fibers, the composite nonwoven presents good mechanical property. Thus, this nonwoven can be used as the support to immobilize the AuNP and then used in the catalytic reactions. In addition, functional BTA employed to attach the noble metal has been reported in the literature.<sup>172-174</sup> For example, the peripheral terpyridine moieties, and the terpyridine-substituted BTA can be employed to produce the supramolecular gels with luminescent properties.<sup>175</sup>

#### 4.2.1 Fabrication of the composite nonwoven

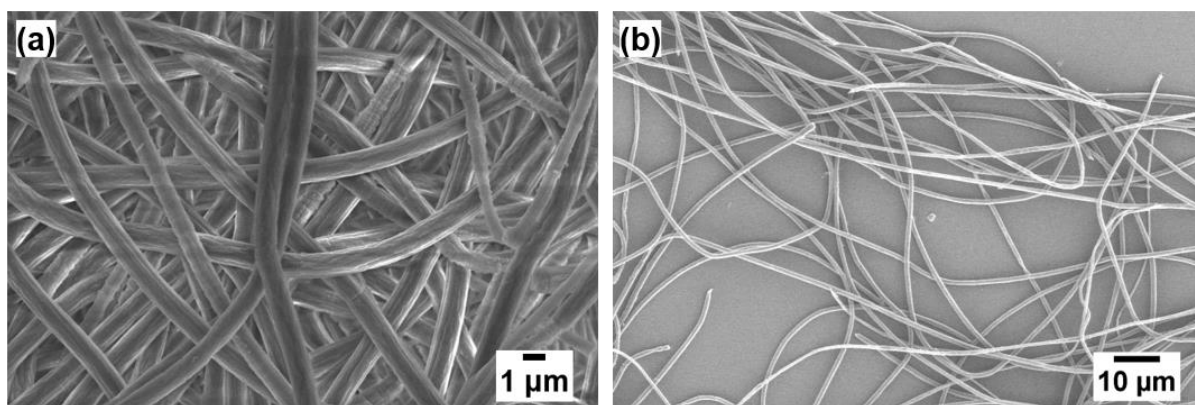


**Figure 4.2.2.** SEM images of as-spun PAN fibers (a) and short PAN fibers (b).<sup>171</sup> Adaption from reference 171 with permission.

There are two main paths to fabricate the interpenetrating mesoscale nonwoven via the wet-laid process. Route A (Figure 4.2.1) is through direct mixing of the BTA nanofibers with short PAN fibers, and Route B (Figure 4.2.1) is via mixing of the BTA solutions of different concentrations with the dispersion of the short PAN fibers. The BTA

consisting of peripheral terpyridine substituents (BTA) was selected as the functional material, which can absorb AuNP onto their surfaces, and can form nanofibers in the mixture of isopropanol and water well. The BTA can normally be dissolved at elevated temperature in the mixture of isopropanol and water. The supramolecular nanofibers can then be generated by cooling down these mixtures, and the diameter of the BTA nanofibers ranges from 100 to 150 nm. The PAN copolymer was selected as another composite to fabricate the nonwoven, as it has good electrospinnability and wettability in water. Thus, the short PAN fibers can be homogeneously dispersed in water. The redissolution of the BTA nanofibers in the mixtures can be avoided. In addition, the wet-laid process can be carried out in aqueous media. The electrospun PAN nonwovens were prepared for the wet-laid process with a diameter of about  $1.10 \pm 0.28 \mu\text{m}$ , and the morphology can be seen in Figure 4.2.2a. The PAN nonwoven was then cut with the blender at a concentration of 0.05 wt% in water. Finally, a homogeneous dispersion of short PAN fibers was obtained with a length of about  $442 \pm 171 \mu\text{m}$  (Figure 4.2.2b).

**Table 4.2.1.** The composition of the nonwoven fabricated via the wet-laid process, and the compositions of the PAN dispersion and BTA solution; theoretical amounts of the BTA in the composite nonwoven; amounts of the BTA characterized experimentally determined by NMR; and the thicknesses of the fabricated nonwoven.

Entry	Composition of dispersions <sup>[d]</sup>			Composite nonwoven		Thickness ( $\mu\text{m}$ )
	PAN dispersion (mL)	BTA solution Conc. (wt%)	Vol. (mL)	Theor. Ratio of PAN:BTA	Exp. Ratio of PAN:BTA <sup>[e]</sup>	
Ref. <sup>[a]</sup>	838	-	-	-	-	$61 \pm 5$
1 <sup>[b]</sup>	838	0.05	410	2.4:1	3.8:1	$68 \pm 3$
2a <sup>[c]</sup>	838	0.01	410	12:1	>12:1	$66 \pm 2$
2b <sup>[c]</sup>	838	0.05	410	2.4:1	3:1	$74 \pm 4$
2c <sup>[c]</sup>	838	0.1	410	1.3:1	1.3:1	$82 \pm 6$

[a] The total volume of the dispersion for the preparation of the reference nonwoven is 3334 mL (838 mL of PAN dispersion, 1742 mL of H<sub>2</sub>O and 754 mL of isopropanol).

[b] The fabrication of the nonwoven was carried out via route A.

[c] The fabrication of the nonwoven was carried out via route B.

[d] The total volume of the dispersion for the fabrication of the nonwoven is 3744 mL, namely, 838 mL of the dispersion of the short PAN fibers, 410 mL of the BTA solution together with the mixture of 1742 mL of H<sub>2</sub>O and 754 mL of isopropanol.

[e] The amount of the BTA was evaluated with the help of <sup>1</sup>H-NMR spectroscopy.

In route A, short PAN fiber dispersion in water was mixed with BTA nanofibers at a concentration of 0.05 wt% in a mixture of isopropanol and water directly, and the formation of the BTA nanofibers is described in the experimental part. In route B, the short PAN fiber dispersion in water and a fresh solution of the BTA molecule in a mixture of isopropanol and water were mixed. The concentration of the BTA was adjusted to be from 0.01 to 0.1 wt%, in order to fabricate the composite nonwovens with different amounts of the BTA. Meanwhile, the concentration of the PAN dispersion was kept identical for all cases. During the addition of the solution of the BTA molecule into the dispersion of the short PAN fibers, the BTA molecule immediately self-assemble into supramolecular nanofibers *in situ* because of the change of the solubility of BTA in the dispersion. It should be noticed that, as the sheet forming process requires a large volume, the dispersion of the mixture of short PAN fibers and BTA supramolecular nanofibers should be diluted to a total volume of 3.7 L. After the sheet forming and drying processes, the composite nonwoven 1 and 2a-2c were successfully fabricated (Figure 4.2.1).

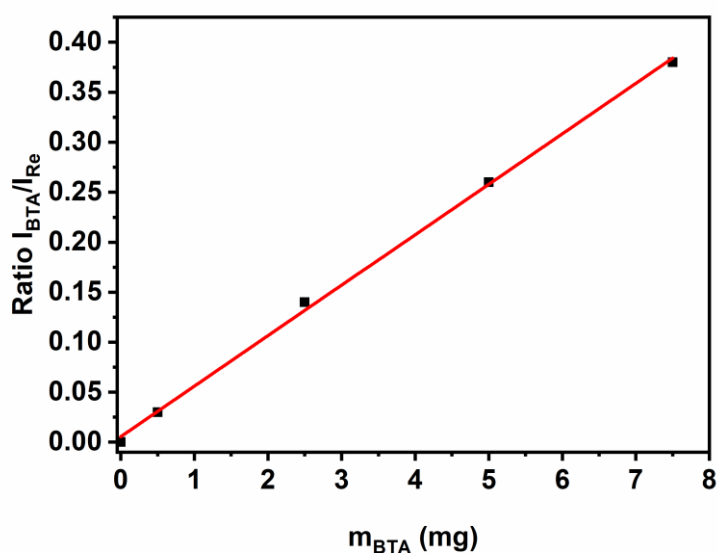


**Figure 4.2.3.** A five-point calibration curve of the ratio between the integral peak at 4.41 ppm of the BTA ( $I_{\text{BTA}}$ ) and the integral peak at 3.87 ppm of the reference ( $I_{\text{Re}}$ ) against the mass of the BTA investigated.<sup>171</sup> Adaption from reference 171 with permission.

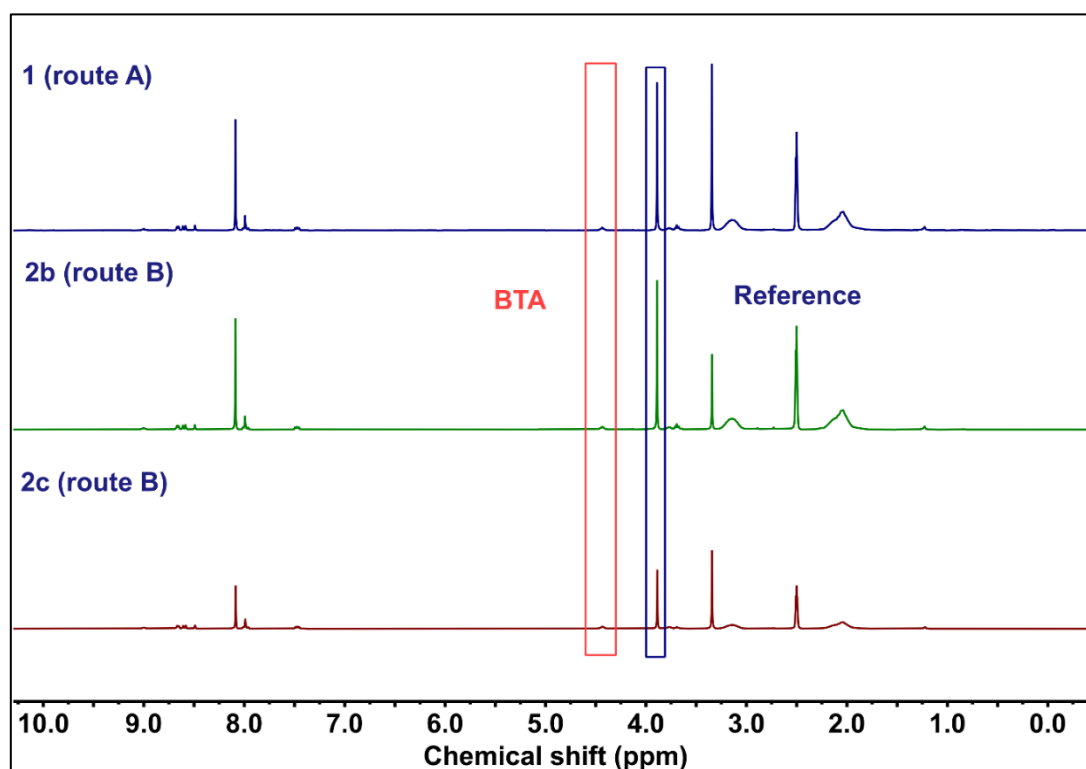


**Figure 4.2.4.** The  $^1\text{H}$ -NMR spectra of the composition nonwoven 1, 2b and 2c. An amount of 3 mg dimethyl terephthalate was selected as the reference and added to

the solution of the composite nonwoven in 1 mL deuterated DMSO.<sup>171</sup> Adaption from reference 171 with permission.

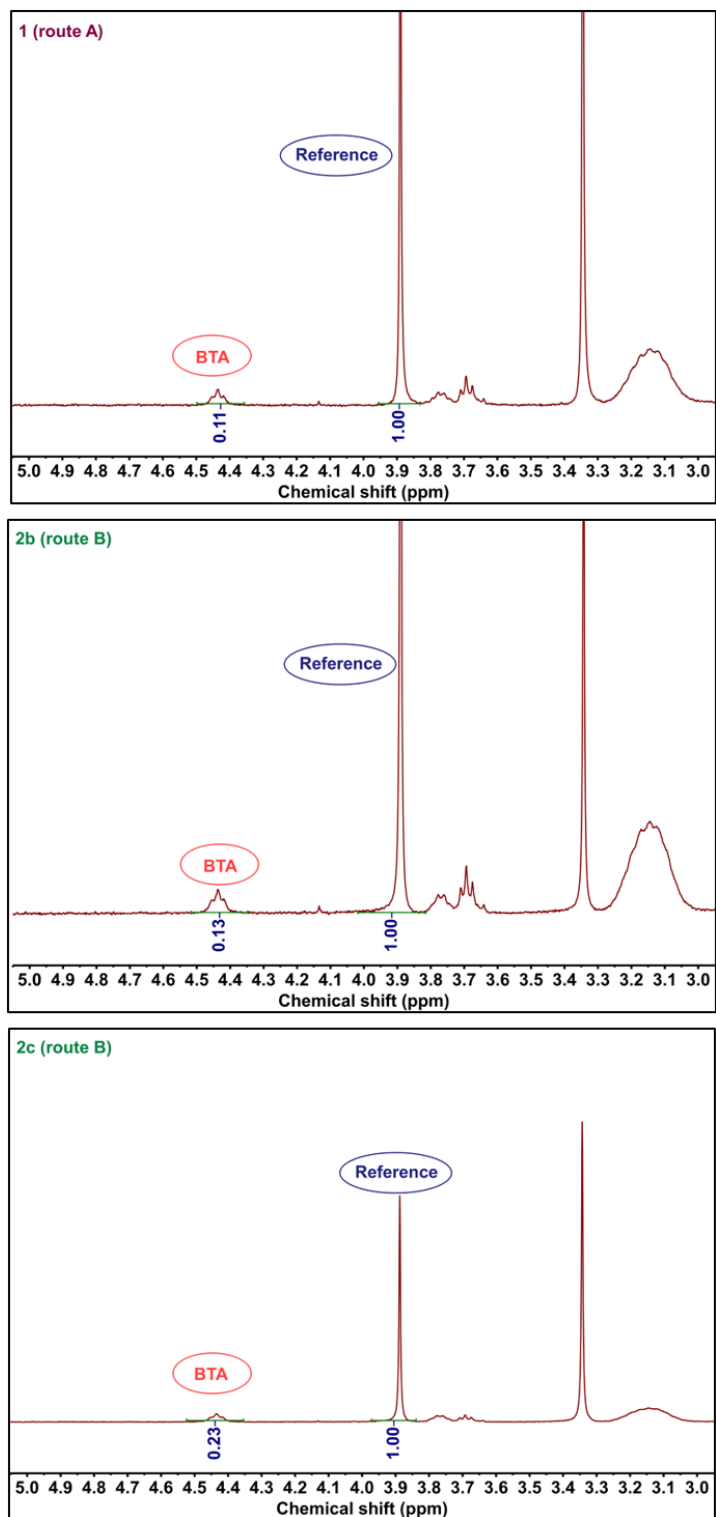


**Figure 4.2.5.** The ratio between the integral peak at 4.41 ppm of the BTA ( $I_{\text{BTA}}$ ) and the integral peak at 3.87 ppm of the reference ( $I_{\text{Re}}$ ) in the composition nonwoven 1, 2b and 2c.<sup>171</sup> Adaption from reference 171 with permission.

#### 4.2.2 Characterization of the composite nonwovens

The composite nonwovens 1 and 2a-2c were characterized by  $^1\text{H-NMR}$  spectroscopy to estimate the concentration of the BTA in the final nonwovens and the results revealed that a similar amount of the BTA in the composite nonwoven can be determined as that in the solution of the BTA molecule investigated. (Table 4.2.1). The amount of BTA in the nonwoven can be evaluated by  $^1\text{H-NMR}$ . Firstly, a five-point calibration curve was obtained by mixing BTA of different masses (0, 0.5, 2.5, 5, and 7.5 mg) with 3 mg dimethyl terephthalate as reference in 1 mL DMSO. It should be pointed out that, the terephthalate can be selected as the reference because its integral peak did not overlap with the peak from the BTA molecule, and it is quite stable in DMSO. The ratio of the integral peak of the BTA molecule at  $I_{\text{BTA}}$  at 4.41 ppm and the integral  $I_{\text{reference}}$  at 3.87 ppm versus the mass of the BTA molecule investigated was then illustrated in Figure 4.2.3. It can be further adopted to determine the content of BTA in the composite nonwoven. The composite nonwoven (1, 2a, 2b, 2c) can be dissolved completely in 1 mL DMSO containing 3 mg dimethyl terephthalate as reference, and the  $^1\text{H-NMR}$  spectra were recorded and shown in Figure 4.2.4. Remarkably, the content of BTA in the composite nonwoven 2a cannot be detected due to its low amount in the mixture. In addition, the ratio of the integral peak of the BTA and reference was shown in Figure 4.2.5. Thus, the experimental content of the BTA in the composite nonwoven can be estimated using the calibration curve in Figure 4.2.3. The results indicated that the BTA contents in the fabricated nonwovens were similar to those in the BTA dispersions investigated (Table 4.2.1). Furthermore, the resulting composite nonwoven has a thickness in the range of 60 to 80  $\mu\text{m}$ , which presents an increase with the increasing content of BTA in the nonwoven.

The chemical structures of the composite nonwoven were determined by Fourier transform infrared (FT-IR) spectra (Figure 4.2.6). The FT-IR spectra of the composite nonwoven 2b and 2c show typical characteristic peaks of Amide A (N-H stretch) at  $3262\text{ cm}^{-1}$ , Amide I (C=O stretch) at  $1667\text{ cm}^{-1}$  and Amide II (N-H bend & C-N stretch) at  $1565\text{ cm}^{-1}$ . Defined FT-IR vibrations indicate threefold intermolecular hydrogen

bonding.<sup>1</sup> The N-H stretching vibration at  $\sim 3262\text{ cm}^{-1}$  and N-H bending and C-N stretching vibration at  $\sim 1565\text{ cm}^{-1}$  give information about the crystallographic order, whereas the C=O stretching vibration at  $\sim 1650\text{ cm}^{-1}$  comes from an amide compound. However, there are no significant peaks observed in the 2a, because of the low amount of BTA in the composite nonwoven.

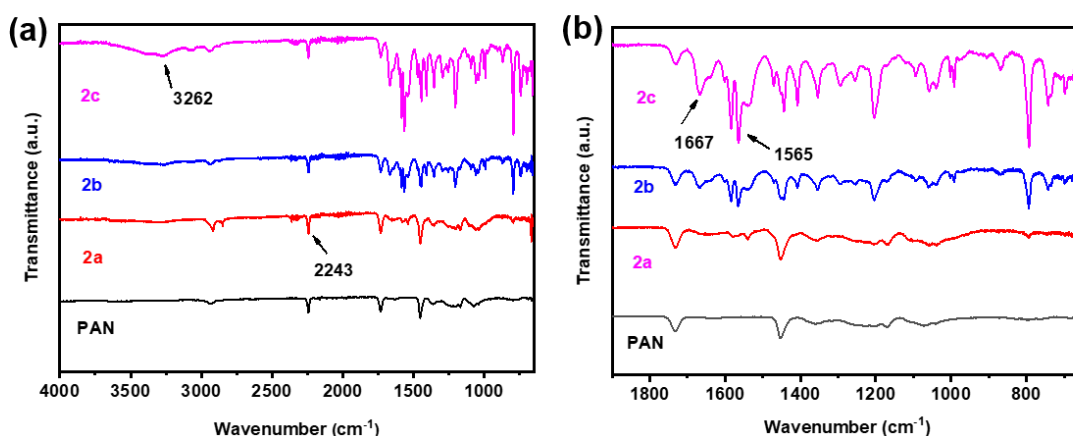


**Figure 4.2.6.** (a) Fourier transform infrared (FT-IR) spectra of the composite nonwoven (2a-2c) with the PAN nonwoven as reference and (b) zoomed-in spectra of the range from  $1800\text{ cm}^{-1}$  to  $650\text{ cm}^{-1}$ .

Figure 4.2.7 shows the morphologies of the composite nonwoven with different contents of BTA nanofibers. It indicates that the short PAN fibers and the BTA nanofibers are homogeneously distributed in the nonwovens. It should be pointed out that only a small number of BTA nanofibers distributed around the short PAN fiber in the nonwoven 2a. An interpenetrating network of BTA nanofibers between short PAN fibers are generated with the increasing content of the BTA in the nonwovens 2a and 2c. Moreover, the BTA nanofibers entangle with short PAN fibers tightly. It should be noted that the BTA nanofibers packed less densely within the composite nonwoven 2b compared to 2c (Figure 4.2.8). In order to further confirm the homogeneous distribution of BTA nanofibers and short PAN fibers, SEM images of the cross-section of the composite nonwoven were recorded and the results showed that the BTA nanofibers are evenly distributed around the short PAN fibers (Figure 4.2.9). In contrast, the SEM images in Figure 4.2.10 showing the morphologies of the composite nonwoven 1 indicate that the BTA nanofibers and short PAN fibers are not homogeneously distributed within the composite nonwoven prepared via route A.

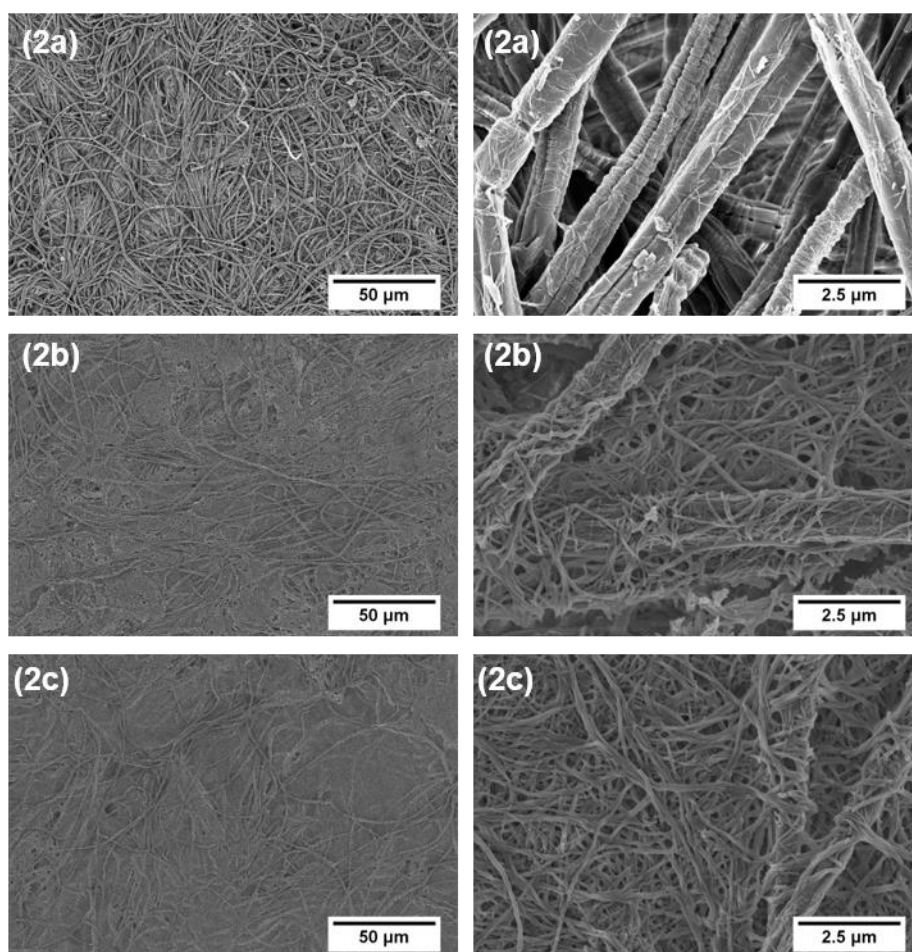


**Figure 4.2.7.** SEM images showing the morphology of the composite nonwovens (2a–2c) with different ratios between the short PAN fibers and supramolecule BTA nanofibers at two different magnifications.

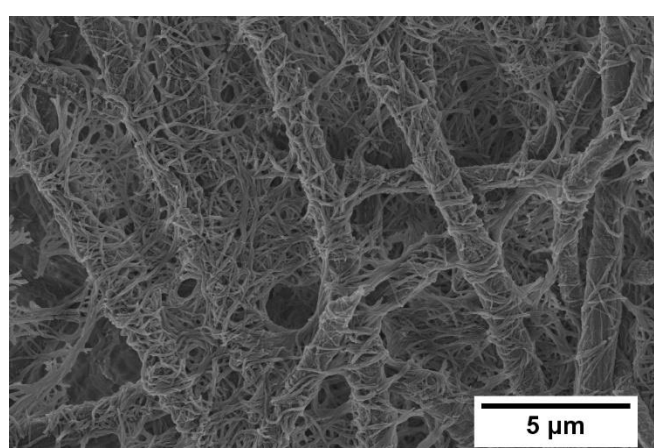


**Figure 4.2.8.** SEM image showing the morphology of the composite nonwovens 2b.

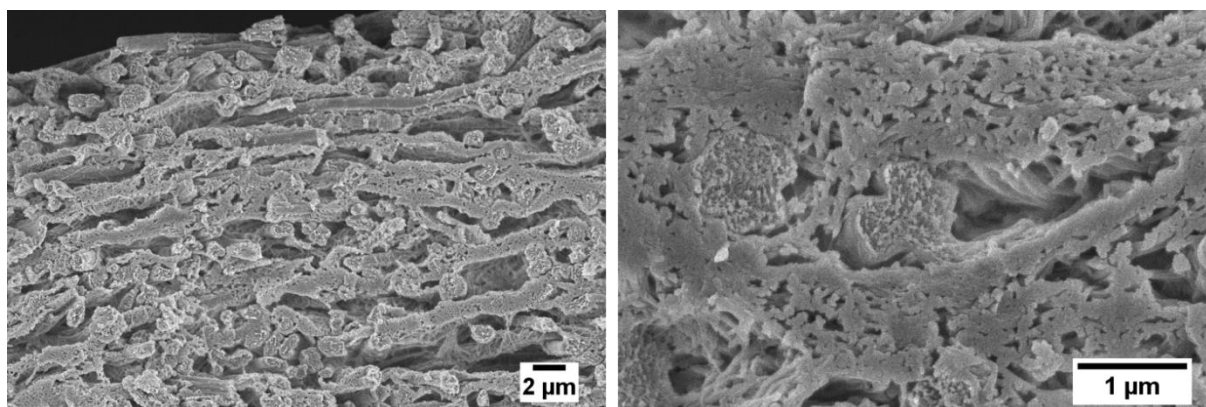


**Figure 4.2.9.** SEM images of the cross-section of the composite nonwoven 2b at two different magnifications.<sup>171</sup> Adaption from reference 171 with permission.

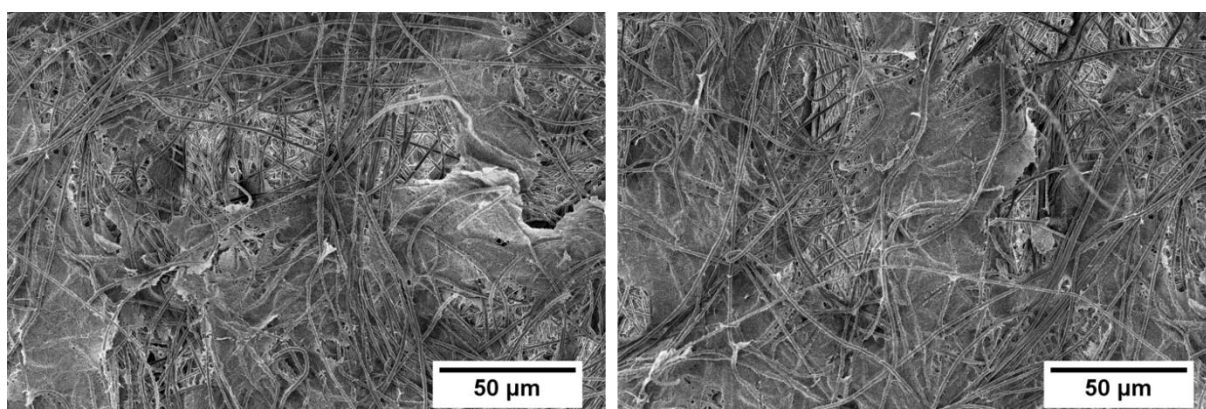


**Figure 4.2.10.** SEM images for comparison of the morphology of composite 1 prepared via route A at low magnification.

Mechanical property is an important factor to consider for the further modification of the composite nonwovens, as sufficient mechanical stability is necessary to ensure the integrity of the composite nonwoven during catalytic reactions. Therefore, tensile and stability tests were performed to evaluate the mechanical properties of the nonwoven fabricated. Regarding the tensile tests, the nonwoven composed only of short PAN fibers was selected as the reference (Figure 4.2.11). The results indicated that the reference nonwoven and the composite nonwoven 2a presented poor mechanical property due to the weak interconnection of the fibers in the nonwoven. The tensile strength of the neat short PAN fibers is smaller than 0.2 MPa. By contrast, the tensile strength of the composite nonwovens 2b and 2c increased to  $0.78 \pm 0.19$  and  $1.09 \pm 0.15$  MPa, respectively. These results revealed that an increasing amount of the BTA nanofibers brings the benefit of an improved mechanical property of the composite as

a sufficient amount of entanglement of the BTA nanofibers with the short PAN fibers lead to the formation of a stable nonwoven. It should also be noted that the composite nonwoven 2b has already presented good mechanical properties, which is further improved in 2c composite nonwoven because of an increasing amount of BTA nanofiber content.

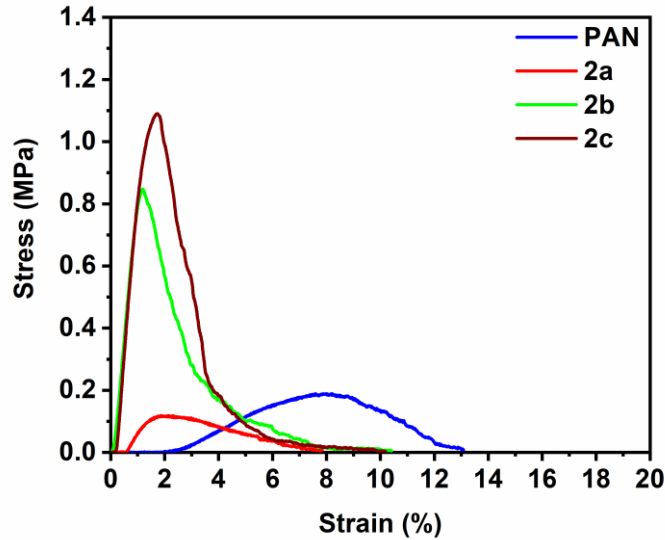


**Figure 4.2.11.** Stress-strain curves of the composite nonwovens 2a–2c and the nonwoven containing only short PAN fibers.<sup>171</sup> Adaption from reference 171 with permission.

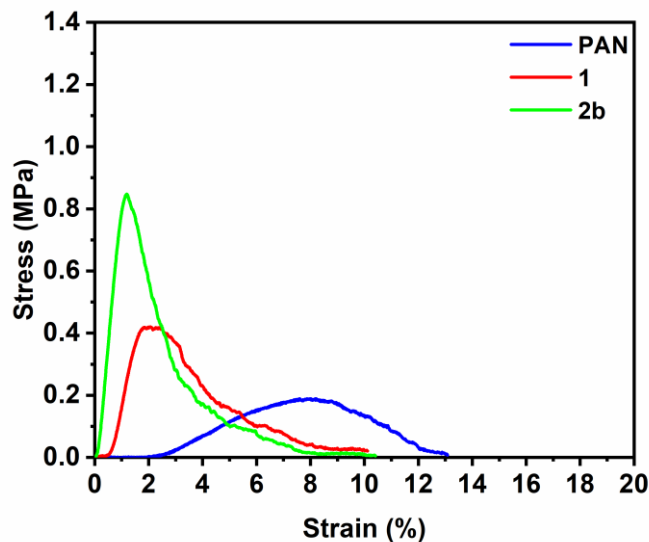


**Figure 4.2.12.** Stress-strain curves of the composite nonwovens 1 and 2b containing a similar amount of the BTA nanofibers from different fabrication routes and the nonwoven containing only short PAN fibers.<sup>171</sup> Adaption from reference 171 with permission.

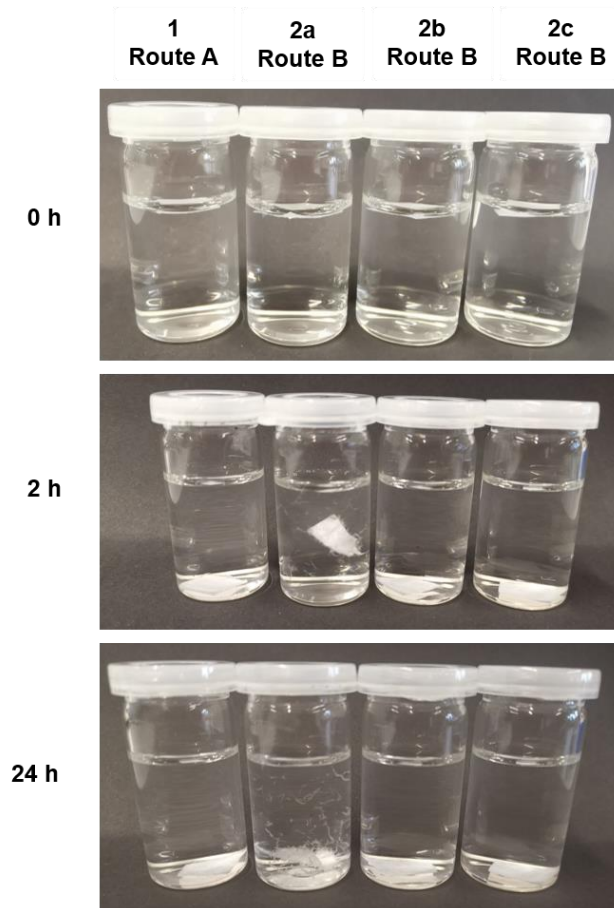


**Figure 4.2.13.** Photos of the stability test of the composite nonwovens (1, 2a–2c) in water with shaking at 500 rpm for 24 h. The status of the composite nonwovens was recorded at the beginning, after 2 h and after 24 h.

Furthermore, the mechanical property of the composite nonwoven 1 fabricated through route A and that of 2b fabricated through route B were compared, with the neat short PAN fibers selected as the reference (Figure 4.2.12). The results indicated that the composite nonwoven 2b presents higher tensile strength than the composite nonwoven 1. The reason might be that route B provides more likelihood for a homogenous dispersion of BTA nanofibers around the short PAN fibers in the dispersion, and provides more opportunity for the entanglement of the BTA nanofibers with the short PAN fibers.

Since the composite nonwoven will be further modified and used as the carrier for the AuNP and the processing will be performed in water, the stabilities of the composite nonwovens 1 and 2a–2c in aqueous media were evaluated by immersing them in water with shaking for 24 h. The composite nonwoven 2a started deforming after 2 h, whereas the other nonwovens were still intact. After 24 h, the composite nonwoven 2a completely lost its form and the other nonwovens were still stable. Therefore, it can be concluded that the composite nonwovens (1, 2b and 2c) present good shape persistence in aqueous media and can be investigated in the aqueous media for further applications (Figure 4.2.13).

To conclude the study of the composite nonwovens (1, 2a-2c) morphology and mechanical properties: it can be deduced that route B led to more desired properties of the composite nonwovens fabricated that route A, such as significantly improved mechanical property and more homogeneously distributed BTA nanofibers within the nonwovens. Therefore, the following part only addresses the composite nonwovens fabricated via route B.

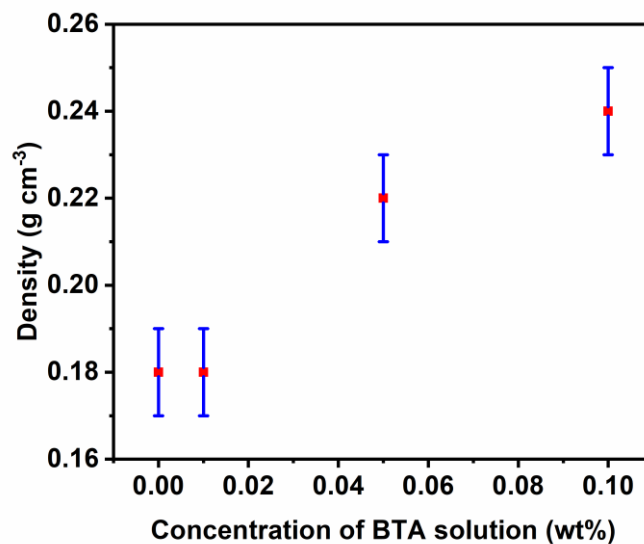


**Figure 4.2.14.** The plot of the density of the composite nonwovens 2a–2c and the pure PAN nonwoven containing the short PAN fibers as reference against the concentration of the BTA solution.<sup>171</sup> Adaption from reference 171 with permission.

Porosity and pore size also play important roles in the applications of the composite nonwoven. They can be regarded as important parameters determining the ability of

the accessibility, which may influence the further modification and application of the composite nonwovens. Calculation of the porosity is performed with the following Equation 4.2.1.

$$\text{Porosity (\%)} = \left(1 - \frac{\rho_{nonwoven}}{\rho_{BTA}\phi_{BTA} + \rho_{PAN}\phi_{PAN}}\right) \cdot 100 \quad \text{Equation 4.2.1}$$

The density of the composite nonwoven was characterized from the size (measured using a Vernier caliper) and the weight (measured by a microbalance). The density values of the nonwoven are summarized in Table 4.2.2 and Figure 4.2.14. It can be seen that an increasing content of the BTA nanofibers in the nonwoven led to an increase in density. The density ranges from 0.18 to 0.24 g/cm<sup>3</sup>. The porosity of the composite nonwoven can then be deduced from this equation, with the help of the measured nonwoven density and the theoretical bulk density of the corresponding composite of the nonwoven. The experimental bulk density of the BTA is 1.1 g/cm<sup>3</sup> and the bulk density of PAN is 1.184 g/cm<sup>3</sup>. The weight fraction of the BTA and PAN can be deduced from the NMR measurement.

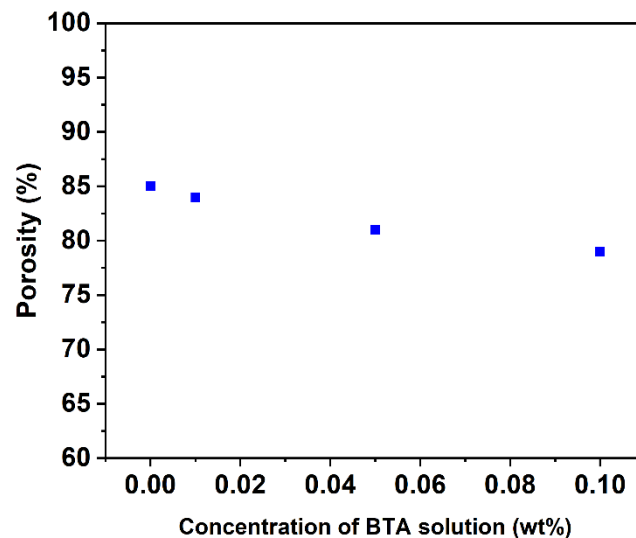


**Figure 4.2.15.** The porosity of the composite nonwoven 2a-2c and the pure PAN nonwoven containing the short PAN fibers as reference against the concentration of the BTA solution.<sup>171</sup> Adaption from reference 171 with permission.

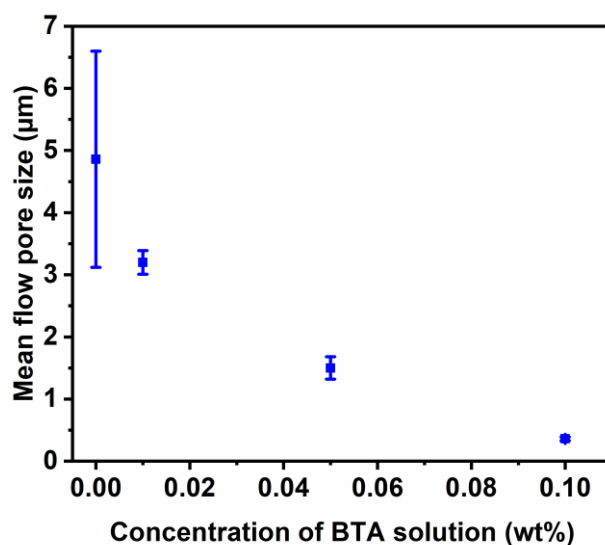


**Figure 4.2.16.** Pore size of the composite nonwovens 2a–2c with different contents of the BTA nanofibers and the nonwoven containing only short PAN fibers as reference. At least two repeated measurements were performed for every sample and the error bar indicates the standard deviation of the measurements.<sup>171</sup> Adaption from reference 171 with permission.

**Table 4.2.2.** Characterization results of the density, pore size and porosity of the composite nonwovens.

Entry	Density (g/cm <sup>3</sup> )	Pore Size (µm)	Porosity (%)
Reference	0.18 ± 0.01	4.86 ± 1.74	85
2a	0.18 ± 0.00	3.20 ± 0.19	84
2b	0.22 ± 0.01	1.50 ± 0.18	81
2c	0.24 ± 0.01	0.36 ± 0.03	79

The results of the calculation of the porosity of the composite nonwovens 2a–2c and the nonwoven with neat short PAN fibers are summarized in Table 4.2.2. The results indicated that the porosity of the nonwoven displays a decreasing tendency (from 85 to 69 %) with an increasing content of BTA nanofibers (Figure 4.2.15). Meanwhile, the pore size of the neat PAN nonwoven and the composite nonwoven 2a–2c presents the same tendency. It ranges from 4.86 ± 1.74 to 0.36 ± 0.03 µm, accordingly (Figure

4.2.16). The reason behind this observation is that increasing content of BTA nano-fibers within the short PAN fibers formed much denser interpenetrating network.

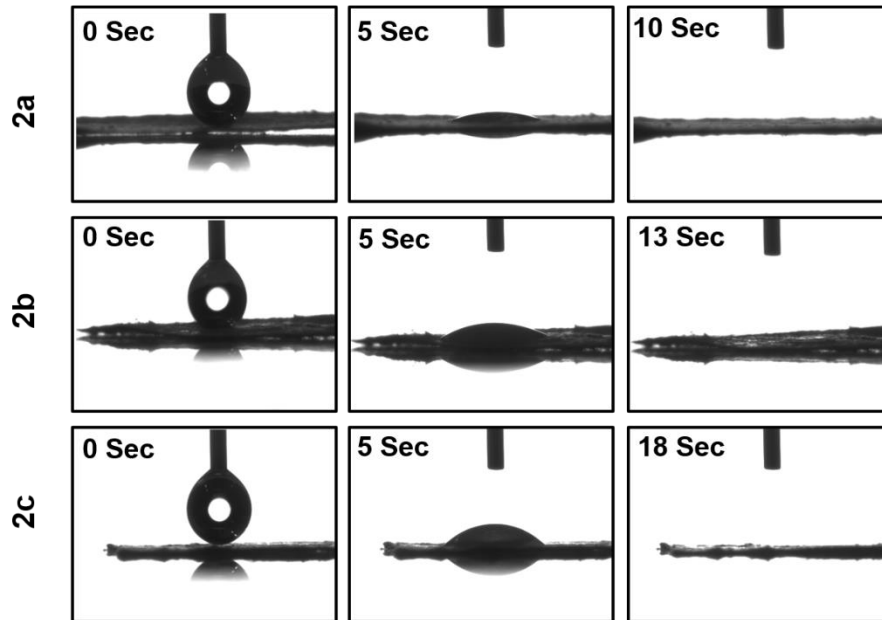


**Figure 4.2.17.** Wettability of the composite nonwovens 2a-c.

A drop-shape analyzer was used to determine the wettability of the composite nonwovens 2a, 2c and the neat PAN nonwoven. All samples showed wettability with time. A full droplet is absorbed by the composite nonwoven 2b and 2c within 13 s and 18 s respectively. This provides a huge advantage for the immobilization of the AuNP within the nonwoven in water and is described in detail in the following section (Figure 4.2.17).

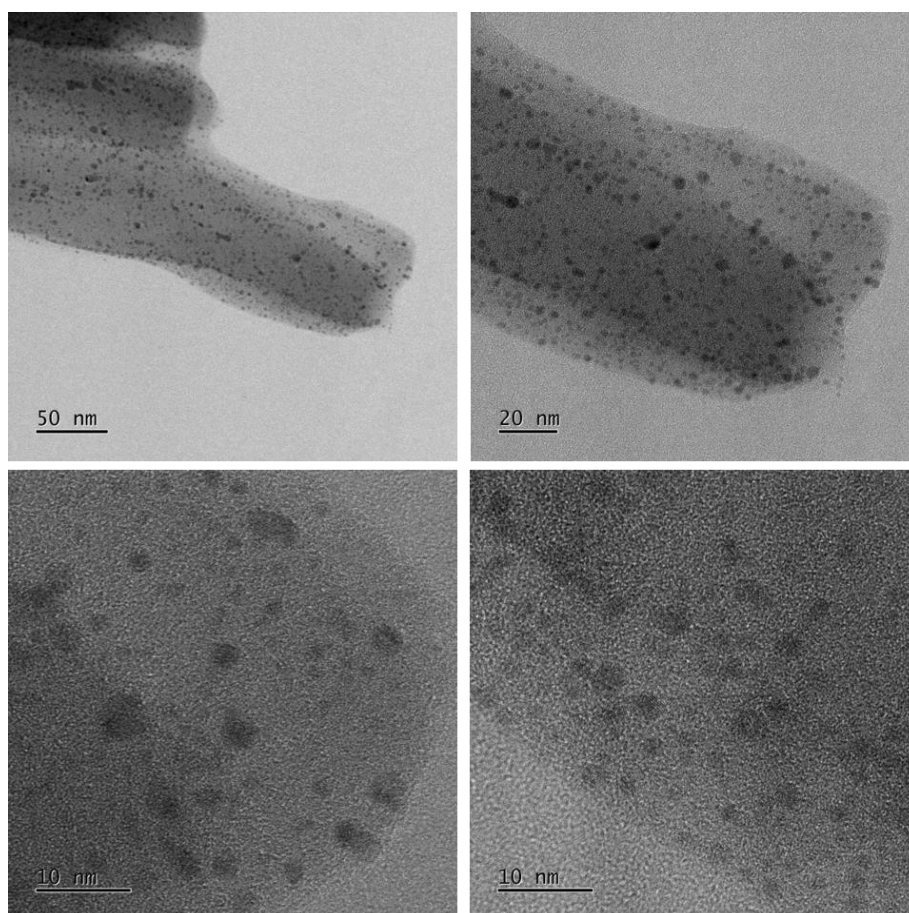


**Figure 4.2.18.** TEM images of the AuNP decorated supramolecular BTA nanofibers of the composite nonwoven 2b at different magnifications.

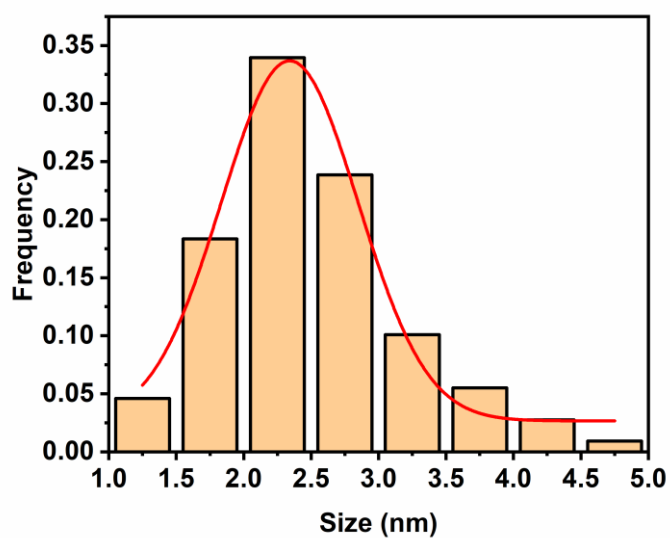


**Figure 4.2.19.** Size distribution of the AuNP evaluated from a TEM micrograph with a diameter of  $2.3 \pm 0.5$  nm.

### **4.2.3 *In situ* formation of the AuNP within a composite nonwoven.**

Based on the discussion mentioned previously, the composite nonwovens (2b and 2c) show good wettability and shape persistence in aqueous media (Figure 4.2.13 and 4.2.17). This provides possibilities for the composite nonwovens to be used in aqueous solutions. Hence, the composite nonwovens can be immersed directly in the gold acid solution for the immobilization of the AuNP. The gold ion was then absorbed onto the surface of the nonwovens owing to the terpyridine functional group on the BTA. Afterwards, the nonwoven was washed with water in order to remove the unbound gold ion within the composite nonwoven. The nonwoven was then placed in the NaBH<sub>4</sub> solution for 10 min and it can be observed that the color of the nonwoven changed immediately to orange-brown following the immersion. This is the indication of the immediate formation of the AuNP occurring from immersing the nonwoven in the NaBH<sub>4</sub> solution. It should be noted that the composite nonwoven decorated with AuNP was washed with water again to remove the unbound AuNP, which avoids the leaching of the AuNP during the catalytic reaction. Thus, AuNP-decorated composite nonwoven can be used in catalyzing the nitrophenol reduction. As the average size of the AuNP plays an important role for the AuNP catalyst, the characterization of the AuNP-decorated composite nonwoven was performed before the nitrophenol reduction to determine the size distribution of the AuNP within the nonwoven. Transmission electron microscopy indicated that the AuNP were homogeneously distributed on the surface of the BTA without obviously aggregation, which give a huge advantage to the catalysis of the nitrophenol reduction (Figure 4.2.18), and the average diameter of the AuNP is  $2.3 \pm 0.5$  nm, determined by counting at least 100 NP (Figure 4.2.19).

### **4.2.4 Catalytic study of the AuNP-immobilized composite nonwoven**

The catalytic performance of the AuNP-decorated composite nonwovens (AuNP-2b and AuNP-2c) was studied in the nitrophenol reduction reaction. Due to the poor mechanical property of the composite nonwoven 2a it was not investigated as the support for AuNP for catalytic reaction. The reason for choosing the nitrophenol reduction as the model reaction was introduced in the first part of the work. The AuNP-decorated 2b and 2c catalysts were added to the mixture of 4-nitrophenol and NaBH<sub>4</sub> to initiate the catalytic reaction for the catalytic experiments. The catalytic reaction was then monitored by UV-Vis absorption spectroscopy at an interval of 2 min. Figure

4.2.20 shows the UV-Vis absorption spectra of the conversion of 4-nitrophenol to 4-aminophenol with time using AuNP-decorated 2b and 2c. The running spectra ranges from 250 to 600 nm. It can be observed that the characteristic peak of the UV-Vis spectra of the nitrophenol red shifted from 317 to 400 nm with the addition of NaBH<sub>4</sub>, which is attributed to the formation of the 4-nitrophenolate ions due to the increasing alkalinity from investigating NaBH<sub>4</sub> in solution. The color of the nitrophenol solution changed from light to bright yellow. Remarkably, the mixture of nitrophenol and NaBH<sub>4</sub> remained unreactive for one week without the catalyst. The 4-nitrophenolate peak at 400 nm presents a decrease by adding the AuNP-2b and AuNP-2c to the catalytic solution, as shown in Figure 4.2.20. Meanwhile, a peak around 300 nm emerges due to the conversion of 4-nitrophenol to aminophenol. The catalytic reaction followed the pseudo first-order reaction kinetics because of the excessive amount of NaBH<sub>4</sub> used in the reaction and can be described by the following Equation 4.2.2:

$$-\ln \frac{A_t}{A_0} = kt \quad \text{Equation 4.2.2}$$

A<sub>t</sub> represents the intensity of the maximal absorptive peak of 4-nitrophenolate at 400 nm at time t, and A<sub>0</sub> represents the initial intensity.

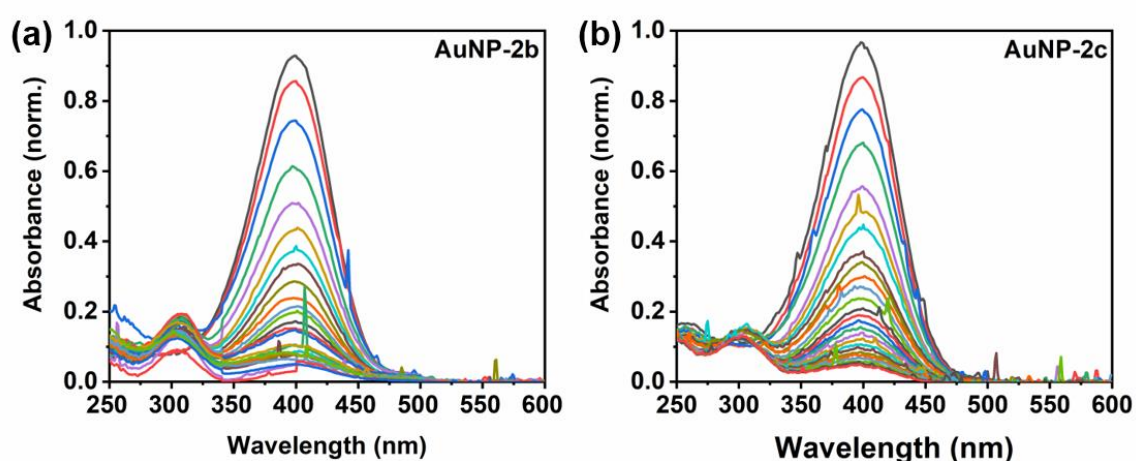


**Figure 4.2.20.** Time dependence of UV-Vis absorption spectra from 250 to 600 nm of the 4-nitrophenol reduction by NaBH<sub>4</sub> by using AuNP-2b (a) and AuNP-2c composite nonwoven as the catalysts (b).

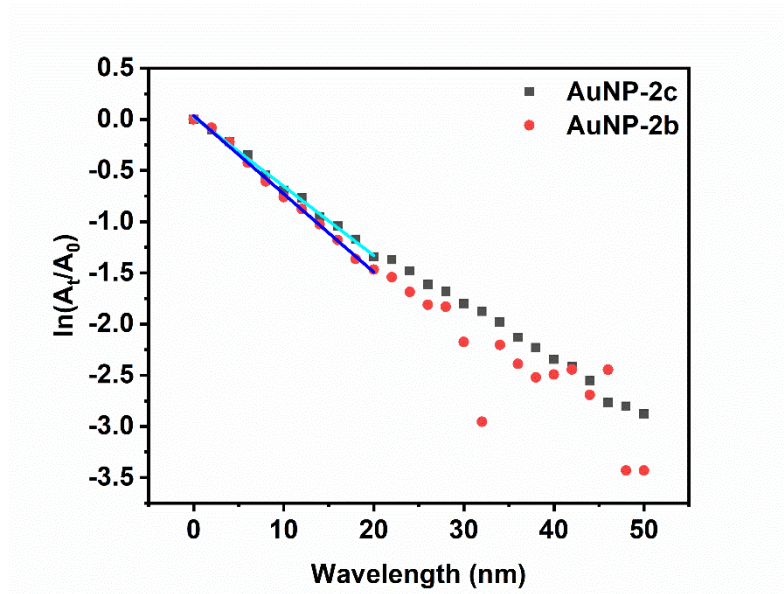


**Figure 4.2.21.** Plot of  $\ln(A_t/A_0)$  of the 4-nitrophenol reduction by investigating AuNP-2b and AuNP-2c composite nonwoven as the catalyst against the reaction time under ambient condition.

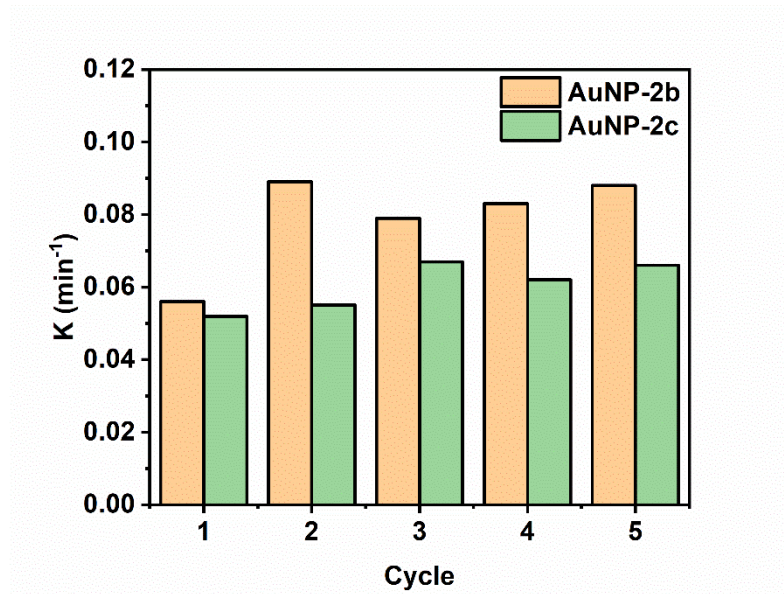


**Figure 4.2.22.** The apparent catalytic reaction rate of the 4-nitrophenol reduction by using AuNP-2b and AuNP-2c composite nonwovens as the catalysts versus the catalytic cycle.

**Table 4.2.3.** Summary of the apparent rate constant  $k_{app}$  for every catalytic cycle under ambient conditions by investigating AuNP-immobilized composite nonwovens.

	$k_1$	$k_2$	$k_3$	$k_4$	$k_5$
	(min <sup>-1</sup> )				
<b>AuNP-2b</b>	0.056	0.089	0.079	0.083	0.088
<b>AuNP-2c</b>	0.052	0.055	0.067	0.062	0.066

A good linear relationship between  $\ln(A_t/A_0)$  versus time can be observed, as shown in Figure 4.2.21. Thus, the apparent catalytic reaction rate can be extracted directly by the slope of the linear fitting of the  $\ln(A_t/A_0)$  versus time. The apparent catalytic reaction rate of the 1<sup>st</sup> cycle of the catalytic reaction by using AuNP-2b and AuNP-2c as the catalyst are 0.056 min<sup>-1</sup> and 0.052 min<sup>-1</sup>, respectively, whereas they increased after five cycles to 0.088 min<sup>-1</sup> and 0.066 min<sup>-1</sup> respectively (Table 4.2.3 and Figure 4.2.22). These results indicated that the apparent catalytic reaction rates are in the same range, and the reasons might be that similar amounts of gold were decorated within nonwoven 2b and 2c (Table 4.2.4) and the size distributions of the AuNP should also be similar, as the same procedure was followed to immobilize the AuNP within the nonwoven. Even the wettability of the composite nonwoven AuNP-2b and AuNP-2c displayed no significant differences. Regarding the possibility of recycling, the AuNP-2b and AuNP-2c composite nonwovens as catalysts present good reusability. The slight increase of the apparent catalytic reaction rate can be attributed to the increasing wettability of the composite nonwoven after five cycles. consequently, the reactant can diffuse much faster into the nonwoven and more AuNP can be efficiently utilized for the catalytic reaction. As leaching of the AuNP is also a significant challenge in the field of catalysis, it is considered an important parameter to estimate the catalytic performance of the catalyst and catalyst carrier. The leaching tests in our work were carried out with the help of ICP-OES measurements and the results are summarized in Table 4.2.4. The results indicated that only a very small amount of the gold catalyst can be detected leaching after the catalytic reaction. Only an estimated value can be provided here because the measurement range of the ICP-OES is limited. The gold detectable in the

catalytic solution might be a result of the loss of the fibers at the edge of the nonwoven. AuNP-2b and AuNP-2c have already presented good performance regarding the preventing of the leaching during the catalytic reaction. The apparent reaction rate constants of our system are in a similar range in comparison with the other systems in the literatures (Figure 4.2.23).

**Table 4.2.4.** Summary of gold contents in composite nonwovens 2b and 2c, the average apparent rate constant  $k_{app}$  of five cycles with error bar, and the leaching amount of AuNP after the catalytic reactions.

	$m_{Au}^{[a]}$ ( $\mu\text{g}$ )	$k_{app}^{[b]}$ ( $\text{min}^{-1}$ )	Leaching <sup>[c]</sup> (wt%)	Leaching <sup>[d]</sup> (wt%)
<b>AuNP-2b</b>	42	$0.079 \pm 0.012$	1	0.1
<b>AuNP-2c</b>	42	$0.06 \pm 0.006$	0.2	0

[a] The content of the gold investigated in the catalytic reaction was determined by ICP-OES.

[b] The apparent catalytic reaction rate was evaluated with an error bar, which presents the average value of the five cycles with standard deviation.

[c] The approximate value of leaching of the AuNP after the first and five cycle of nitrophenol reduction, determined by ICP-OES.

[d] The leaching of the AuNP after five cycles of nitrophenol reduction, determined by ICP-OES.

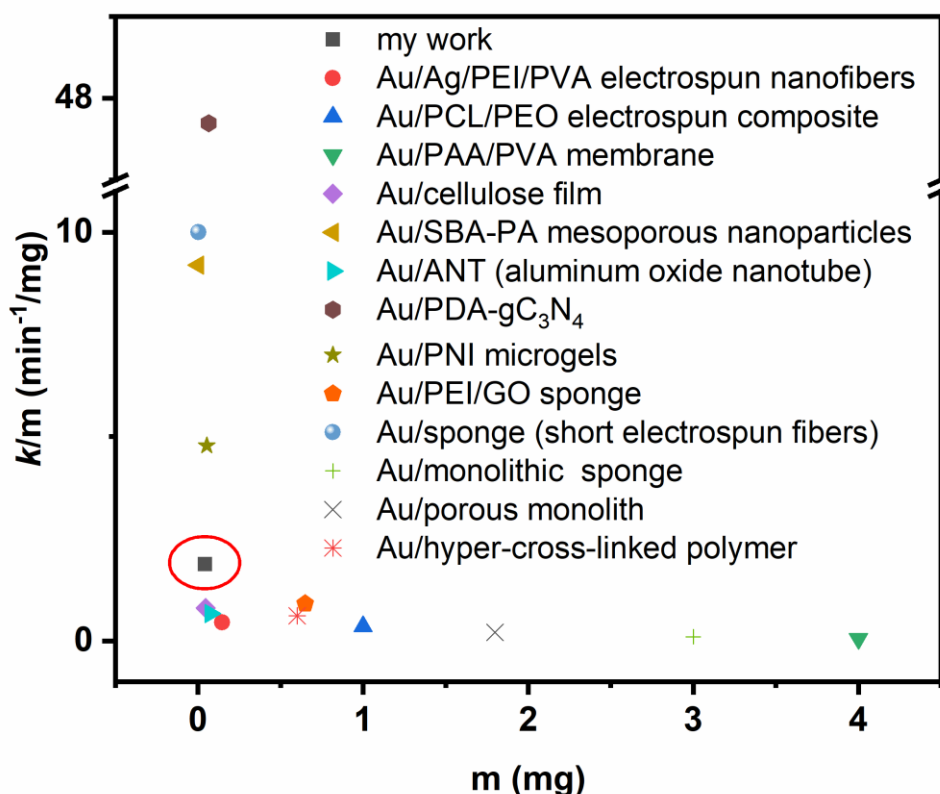


**Figure 4.2.23.** Ashby plot of the apparent catalytic reaction rate constant  $k$  against the amount of gold (mg) with different supports for nitrophenol reduction. Au/Ag/PEI/PVA electrospun nanofibers,<sup>176</sup> Au/PCL/PEO electrospun composite,<sup>177</sup> Au/PAA/PVA membrane,<sup>178</sup> Au/Cellulose film,<sup>179</sup> Au/SBA-PA mesoporous nanoparticles,<sup>180</sup> Au/ANT (aluminum oxide nanotube),<sup>181</sup> Au/PDA-gC<sub>3</sub>N<sub>4</sub>,<sup>182</sup> Au/PNI microgels,<sup>183</sup> Au/PEI/GO sponge,<sup>184</sup> Au/sponge (short electrospun fibers),<sup>185</sup> Au/Monolithic sponges,<sup>186</sup> Au/porous monolith,<sup>187</sup> Au/TR-HCP-TPMT (Hyper-Cross-Linked Polymer).<sup>188</sup>

#### 4.2.5 Conclusion

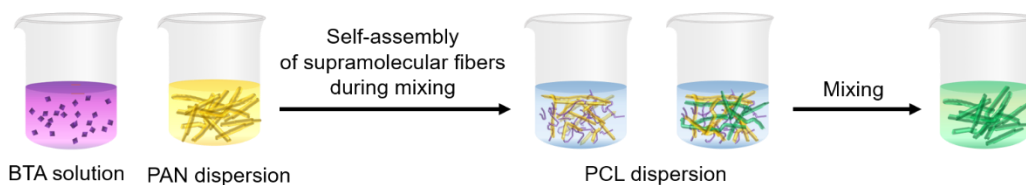
Composite nonwovens containing supramolecular BTA nanofibers were prepared by combined the electrospinning and the wet-laid process. The fabrication can be carried out through two different routes A and B, respectively, precipitated BTA nanofibers and BTA solution were used for the sheeting forming wet-laid process. The results indicated that the composite nonwovens fabricated via route B presented better mechanical property and morphology, as evidenced by the homogenous distribution of the BTA nanofibers and short PAN fibers within the nonwovens. The AuNP

immobilized composite nonwovens can be obtained by *in-situ* reduction. The results showed that the AuNP can be immobilized within the nonwovens without obvious aggregation. The nitrophenol reduction was then performed to examine the catalytic performance of the AuNP-containing nonwovens. It can be deduced that the AuNP containing nonwovens presented comparable catalytic activity in comparison with those reported in literatures. In addition, they presented good reusability without significant leaching.

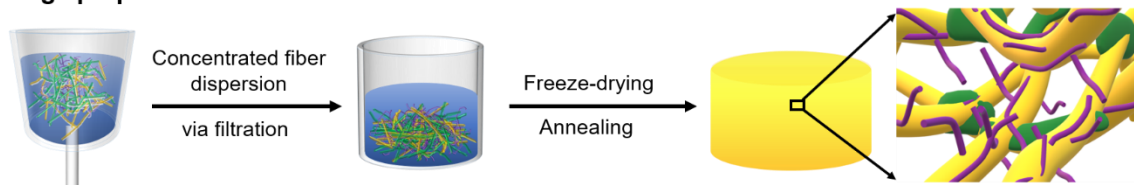
### 4.3 Multifunctional sponge combining the network of supramolecular nanofibers and short electrospun fibers

After a thorough study of the composite nonwoven consisting of BTA nanofibers and short PAN fibers in the second part of the work, some imperfections are still present due to the low porosity of the nonwoven. Thus, the thinking behind this work is to exploit a new material to improve this aspect. Sponge material has attracted great attention as it is ultralight and soft and consists of an interconnected construction. Thus, porosity improvement can be expected compared with nonwoven. Sponge as a carrier of AuNP can potentially enhance the catalytic performance and even be used as the supporter for the separation of the AuNP.

#### I. Preparation of fiber dispersions



#### II. Sponge preparation



#### III. Immobilisation of AuNP

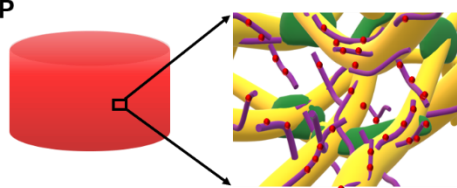


**Figure 4.3.1.** Processing diagram describing the fabrication steps of BTA-sponge. I. The preparation of the dispersions by self-assembly of supramolecular BTA nanofibers, short PAN and PCL fibers. II. The preparation of the BTA-sponge by concentrating the fiber dispersions, freeze-drying and thermal annealing. III. The formation of AuNP *in situ* reduction.

### 4.3.1 Fabrication of BTA-sponge

In this study, a facile method was developed to prepare the BTA-sponge consisting of self-assembly BTA nanofiber and short electrospun fibers. The fabrication procedure of the BTA-sponge was illustrated in Figure 4.3.1. Briefly, the fabrication procedure can be divided into several steps. Firstly, the BTA molecules were totally dissolved in a mixture of isopropanol and water at elevated temperature and then cooled down to room temperature (Figure 4.3.2). Subsequently, BTA molecule solution was added to the dispersion of the short PAN fibers in water. The BTA nanofibers were immediately generated via the self-assembly process in the mixture of isopropanol and water. A higher amount of water accelerated the process of BTA nanofiber generation.

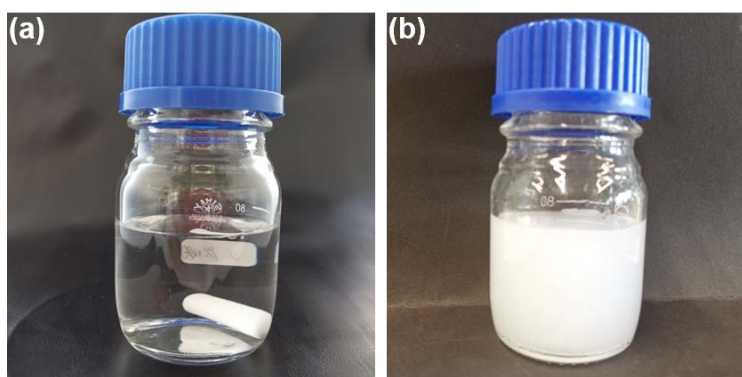


**Figure 4.3.2.** (a) Photograph of the solution of BTA molecules. (b) The dispersion of the mixture of short PAN fibers, short PCL fibers and self-assembly BTA nanofibers for preparing the BTA-sponge II.

The short PCL fibers were then added to the dispersion of the mixture of the BTA nanofibers (Figure 4.3.1). It is worth noticing that the homogenous distribution of the short PAN fibers, BTA nanofibers and short PCL fibers in the dispersion play an important role in fabricating a uniform sponge. This dispersion was then concentrated and freeze-dried into sponge. An annealing process at 70 °C is necessary to obtain mechanically stable sponge since physically cross-linked BTA-sponge can be produced by melting the short PCL fibers at 70 °C for 2 h. Thus, the short PAN fibers served as the skeleton for this sponge, and supramolecule BTA nanofibers via self-assembly were generated and entangled with short PAN and PCL fibers, the short PCL fibers being regarded as the glue. The electrospun PAN fibers with a diameter of  $1.4 \pm 0.3 \mu\text{m}$  were prepared by dissolving the polymer in dimethylformamide and

electrospinning (shown in Figure 4.3.3a and 4.3.3c). Afterwards, the PAN nonwovens were cut into short fibers in a mixture of isopropanol: H<sub>2</sub>O 7: 3 (w/w) and the length of the short PAN fibers was  $523 \pm 265 \mu\text{m}$  (Figure 4.3.4a and 4.3.4c). In addition, the diameter of the short PCL fibers was in the range of  $1.5 \pm 0.3 \mu\text{m}$  according to SEM analysis (shown in Figure 4.3.3b and 4.3.3d). These short PCL fibers were homogenously dispersed in the mixture of isopropanol: H<sub>2</sub>O 7:3 (w/w) and the length of the short PCL fibers was in the range of  $325 \pm 125 \mu\text{m}$  according to the optical microscope (Figure 4.4.4b and 4.4.4d). Regarding this part of the work, different contents of BTA nanofibers in the sponge were prepared by varying the amount of the BTA solution while keeping the amount of short PAN fibers and PCL fibers the same for all cases. Solutions of 0.05 and 0.1 wt % BTA were prepared for fabricating sponges containing BTA nanofibers. The supramolecular BTA can be totally dissolved in a mixture of isopropanol and H<sub>2</sub>O (9:1 w:w) by heating. When it is mixed with short PAN fibers in water, BTA nanofibers are immediately generated due to self-assembly.

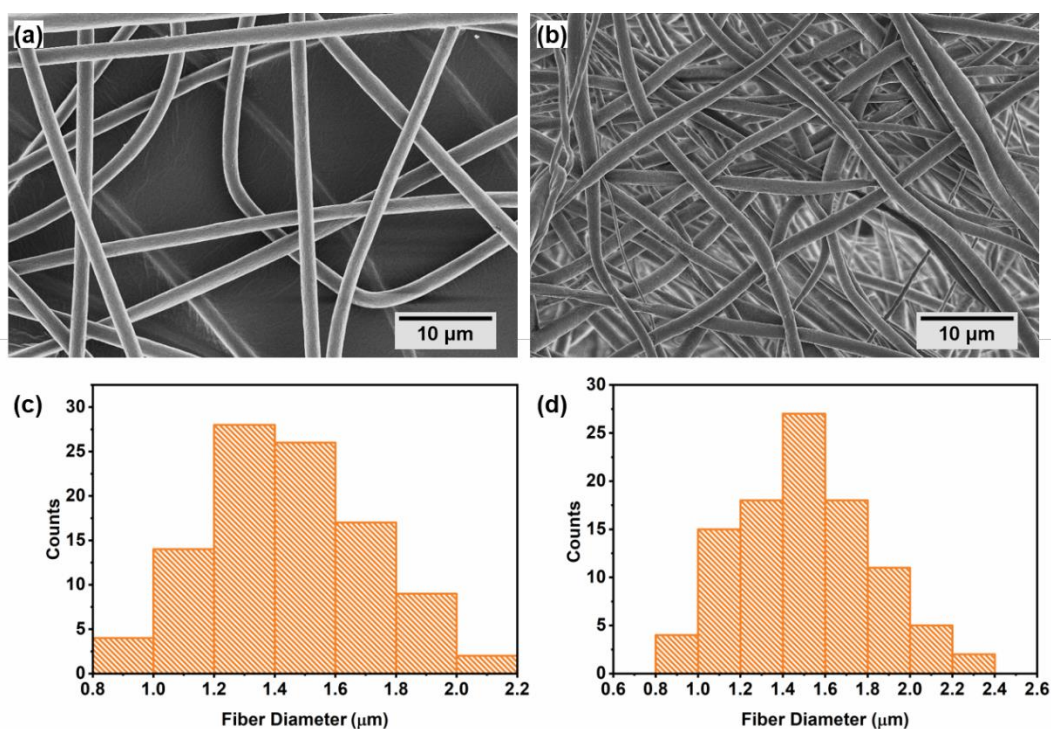


**Figure 4.3.3.** (a–b) SEM images of PAN and PCL electrospun fibers and (c–d) their diameter distribution of the corresponding fibers.

**Table 4.3.1.** The parameters of the preparation of the sponge with different amounts of BTA, together with the apparent density of the functional BTA-sponges.

Entry	PAN Dispersion (mL) <sup>[a]</sup>	PCL Dispersion (mL) <sup>[c]</sup>	BTA Solution (w/w %)	The content of BTA (wt%) <sup>[e]</sup>	Density of sponge (mg/cm <sup>3</sup> )
Reference	20	3.6	-	-	26 ± 5
BTA-sponge I	20	3.6	0.05	14	24 ± 1
BTA-sponge II	20	3.6	0.1	25	28 ± 2
BTA-sponge III	40 <sup>[b]</sup>	3.6	0.1 <sup>[d]</sup>	39	34 ± 4

[a] The concentration of PAN short fibers is 0.5 mg/mL.

[b] The concentration of PAN short fibers is 0.25 mg/mL.

[c] The concentration of the short PCL fibers is 2.8 mg/mL.

[d] The volume of the BTA solution is 20 mL, the other is 10 mL.

[e] The content of the BTA in the sponge can be determined by <sup>1</sup>H-NMR.

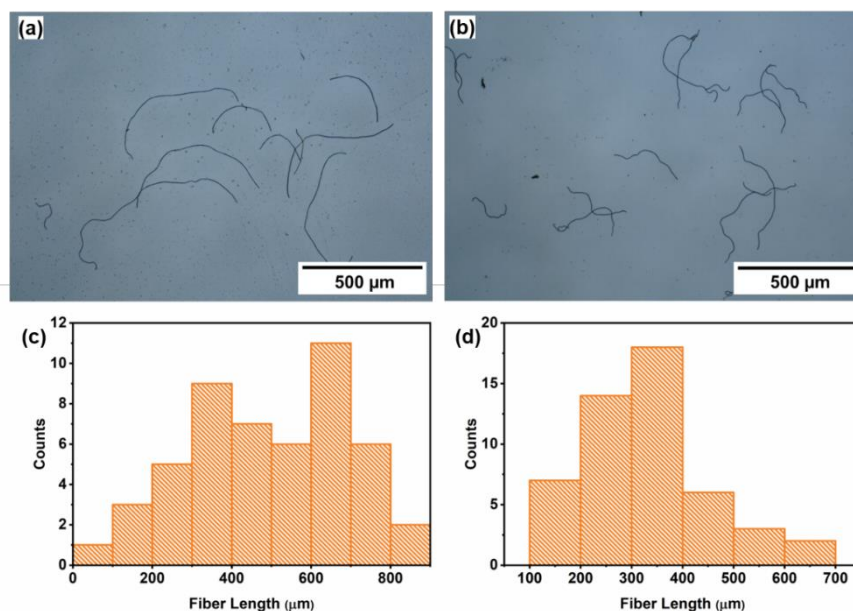


**Figure 4.3.4.** Photograph of short PAN and PCL fibers (a-b) and their corresponding fiber length distributions (c-d).

### 4.3.2 Characterization of the BTA-sponge

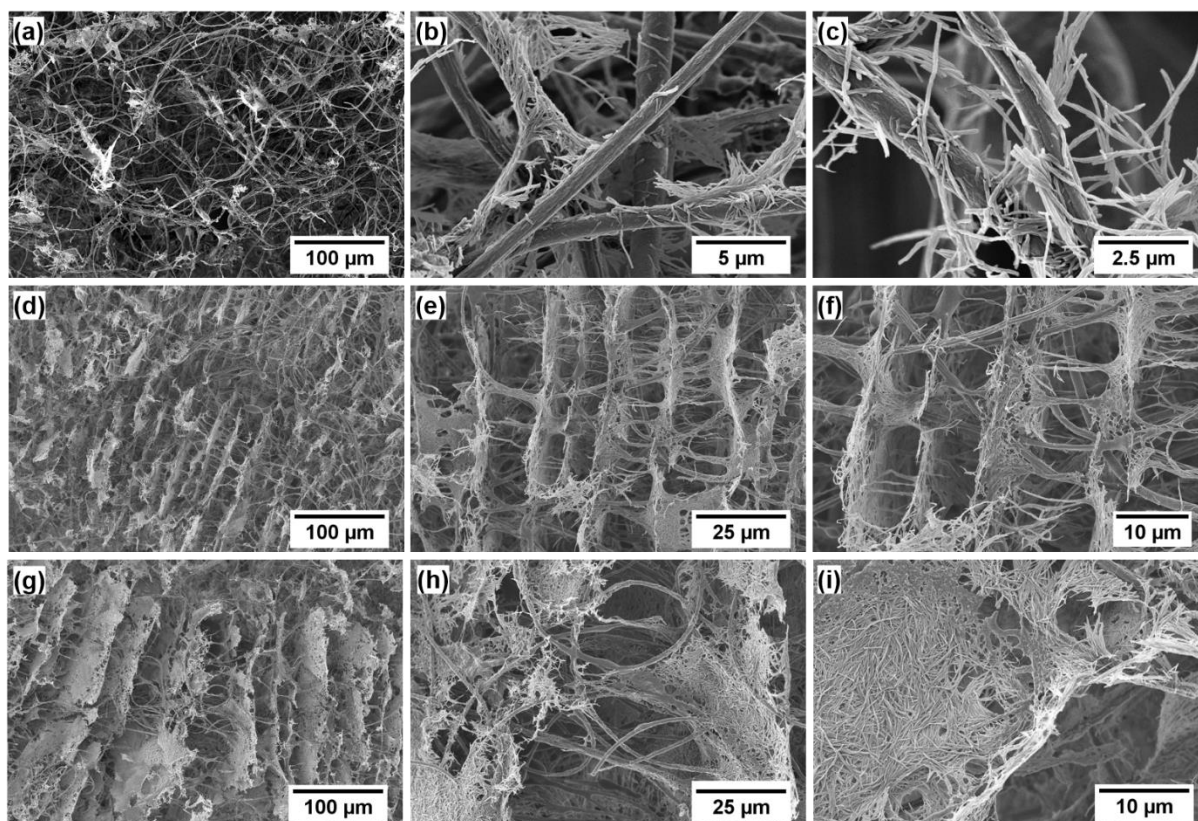


**Figure 4.3.5.** SEM images of the BTA-sponge with different contents of BTA nanofibers. (a–c) The morphology of the BTA-sponge I at different degrees of magnification. (d–f) The morphology of the BTA-sponge II at different degrees of magnification. (g–i) The morphology of the BTA-sponge III at different degrees of magnification.

After successful fabrication of the sponge containing the BTA nanofibers, thorough characterizations of the BTA-sponge were carried out with the help of various analytical tools. Firstly, Figure 4.3.5 depicts the top-view SEM images of the BTA-sponges I to III prepared by increasing the content of the BTA accordingly. The corresponding top-view SEM images indicated that different contents of BTA nanofibers presented different morphologies. The BTA nanofibers within BTA-sponge I are wrapped around the short PAN fibers via electrostatic adsorption, and the short PAN fibers act as the framework of the sponge and are physically cross-linked (Figure 4.3.5 a–c). With an increasing amount of BTA nanofibers fabricated in BTA-sponge II, the sponge obviously presented different morphology compared with BTA-sponge I mentioned above. The sponge was composed of the short PAN fibers framework connected by

the interpenetrating BTA nanofibers. With the highest content of the BTA nanofibers, more densely packed interpenetrating BTA nanofibers can be observed within short PAN fibers. It is shown that short PCL fibers, when melted through thermal annealing at 70 °C, functioned as the glue for short PAN fibers and BTA nanofibers at the cross-linking point (Figure 4.3.6). Thermogravimetric analysis shows that the PCL polymer remains stable up to 350 °C (Figure 4.3.7a), while the melting point of the PCL polymer is around 58 °C determined by differential scanning calorimetry (Figure 4.3.7b). Again, this proves that the PCL can be melted at 70 °C, presenting high viscosity and functionalizing as an adhesive.

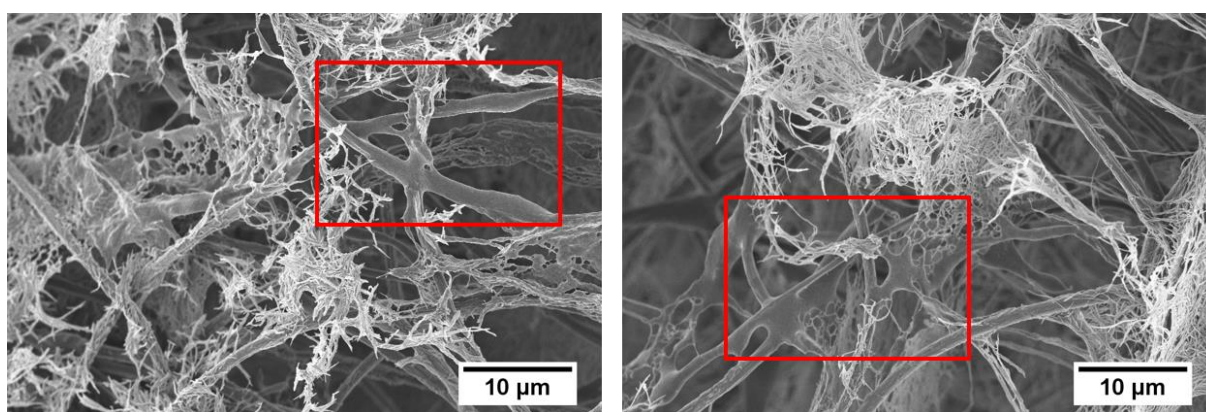


**Figure 4.3.6.** SEM images of click point (in the red rectangle) of BTA-sponge I at different positions.

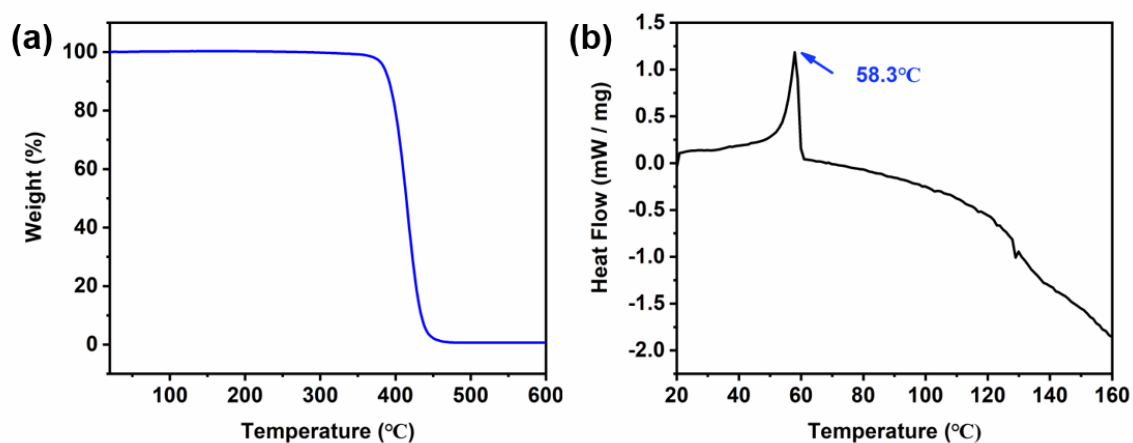


**Figure 4.3.7.** (a) Thermogravimetric analysis of the PCL powder. (b) Differential scanning calorimetry 1<sup>st</sup> heating curve of the PCL powder.

To have a comprehensive understanding of the compositions of the sponges of different types and their corresponding chemical structures, Fourier transform infrared (FT-IR) analysis was performed. The spectra of the sponge containing only short PAN fibers and short PCL fibers and the BTA-sponges I–III were recorded (Figure 4.3.8). The peaks of the sponge consisting of short PAN and PCL fibers at  $2243\text{ cm}^{-1}$  is assigned to the  $-\text{CN}$  (nitrile stretching) of the PAN polymer. However, the peak at  $1750\text{ cm}^{-1}$  that is assigned to the  $\text{C}=\text{O}$  ( $\text{C}=\text{O}$  stretching) might come either from either the PCL or PAN polymer (containing smaller than 7 wt% poly(methyl methacrylate) and sodium methallylsulfonate). Therefore, the information exacted from the FT-IR shows that there is no significant peak proving the existence of the PCL polymer inside. The FT-IR spectroscopy shows the characteristic peak of the terpyridine functional BTA at  $3260\text{ cm}^{-1}$  from N-H stretch vibration; at  $1667\text{ cm}^{-1}$  from amide I vibration and  $1563\text{ cm}^{-1}$  from amide II vibrational mode. These peaks have contributed to proving the presence of the threefold helical intermolecular hydrogen bonds of the BTA supramolecular. The peak at  $1580\text{ cm}^{-1}$  is attributed to the azomethine moiety, implying the existence of a  $-\text{CH}=\text{N}$  bond from the terpyridine functional group. However, there is no solid evidence that can be extracted from FT-IR spectroscopy proving the presence of PCL in the sponge.

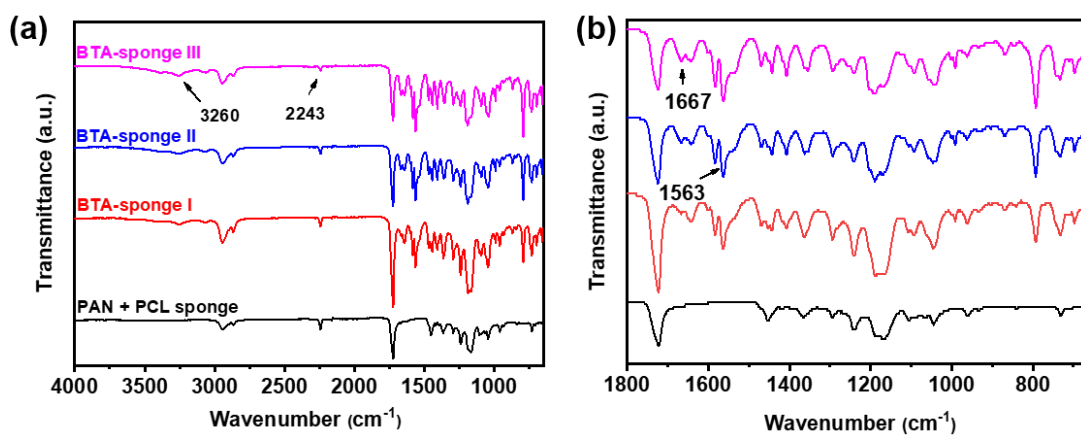


**Figure 4.3.8.** (a) FT-IR spectra of the BTA-sponge with different contents of BTA, respectively BTA-sponges I–III. It can be the proof that the PAN and BTA have been successfully fabricated in the sponge, and the sponge containing only short PAN fibers and short PCL fibers is the reference. (b) Zoomed in FT-IR spectra of the range from  $1800\text{ cm}^{-1}$  to  $650\text{ cm}^{-1}$ .

Nuclear magnetic resonance spectroscopy was further performed to confirm the content of each composite in the sponge. The NMR spectra clearly indicated that the sponge contains PAN, PCL and BTA, when compared with those in the literature.<sup>189, 190</sup> The signals at 4.43 ppm, 3.97 ppm and 3.14 ppm originated from the composite BTA, PCL and PAN in the BTA-sponge, respectively (Figure 4.3.9 and Figure 4.3.10). <sup>1</sup>H-NMR analysis can also be used to obtain the mass ratio of the BTA, PCL and PAN in the sponge. The ratios (about 1.12 to 1) between the integral intensities of the PCL and PAN signals were almost identical for sponges of different types (Figure 4.3.10). The ratio between BTA and PAN increases proportionally from BTA-sponge I to III (1:2:4), which is in good agreement with the amount of the BTA investigated in the corresponding sponges. These results implied that almost all BTA investigated have been fabricated into the sponge successfully, while the amounts of the PAN and PCL were kept constant for all cases. In addition, it can be estimated that the weight percent of the BTA content in BTA-sponges I–III is 14, 25 and 39 wt% (Table 4.3.1). With an increasing content of BTA in the sponge, the volume density increased from an average of 24 to 34 mg/cm<sup>3</sup> (Table 4.3.1). The porosity of the sponge at the same time decreased gradually from 97 to 94 % (Figure 4.3.11).

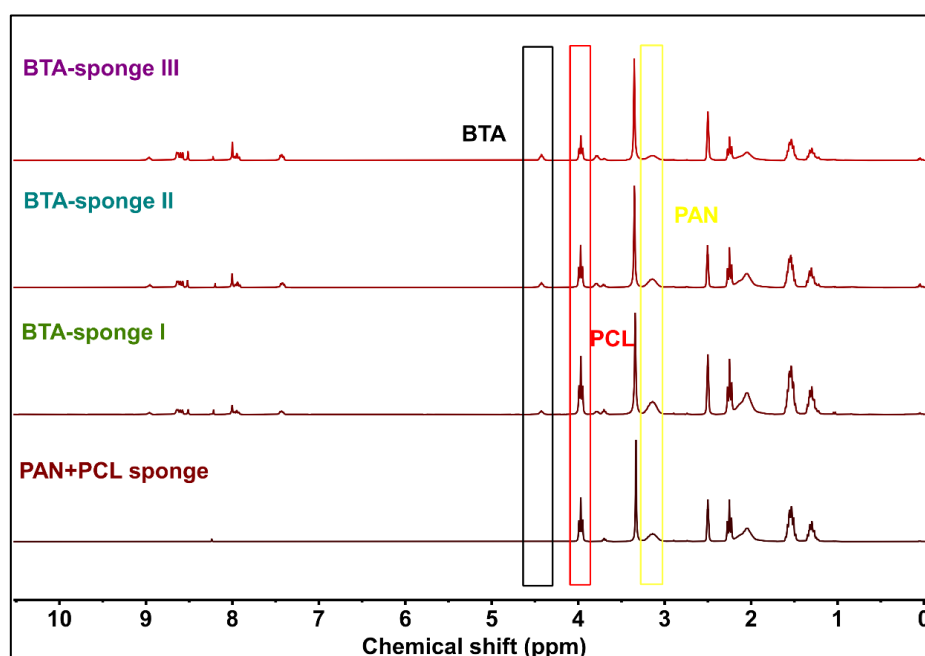


**Figure 4.3.9.** <sup>1</sup>H-NMR spectra of the sponges with different contents of BTA (BTA-sponge I–III), with the sponge containing only short PAN fibers and short PCL fibers as reference.

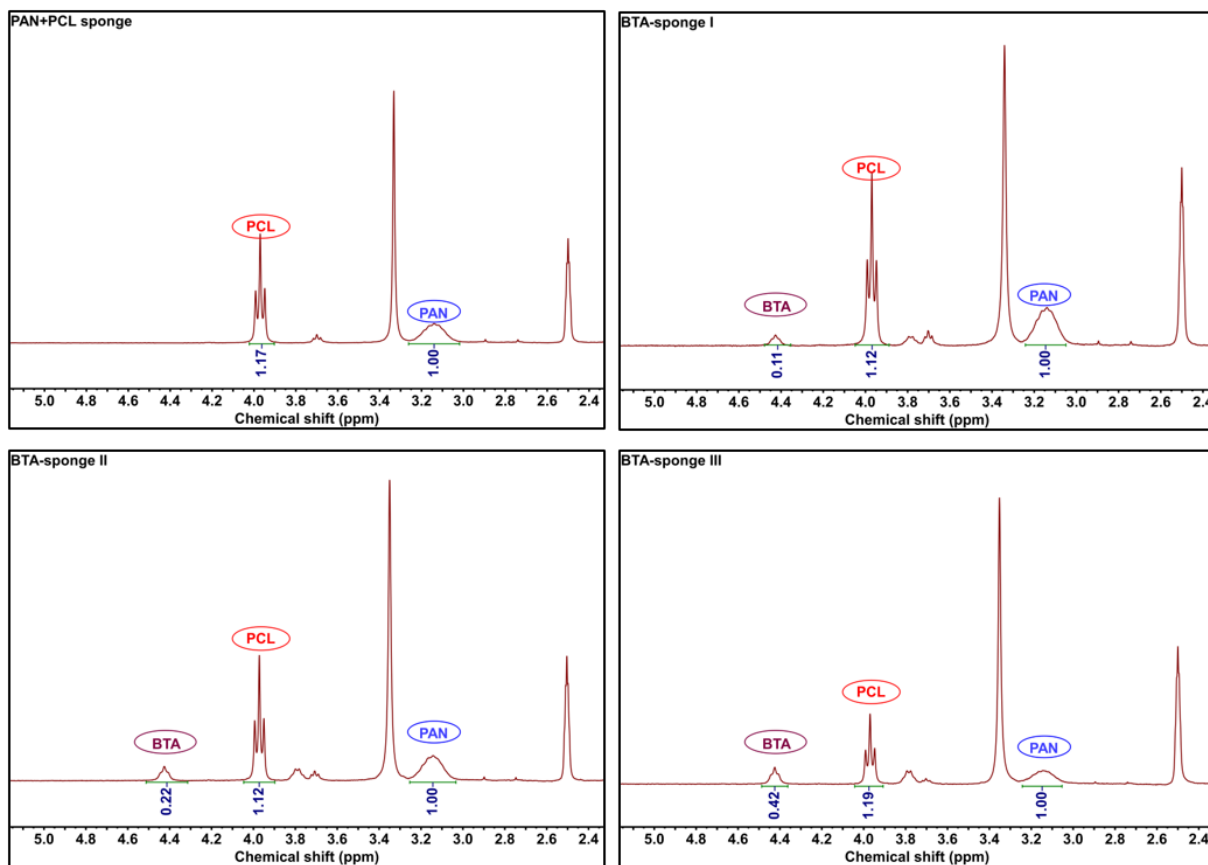
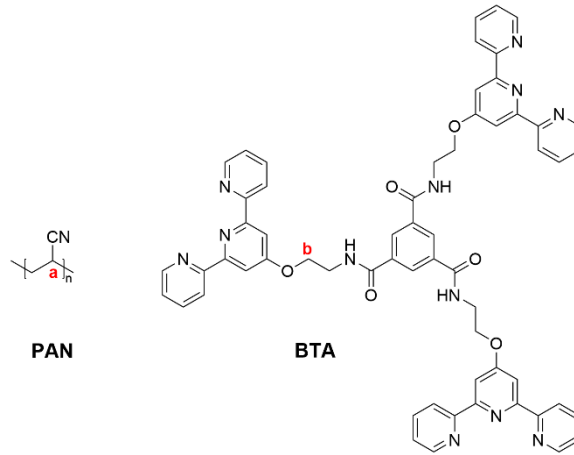


**Figure 4.3.10.** <sup>1</sup>H-NMR spectra of the sponge containing short PAN fibers and short PCL fibers and the BTA-sponge with different contents of BTA, together with the corresponding ratio of the integral of the different composites.

## The calculation of the BTA content in BTA-sponge

For example, for the BTA-sponge III.



$$n_{\text{monomer}} = \frac{93\% \times 10 \text{ mg}}{53 \frac{\text{g}}{\text{mol}}} = 0.175 \text{ mmol}$$

$$n_{\text{BTA}} = \frac{\frac{0.42}{1} \times n_{\text{monomer}}}{6} = 0.0123 \text{ mmol}$$

$$m_{\text{BTA}} = n_{\text{BTA}} \times M_{\text{BTA}} = 0.0123 \text{ mmol} \times 1031 \frac{\text{g}}{\text{mol}} = 12.6 \text{ mg}$$

$$\text{wt}\% = \frac{12.6 \text{ mg}}{12.6 \text{ mg} + 10 \text{ mg} + 10 \text{ mg}} = 39\%$$

## Calculation of sponge porosity<sup>191</sup>

The porosity of the sponges can be determined according to a standard method using the following Equation 4.3.1:

$$\eta = (V - m_1/\rho_1 - m_2/\rho_2 - m_3/\rho_3)/V \times 100\% \quad \text{Equation 4.3.1}$$

where  $\eta$  is the porosity,  $V$  represents the volume of the sponge, and  $m_1$ ,  $m_2$  and  $m_3$ , are the mass of the PAN fibers, the mass of the PCL fibers and the mass of BTA fibers, respectively.  $\rho_1$ ,  $\rho_2$  and  $\rho_3$  are the densities of the bulky materials, and the corresponding values are 1.18, 1.14 and 0.24 g/cm<sup>3</sup>, respectively. The diameter and mass of the sponge are shown in Figure 4.3.12, and the shape of the sponge can be regarded as cylindrical.

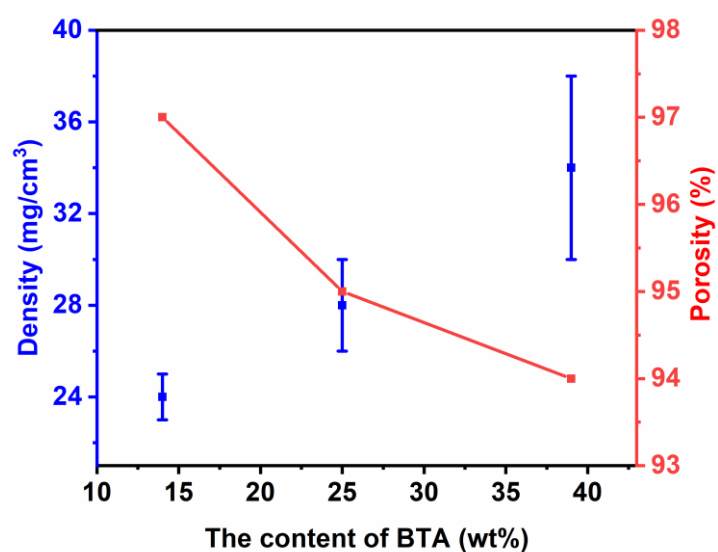


**Figure 4.3.11.** The plot of the density and porosity of the BTA-sponges I-III versus the content of BTA nanofibers within sponges.

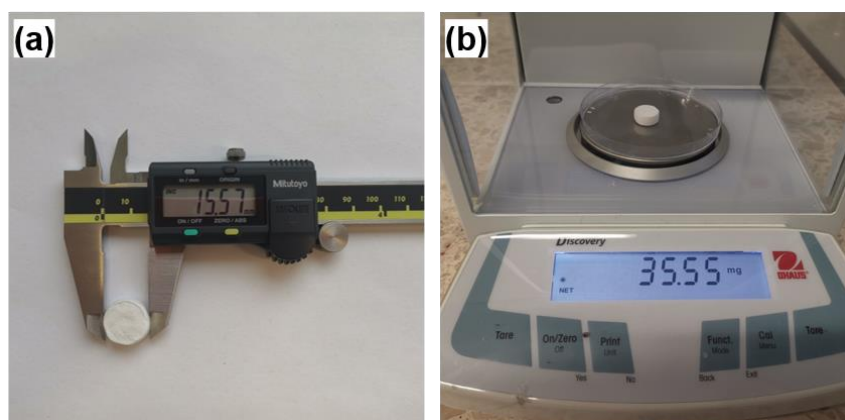


**Figure 4.3.12.** Photographs showing the size and mass measurement of BTA-sponge III with a volume of 1.0 cm<sup>3</sup> (a) and a mass of 35.6 mg, and a corresponding density of 35.6 mg/cm<sup>3</sup> (b).

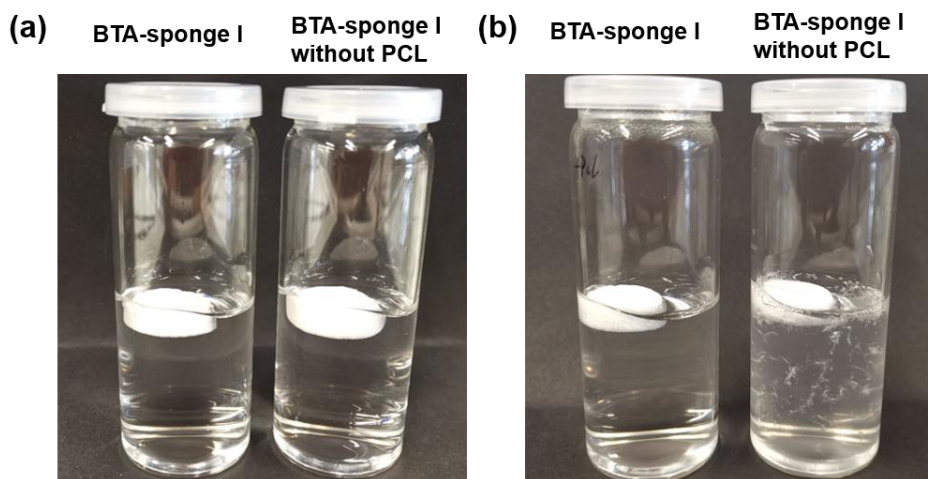


**Figure 4.3.13.** (a) Structural stability test of BTA-sponge I in water. BTA-sponge I without PCL was used as reference. (b) Sponges in water after being shaken at 500 rpm for 90 min.

As the sponge would be further modified or used in an aqueous environment, the stability test of sponge I in water was carried out and sponge I without PCL was used as the reference. Both sponges were submerged in water and shaken at 500 rpm for 90 min. The results showed that sponge I without PCL was destroyed, whereas sponge I remained intact (Figure 4.3.13). Thus, the BTA-sponge is more mechanically stable with the presence of short PCL fibers as glue.

#### 4.3.3 *In situ* formation of the AuNP within the BTA-sponge

After characterization of the sponge containing BTA nanofibers, the sponge was modified with AuNP and investigated in catalytic reactions as the carrier for the catalyst. The sponge-supported AuNP were obtained by impregnation of  $\text{HAuCl}_4$  into the sponge via the filtration method under ambient conditions (Figure 4.3.14a). Gold ion contained in the sponge can then be reduced to AuNP in the presence of sodium borohydride as the reductive reagent. After the *in situ* formation of the AuNP, the BTA-sponge was washed with Milli-Q water to remove unbound AuNP and unstable BTA nanofibers. A change of the sponge color from white to brown-orange can be observed, which implies that the AuNP have been fabricated into the sponge (Figure 4.3.14 b and c). This AuNP-BTA-sponges can be further characterized by TEM to verify the average size of AuNP and their distribution. The TEM images of BTA-sponge III indicate that AuNP distributed on the surface of the BTA nanofiber without obviously aggregation (Figure 4.3.15) and display a narrow size distribution of  $2.4 \pm 0.7$  nm (Figure 4.3.16).

They indicate that this sponge containing BTA offers the advantage of the immobilization of small AuNP without aggregation. The AuNP with an average size of 2.4 nm are not normally stable in the colloidal dispersion because of the high surface energy. However, the AuNP immobilization in this method provide the chance for long-term storage of the AuNP and their use for the catalytic application.

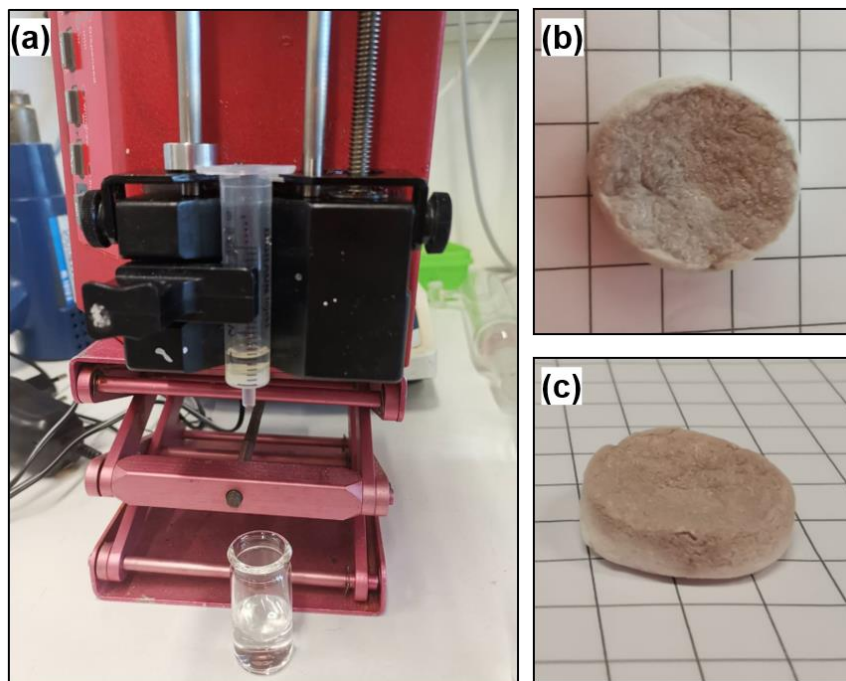


**Figure 4.3.14.** (a) Set-up for the preparation of AuNP-immobilized BTA-Sponge. Gold ion immobilized in BTA-sponge via the filtration of  $\text{HAuCl}_4$  solution through the sponge; (b) image of the top-view of the AuNP-immobilized BTA-sponge II and (c) image of the side view of the AuNP-immobilized sponge II.

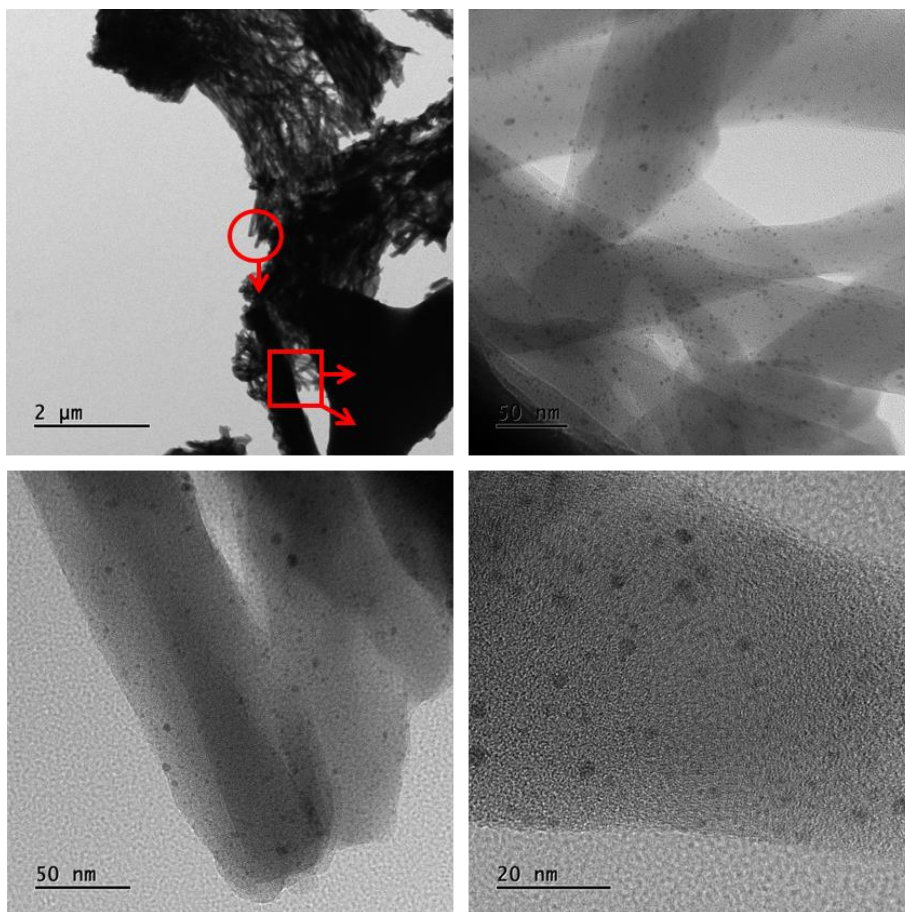


**Figure 4.3.15.** TEM images of BTA-sponge III at different magnifications.

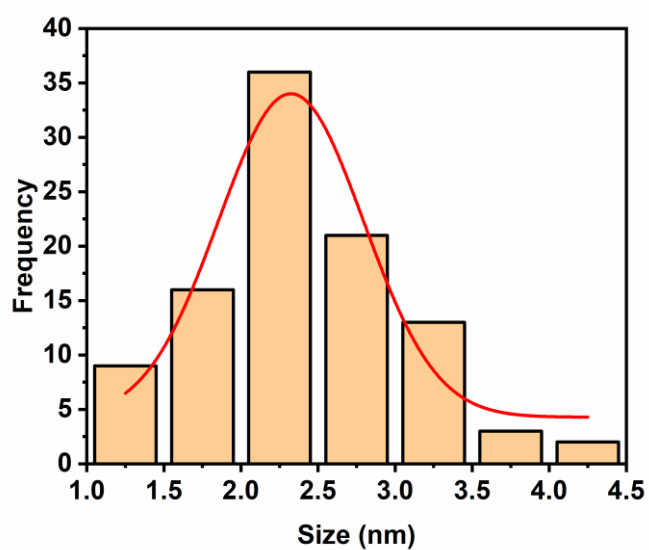


**Figure 4.3.16.** Size distribution of AuNP within BTA-sponge III determined by TEM.

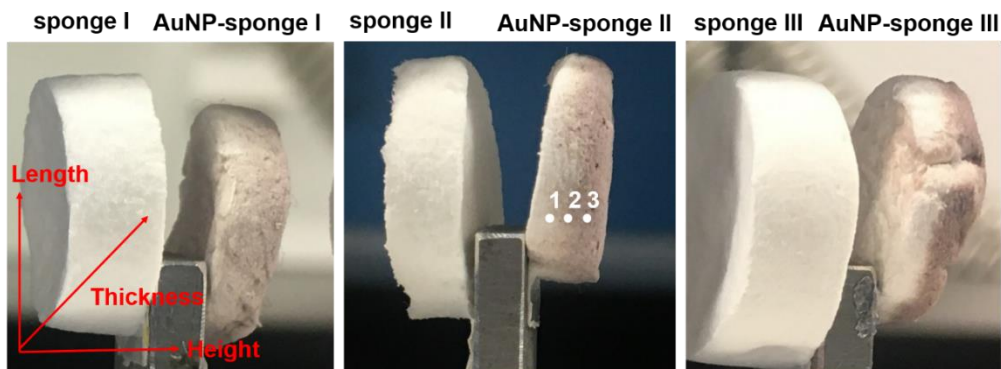


**Figure 4.3.17.** Photograph of a AuNP-BTA sponge (right, AuNP distribution leads to color gradient) and the corresponding non-loaded BTA sponge (left, white color). The white dots labelled 1,2 and 3 illustrate exemplarily the chosen SAXS measuring positions. Both sponges contain 25 wt% BTA, equal to sponge type II. Additionally, a sketch of the sample to beam direction and the corresponding coordinate system is given.

### Small-Angle-X-ray scattering (SAXS)

The regional size distribution of the AuNP inside the 1,3,5-benzotrisamides (BTA) sponges with different BTA content is investigated further by SAXS measurements. In detail, the BTA amount was 14 wt% (BTA-sponge I), 25 wt% (BTA-sponge II) and 39 wt% (BTA-sponge III). For each sample (non-loaded and AuNP loaded BTA-sponge I-III) three measuring positions (point 1, 2 and 3) were chosen, located approximately at 25% (1), 50% (2) and 75% (3) of the total sponge height (Figure 4.3.17). Figures 4.3.18-4.4.20 show the 1D-SAXS intensities of the different types of AuNP-BTA sponges and the corresponding non-loaded BTA-sponges (called blank). In the nomenclature I-III denotes the sponge type and 1-3 the measuring point (low to high AuNP content).

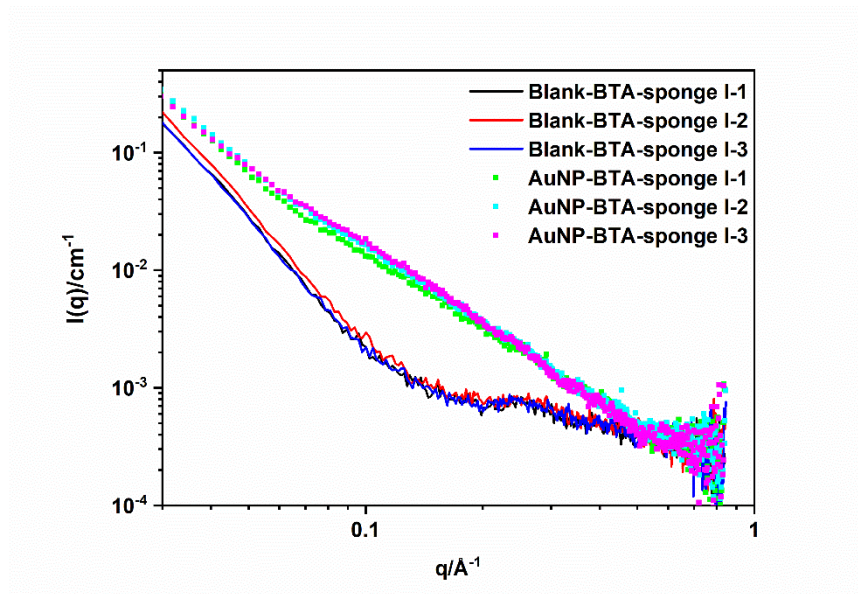


**Figure 4.3.18.** SAXS intensities from BTA-sponge I without AuNP at different measured points 1-3 (black, red and blue solid lines), and with immobilized AuNP (green, light blue, and pink scatter lines) before catalytic reaction.

The scattering intensities of the non-loaded samples are characterized by (a) a  $q^4$  power law (Porod law,  $q < 0.15 \text{ \AA}^{-1}$ ) resulting from the 3D mesoporous interfaces of the sponge structure, (b) a  $q^1$  scaling for  $q > 0.15 \text{ \AA}^{-1}$  typically for the particle structure of rod-like structures like fibers. The cross-over point between  $q^4$  to  $q^1$  points to a correlation length  $\xi$  of ca. 5 nm (approximation  $2\pi/q = \xi$ ) as a typical structure size inside the material, and (c) a broad shoulder at a maximal value around  $q = 0.26 \text{ \AA}^{-1}$ , which corresponds with the interaction size/correlation length of  $d = 2\pi/q \approx 2.5 \text{ nm}$ . This value results from a liquid crystalline arrangement in consequence of self-assembly of BTA molecules. Since self-assembly is more pronounced with increasing BTA content the shoulder sharpness increases slightly with the BTA content of the sponges.

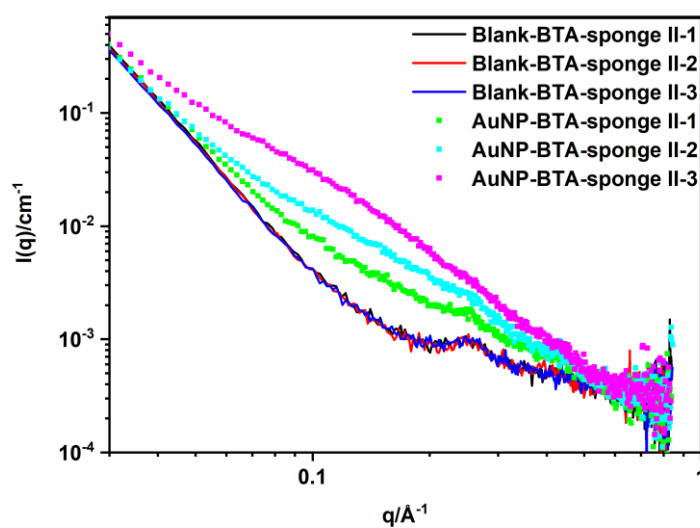


**Figure 4.3.19.** SAXS intensities from BTA-sponge II without AuNP at different measured points 1-3 (black, red and blue solid), and with immobilized AuNP (green, light blue, and pink scatter) before catalytic reaction.

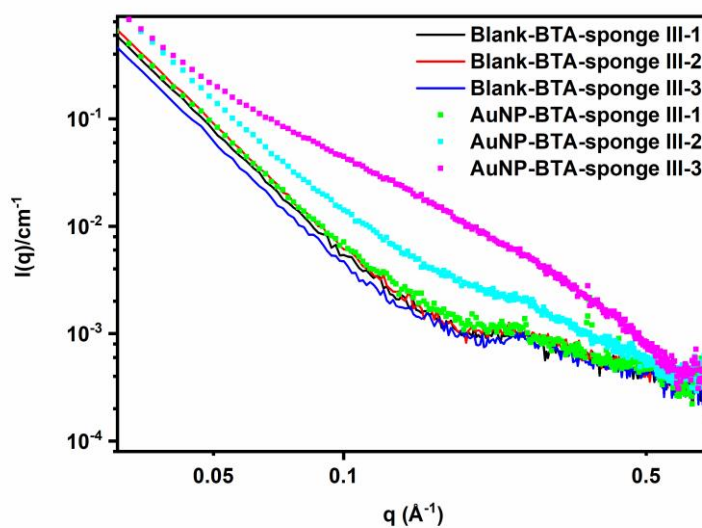


**Figure 4.3.20.** SAXS intensities BTA-sponge III without AuNP at different measured points 1-3 (black, red and blue solid), and with immobilized AuNP (green, light blue, and pink) before catalytic reaction.

The scattering patterns of the AuNP loaded sponges differ significantly from the corresponding profiles of the blanks and in contrast to non-loaded sponges the scattering profile for a given AuNP-BTA dependent in most cases on the SAXS measuring position -- a feature which can only be explained by local differences in the AuNP load. Visual inspection of the different AuNP-BTA sponge types reveals a color gradient from brown (high AuNP load) to white (none or small AuNP load) (Figure 4.3.17). This gradient is most pronounced for sponge type III (39 wt% BTA) and least obvious for type I (14 wt% BTA). Since the color code was in accordance with the scattering intensity (darkest brown corresponds to highest intensity and therefore to highest AuNP load) we addressed the local AuNP size distribution inside the sponges. Therefore, for each loaded sample the corresponding blank (average of 3 measuring points) was subtracted, and the resulting data were normalized to the same scale in a scattering region ( $q > 0.15 \text{ \AA}^{-1}$ ) which is sensitive to the amount (and size) of individual AuNP (Figure 4.3.21). These scaling factors  $K_x$  ( $K_x = I(q > 0.1 \text{ \AA}^{-1})_{\text{point 3}} / I(q > 0.1 \text{ \AA}^{-1})_{\text{point } x}$ ,  $x = \text{point 1, 2, or 3}$ ) demonstrated that dark brownish colored regions contains significantly more AuNP compared to less brownish or even white colored regions of the sponges. Table 4.3.2 gives an overview over the obtained values of  $K_x$ . Further, it underlines the fact that a higher content of BTA leads to significant increase in AuNP immobilization -- most AuNP are immobilized directly at/near the surface after application of the corresponding solution. Nevertheless, some AuNP drains more into the bulk of the sponges. Note, that in all cases the scattering intensities merge for  $q > 0.1 \text{ \AA}^{-1}$  underlining the fact that the AuNP size distributions are similar, thus at the sponge surface a preferred immobilization of special AuNP sizes can be ruled out.

**Table 4.3.2.** Relative amount of AuNP inside the sponges in dependence of the measurement position.

sample	factor $K_x$	AuNP amount	BTA content (wt%)
AuNP-BTA-sponge I-3	1	high	14
AuNP-BTA-sponge I-2	1/1.1	middle	14
AuNP-BTA-sponge I-1	1/1.3	low	14
AuNP-BTA-sponge II-3	1	high	25
AuNP-BTA-sponge II-2	1/3	middle	25
AuNP-BTA-sponge II-1	1/7	low	25
AuNP-BTA-sponge III-3	1	high	39
AuNP-BTA-sponge III-2	1/5	middle	39
AuNP-BTA-sponge III-1	1/30	low	39

The total scattering intensity  $I(q)$  contains the partial scattering intensity contributions of the BTA-sponge  $I(q)_{BTA}$  and the AuNP  $I(q)_{AuNP}$ , where the ratio of  $I(q)_{BTA}$  and  $I(q)_{AuNP}$  can vary from position to position and fitting the data with simple models without input of additional knowledge is considered as over the scope of this study. Most probably, the variation in the ratio of the partial intensities is the reason for the discrepancies in the scattering patterns for  $q < 0.1 \text{ \AA}^{-1}$ . Nevertheless, independent of a nanoparticle model from the cross point to the base line ( $q \approx 0.5 \text{ \AA}^{-1}$ ) one can conclude that at least the smallest size range of the AuNP is expected in the range of 2 nm (approximation of  $R_{small} = 4.5/q$ ).

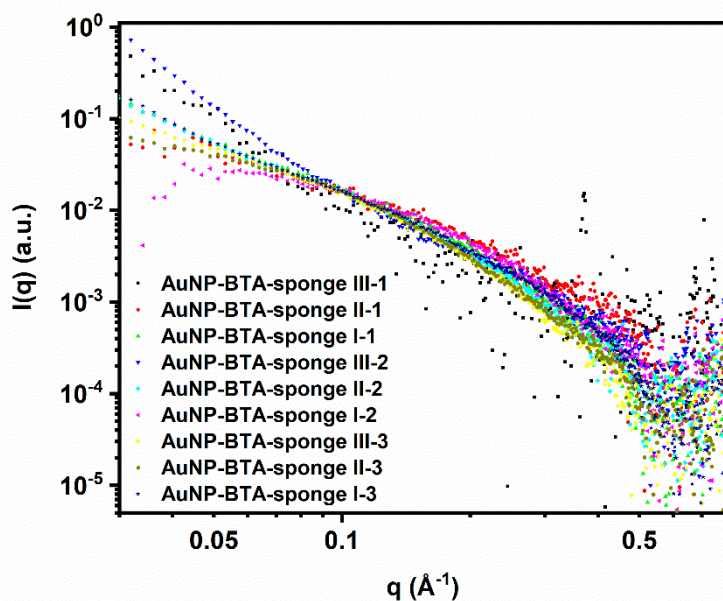


**Figure 4.3.21.** The scattering intensities of the AuNP in the decorated BTA-sponge I-III samples were determined by deduction of the intensity of the corresponding nonwovens.

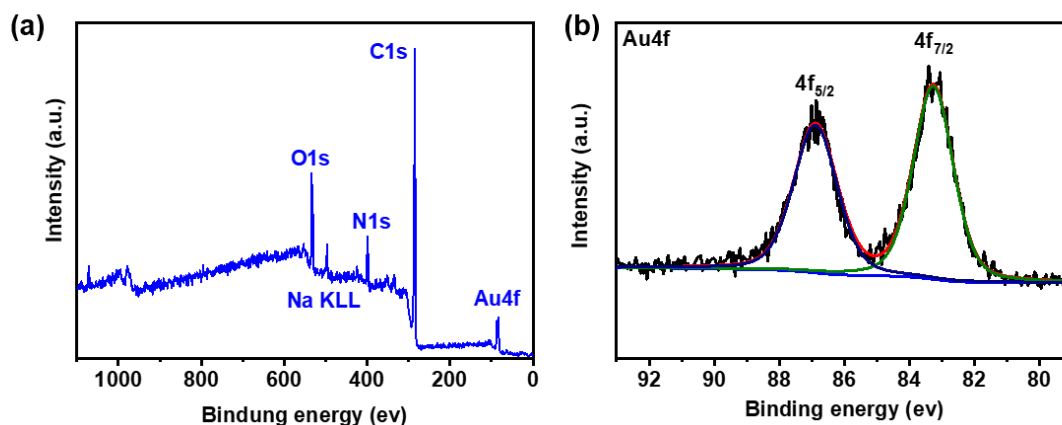


**Figure 4.3.22.** (a) X-ray photoelectron spectroscopy (XPS) survey spectrum of AuNP-immobilized sponge (BTA-sponge III), (b) and the high-resolution XPS spectrum of the Au element in the BTA-sponge III.

### X-ray photoelectron spectroscopy (XPS) measurement

In order to further investigate the chemical composition of the AuNP-immobilized BTA-sponge, XPS analysis was performed to study the chemical composition of the surface, as well as the oxidation states of BTA-sponge III, which has a huge impact on the

catalytic reaction. Element peaks corresponding to Au, C, O, N and Na in the XPS spectrum can be seen in Figure 4.3.22a. Figure 4.3.22b is the high-resolution spectrum of the Au4f electrons of BTA-sponge III. Two peaks at 83.3 and 86.9 eV, corresponding to the Au 4f<sub>7/2</sub> and 4f<sub>5/2</sub> bands respectively, can be observed in the spectrum. The two peaks are separated by 3.6 eV. The bonding energies of this line pair are slightly lower than those of bulk metallic gold, for which the Au 4f<sub>7/2</sub> and 4f<sub>5/2</sub> band peaks are found at 84.0 and 87.3 eV respectively.<sup>192</sup> Since the terpyridine as the N-donating function group in the BTA molecule can provide the electron that is accepted by the orbitals of the gold atoms. An increasing electron density of the gold atoms can result in a decrease of the apparent binding energy. The spectral positions and the energy separation verified the presence of zero-valent gold in the BTA-sponge III. Furthermore, there is no other peaks observed that can be attributed to Au<sup>3+</sup>, which is an indication that Au<sup>3+</sup> was completely reduced to Au<sup>0</sup> during the *in-situ* reduction process. The contents of the BTA contained on the surface of BTA-sponge III can be deduced from the XPS analysis. Figure 4.3.23 shows the N1s peaks of the BTA molecule, polyacrylonitrile and the AuNP-BTA-sponge III, respectively. The N1s peak of the BTA molecule and polyacrylonitrile were used as reference to analyze the composition of the AuNP-BTA-sponge III. For the AuNP-BTA-sponge III, two peaks can be found at 400.6 and 398.6 eV, which originated from the amide and terpyridine functional groups of the BTA molecule, respectively. The corresponding mass ratio is about 1:3.3 and is in good agreement with each nitrogen containing element in the BTA molecule. The peak at 399.6 eV represents the nitrile (-CN) moiety of polyacrylonitrile. The mass ratio between the nitrogen elements of the BTA molecule and those of polyacrylonitrile is approximately 47:53, respectively. As mentioned previously, the contents of BTA and polyacrylonitrile determined from the <sup>1</sup>H-NMR results are about 39 and 30 wt%, respectively. Thus, the mass ratio between the nitrogen elements from the two composites can further be recalculated as 47:56. The calculation process is shown in the Equation 4.3.2. To conclude, XPS analysis can also prove the accuracy of the <sup>1</sup>H-NMR results.

$$\frac{m_{N-BTA}}{m_{N-PAN}} = \frac{\frac{12.6 \text{ mg}}{1031 \text{ g/mol}} \times 12}{\frac{93\% \times 10 \text{ mg}}{53}} = \frac{147}{175} = \frac{47}{56} \quad \text{Equation 4.3.2}$$

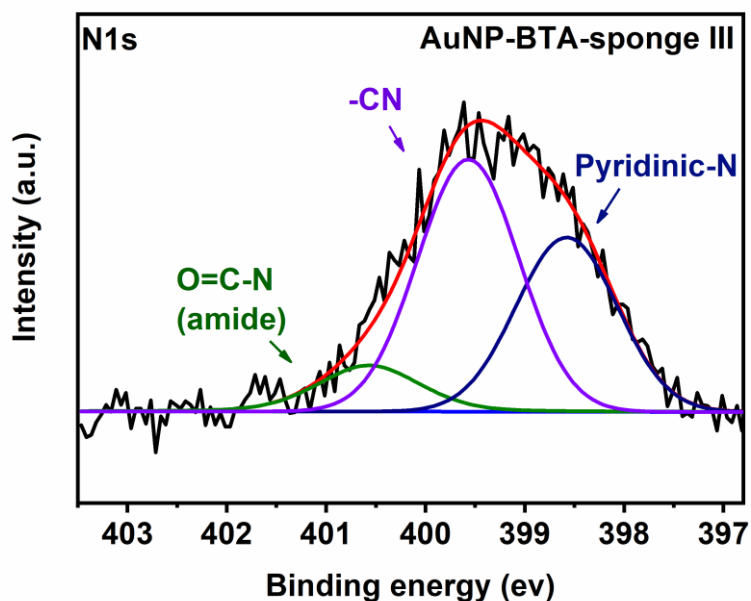


**Figure 4.3.23.** N1s high-resolution XPS spectrum of AuNP containing BTA-sponge III.

The drop shape analyzer was carried out to examine the sponges' affinities for water. Figure 4.3.24 displays the wettability of BTA-sponges I–III: 4  $\mu\text{L}$  of water was placed onto the surfaces of the sponges and the change of the adsorption of the water droplet was recorded. It could be observed that the water droplets were absorbed into the BTA-sponges within about 2 s. This behavior was attributed to the fact that there are degraded  $\text{NaBH}_4$  remaining on the surface of the BTA-sponge. This proves that the BTA-sponges I–III modified with AuNP have good affinity for water, so they can provide huge advantages for the further application in an aqueous environment. However, with an increasing amount of BTA molecules contained in the BTA-sponges, obvious differences could not be observed among them. This is because various parameters of the BTA-sponges have an impact on their affinity for water, for example, the roughness of the surface of the sponge, that cannot be controlled in a precise fashion.

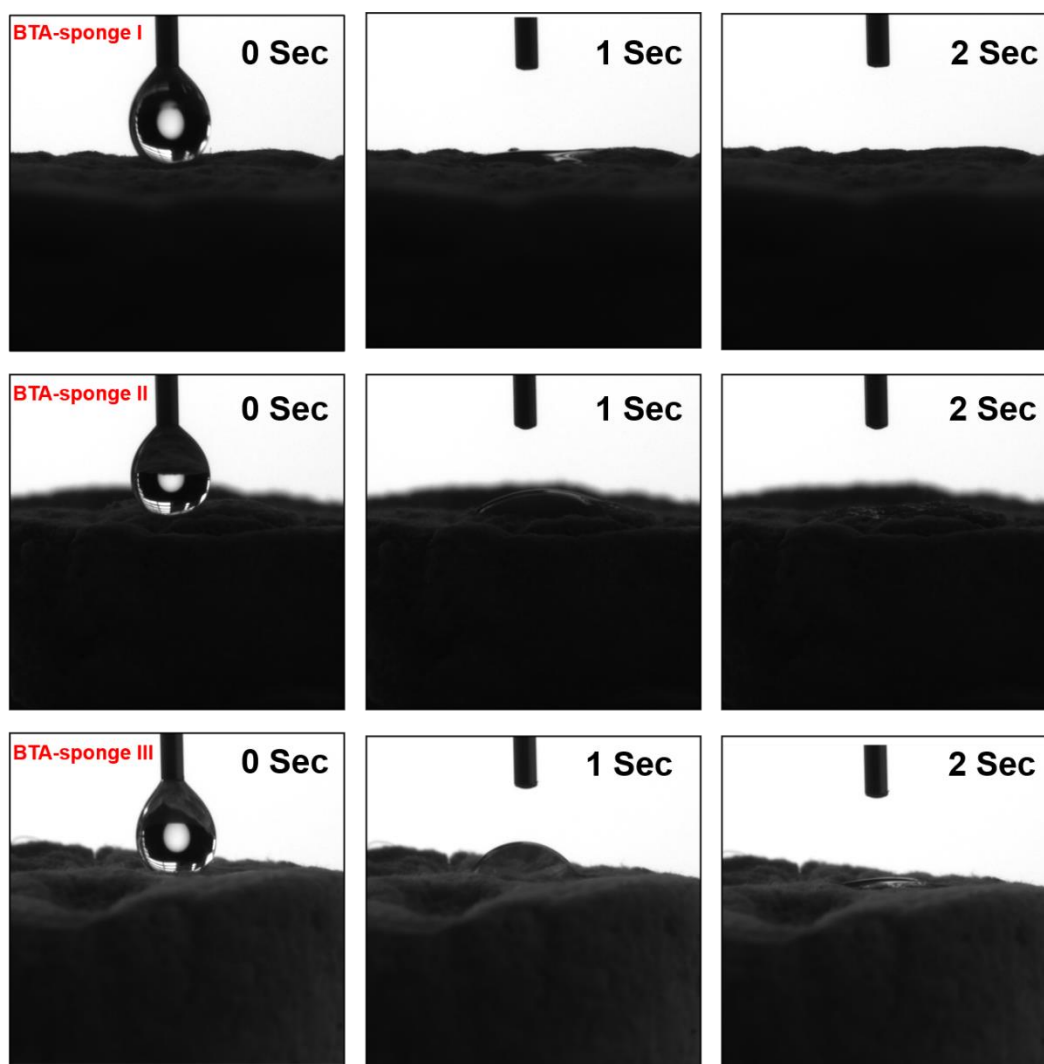


**Figure 4.3.24.** wettability behavior of the AuNP containing BTA-sponge I, II and III.

#### 4.3.4 Filtration of the AuNP

Water shortage and pollution have become major global problems in modern society. One ineligible source of pollution comes from the use of AuNP in daily life, such as in cosmetics and medicines, which unavoidably causes the release of the AuNP into wastewater. Therefore, there is an increasing demand for efficient removal of these AuNP and NP of other types. Many different approaches have been proposed in the past decade as a potential solution to this problem. Herein, membrane-based materials have been widely investigated in NP separation because of their high efficiency, easy scaling up and low cost. However, membrane-based materials still present a few major drawbacks, such as the blocking of pores after longtime use in filtering a large amount of NP and susceptibility to high pressure drops during the filtration. In recent years,

sponge materials have attracted increasing attention regarding NP separation. Sponges present large specific surface areas for filtration with relatively lightweight structures and high porosities.<sup>193</sup> In this work, BTA-sponges comprising a 3D adjustable construction were studied as support for AuNP separation. The surface composition of the fibers has an impact on the filtration efficiency of the sponge. Due to the terpyridine functional group on the BTA nanofibers, the BTA-sponges I–III can be used as the support for AuNP filtration.<sup>194</sup> The BTA-sponge demonstrated a high potential in AuNP removal in the aqueous media and, therefore, holds a high potential for the removal of NP from wastewater.

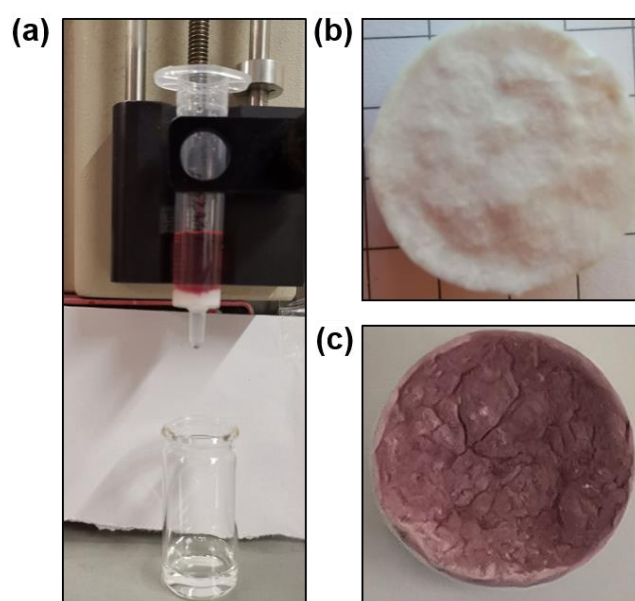


**Figure 4.3.25.** (a) The scheme of the filtration of AuNP with BTA-sponge I under atmospheric pressure. (b and c) The images of BTA-sponge I before and after filtration.

**Table 4.3.3.** AuNP filtration efficiency of the BTA-sponges and the PAN+PCL sponge as reference, the volumes of the PVP@AuNP used in the filtration are also summarized.

Sample	Volume of PVP@AuNP <sup>[a]</sup> (mL)	Adsorption efficiency <sup>[b]</sup> (%)	Adsorption efficiency <sup>[c]</sup> (%)	Au amount ( $\mu\text{g}$ )
Reference	3	9	8	7
BTA-sponge I	3	100	100	90
BTA-sponge II	3	100	100	90
BTA-sponge III	3	100	100	90
BTA-sponge I	15	99	-	447
BTA-sponge II	50	99	-	1481

[a] 1 mL contains 30  $\mu\text{g}$  gold.

[b] The adsorption efficiency determined by UV-Vis spectroscopy.

[c] The adsorption efficiency determined by ICP-OES spectroscopy.

The PVP@AuNP filtration performance of BTA-sponges I–III was determined in this part. Each BTA-sponge I–III was placed in the cell of a syringe (inner diameter: 12.45 cm) filter. The setup for performing the AuNP filtration can be seen in Figure 4.3.25a. The sponge was carefully wetted with distilled water before AuNP filtration until all the air in the sponge was eliminated. The filtration of AuNP can then be carried out in the flow by the adsorption device under pressure. The filtration performance can be evaluated by UV-Vis spectroscopy and ICP-OES. The results in Table 4.3.3 indicated that these functionalized BTA-sponges exhibited high adsorption capacities for capturing AuNP, which can be attributed to their high specific surface areas. An amount of 3 mL aqueous dispersion of PVP@AuNP at a concentration of 30  $\mu\text{g}/\text{mL}$  determined by ICP-OES was first filtrated by BTA-sponges I–III and then washed once with 3 mL distilled water and once with 2 mL distilled water. The AuNP capture efficiency can be calculated from the ratio of the maximal absorption of the PVP@AuNP at 524 nm in the UV-Vis spectra before and after filtration (Figure 4.3.26). The results revealed that

almost all of PVP@AuNP were rejected by BTA-sponges I–III with a separation efficiency achieved of  $\geq 99\%$ . Moreover, these results were examined with the help of ICP-OES by calculating of the mass difference between the feed dispersion and the filtrate dispersion. The results of the ICP-OES analysis presented good agreement with those of the UV-Vis. The high separation efficiency of the AuNP by utilizing BTA-sponges I–III can result from the interconnection network of the BTA nanofibers and short PAN fibers, as well as the high affinity of the terpyridine functional groups on BTA nanofibers towards AuNP. The pressure drop is no longer an issue thanks to the good wettability and high porosity of the sponges.

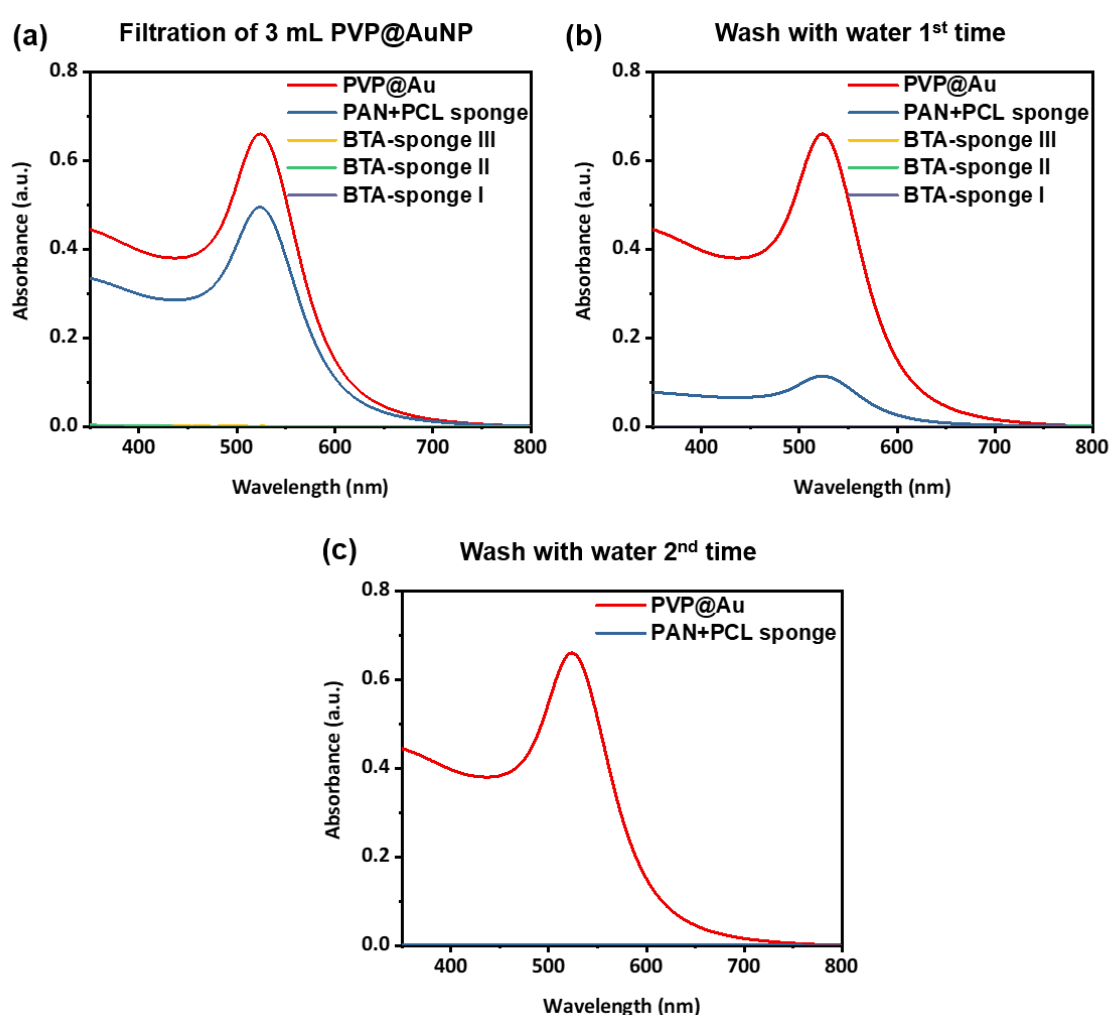


**Figure 4.3.26.** (a) UV-Vis spectrum of the filtrate after going through BTA-sponges I–III and the PAN+PCL sponge. (b) UV-Vis spectrum of the filtrate after washing BTA-sponges I–III and the PAN+PCL sponge with 3 mL water. (c) UV-Vis spectrum of the

filtrate after washing BTA-sponges I–III and the PAN+PCL sponge with an additional 2 mL of water.

After the filtration of the PVP@AuNP, the morphologies of BTA-sponges I–III were checked by SEM. The sponge containing neat short PAN and PCL fibers was used as a reference in this study. After the filtration process and water rinsing, only a very few NP were incorporated on the surface of the PAN fibers. This could be the result of electronic interactions between the materials and AuNP (Figure 4.3.27). The PVP@AuNP was evenly distributed solely on the surface of the BTA nanofibers within BTA-sponge I, instead of on the surface of the short PAN fibers (Figure 4.3.28). The distribution of PVP@AuNP on the surface of the BTA nanofibers is highly even without observable aggregations for the BTA-sponges II and III (Figure 4.3.29 and 30). These findings were further confirmed by backscattering spectroscopy and the PVP@AuNP distributions on BTA-sponge I and III are shown in Figure 4.3.31 a and b, respectively. Backscattering spectroscopy images of the AuNP-decorated BTA-sponge I and III again suggested a highly homogenous distribution of AuNP on the BTA fibers without aggregation. All these results indicated that BTA-sponge can be regarded as a good supporting material for AuNP separation.

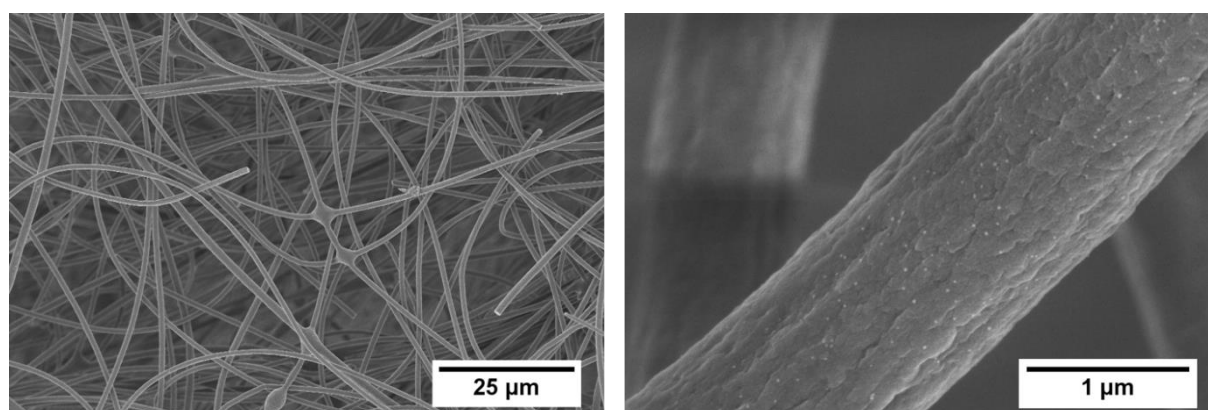


**Figure 4.3.27.** SEM images of the sponge containing short PAN and PCL fibers at different magnifications after filtration of 3 mL PVP@AuNP colloidal solution and washing with water.

Subsequently, the capacities of AuNP capture using BTA-sponges I and II as support were determined. An amount of 15 and 50 mL PVP@AuNP were continuously passed through BTA-sponge I and III, respectively, until all the AuNP were adsorbed within the sponges. The UV-Vis absorption spectra of the filtrate were recorded, and the

separation efficiency can then be calculated from the difference in absorption of PVP @AuNP before and after filtration (Figure 4.3.32). A separation efficiency of 99 % could be achieved for the PVP@AuNP with the BTA-sponges I and II, and the amounts of gold rejected were 447  $\mu\text{g}$  and 1481  $\mu\text{g}$ , respectively. All the results pointed out conclusively that BTA-sponges possess a high potential in the separation of a large number of AuNP, which is a difficult task for the membrane-based materials, as their nanopores tend to be easily blocked by the NP.

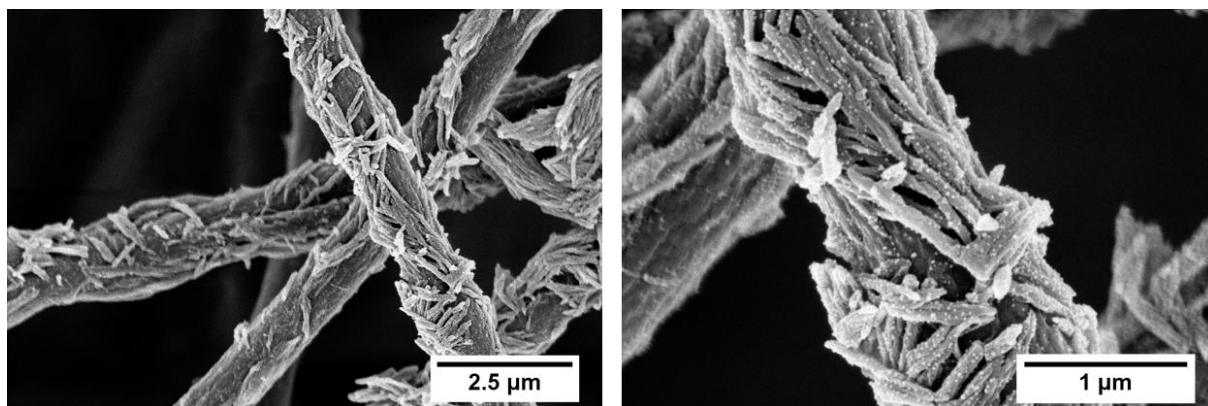


**Figure 4.3.28.** SEM images of AuNP distribution in the BTA-sponge I at different magnifications after filtration of 3 mL PVP@AuNP colloidal solution and washing with water.

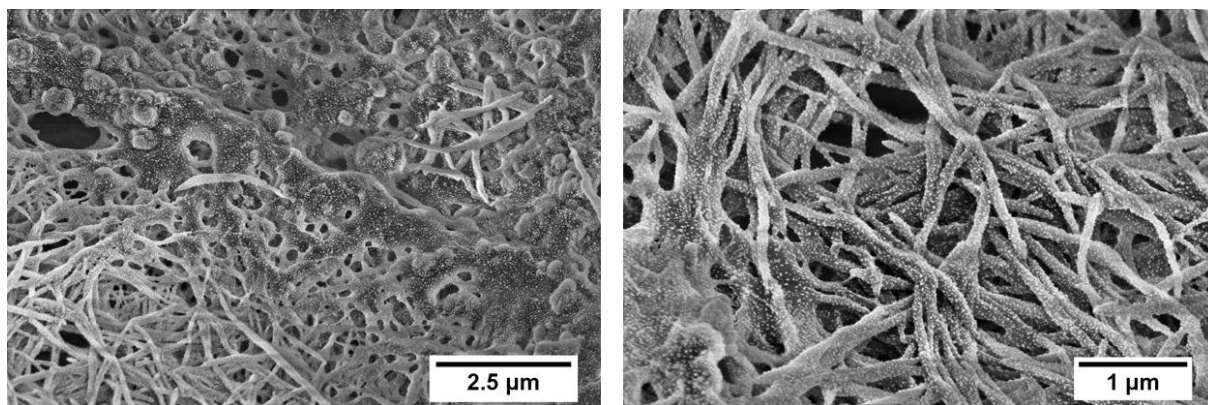


**Figure 4.3.29.** SEM images of AuNP distribution on the BTA-sponge II at different magnifications after filtration of 3 mL PVP@AuNP colloidal solution and washing with water.

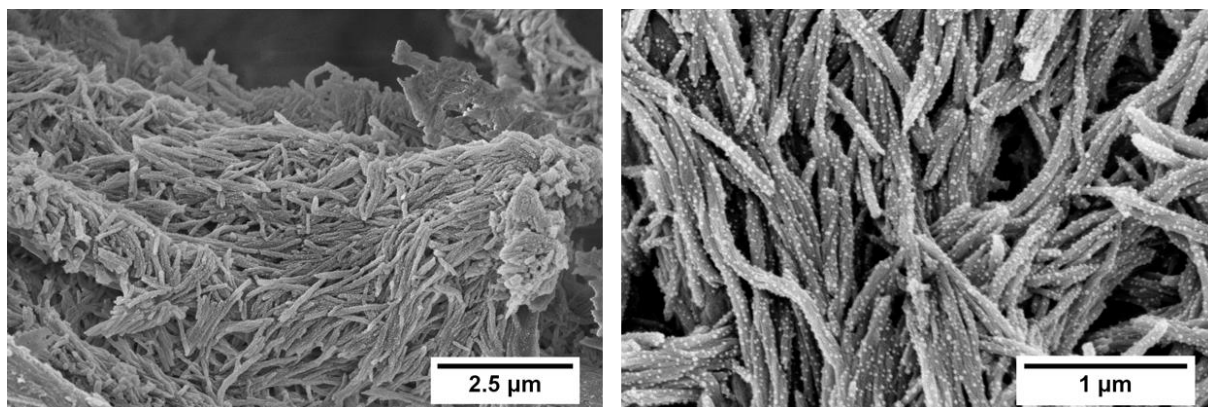


**Figure 4.3.30.** SEM images of AuNP distribution on the BTA-sponge III at different magnifications after filtration of 3 mL PVP@AuNP colloidal solution and washing with water.

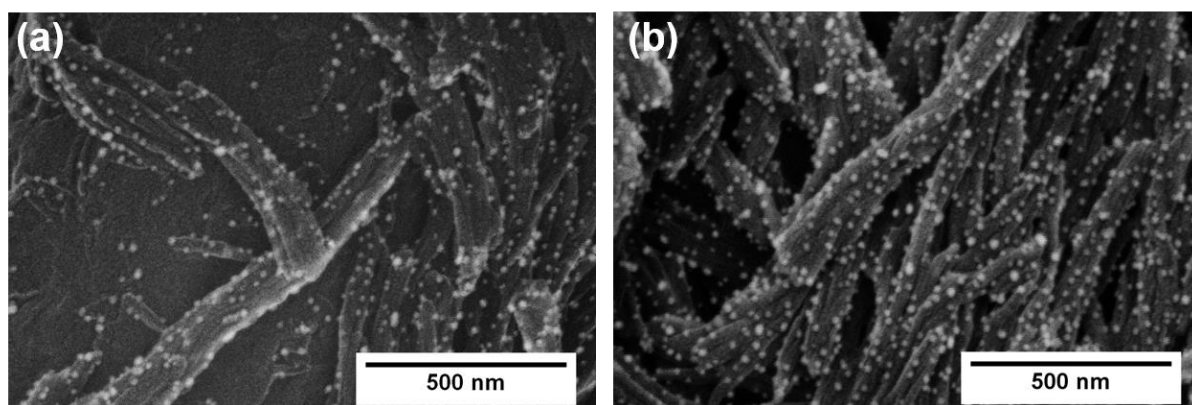


**Figure 4.3.31.** Backscattering spectroscopy images of AuNP distribution on the BTA-sponge I (a) and the BTA-sponge III (b) after filtration of 3 mL PVP@AuNP colloidal solution and washing with water.

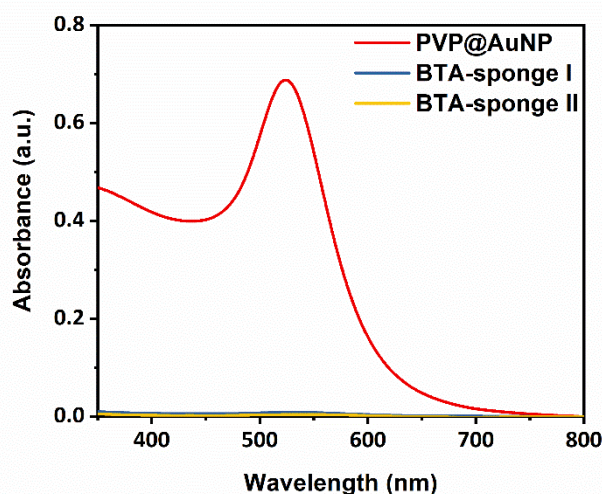


**Figure 4.3.32.** UV-Vis spectroscopy of the AuNP filtration efficiency maximal absorption of the BTA-sponge I and II.

#### 4.3.5 Catalytic reduction of 4-nitrophenol in batch system

Due to high surface energy, AuNP with an average size of 2.4 nm are normally unstable in colloidal dispersions. This often induces the aggregation of the AuNP and decreases their catalytical performances. This work presents a facile method to immobilize AuNP with an average size of 2.4 nm into the sponge. The catalytic performance of the AuNP-incorporated BTA-sponges I–III are also studied. As the 4-nitrophenol reduction by  $\text{NaBH}_4$  in the presence of the AuNP catalyst has been well described in the batch system in the second work. It will not be introduced in detail here (Figure 4.3.33a). The parameters and conditions adopted for the catalytic reduction by using the AuNP-decorated BTA-sponges I–III are the same as those used in the second work. It should be noted that the AuNP decorated BTA-sponges I–III should be immersed in water overnight to ensure their wettability. The catalytic experiments were first performed in a batch system with the AuNP-incorporated BTA-sponge. The catalytic reaction rate constant  $k$  of the 4-nitrophenol reduction catalyzed by BTA-sponges I–III supporting AuNP can be extracted from the pseudo first-order rate law (shown in Figure 4.3.33b).  $C_0$  is the initial concentration and  $C_t$  represents the concentration of nitrophenolate at time  $t$ . Correspondingly,  $A_0$  and  $A_t$  stand for the maximal adsorption peak of nitrophenolate at the beginning and at time  $t$ , respectively. Representative plots showing the change of the adsorption peak of nitrophenolate along with time induced by the use of AuNP-BTA-sponge I-III as catalysts is depicted

in Figure 4.3.33 c-e, respectively. The corresponding  $k$  values can then be obtained by the linear fitting of  $\ln I_t/I_0$  versus time  $t$  at the early stage (Figure 4.3.33f).

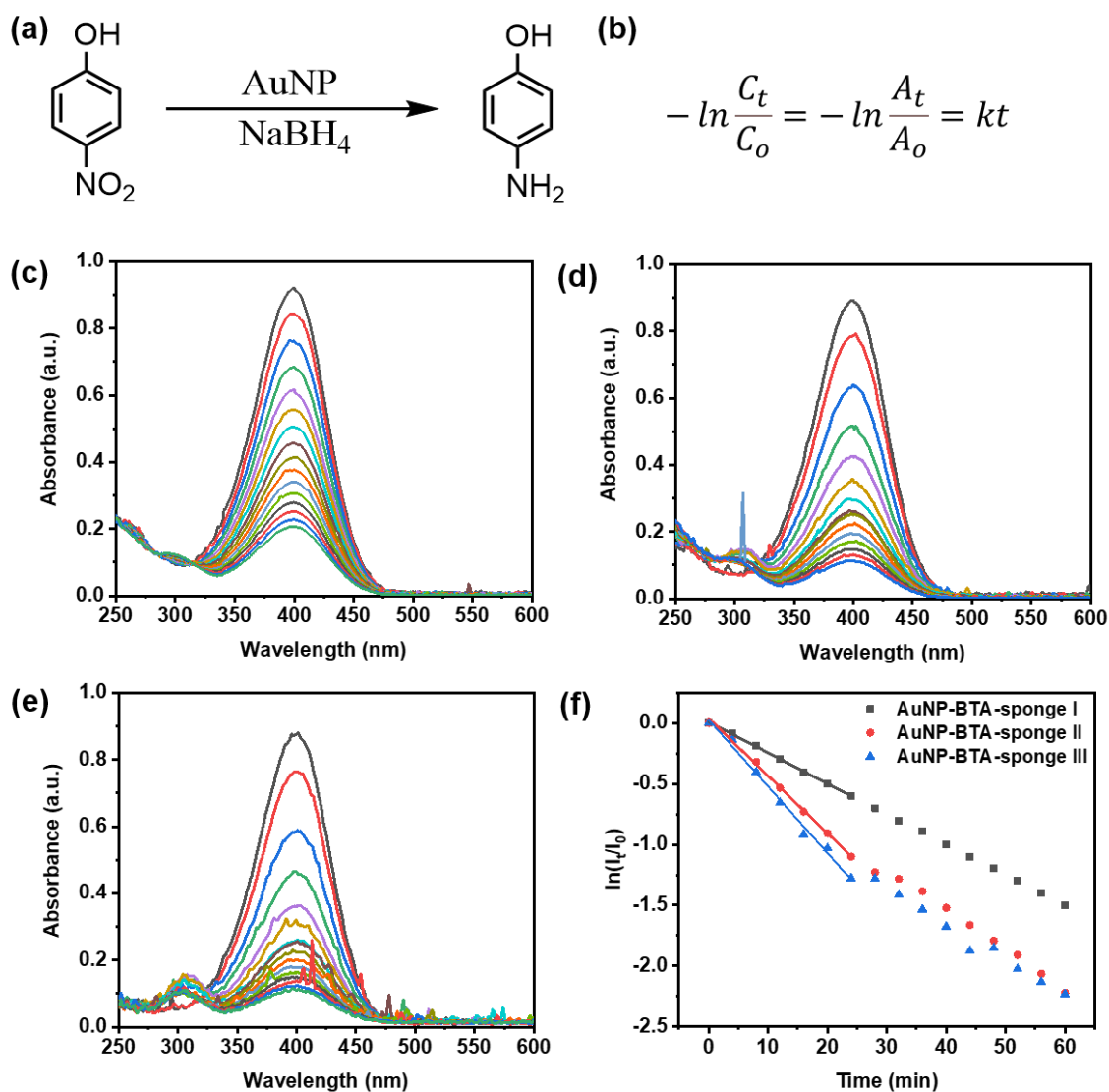


**Figure 4.3.33.** (a) 4-nitrophenol reduction in the presence of the AuNP-incorporated BTA-sponges I–III as catalysts. (b) Equation used for the calculation of the catalytic reaction rate constant of nitrophenol reduction. (c–e) Time-dependent change of the UV-Vis adsorption peak of nitrophenolate in the reaction catalyzed by AuNP-BTA-sponge I–III. (f) The plot of linear fitting of  $\ln I_t/I_0$  against time  $t$  of the catalytic reaction and  $k$  can be determined from the slope as the reaction can be treated as first order.

**Table 4.3.4.** The apparent catalytic reaction rate constant of the 4-nitrophenol reduction at each catalytic cycle.

	$k_1$	$k_2$	$k_3$	$k_4$	$k_5$
	(min <sup>-1</sup> )				
<b>AuNP-BTA-sponge I</b>	0.039	0.023	0.025	0.027	0.029
<b>AuNP-BTA-sponge II</b>	0.066	0.034	0.046	0.039	0.069
<b>AuNP-BTA-sponge III</b>	0.061	0.057	0.055	0.073	0.043

**Table 4.3.5.** Characterization of the catalytic activity of AuNP-incorporated BTA-sponges I–III for 4-nitrophenol reduction.

	$m_{Au}^{[a]}$	$k_{app}$	TOF <sup>[b]</sup>	Conversion	Leaching <sup>[c]</sup>
	( $\mu$ g)	(min <sup>-1</sup> )	(h <sup>-1</sup> )	(%/h)	(wt%)
<b>AuNP-BTA-sponge I</b>	40	0.029 ± 0.006	0.4	80 ± 2	≤ 0.5
<b>AuNP-BTA-sponge II</b>	52	0.051 ± 0.016	0.4	91 ± 5	≤ 0.7
<b>AuNP-BTA-sponge III</b>	34	0.058 ± 0.011	0.6	92 ± 2	≤ 0.5

[a] the amount of gold was determined by ICP-OES. The sponge was digested in microwave before the analysis, as the AuNP distribution is not totally homogenous in the sponge.

[b]  $TOF = \frac{N_{AP}}{t \cdot N_{Au}}$   $N_{AP}$  is the number of 4-AP molecules at time  $t$ .  $N_{Au}$  is the number of gold atoms as the catalyst.

[c] An approximate amount of leaching after each cycle of the catalytic reaction is given (determined with ICP-OES analysis).

Five cycles of catalytic reaction were carried out for each AuNP incorporated BTA-sponge I–III and the results are summarized in Table 4.3.4. The average apparent catalytic reaction rate constants by using AuNP-incorporated BTA-sponges I–III are

$0.029 \pm 0.006 \text{ min}^{-1}$ ,  $0.051 \pm 0.016 \text{ min}^{-1}$  and  $0.058 \pm 0.011 \text{ min}^{-1}$ , respectively. The conversions and turnover frequency (TOF) values of the catalytic reactions were calculated according to the equation in the following part and the results are summarized in Table 4.3.5. The AuNP-incorporated BTA-sponge I yielded the lowest 4-nitrophenol to aminophenol conversion (80%), whereas the BTA-sponges II and III led to conversions as high as 91% and 92% under the same conditions. The TOF values of the catalytic reaction are in the range of  $0.4 \text{ h}^{-1}$  to  $0.6 \text{ h}^{-1}$  by investigating AuNP-incorporated BTA-sponges I, II and III. In addition, the apparent catalytic rate constants per mg at each cycle by using AuNP-BTA-sponges I–III are compared in Figure 4.3.34. After normalization with the mass of the gold investigated in the catalytic reactions, the results show that the AuNP BTA-sponge III presented the highest catalytic reaction rate constant. Remarkably, since only a small piece of the sponge was used for the catalytic reaction and the AuNP are not totally homogeneously distributed in the sponge, the gold contents of the BTA-sponges can be further examined by digesting the sponges in a microwave followed by ICP-OES quantification. The results of the ICP-OES analysis are summarized in Table 4.3.5. As the catalytic reaction rate constant is highly dependent on the mass of the AuNP, the size of the AuNP and the wettability of the BTA-sponge. The average size of the AuNP has been determined by TEM and SAXS. The SAXS results proved that BTA-sponges I–III contain AuNP of very similar average sizes. In addition, BTA-sponges I–III have similar wettability, thus, the diffusions of reactants into the different sponges can be expected to be quite similar. The increasing catalytic activities from the AuNP-incorporated BTA-sponge I–III can be explained by the fact that BTA-sponge III contains the highest amount of BTA nanofibers, whereas BTA-sponge I has the lowest amounts. Correspondingly, the AuNP tend to distribute better onto the surface of BTA-sponge III, by contrast, the AuNP diffuse more deeply into BTA-sponge I, which has been proven by the SAXS measurements. As the diffusion of reactants into the inside of the BTA-sponges were expected to be generally difficult, it can be deduced that the AuNP-BTA-sponge III possess high catalytic activity due to more efficient AuNP distribution on the surface of the sponge.

It is well-known that many catalysts suffer from AuNP leaching. Therefore, the AuNP leaching was quantified by ICP-OES analysis after the catalytic reactions in our work. The results demonstrated that the amount of Au leached reached the limit of detection

of the ICP-OES, which suggested that no obvious AuNP leaching took place when AuNP BTA-sponges I–III were used as the catalysts. To conclude, the BTA-sponges showed many advantages as the support for the AuNP, such as small AuNP stabilization without inducing obvious aggregation, good catalytic activity, long-term reusability and low leaching during each catalytic cycle.

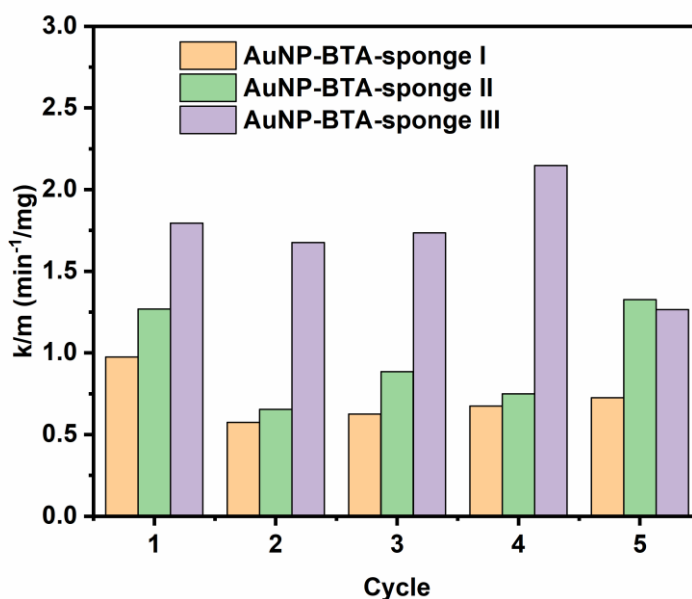


**Figure 4.3.34.** The comparison of the  $k/m$  values (the ratio between the apparent catalytic reaction rate constant and the mass of the Au determined by ICP-OES) obtained in each reaction cycle of 4-nitrophenol reduction using the AuNP-decorated BTA-sponges I-III as catalysts.

#### 4.3.6 Catalytic reduction of 4-nitrophenol in continuous flow system

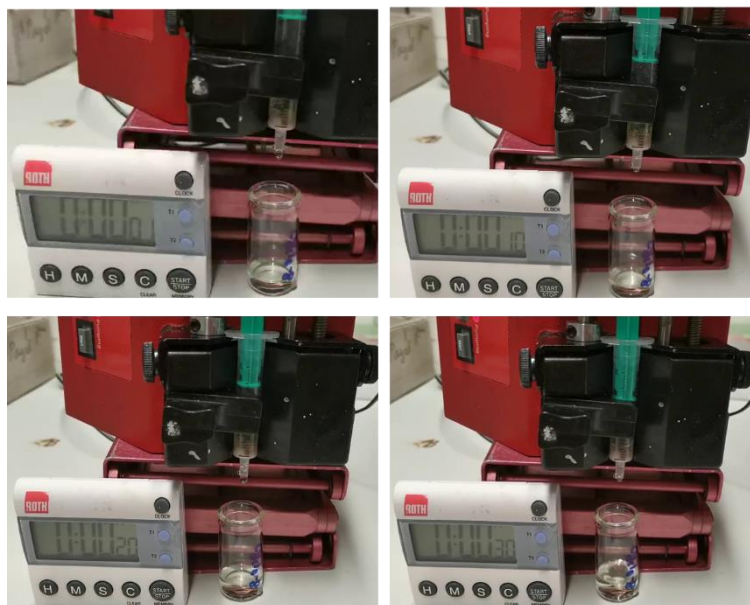


**Figure 4.3.35.** Digital photographs showing 1.3 mL feed solution passing through AuNP decorated BTA-sponge I versus time at 8<sup>th</sup> cycle with an average flow rate of 2.6 mL/min.

Compared with the batch system, the AuNP-incorporated BTA-sponge presents higher efficiency in the continuous flow catalytic reaction model due to the high availability of the AuNP in the catalytic system. The AuNP-incorporated BTA-sponge suffers from the inefficient diffusion of the reactants into the inside of the sponge in the batch system. Thus, the catalytic experiments of 4-nitrophenol reduction using the AuNP-incorporated BTA-sponge as the catalyst was carried out in continuous flow systems. Regarding the continuous flow catalytic system, AuNP-incorporated BTA-sponge I was tightly packed into a syringe (inner diameter: 0.94), and the syringe was then stacked in the injection pump. Figure 4.3.35 illustrates the self-made continuous flow reactor. Distilled water was first pumped to pass through sponge until the sponge became thoroughly wetted. The reaction was carried out afterwards by pumping a mixture of 4-nitrophenol and NaBH<sub>4</sub> aqueous solutions to pass through the AuNP-incorporated BTA-sponge I, while the flow rate was being constantly recorded (the volume of the filtered solution divided by the corresponding time counted by stopwatch) (Figure 4.3.35). It can be clearly observed that the color of the feed solution fades away almost completely after passing through the catalyst. In the next step, the feed solution and the filtered solution were measured by UV-Vis spectroscopy. The intensity of the

nitrophenolate adsorption peak in the UV-Vis spectra could be observed to decrease dramatically at 400 nm, while the peak around 300 nm increased significantly, which suggests the formation of 4-aminophenol (Figure 4.3.36). The 4-nitrophenol to aminophenol conversion catalyzed by AuNP-decorated BTA-sponge I was determined for each cycle to evaluate the specific catalytic performance and the results are summarized in Table 4.3.6. The results revealed that the conversion firstly reached 96 %, after which the conversion remained almost constantly at around 92 % until the seventh cycle, except during the second cycle. A slight decrease of the conversion can be observed after the seventh cycle (Figure 4.3.36), possibly due to the fact that the BTA-sponge can no longer be securely fixed within the syringe. In addition to the conversion of the catalytic reaction, catalytic TOF is another important index describing the catalytic activity of the catalyst. The calculation process of TOF is the same as that described in the second part of the work. The amount of gold loaded within BTA-sponge I can be determined by ICP-OES analysis. The average size of the AuNP can be determined by TEM. A maximal TOF value of  $14 \text{ h}^{-1}$  can be achieved, as shown in the results, while the TOF values for 10 cycles ranged from 9 to  $14 \text{ h}^{-1}$ . In order to evaluate the recyclability of the AuNP BTA-sponge I, gold leaching from the catalyst was analyzed by ICP-OES after each cycle of the catalytic reaction. The analysis results showed that the amount of gold in the filtered solution was below the limit of detection of ICP-OES. Therefore, no obvious leaching occurred during the catalytic reaction (Table 4.3.6).

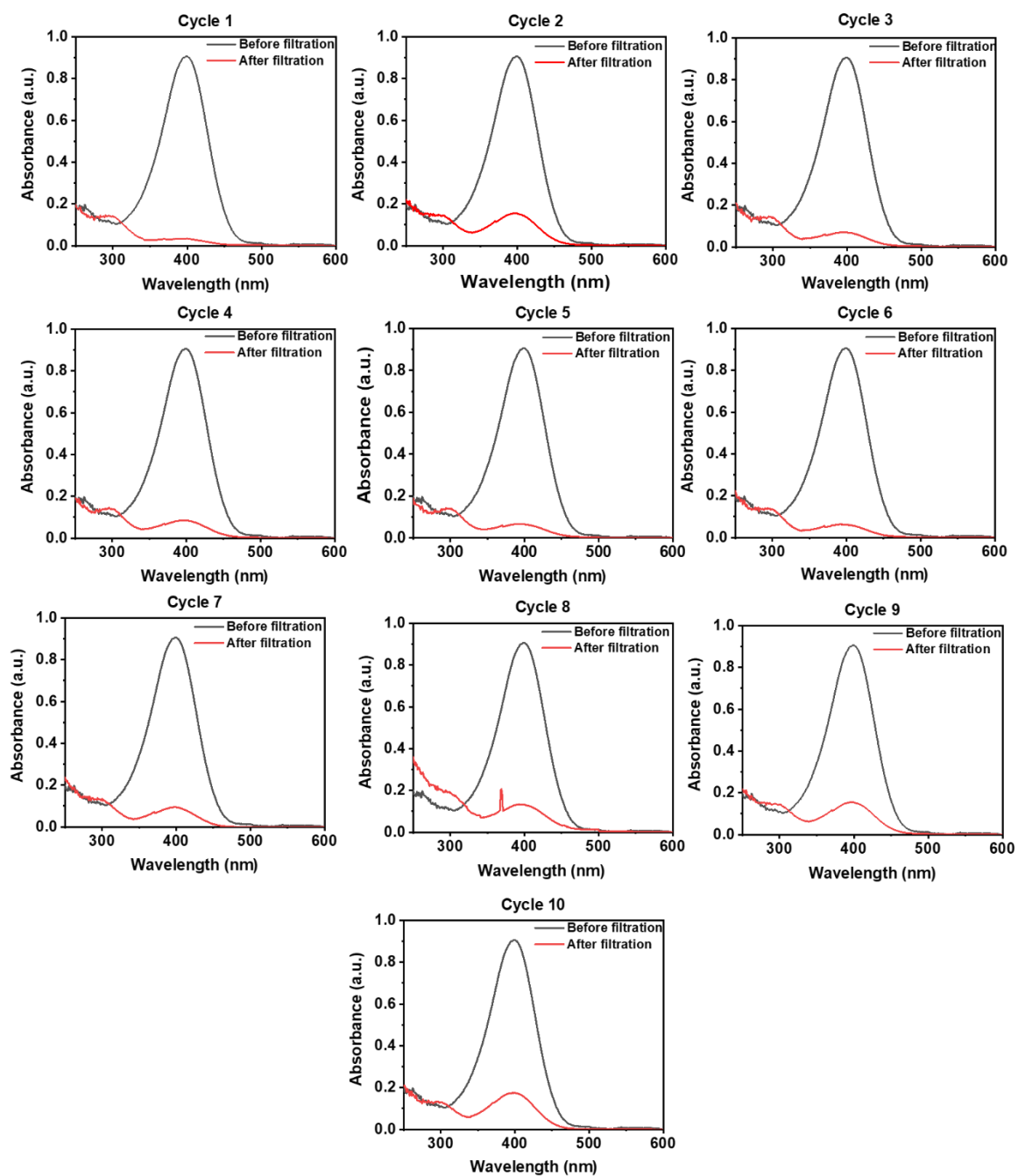


**Figure 4.3.36.** UV-Vis spectra of initial mixture of 4-nitrophenol and  $\text{NaBH}_4$ , and the mixture after passing through the AuNP-decorated BTA-sponge I reactor during a flow through process obtained in each cycle.

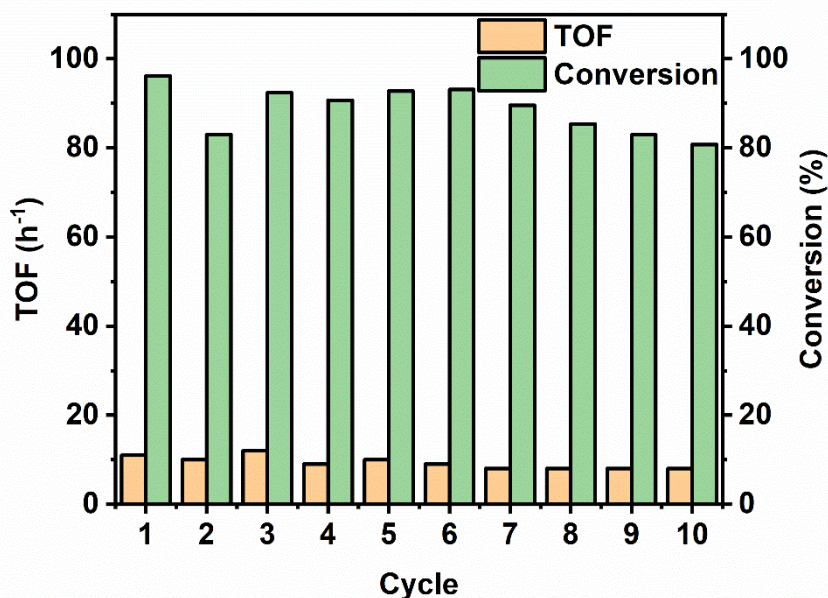


**Figure 4.3.37.** The conversion and TOF of 4-nitrophenol to 4-aminophenol at different cycle by maintaining similar flow rates of the 4-nitrophenol passing through the AuNP-BTA-sponge I reactor.

The TOF values of the catalytic reactions were analyzed to compare the catalytic performances of the same AuNP-decorated BTA-sponge as the catalyst in the conventional batch model and the continuous flow model. The TOF value was 28 times higher in the conventional model (Table 4.3.6) than in the batch model (Table 4.3.5), demonstrating the AuNP-decorated BTA-sponge's higher catalytic activity in the conventional model than in the batch model. The reason is that most AuNP were efficiently used to provide a high accessibility of the active sites in the conventional model. Additionally, fast mass transfer of reagents to the active sites of the AuNP took place in the continuous flow model, thus, the reactants can attach and detach sufficiently from the active sites of the catalyst. The conventional batch model only offers limited mass transfer and AuNP active site accessibility. In addition, the estimated  $k$  value (determined from the first cycle of the reaction) against the amount of gold (mg) of the nitrophenol reduction carried out at a continuous flow model is comparable with those in the literatures. It is obviously higher than that in the batch system performed in this part of the work. (Figure 4.3.38) The estimated  $k$  value can be obtained through the following Equation 4.3.3.

$$k = -\frac{\ln\left(\frac{c_t}{c_0}\right)}{t} \quad \text{Equation 4.3.3}$$

**Table 4.3.6.** Summary of the catalytic performances of AuNP-decorated BTA-sponge I on 4-nitrophenol reduction in a continuous flow reactor.

<b>Cycle</b>	<b>Flow rate (mL/min)</b>	<b>Conversion<sup>[a]</sup> (%)</b>	<b>TOF<sup>[b]</sup> (h<sup>-1</sup>)</b>	<b>Leaching<sup>[c]</sup> (wt%)</b>
1	3	96	11	-
2	3	83	10	-
3	3.4	92	12	-
4	2.6	91	9	-
5	2.9	93	10	-
6	2.5	93	9	-
7	2.4	90	8	-
8	2.6	85	8	-
9	2.7	83	8	-
10	2.4	81	8	-

[a] The conversion can be determined from the amount of nitrophenol consumed while going through the sponge, taking into consideration of the small amount of solution unavoidably passed through during the loading the solution on the sponge.

[b] The mass of gold in BTA-sponge I determined by the ICP-OES is 142 µg. The turnover frequency was calculated by the same equations as those used for the batch system.

[c] The mass of the gold leached after the catalytic reaction is determined by ICP-OES.

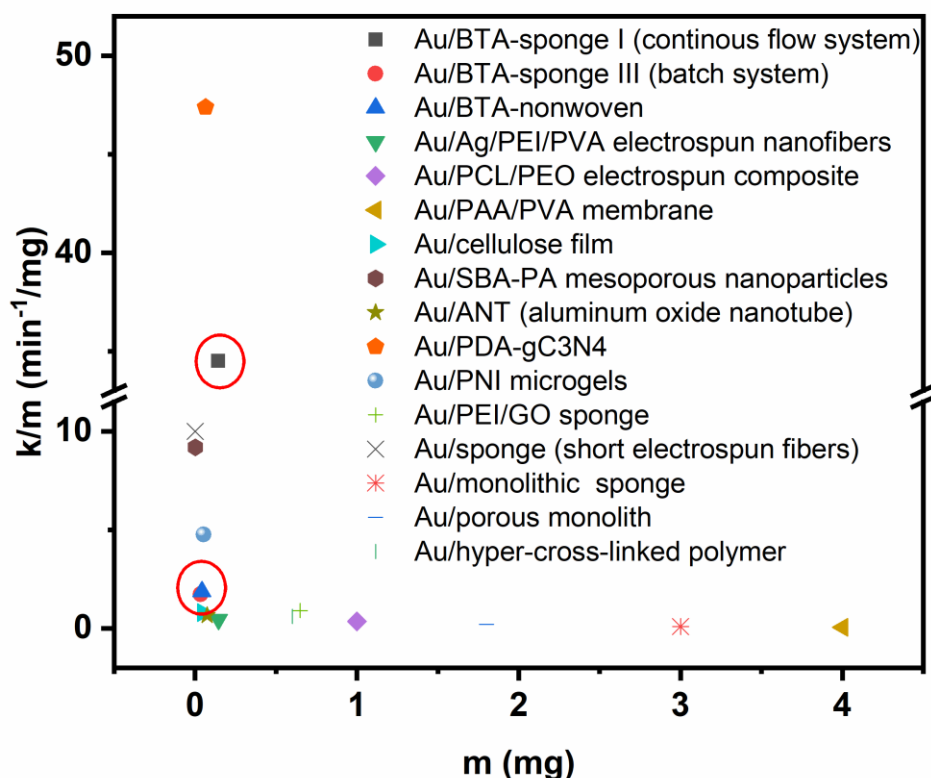


**Figure 4.3.38.** Ashby plot of the apparent catalytic reaction rate constant  $k$  against the amount of gold (mg) with different supports for nitrophenol reduction. The estimated  $k$  value was used for the continuous flow reaction. Au/Ag/PEI/PVA electrospun nanofibers,<sup>176</sup> Au/PCL/PEO electrospun composite,<sup>177</sup> Au/PAA/PVA membrane,<sup>178</sup> Au/Cel-lulose film,<sup>179</sup> Au/SBA-PA mesoporous nanoparticles,<sup>180</sup> Au/ANT (aluminum oxide nanotube),<sup>181</sup> Au/PDA-gC3N4,<sup>182</sup> Au/PNI microgels,<sup>183</sup> Au/PEI/GO sponge,<sup>184</sup> Au/sponge (short electrospun fibers),<sup>185</sup> Au/Monolithic sponges,<sup>186</sup> Au/porous monolith,<sup>187</sup> Au/TR-HCP-TPMT (Hyper-Cross-Linked Polymer).<sup>188</sup>

#### 4.3.7 Conclusion

BTA nanofiber-containing sponge was prepared via the facile wet-laid process and the freeze-drying method. The mechanical stability of the sponge can be improved by using the short PCL fibers as glue. As the obtained sponge can be potentially used as support for AuNP, the application potential of the BTA-nanofibers containing sponge was investigated in catalysis and filtration of the metal nanoparticles. The results indicated that the efficiency of the AuNP filtration can reach 99% by using BTA-sponges under atmospheric pressure. The catalytic performance of the BTA nanofiber-

containing sponge was examined in both batch and continuous flow systems. In the batch system, the AuNP decorated BTA-sponges presented comparable apparent catalytic reaction rates in comparison with those reported in literatures. Remarkably, the catalytic activity of the AuNP incorporated BTA-sponges can be significantly improved in the continuous flow system.

## **4.4 Photobiologically directed assembly of gold nanoparticles**

Gold nanoparticles are well-known to have great potential in electronic, magnetic, photonic and catalytic applications. The assembly of AuNP into 2D or 3D structures can further expand their applicability through precise control. In this work, the photobiologically directed assembly of AuNP is investigated to provide a way to construct their 3D architectures induced by blue light. This is achieved by controlling the assembly of AuNP by leveraging the homodimerization of LOV photoreceptors stimulated by light. The NP conjugated to genetically encodable LOV proteins are monodispersed in the dark, whereas they assemble rapidly into large aggregates upon exposure to blue light. A new modality for reaction control in macromolecular chemistry is built up in this work, which greatly increases the possibility of the precise control of AuNP assembly in space and time and expands their applications in many areas.

### **4.4.1 Introduction of the LOV protein**

Firstly, adaptations to light have an abundant presence across time and length scales in biology. Sensory photoreceptor proteins, which absorb photons and trigger biochemical and photochemical reaction cascades with precise resolution in time and space, are the key to these adaptations at the molecular level. The formation or dissolution of non-covalent interactions among proteins and other biomolecules, in many cases, is essential for these reactions. Notably, genetically encoded photoreceptors generally respond in aqueous media under facile reaction conditions. The LOV photoreceptor class, for example, responds to blue light via flavin nucleotide chromophores (Figure 4.4.1a).<sup>195</sup> Homo- or heterodimerization reactions are controlled by light among certain LOV receptors (Figure 4.4.1b) and have been utilized to take control of a cohort of cellular processes optogenetically.<sup>196</sup>

### **4.4.2 Concept and preparation of LOV protein conjugated AuNP**

In this work, the concept of light-controlled photobiological reaction is introduced to material science. In order to unlock these traits, the AuNP conjugated to genetically encodable LOV receptors were prepared (Figure 4.4.1c), to test the photobiologically directed assembly of AuNP induced by blue light. Initially, the AuNP conjugation to the photoreceptor proteins was made directly. This design is based on the fact that the original citrate capped AuNP can undergo facile ligand exchange with the light-

responsive LOV protein, as covalent bonding can be generated between gold and sulfide bonding of the cysteine residues with the protein. However, this attempt was unsuccessful due to the high amount of salt present in the buffer solution, which makes the stabilization of the LOV protein challenging.<sup>197, 198</sup> Immediate aggregation and precipitation of the Ct@AuNP took place right after adding the LOV protein. Hence, we later designed a linker between the AuNP and the LOV receptors, which can attach to the LOV receptors through nickel coordination chemistry. In this way, AuNP can be stabilized in the buffer solution even when it contains a high amount of salt. A small distance is kept between the AuNP and the LOV receptor, so that the LOV receptor can retain its functionality, which will be affected or blocked by the AuNP. The LOV proteins should be introduced with hexa-histidine (His<sub>6</sub>) tags and the AuNP should be equipped with Ni<sup>2+</sup>-nitrilotriacetic acid (NTA) for this construction to be successfully realized. (Figure 4.4.1c and 4.4.2)<sup>199-201</sup>

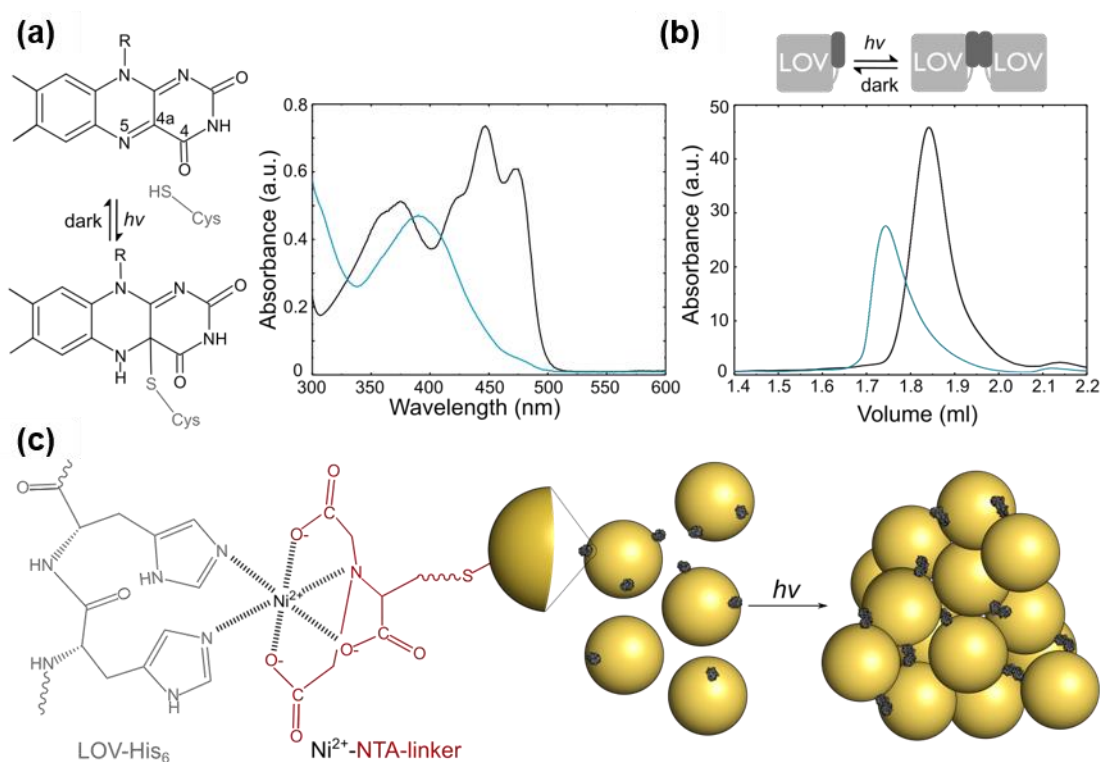


**Figure 4.4.1.** The photobiologically directed assembly AuNP was induced by light-oxygen-voltage (LOV) photoreceptors. (a) Simplified LOV photocycle showing the flavin nucleotide in the oxidized quinone state while being non-covalently bound within the LOV domain in the dark, as well as the formation of a covalent thiol adduct between the C(4)a atom of the flavin molecule and the  $\gamma$ -sulfur atom of a conserved cysteine



(blue) and the dark states (black) in the UV-Vis spectroscopy, while the appearance of the dark state of LOV proteins (black curve) and the corresponding light states (blue curve) are detected by size-exclusion chromatography.

#### 4.4.3 Characterization of LOV protein conjugated AuNP

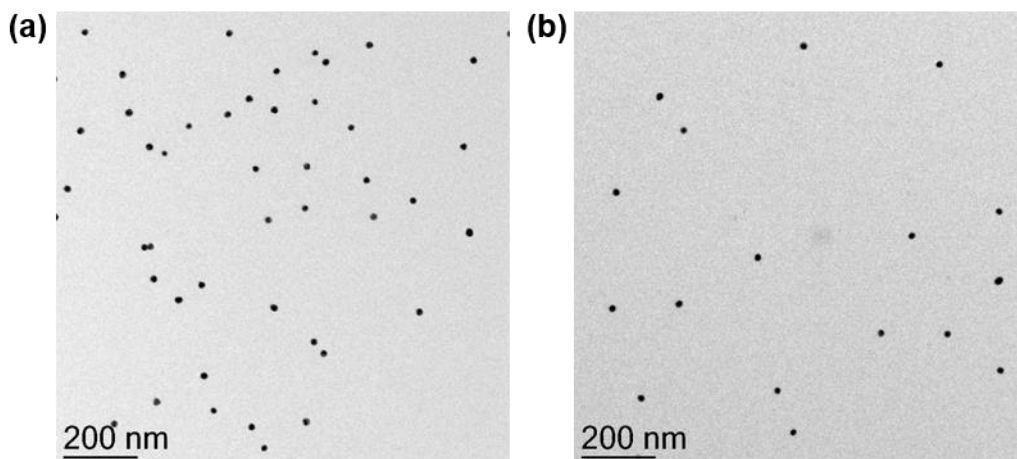


**Figure 4.4.3.** Determination of AuNP by transmission electron microscopy (TEM). (a) TEM image of Ct@AuNP; (b) TEM image of Ni<sup>2+</sup>-NTA-functionalized AuNP. Adaption from reference 202 with permission.<sup>202</sup>

Regarding the preparation of the Ni<sup>2+</sup>-NTA-equipped AuNP, the initial Ct@AuNP were prepared according to the traditional Frens method (discussed in the first work). The morphology and size distribution of the Ct@AuNP were determined by TEM (Figure 4.4.3a). The results indicated that the Ct@AuNP is monodispersed with an average size of  $17.7 \pm 1.6$  nm (Figure 4.4.4), which is in good agreement with the average size determined by DLS analysis ( $21.8 \pm 3.6$  nm) (Figure 4.4.5). The synthetic route of the NTA ligand is described in Figure 4.4.2, according to the literature. The NTA ligand is characterized by <sup>1</sup>H-NMR, <sup>13</sup>C-NMR and mass spectrometry and the results are recorded in the experimental part. The Ct@AuNP was then conjugated with NTA ligand via the ligand exchange method and, subsequently, coordinated with Ni<sup>2+</sup>. The incorporation of the Ni<sup>2+</sup>-NTA with AuNP can be characterized by UV-Vis spectroscopy: A red shift from 518 to 524 nm of the maximal adsorption band of the Ct@AuNP and the corresponding Ni<sup>2+</sup>-NTA-equipped AuNP can be observed (Figure 4.4.6). This is caused by the compositional change of the capping ligand. The TEM analysis shows that the Ni<sup>2+</sup>-NTA@AuNP is monodispersed and has the same average diameter as

that of the Ct@AuNP (Figure 4.4.4), whereas the DLS shows an increased average size of  $30.6 \pm 3.4$  nm due to the change of the ligand and the chemical environment (Figure 4.4.5).

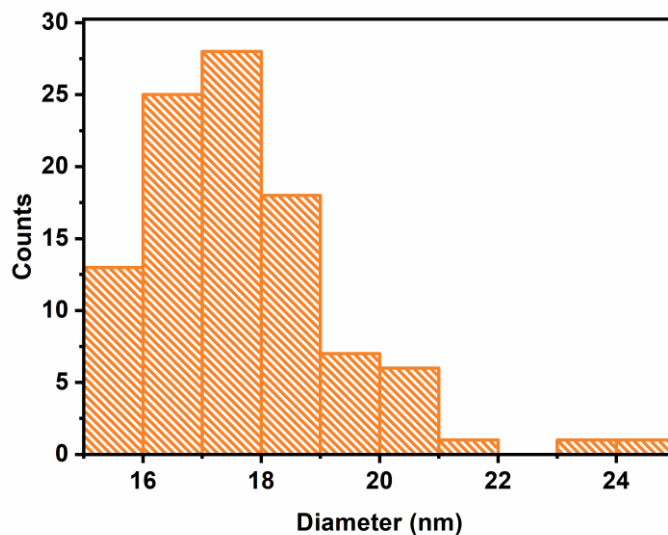


**Figure 4.4.4.** Size distribution of the Ct@AuNP and Ni<sup>2+</sup>-NTA-AuNP. Adaption from reference 202 with permission.<sup>202</sup>

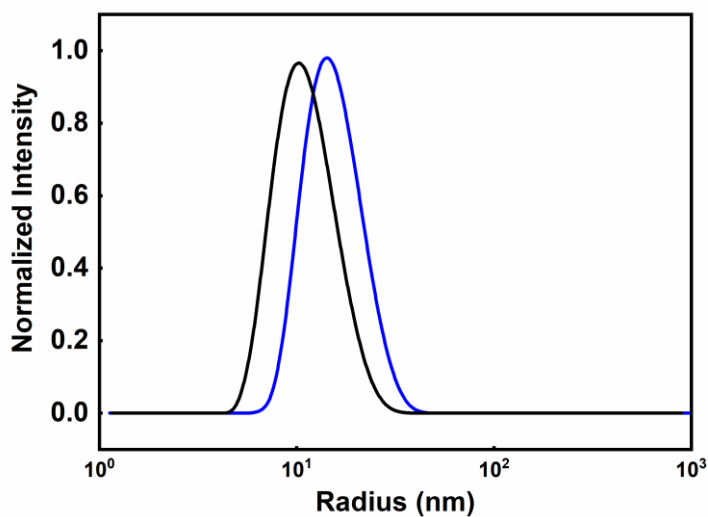


**Figure 4.4.5.** Characterization of gold nanoparticles by dynamic light scattering spectroscopy (DLS): hydrodynamic radius distribution of citrate-capped (black line)

and Ni<sup>2+</sup>-NTA-functionalized AuNP (blue line). Adaption from reference 202 with permission.<sup>202</sup>

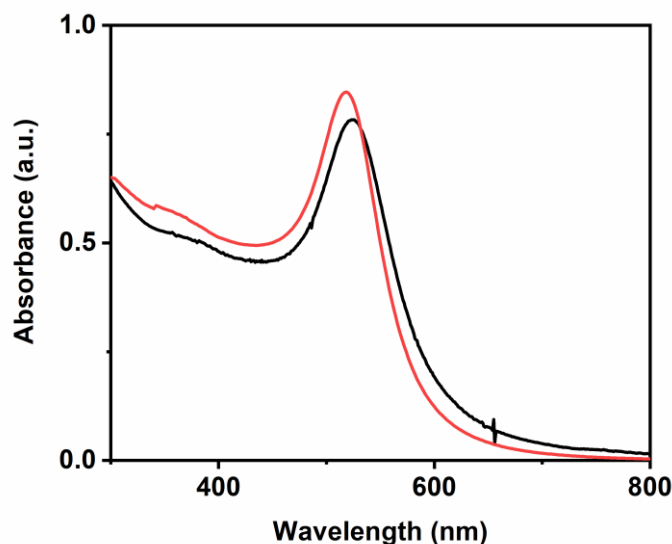


**Figure 4.4.6.** The UV-Vis spectra of Ct@AuNP (red) and Ni<sup>2+</sup>-NTA functionalized AuNP (black). A red shift from 518 to 524 nm can be observed. Adaption from reference 202 with permission.<sup>202</sup>

#### 4.4.4 Characterization of assembly of the LOV protein conjugated AuNP

The kinetic light-triggered assembly of the LOV protein-conjugated AuNP can be monitored by UV-Vis spectroscopy (Figure 4.4.7).  $25 \times 10^{-9}$  or  $50 \times 10^{-9}$  M *NcVVD*-His<sub>6</sub> protein was added into the Ni<sup>2+</sup>-NTA-functionalized AuNP in dark, and their UV-Vis spectra showed no significant difference from that of the Ni<sup>2+</sup>-NTA-functionalized AuNP in the buffer solution. After the samples were illuminated by the 450 nm blue light for 90 min, a dramatical red shift of the adsorption band up to 630 nm could be observed in the spectra. This is the indication of the assembly of AuNP into heterogenous, large-scale dimensions. It can also be deduced that the addition of  $50 \times 10^{-9}$  M *NcVVD*-His<sub>6</sub> protein led to a faster kinetic assembly process than the addition of  $25 \times 10^{-9}$  M *NcVVD*-His<sub>6</sub> protein. Using a spherical model, the *NcVVD*-His<sub>6</sub> protein is estimated to have an average diameter of 4 nm. Additionally, about 4000 NTA ligands are estimated to be attached on the surface of a single AuNP based on literature published previously where an AuNP was equipped with a similar ligand.<sup>170</sup> Therefore, a maximal of about 30 proteins are attached to the surface of a single NP. According to the calculation, the

$25 \times 10^{-9}$  M and  $25 \times 10^{-9}$  M *NcVVD*-His<sub>6</sub> proteins means 28 and 56 proteins per single NP, respectively. The kinetic rate of the assembly process can be decreased by decreasing the amount of the protein. Exemplarily, if the amount of the protein is reduced to  $6.25 \times 10^{-9}$  M, no apparent difference can be observed in the UV-Vis spectra of Ni<sup>2+</sup>-NTA-functionalized AuNP before and after the addition of *NcVVD*-His<sub>6</sub> proteins and illumination with blue light (Figure 4.4.8). Remarkably, upon adding imidazole to compete for the *NcVVD*-His<sub>6</sub> proteins, the Ni<sup>2+</sup>-NTA-functionalized AuNP displayed no change when exposed to 450 nm blue light after protein addition (Figure 4.4.7 and 4.4.8). This indicates that protein conjugation with Ni<sup>2+</sup>-NTA-functionalized AuNP is crucial to AuNP assembly triggered by light.

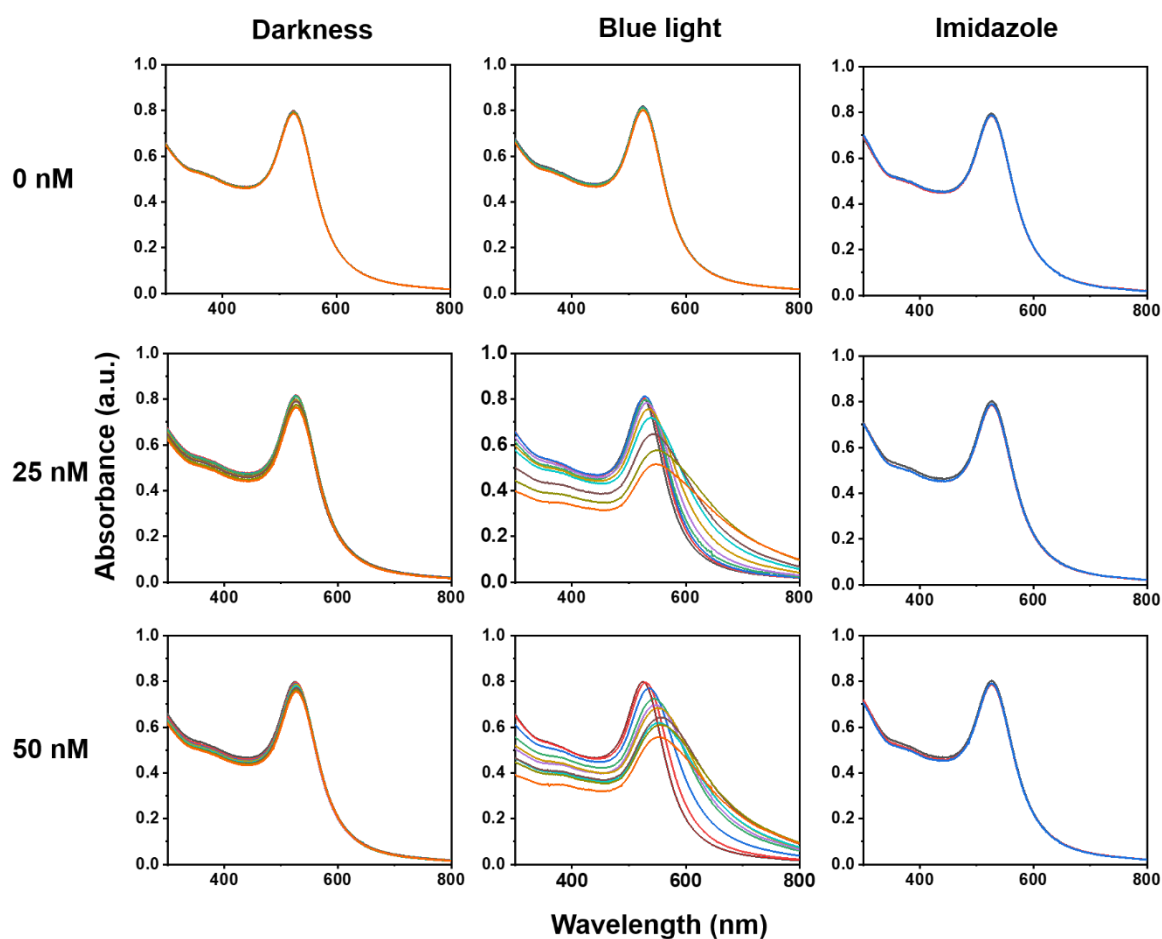


**Figure 4.4.7.** The assembly of Ni<sup>2+</sup>-NTA functionalized AuNP conjugated to *NcVVD*-His<sub>6</sub> driven by exposure to blue light. Time series of UV-Vis spectra of Ni<sup>2+</sup>-NTA functionalized AuNP in both presence and absence of 25 nM or 50 nM *NcVVD*-His<sub>6</sub>. Spectra were recorded at 2, 5, 10, 15, 20, 30, 40, 60 and 90 minutes after addition of

protein (from top to bottom). A strong absorption with a maximum at 524 nm can be observed for non-conjugated Ni<sup>2+</sup>-NTA functionalized AuNP, and is independent of illumination. Blue light induces a plasmon peak broadening and a shift towards higher wavelengths in the presence of *NcVVD-His<sub>6</sub>*, which is attributed to the assembly of AuNP. The velocity of light-directed assembly can be set by controlling the LOV protein concentration. Ni<sup>2+</sup>-NTA functionalized AuNP were incubated with or without *NcVVD-His<sub>6</sub>* of different concentrations (right panels), in the presence of imidazole. After incubation for 90 min either under constant blue light or in dark, no significant spectral changes could be detected. Imidazole competes with the His<sub>6</sub>-tag for NTA binding, thus preventing light-induced particle assembly. Adaption from reference 202 with permission.<sup>202</sup>

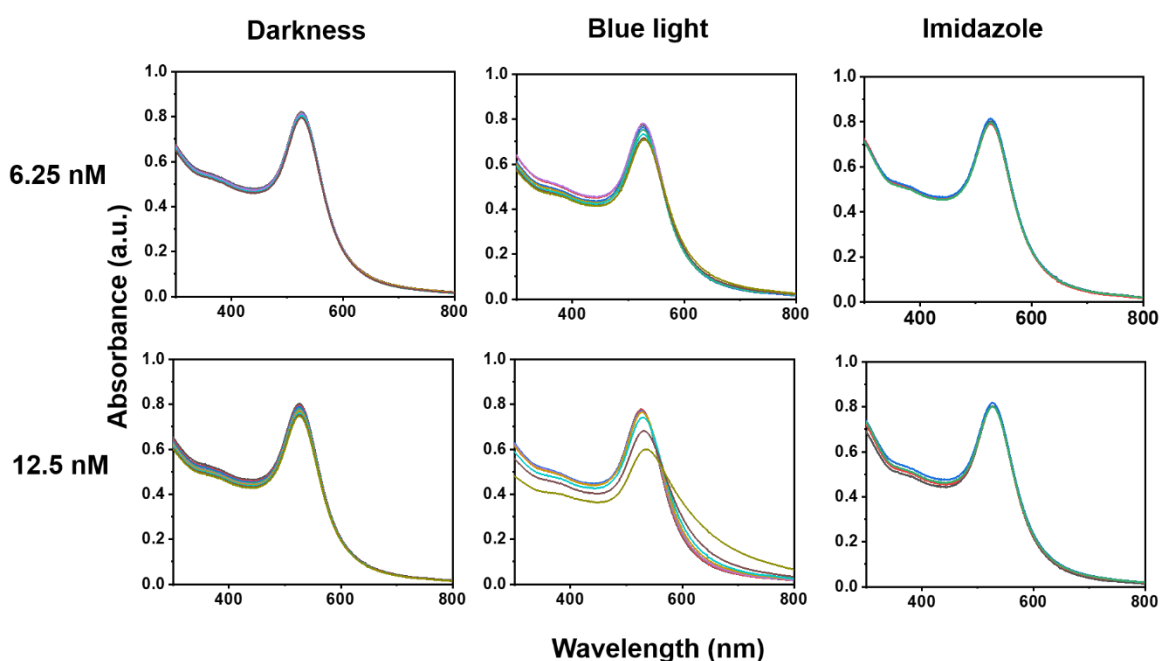


**Figure 4.4.8.** UV-Vis analysis of the assembly of the *NcVVD-His<sub>6</sub>* binding Ni<sup>2+</sup>-NTA-functionalized AuNP triggered by exposure under blue light. Time dependence of the UV-vis spectra of Ni<sup>2+</sup>-NTA-functionalized AuNP without and with 6.25 nM or 12.5 nM *NcVVD-His<sub>6</sub>* in 50 mM Tris/HCl, 300 mM NaCl and 10% (w/v) glycerol buffers at pH 8.0. UV-Vis spectra were recorded at after 2, 5, 10, 15, 30, 40, 60 and 90 minutes incubation of the protein with Ni<sup>2+</sup>-NTA-functionalized AuNP under the dark state (left) or under blue light (middle). The reference experiment was carried out by adding 0.56 M imidazole into the mixture of the protein and Ni<sup>2+</sup>-NTA-functionalized AuNP in 50

mM Tris/HCl, 300 mM NaCl and 10% (w/v) glycerol buffer at pH 8.0 (right). Adaption from reference 202 with permission.<sup>202</sup>

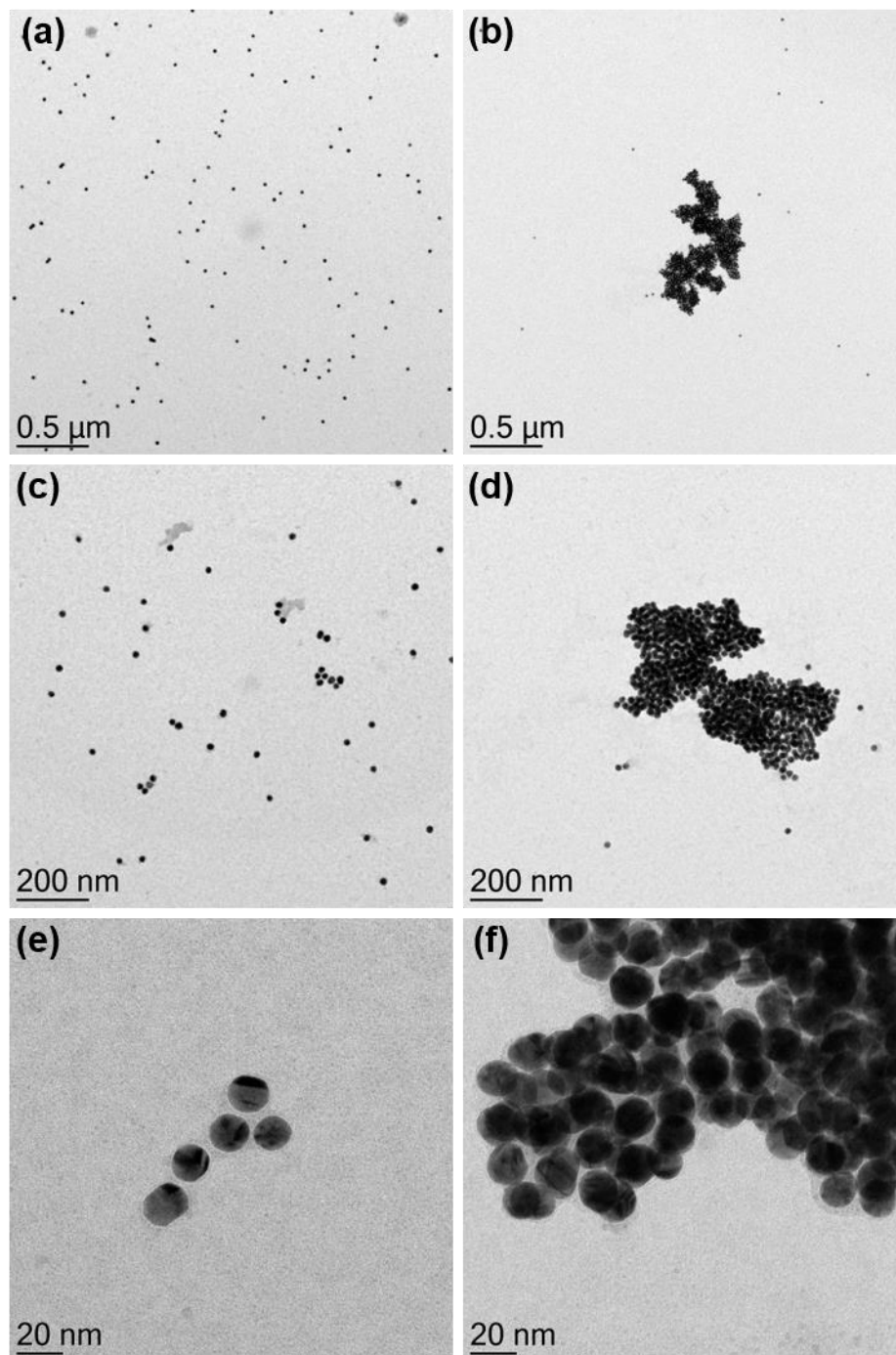


**Figure 4.4.9.** Assembly of AuNP oligomers induced by light. TEM images of Ni<sup>2+</sup>-NTA functionalized AuNP in the presence of *NcVVD-His<sub>6</sub>* in dark (a,c,e) or following exposure under blue light (b,d,f). LOV-coupled AuNP present an even distribution and

do not interact in dark, whereas the assembly of AuNP is directed by light-programmed association of the LOV receptors, which culminates in the formation of extended networks with up to  $\mu\text{m}$  dimensions. Adaption from reference 202 with permission.<sup>202</sup>

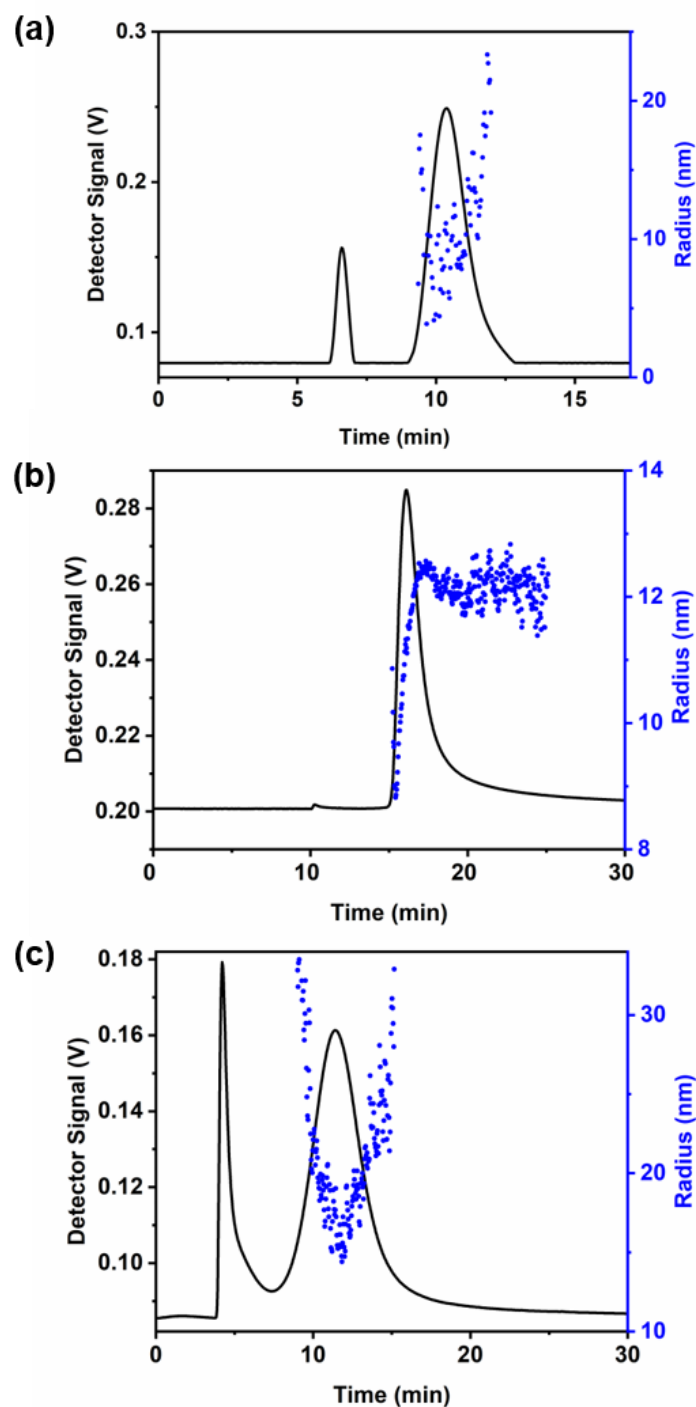


**Figure 4.4.10.** Asymmetric flow field-flow fractionation characterization of the AuNP. (a) Elution profiles of Ct@AuNP. (b) Elution profiles of Ni<sup>2+</sup>-NTA-functionalized AuNP.

(c) Elution profiles of *NcVVD*-His<sub>6</sub> coupled to Ni<sup>2+</sup>-NTA-AuNP. Adaption from reference 202 with permission.<sup>202</sup>

The LOV proteins inducing the assembly of the AuNP were further characterized by TEM to visualize the morphology of the status of the *NcVVD*-His<sub>6</sub> conjugated Ni<sup>2+</sup>-NTA-AuNP in the dark and under exposure to the blue light (Figure 4.4.9). The AuNP were evenly distributed on the TEM grid without significant aggregation when the sample was prepared in the dark. By contrast, after being illuminated with 450 nm light assembly of the AuNP reached a size of 1.5 μm. It should be noted that the photobiologically directed assembly of the AuNP is an irreversible process and cannot be improved by incubation in the dark again or the addition of imidazole. The irreversibility of the assembly of the AuNP might be due to AuNP fusion taking place when the NP are taken into spatial proximity and attempts to revert the process would not be successful.

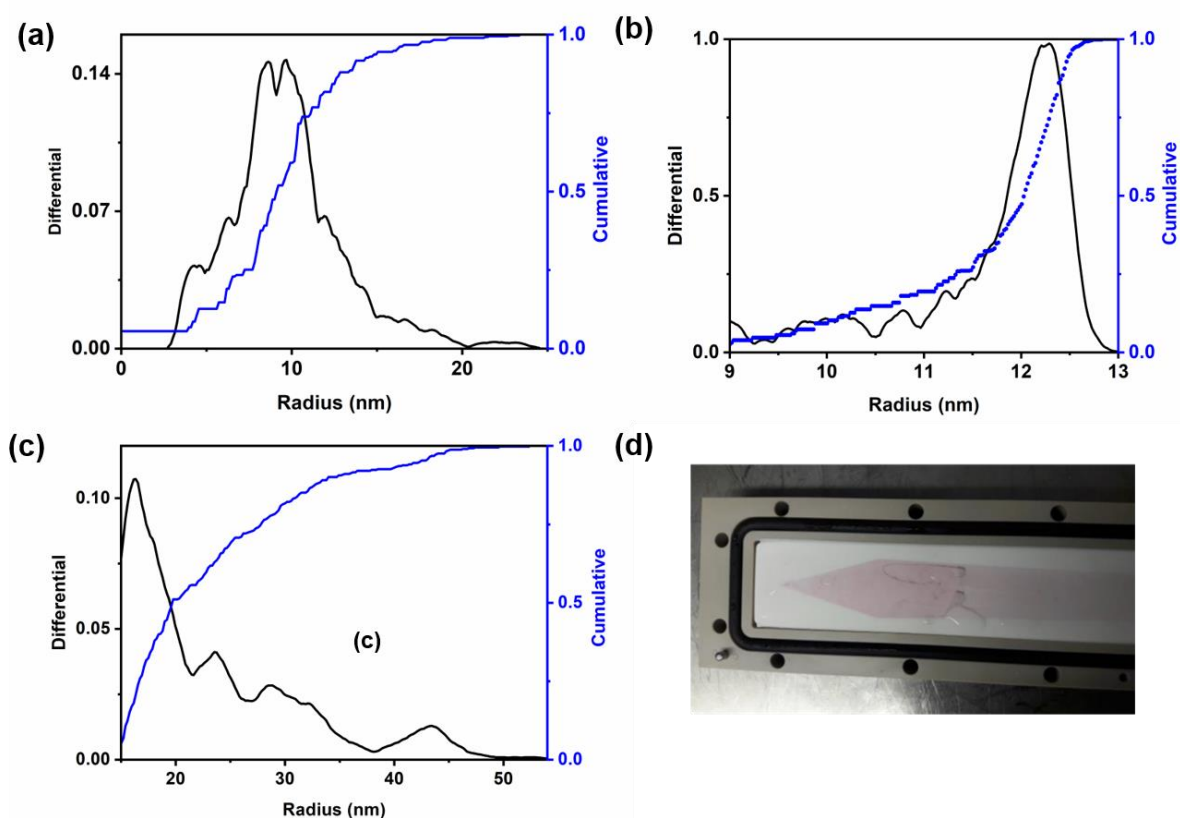


**Figure 4.4.11.** (a, b and c) The main particle fractions of Ct@AuNP, Ni<sup>2+</sup>-NTA-functionalized AuNP and Ni<sup>2+</sup>-NTA-functionalized AuNP Incubated with the *NcVVD*-His<sub>6</sub> protein under dark condition determined by the asymmetric flow field-flow fractionation (AF4). (d) Ni<sup>2+</sup>-NTA-functionalized AuNP Incubated with the *NcVVD*-His<sub>6</sub>

protein when exposed to blue light promote large particle clusters formation, leading to a purple precipitate on the analysis membrane. Adaption from reference 202 with permission.<sup>202</sup>

A DLS measurement was performed initially as another effective tool to assess the conjugation of the *NcVVD-His<sub>6</sub>* protein to the Ni<sup>2+</sup>-NTA-functionalized AuNP and the assembly of the AuNP. However, it was later found to be unsuitable to obtain an accurate average size and the size distribution of the AuNP assemblies, as the DLS signal is sensitive to the larger particles in the dispersion. Therefore, asymmetric flow field-flow fractionation (AF4) was carried out as an alternative. The conditions for performing AF4 are summarized in Table 4.4.1. The apparent radius of the citrate and Ni<sup>2+</sup>-NTA-functionalized AuNP are 11 ± 2 nm and 12 ± 2 nm respectively, as determined by AF4 (Figure 4.4.10 and 4.4.11). The addition of 50 molar excess of the LOV protein induced a shift to 18 ± 2 nm of the main particle fraction, revealing that the conjugation of the LOV protein to AuNP was successful. By contrast, if the sample was illuminated with blue light, all fractions were not eluted and retained on the membrane due to the formation of large-scale particle assemblies (Figure 4.4.11d).

#### **4.4.5 Conclusion**

Photobiologically directed assembly of the AuNP was carried out by conjugating LOV protein to AuNP. The NTA ligand was selected as linker to connect LOV protein to AuNP in buffer solutions. The assembly of AuNP into a large aggregate can be triggered by exposure to blue light in the buffer solution at low temperature, whereas the LOV protein conjugated AuNP is stable in dark.

**Table 4.4.1.** Parameters of AF4 measurements of Ct@AuNP, Ni<sup>2+</sup>-NTA-AuNP, NcVVD-His<sub>6</sub> coupled to Ni<sup>2+</sup>-NTA-AuNP.

<i>Step</i>	<i>Parameter</i>	<i>Citrate-capped AuNP</i>	<i>Ni<sup>2+</sup>-NTA-AuNP</i>	<i>NcVVD-His<sub>6</sub> coupled to Ni<sup>2+</sup>-NTA-AuNP</i>	
	Injection volume (μL)	20	20	20	
	Detector flow (mL min <sup>-1</sup> )	0.5	0.5	0.5	
<b><i>Focusing</i></b>	Injection flow (mL min <sup>-1</sup> )	0.2	0.2	0.2	
	Injection time (min)	5	9	3	
	Crossflow (mL min <sup>-1</sup> )	0.7	0.7	0.5	
	Transition time (min)	0.5	0.5	0.3	
<b><i>Elution</i></b>	Step 1	Elution time (min)	3	3	0.5
		From (mL min <sup>-1</sup> )	0.7	0.7	0.5
		To (mL min <sup>-1</sup> )	0.7	0.7	0.5
		Type	const.	const.	const.
	Step 2	Elution time (min)	20	20	25
		From (mL min <sup>-1</sup> )	0.7	0.7	0.5
		To (mL min <sup>-1</sup> )	0	0	0.05
		Type (Power)	0.15	0.15	0.3
	Step 3	Elution time (min)	0	0	10
		From (mL min <sup>-1</sup> )	0	0	0.05
		To (mL min <sup>-1</sup> )	0	0	0
		Type	0	0	const.
	<b><i>Rinsing</i></b>	Time (min)	5	5	5

## 5 Summary

Gold nanoparticles have been widely studied in the fields of nanoscience and nanotechnology in the past few decades, the AuNP have one of the most popular functionalized building platforms. In my work, the AuNP conjugate with small molecules, supramolecular and macromolecular, and proteins were prepared and their applications in catalysis and photobiology were studied thoroughly.

For the first part of my work, the size-dependent catalytic activity of Ct@AuNP and PVP@AuNP with an average size in the range of 10 to 58 nm were studied by keeping the total surface area of the AuNP in the catalytic reaction the same. The results indicated that the apparent catalytic reaction rate constant presents an increasing tendency with an increase of the average size of the AuNP, for either Ct@AuNP or PVP@AuNP. To exploit the reason behind it, the results revealed that the large NP might contain more defects than the smaller NP, and this might be the crucial factor resulting in their higher catalytic activity in the 4-nitrophenol reduction. The reagent can attach or detach more easily, or it can leach more gold clusters or gold atoms during the catalytic reaction. The influence of ligand density and the diffusion of the reactant to the active site of the AuNP are excluded.

For the second part of this work, composite nonwovens containing supramolecular BTA nanofibers and short PAN fibers were developed. Such composite nonwovens can be fabricated by the facile electrospinning technique and self-assembly combined with a sheet forming wet-laid process via two different routes. These composite nonwovens presented good mechanical properties via route B (wet-laid processing by using mixture of the BTA solution and dispersion of short PAN fibers), because the homogeneously distributed BTA nanofibers and short PAN fibers within, an interpenetrating mesoscale network and the entanglement of the BTA nanofibers with the short PAN fibers all contributed to achieve good mechanical property. The formation of the AuNP within the composite nonwovens can be achieved by *in situ* reduction. The results revealed that the AuNP distributed on the BTA nanofibers homogeneously and the obviously aggregation of the AuNP cannot be observed. The catalytic activity of the AuNP-decorated composite nonwoven was studied in the batch system. The results indicated that catalysts of this type yield comparable apparent catalytic reaction rate constants in comparison with those in the literature. These fabricated AuNP-decorated

composite nonwovens can be used continuously for five cycles without any obvious deactivation of the AuNP. In addition, no significant amount of leaching can be observed during the catalytic reaction.

Based on the groundwork mentioned above, a versatile BTA-sponge with 3D porous architecture was readily fabricated by combining a wet-laid process and the freezing dry method. It can serve as an effective AuNP carrier and exhibits excellent performance at the separation of the AuNP under gravitational force due to their porous structure and the high affinity of the functional terpyridine group to the AuNP. The efficiency of the separation of the AuNP can be 99 % reach by using BTA-sponges I–III. Subsequently, the catalytic activity of the AuNP-incorporated BTA-sponge was studied in this work in both the batch and the continuous flow system. The immobilization of the AuNP within the BTA-sponge can be achieved by an formation method *in situ*. Regarding the study of the catalytic performance of the AuNP-incorporated BTA-sponge in the batch system, the apparent catalytic reaction rate constant per mg was comparable with those in the literature. It presents high reusability without obviously leaching of gold during the catalytic reaction. Regarding the comparison with the batch system, the 4-nitrophenol reduction was carried out in the continuously flow model. The results indicated that the catalytic performance of the AuNP-incorporated BTA-sponge can be significantly improved compared to the batch system, since the excellent accessibility of the reagent to the active site of the AuNP and the improved mass transportation in the catalytic reaction can be dramatically developed.

In the last part of this work, photobiologically directed assembly of the AuNP was realized by conjugating LOV receptors with AuNP in the presence of a NTA ligand as the linker. A novel composite system was developed here by incorporating the AuNP, the linker and LOV receptors. This created a pathway to control the light-stimulated self-assembly of the AuNP. After thorough characterization, it could be deduced that the AuNP conjugated with a proteinaceous building block can remain stable in the dark, whereas the assembly of the AuNP into a large aggregate is initiated when exposed to blue light. Hence, the assembly of the AuNP can be stimulated by light with spatial resolution due to their conjugation to the genetically encodable LOV proteins.

## 6 Zusammenfassung

Goldnanopartikel wurden in den letzten Jahrzehnten in den Bereichen Nanowissenschaften und Nanotechnologie umfassend untersucht. Insbesondere Goldnanopartikel stellen eine der beliebtesten funktionalisierten Plattformen dar. In meiner Arbeit wurden Goldnanopartikelkonjugate mit kleinen Molekülen, Supramolekülen, Makromolekülen und Proteinen hergestellt und ihre Anwendungen in der Katalyse und Photobiologie gründlich untersucht.

Im ersten Abschnitt der Arbeit wurden die größenabhängigen katalytischen Aktivitäten von Ct@AuNP und PVP@AuNP mit durchschnittlichen Größen im Bereich von 10 nm bis 58 nm untersucht, indem die Gesamtoberfläche des AuNP in der katalytischen Reaktion konstant gehalten wurde. Die Ergebnisse zeigten, dass die scheinbare katalytische Reaktionsgeschwindigkeitskonstante eine steigende Tendenz mit einer Zunahme der durchschnittlichen Größe der AuNP sowohl für Ct@AuNP als auch für PVP@AuNP zeigte. Die Untersuchung auch zeigten, dass die großen Partikel möglicherweise mehr Defekte enthalten als die kleineren, was der entscheidende Faktor sein könnte, der zu ihren höheren katalytischen Aktivitäten bei der 4-Nitrophenol-Reduktion führt. Die Reagenzien können sich leichter an den größeren Partikeln anlagern oder von diesen lösen. Es ist auch möglich, dass während der katalytischen Reaktion mehr Goldcluster oder Goldatome freigesetzt wurden. Die Einflüsse der Ligandendichte und der Diffusion des Reaktanten zu den aktiven Stellen des AuNP wurden jedoch durch Berechnung und Simulation ausgeschlossen.

Im zweiten Teil der Arbeit wurde ein neuartiger Verbundvliesstoff, der sowohl supramolekulare BTA-Nanofasern als auch kurze PAN-Fasern enthält, entwickelt. Solche Verbundvliese können durch Elektrospinnen und Vliesbildung in Kombination mit der Nasslegung in einer Blattbildungsanlage durch zwei unterschiedliche Routen hergestellt werden. Die Verbundvliese zeigten eine gute mechanische Eigenschaft durch Route B ((Nassgelegte Verarbeitung durch Verwendung einer Mischung aus BTA-Lösung und Dispersion von kurzen PAN-Fasern), weil BTA-Nanofasern und kurze PAN-Fasern innerhalb des Verbundvlieses homogen verteilt waren und ein durchdringendes mesostrukturiertes Netzwerk und die Verschränkung der BTA-Nanofasern mit den kurzen PAN-Fasern trugen zur guten mechanischen Eigenschaft der Vliesstoffe bei.

Die Bildung von AuNP innerhalb der Verbundvliese kann durch In-situ-Reduktion erreicht werden. Die katalytische Aktivität des AuNP-dekorierten Verbundvlieses wurde im Chargensystem bewertet. Die Ergebnisse zeigten, dass diese Art von Katalysator eine vergleichbare scheinbare katalytische Reaktionsgeschwindigkeit aufwies wie die in der Literatur angegebenen. Darüber hinaus kann dieser hergestellte AuNP-dekorierte Verbundvliesstoff kontinuierlich für fünf Zyklen verwendet werden, ohne dass das AuNP offensichtlich deaktiviert wird. Außerdem kann während der katalytischen Reaktion keine signifikante Auslaugung beobachtet werden.

Im dritten Teil der Arbeit wurde ein vielseitiger BTA-Schwamm mit poröser 3D-Architektur leicht durch die Kombination eines Nassverlegungsverfahrens und des Gefrier-trocknungsverfahrens hergestellt. Es kann als effizienter AuNP-Träger dienen und zeigte aufgrund der porösen Struktur und der hohen Affinität der funktionellen Terpyridingruppe zum AuNP eine ausgezeichnete Leistung bei der gravimetrischen Trennung. Die Trennleistung des AuNP erreichte unter Verwendung des BTA-Schwamms I-III 99%. Die katalytische Aktivität des in AuNP eingebauten BTA-Schwamms wurde in dieser Arbeit im Chargensystem bzw. im Durchlaufsystem untersucht. Die Immobilisierung des AuNP innerhalb des BTA-Schwamms kann über ein In-situ-Bildungsverfahren erreicht werden. Bezüglich der Untersuchung der katalytischen Leistung des AuNP-eingebauten BTA-Schwamms im Chargensystem lag die scheinbare katalytische Reaktionsgeschwindigkeitskonstante pro mg vergleichbar mit denen in der Literatur vor. Das Katalysatorsystem zeigte auch eine hohe Wiederverwendbarkeit ohne Auswaschen von Gold während der Katalyse. Für den Vergleich mit dem Chargensystem wurde auch im Continuous-Flow-Modell eine 4-Nitrophenol-Reduktion durchgeführt. Die Ergebnisse legen nahe, dass die katalytische Leistung der auf den BTA-Schwamm abgelegten AuNP signifikant verbessert werden kann. Dies ist auf die hervorragende Zugänglichkeit der Reagenzien zu den aktiven Stellen des AuNP sowie auf einen verbesserten Stoffübergang im katalytischen Prozess zurückzuführen.

Für die vierten Teil der Arbeit wurde die photobiologische Steuerung der Goldnanopartikel durch konjugierte LOV-Rezeptoren mit AuNP in Gegenwart eines NTA-Liganden als Linker realisiert. Hier wurde ein neuartiges Verbundsystem durch Einbau der AuNP, des Linkers und der LOV-Rezeptoren entwickelt und ein Weg zur Steuerung der Selbstorganisation der durch Licht stimulierten AuNP geschaffen. Nach gründlicher

Charakterisierung kann darauf geschlossen werden, dass jene mit proteinhaltigen Bausteinen konjugierte AuNP in der Dunkelheit stabil sind, während durch die Bestrahlung mit blauem Licht eine Agglomeration der AuNP erfolgt. Daher kann der Aufbau der AuNP aufgrund ihrer Konjugation an die genetisch programmierbaren LOV-Proteine durch Licht mit besonderer räumlicher Auflösung stimuliert werden.

## 7 Outlook

The size-dependent catalytic activity of the AuNP investigated in the first part of this work provides another perspective to understand the influencing factor of the catalytic activities. It is traditionally believed that smaller NP possess higher catalytic activities because of their larger surface area. However, factors influencing the catalytic activity of the AuNP is not only limited to the amount of AuNP investigated in the catalytic reaction and their surface area. Other factors include the defects and the ligand density on the surface of the AuNP, which might decide the accessibility of the reagent to the active sites of the AuNP. The dissociation of the ligand, together with the accessing of the reagent to the surface of the AuNP, and even the attachment of the active species of the reaction to the surface of the AuNP might play important roles in the catalytic performance of the AuNP. This aspect certainly deserves more research efforts. In addition, it can be deduced from this work that defects on the surface can facilitate the catalytic reaction. Therefore, this should be taken into account for catalyst design in the future in order to enhance the catalytic performance of the AuNP.

The composite nonwoven fabricated as the carrier for AuNP in the second part of this work presented high catalytic efficiency and good recyclability without any loss of catalytic activity and obvious gold leaching from the catalyst. However, the catalyst of this type was only investigated in the batch system for the catalytic reaction. A continuous flow system might potentially yield even better results with this catalyst, which could be investigated in the future. The removal of metal NP from wastewater could be considered as another application of the composite nonwoven. In addition to gold, other metallic NP could potentially also be separated from aqueous solutions with this composite nonwoven due to the BTA functional group.

The third part of the work opens up another possibility to fabricate supramolecular nanofibers containing sponges. Sponges of this type do not only present excellent performance in the removal of AuNP from aqueous media but also serve as a good support for the catalyst. In addition to AuNP, other common NP can also be captured with this sponge. It is expected that this kind of architecture is promising in a variety of applications, such as purification of proteins, and carriers for proteins, antibodies and drugs. Moreover, this work provides a novel route for material fabrication in air filtration. The nanopores generated by the supramolecular nanofibers and the micropores in the

sponge can be utilized during the process of air filtration. This method can effectively reduce the pressure drop during air filtration. Moreover, the resulting sponge might present an excellent efficiency and high capacity in capturing the small NP owing to the high surface area and the small nanopores.

The outcome of the last part of the work introduced in this thesis is a novel route to achieve the assembly of the AuNP stimulated by light in the presence of the proteinaceous building blocks. Thus, it helps to establish the fundamental aspects for further applications in the area of colloidal chemistry and biochemistry. The NP of metals other than gold or inorganic NP of different sizes, shapes and composites can also be investigated. In addition, genetic encoding and identity, as well as sensory photoreceptors can also be incorporated into other proteins, biomolecules or the surface of the cells. Therefore, the work can provide a paradigm to decorate NP into the biological circuits. This incorporated NP light-responsive biological system presents high potential in biological and material science applications. Exemplarily, light-triggered assembly of AuNP can be employed for security checks to detect the light exposure of sensitive materials.

## 8 Materials and Experimental Methods

### 8.1 Materials

4-nitrophenol (99.5%, Fluka), polyvinylpyrrolidone K25, 11-Mercaptoundecanoic acid, trisodium citrate dihydrate ( $\geq 99\%$ ), sodium borohydride (purum p.a.,  $\geq 96\%$ ) and sodium hydroxide were purchased from Sigma-Aldrich. Hydrogen tetrachloroaurate (III) trihydrate ( $\geq 99\%$  metals basis) was bought from Alfa Aesar. Acetonitrile was obtained from VWR. Deuterium oxide ( $D_2O$ , 99.9%) was from deuteron. All water used throughout the experiment is Milli-Q grade. Milli-Q water was obtained from a Millipore-Q Plus purification system with a QPAK® 2 column and an electrical conductivity of 18.2 M $\Omega$ -cm. All glassware and magnetic stirring bars used in the syntheses needed to be cleaned in aqua regia (HCl/HNO<sub>3</sub> 3:1) thoroughly, rinsed in distilled water and dried before use, to avoid undesired aggregation of the AuNP and nucleation during the synthesis process, as well as during the storage. A commercial PAN copolymer with < 7 wt% methyl acrylate and sodium methallylsulfonate from DOLAN GmbH (registry no. 26658-88-8) were used. An average molecular weight of 100,000 was determined by gel permeation chromatography (GPC) using DMF as eluent. Polycaprolactone (PCL, Capa™ 6800, Perstorp), Mn of 140,000 was determined by GPC using chloroform as eluent. *N,N*-dimethylformamide (DMF, p.a. 99.8%, Fisher Chemical), isopropanol ( $\geq 99.7\%$ , Bernd Kraft), technical-grade THF was distilled prior to use. Gold chloride trihydrate ( $> 99\%$ ), *N,N'*-dicyclohexylcarbodiimide (DCC, 99%) and nickel (II) chloride (anhydrous, 98%) were bought from Alfa Aesar. Trisodium salt dihydrate (99%) and hydrazine acetate (97%) were purchased from Acros Organics. *N*<sub>α</sub>,*N*<sub>α</sub>-bis(carboxymethyl)-L-lysine, *N*-hydroxysuccinimide (98%), 11-mercaptoundecanoic acid, 1,2-dimethoxyethane (DME, 99%), and zinc (pure, powder) were purchased from Sigma-Aldrich. Sodium hydrogen carbonate, chloroform were purchased from Fisher Chemical. Acetyl chloride ( $\geq 98\%$ ) was purchased from Merck. Sodium sulphate, tris(hydroxymethyl)-aminomethan (Tris), glycerol sodium chloride and imidazole were bought from Carl Roth. Acetic acid was purchased from VWR.

## 8.2 Material characterization

### UV-Vis Spectroscopy

UV-Vis spectra were recorded using a JASCO double beam UV-Visible Spectrophotometer with quartz glass cuvettes, and the halogen lamp as the light source. It should be noted that UV-Vis spectroscopy was performed with an Agilent 8453 UV-Vis spectroscopy system equipped with an Agilent 89090A temperature control accessory for the work of the photobiologically directed assembly of gold nanoparticles. UV-Vis analysis was performed in buffer solutions containing 50 mM Tris/HCl, 300 mM NaCl and 10% (w/v) glycerol at pH 8.0, added with 0, 6.25, 12.5, 25 or 50 nM of *NcVVD*-His<sub>6</sub> 0.9 nM of Ni<sup>2+</sup>-NTA functionalized AuNP. The buffer solutions of 50 mM Tris/HCl, 300 mM NaCl and 10% (w/v) glycerol at pH 8.0 were used as the blank samples. For kinetic analysis of the light induced photobiologically directed assembly of the AuNP, samples were either constantly illuminated with 450-nm light (30 mW cm<sup>-2</sup>), or incubated at 4°C and kept in darkness for the dark state. Absorption spectra were monitored before the addition of protein and after incubation of the mixture of protein and Ni<sup>2+</sup>-NTA functionalized AuNP at 4°C for 2, 5, 10, 15, 20, 30, 40, 60 and 90 minutes. Low-binding reaction tubes (Eppendorf, DNA LoBind) was used for all experiments. The Ni<sup>2+</sup>-NTA functionalized AuNP was also mixed with 560 mM imidazole and 0, 6.25, 12.5, 25 or 50 nM *NcVVD*-His<sub>6</sub> and analyzed as a reference.

### Dynamic light scattering (DLS)

An ALV DLS/SLS-SP 5022F equipment was used to perform the DLS measurement at a scattering angle of 90°. The DLS equipment is consisted of an ALV/SP125 compact goniometer, an ALV 5000/E correlator, two high QE APDs and a cylindrical He-Ne laser operating at 632.8 nm wavelength (22 mW). Samples were filtered with syringe filters (PTFE, 0.45 µm) before analysis and the measurement was performed at room temperature. The measurement for each sample was repeated three times and each run lasted 60s.

### Inductively Coupled Plasma-Optical Emission Spectrometry (ICP-OES)

A Perkin Elmer Avio 200 equipped with an S10 autosampler, Echelle polychromator, Argon humidifier and a DBI-CCD detector was used for ICP-OES measurement. All samples were filtered with syringe filters (PTFE, 0.22 µm) and dried at an elevated

temperature. The residue was dissolved in 0.5 mL aqua regia (HCl:HNO<sub>3</sub> :3:1) and diluted to 10 mL with Milli Q water. A five gold standard solutions (Perkin Elmer Pure, Gold 1000 mg L<sup>-1</sup> in 10 % HCl) at concentration of 0.05, 0.1, 0.5, 1 and 10 mg L<sup>-1</sup> were used for measurement calibrations. For first part of the work, ICP-OES measurement was also performed on a VARIAN Vista-Pro instrument.

### **Transmission electron microscopy (TEM)**

For the first work, TEM images were obtained using a ZEISS CEM 902 instrument with an accelerate voltage 80kV. Preparation of the sample was done by drop-casting of the concentrated nanoparticle dispersion in water onto a carbon-covered copper grid (Carbon Support Films, 300 mesh, Quantofoil, treated with Argon plasma first). ImageJ software (National Institute of Health, USA, version1.44c) was used to evaluate the micrographs. At least 100 particles were measured for each sample. Cs-corrected Scanning Transmission Electron Microscopy (Cs-STEM, JEM-ARM200F, JEOL) was used to study the crystal structures of AuNP thoroughly. The accelerating voltage was 200 kV. For the second and third work, TEM measurements were performed on a Jeol JEM-2200FS at an acceleration voltage of 200 kV. For the work of photobiologically directed assembly of gold nanoparticles, TEM analysis was carried out on a ZEISS EM922 Omega microscope with an accelerating voltage of 200 kV. Before the analysis, 0.9 nM Ni<sup>2+</sup>-NTA functionalized AuNP were incubated with 50 nM NcVVD-His<sub>6</sub> in dark or under illumination of blue light (450 nm, 30 mW cm<sup>-2</sup>) for 10 min at 4°C. Other procedures were the same as abovementioned.

### **Small Angle X-ray Scattering (SAXS)**

A Ganesha AIR system (SAXSLAB, Denmark) was used to record SAXS data of PVP@AuNP dispersions filled in glass capillaries ( $\phi = 1$  mm, Hilgenberg). A focused monochromatic radiation X-ray beam with a wavelength of  $\lambda = 0.154$  nm was offered by a rotating copper anode (MicroMax 007HF, Rigaku Corporation, Japan). 2D scattering patterns were collected with a position-sensitive detector (PILATUS 300 K, Dectris) placed at different distances from the sample. The radially averaged profiles of the intensity of scattering against the modulus of the scattering vector  $\mathbf{q}$  ( $|\mathbf{q}| = q = \frac{4\pi\sin(\theta)}{\lambda}$ ), with wavelength of the incident beam and  $2\theta$  scattering angle, were corrected for sample thickness and instrument-related background. In the first part of this work,

subtraction of the scattering profile of a water-filled capillary was performed to address the intensity contribution attributable to the sample container and solvent. Data were fitted using the software SASView (version 4.2.2). For the fourth part of my work, the X-ray direction was parallel to the sample thickness. 1D-intensity profiles of  $I(q)$  vs.  $q$  were obtained by radial averaging and are given in absolute scale. During this step we normalized to the measuring time, the absorption and an assumed sample thickness of 1 mm – this value is significantly smaller than the sample thickness of about 0.5 cm to accommodate the air filling of the BTA-sponges.

### **<sup>1</sup>H-NMR Spectroscopy**

<sup>1</sup>H-NMR and <sup>13</sup>C-NMR spectroscopy were performed on a Bruker Avance 300A instrument at 300 MHz and 75 MHz. Deuterated chloroform, D<sub>2</sub>O, DMSO were employed as solvents. Signal of the residual protons of the deuterated solvents were used for spectra calibration. NMR spectra were evaluated with the MestReNova software. For BTA-sponges I-II, the sample was dissolved in a mixture of 870  $\mu$ L DMSO and 330  $\mu$ L CDCl<sub>3</sub>. For BTA-sponges III, the sample was dissolved in a mixture of 1.74 mL DMSO and 660  $\mu$ L CDCl<sub>3</sub>.

### **Asymmetric Flow Field-Flow Fractionation (AF4)**

An AF2000 system with a Smart Stream Splitter (Postnova Analytics, Landsberg am Lech, Germany) was used for AF4 measurements. The channel had a length of 295 nm and a width of 30 mm, and was equipped with a 350  $\mu$ m high spacer. A NovaRC 10 kDa regenerated cellulose membrane was used for separation and the detection was done at a wavelength of 270 nm by a UV detector. In addition, the samples were analyzed in-line by a multiple angle light scattering (MALS) detector (Postnova Analytics), operating with linear polarized laser light at 532 nm and 21 observation angles. Individual runs were conducted using 50 mM Tris/HCl, 300 mM NaCl and 10% (w/v) glycerol at pH 8.0 as eluent. The temperature was maintained at 8°C during the measurement, and sample preparation was done as described in the TEM section. Constant illumination was employed to the run of the light-adapted samples, whereas the run of the dark-adapted sample was conducted with no light. The Postnova AF2000 control software was used to process the data from the the MALS detector. A spherical model was used for acquiring the gyration radius, based on the scattered light angular dependence recorded by the MALS detector.

### **Mass Spectrometry**

Mass spectrometry was performed using direct infusion mode with an Ultimate 3000 UPLC system (Dionex, Sunnyvale, CA, USA) to a Hybrid Quadrupole Orbitrap system with electrospray ionization (ESI, Thermo Fisher Scientific, Waltham, MA, USA). Positive mode was applied in the ion source for the MS analysis. Full scan was performed on a mass range of 80-1200 amu.

### **Fourier-Transform Infrared Spectroscopy (FT-IR)**

A PerkinElmer Spectrum 100 FT-IR spectrometer was used to record the FT-IR spectra. It was equipped with a Universal ATR accessory at a resolution of 4  $\text{cm}^{-1}$ . Four scans were performed for each measurement in a wave number range of 4000  $\text{cm}^{-1}$  to 650  $\text{cm}^{-1}$ .

### **Pore Size Measurement**

A PSM 165/H instrument (Dresden, Germany) was employed to determine the pore size of the prepared PAN/BTA composite nonwovens. A sample holder with a measurement area of 4.15  $\text{cm}^2$  and Topor as test liquid (density: 1.9  $\text{g cm}^{-3}$ ; surface tension = 16.0  $\text{mN m}^{-1}$ , Topas GmbH, Germany) were used. For each sample at least two measurements were performed.

### **Wettability Measurement**

Wettability of the nonwovens and sponges was measured using a Drop Shape Analyzer (Krüss Advance, v1.4.0.1). A 4  $\mu\text{L}$  drop of Milli-Q water was placed on top of the composite nonwovens and sponges. The wettability behavior of the water droplet on each nonwoven and sponge along with the time was visualized using the Drop Shape Analyzer.

### **Tensile Test**

Tensile tests were performed with a tensile tester (ZwickiLine Z0.5; BT1-FR0.5TN. D14; Zwick/Roell, Germany). Specimens (3 cm long and 0.3 cm wide) were cut from each composite nonwoven. A clamping length of 2 cm, a pre-tension of 0.01 N/mm and a crosshead speed of 5 mm/min were applied for each measurement. The load cell was a Zwick/Roell Xforce HP with a nominal load of 20 N. A screw micrometer was used to determine the thickness of the samples.

### **Scanning Electron Microscopy (SEM)**

SEM analysis was done on a Zeiss LEO 1530 instrument (Jena, Germany) equipped with a Schottky field-emission cathode at an acceleration voltage of 3 kV. Before measurements, the samples were sputter-coated with about 3 nm platinum layer by a high-resolution sputter coater (208 HR, Cressington). Backscattered electron (BSE) measurements were performed at an acceleration of 10 kV with Robinson detector, and the working distance was 10 mm. Alumina tips were used to improve the sponge conductivity. The diameter of fiber was measured using imageJ software and at least 100 different fibers were counted.

### **X-ray photoelectron spectroscopy (XPS)**

A PHI 5000 VersaProbe III system was used to conduct XPS measurements. The X-ray source is an Al K $\alpha$  excitation source ( $h\nu = 1486.6$  eV) with a pass energy of 26 eV and a beam diameter of 100.0  $\mu\text{m}$   $\times$  100.0  $\mu\text{m}$ . The software PHI Multipak was used to analyze the high-resolution spectra. All recorded peaks, including C1s, N1s, O1s, Na1s and Au4f, were shifted by the same value. The component peak of Na1s was set to 1071.5 eV to conduct the calibration of the spectra. The signal of Na1s (sodium) was detectable as NaBH<sub>4</sub> was employed for washing the material and a small amount of it was remained. In addition, polyacrylonitrile contains a low amount of sodium methylsulfonate.

### **Thermogravimetric Analysis (TGA)**

Thermogravimetric analysis was performed on a TGA 209 Libra F1 (Netzsch, Selb, Germany) in a aluminum oxide (Thepro 85  $\mu\text{l}$ , 6.8  $\times$  4 mm). The heating rate was set to 10 K/min under the nitrogen condition from 20 to 600  $^{\circ}\text{C}$ .

### **Differential Scanning Calorimetry (DSC)**

DSC measurements were performed by using a DSC Phoenix 204 F1 (Netzsch, Germany) under nitrogen atmosphere. The sample was heated from 20 to 160  $^{\circ}\text{C}$  (1K/min).

### **Gel Permeation Chromatography (GPC)**

The analysis of polymer relative molar mass was performed with a size-exclusion chromatography system consisting of a pump (Agilent Technologies 1260 Infinity), a pre-column (Gram10 $\mu\text{m}$ ), two columns Gram 10 $\mu\text{m}$  100/ 3000 $\text{\AA}$ , a refraction index detector

(RI, Agilent Technologies 1260 Infinity) and a diode array detector (DAD, UV-Vis, Agilent Technologies 1260 Infinity). DMF with lithium bromide (5g/L) was used as the mobile phase and the chromatographic runs were performed at a flow rate of 0.5 mL/min under room temperature. Toluene was used as the internal standard. Narrowly distributed polystyrene (PSS-Polymer standards) was used as standard. The polymer sample was prepared at a concentration of 2 mg/mL in DMF with lithium bromide or toluene and filtered through a 0.22  $\mu\text{m}$  syringe filter before the analysis. The data was evaluated using the software WinGPC8.

## **8.3 Experimental procedures**

### **8.3.1 Synthesis and conjugation of size dependent AuNP**

#### **8.3.1.1 Preparation of Size-dependent AuNP by the Frens Method**

The synthesis of Ct@AuNP was performed based on method reported in previous literature with slight modifications.<sup>156</sup> 25 mL aqueous solution of HAuCl<sub>4</sub> ( $2.5 \times 10^{-4}$  M) was heated until it boiled and different amounts of 1wt% trisodium citrate solution were then added under continuous stirring, to obtain AuNP of different sizes. Within 5 min of boiling, color change of the solution could be observed: yellow to white to gray to faint blue to violet until finally to red, which is the indication of the formation of AuNP. The reaction mixture was kept at boiling for another 30 min before mild stirring was applied until it got back to room temperature. The products were then stored at 4 °C.

#### **8.3.1.2 Synthesis of PVP@AuNP by ligand exchange**

Preparation of PVP@AuNP by ligand exchange was performed according to method described in previous literature with minor modifications.<sup>203</sup> The PVP@AuNP were obtained from the above Ct@AuNP by conventional ligand exchanging reaction. About 16 mL of the Ct@AuNP was transferred into a clean conical flask under room temperature, which was followed by addition of 1.6 mL of 2 wt% PVP solution in a dropwise fashion under constant magnetic stirring. To ensure the complete replacement of surface citrate molecules by PVP molecules, the above reaction mixture was kept under gentle magnetic stirring for 24 hours. After that, purification of the PVP capped AuNP was carried out by centrifugation, followed by washing for one time. It should be noted that the speed of centrifugation was varied depending on the size of AuNP to be prepared. Finally, the PVP@AuNP products were redispersed in Milli-Q water and stored in the dark.

#### **8.3.1.3 Synthesis of 11-mercaptoundecanoic MUA@AuNP by ligand exchange**

The 10 nm and 42 nm Ct@AuNP were prepared by the method mentioned in the previous section. Then the ligand exchange of Ct@AuNP with 11-mercaptoundecanoic (MUA) was carried out according to method described in the literature with some modifications.<sup>170</sup> 30 mL of 42 nm Ct@AuNP or 20 mL of 10 nm Ct@AuNP were transferred into a clean conical flask under room temperature, followed by dropwise

addition of 920  $\mu\text{L}$  or 613  $\mu\text{L}$  MUA (3.26 mg in 3 mL 0.1 M NaOH) under constant stirring. The mixtures were kept at room temperature overnight with stirring at 130 rpm to ensure the complete exchange of citrate by MUA ligand. The AuNP were afterwards washed twice with  $\text{H}_2\text{O}$  and one time with  $\text{D}_2\text{O}$ . Finally, digestion of the concentrated 42 nm and 10 nm MUA@AuNP pallets were performed in fresh aqua regia solution overnight.

#### **8.3.1.4 Characterization of AuNP ligand density**

For the ICP-OES analysis, 10  $\mu\text{L}$  and 15  $\mu\text{L}$  of 42 nm and 10 nm MUA@AuNP digested solution were added into 15 mL and 30 mL 5% aqua regia solution respectively. For  $^1\text{H-NMR}$  analysis, 140  $\mu\text{L}$  and 110  $\mu\text{L}$  of the 42 nm and 10 nm MUA@AuNP digested solutions were used. To make sure that all the MUA ligands were dissolved in  $\text{D}_2\text{O}$ , 10 M NaOH were added into these samples stepwise until the pH about 10 is reached. Then the solutions were diluted to a total volume of 600  $\mu\text{L}$  with  $\text{D}_2\text{O}$ . ACN was employed as reference for quantitative analysis of unknown ligand concentrations of the AuNP solutions. 5  $\mu\text{L}$  of diluted ACN (0.25 v/v %; 5  $\mu\text{L}$  ACN in 2 mL  $\text{D}_2\text{O}$ ) was added into the two samples. The standard calibration curve (consisting of five points) was generated by plotting the integration of a particular MUA peak divided by the integration of ACN against the MUA ligand concentration (0.01, 0.05, 0.10, 0.50, 1.00 mM, in diluted NaOH aqueous solution). Quantitatively determination of the unknown ligands was done by comparing the results to the calibration curve.

#### **8.3.1.5 Characterization of catalytic activity in nitrophenyl reduction**

The catalytic activities of the AuNP catalyst were studied by a reduction reaction of 4-nitrophenol under room temperature (25  $^\circ\text{C}$ ) according to the literature.<sup>185</sup> For UV-Vis measurement, 2.1 mL of fresh sodium borohydride (0.05 M) and 230  $\mu\text{L}$  of 4-nitrophenol (2.78 mg in 40 mL) were added into a 10 mm quartz cuvette with a magnetic stirrer at the bottom. Stirring was applied with a speed of 300 rpm. UV-Vis spectra (250-600 nm) of the sample were detected every 2 min for 40 min, immediately after the addition of the catalyst. After the reduction was completed, the solution turned from light-yellow to colorless, as 4-aminophenol was produced.

### **8.3.2 Fabrication of nonwoven comprising short PAN fibers and self-assembly BTA fibers**

#### **8.3.2.1 Preparation of electrospun PAN nonwoven**

PAN nonwovens were prepared by electrospinning of a 19 wt% PAN solution in DMF. Collection of the nonwovens were done on a rotating collector (length 45 cm; diameter: 16 cm; speed: 65 rpm) at a distance of 25 cm from the needle covered with baking paper. A voltage of +20 kV was applied to the needle with a diameter of 0.8 cm and a voltage of -0.9 kV to the collector. The flow rate of the PAN solution was set to be 0.5 ml/h. All experiments were performed at 20°C with a relative humidity of 17-22 %.

#### **8.3.2.2 Formation of supramolecular BTA nanofibers by self-assembly**

For route A, 0.05 wt% BTA was dissolved in an isopropanol/water (w/w 9:1) solvent mixture at elevated temperature with continuous stirring until a clear solution was obtained. The solution was then slowly cooled down to room temperature. After around 30 minutes, the solution turned turbid as the result of the formation of supramolecular nanofibers by self-assembly upon cooling.

#### **8.3.2.3 Fabrication of PAN/BTA composite nonwoven**

Before the wet-laid process, the electrospun fibers were soaked in water and cut by a mixer (Vital mixer basic, Gastroback, 21.000 rpm) for a short period of time until a homogeneous dispersion of short fiber was obtained.

For route A, the PAN short fiber dispersion was mixed with a BTA fiber dispersion with 0.05 wt% BTA in isopropanol/ H<sub>2</sub>O (w/w 9:1). For route B, freshly prepared BTA solution with a concentration of 0.01 wt%, 0.05 wt% or 0.1 wt% BTA in isopropanol/ H<sub>2</sub>O (w/w 9:1) was mixed with the short PAN fiber dispersion (c = 0.5 mg/mL) in H<sub>2</sub>O at room temperature. Additional solvents (water and isopropanol) were added to the fiber mixture in both cases since a large total volume of 3.7 L is required for the sheet forming process.

The fabrication of the composite nonwovens were carried out using a HAAGE Sheet former BB with a sheet forming column and a vacuum pump. The PAN/BTA mixture was poured into the sheet forming column after being shaken in a canister for a few

seconds. After the dispersion was calmed, the solvents were removed by suction filtration. A round 325 stainless steel mesh placed on top of the sheet forming sieve frame was used to collect the fibers. To keep a slower fiber deposition, four cellulose filtration paper layers with a diameter 20 cm (BS20, Bosch & Schörle GmbH, Stuttgart) were inserted between the sieve frame and the sheet support sieve. The produced composite nonwovens were removed and dried at 60°C for 10 min under vacuum (900 mbar). The thickness was measured by a screw micrometer and at least five positions were determined.

#### **8.3.2.4 *In situ* immobilization of AuNP**

In situ formation of AuNP within the composites was carried out by first placing the nonwoven (spherical shape with a diameter 1.5 cm) in 2 mL diluted tetrachloroauric acid aqueous solution ( $\text{HAuCl}_4 \cdot 3\text{H}_2\text{O}$ ; 50 mM, 25  $\mu\text{L}$  in water) for 10 minutes with shaking at 500 rpm, followed by washing with Milli-Q water for 2 times. Then the gold ion immobilized composite nonwoven was placed in 5 mL sodium borohydride solution ( $\text{NaBH}_4$ ; 50 mM). After another shaking at 500 rpm for 10 minutes, the composite nonwoven was washed twice using Milli-Q water and then freeze-dried under vacuum at room temperature.

#### **8.3.2.5 Catalytic reduction of 4-nitrophenol to 4-aminophenol by AuNP catalyst**

The catalytic activity of the composite nonwovens fabricated was evaluated exemplarily by the reduction reaction of 4-nitrophenol. 220  $\mu\text{L}$  4-nitrophenol solution (0.49 mM) together with 2.1 mL 100 mM sodium borohydride solution were added into a quartz cuvette. The composite nonwoven was then completely immersed in the reaction solution. The reaction mixture was stirred at 25°C and 600 rpm for 1 h. Absorption spectra from 250 nm to 600 nm were recorded every two minutes. A blank sample of Milli-Q water was measured for baseline correction purpose before reaction mixture measurements.

### **8.3.3 Fabrication of multi-functional sponge consisting of short electrospun fibers and self-assembly BTA nanofibers**

#### **8.3.3.1 Preparation of electrospun PCL and PAN fiber**

PCL nonwovens were prepared by electrospinning of a 17 wt% PCL solution in a THF/DMF mixture (70/30 w/w). The 17 wt% PCL solution was filtered with 0,45  $\mu\text{m}$  PTFE syringe filter. An aluminum foil was used to collect the PCL fibers at a distance of 25 cm. the solution was loaded into a 6 mL syringe and a needle of 0.8-mm internal diameter was connected to 16 kV voltage and a voltage of -0.9 kV was applied to the collector. The flow rate of the PCL solution was 0.8 mL/h. All experiments were performed at temperature 20-22 °C with relative humidity 17-22 %. The nonwovens were placed in the fume hood to dry for days before further fabrication.

PAN nonwovens were prepared by electrospinning of a 19 wt% PAN solution in DMF. Collection of the nonwovens were done on a rotating collector (length 45 cm; diameter: 16 cm; speed: 65 rpm) at a distance of 30 cm from the needle covered with baking paper. A voltage of +19 kV was applied to the needle with a diameter of 0.8 cm and a voltage of -0.8 kV to the collector. The flow rate of the PAN solution was set to be 0.5 ml/h. All experiments were performed at 20-25°C with a relative humidity of 10-15%.

#### **8.3.3.2 Preparation of the dispersion of short PCL and PAN fiber**

The PCL short fiber dispersion was prepared by cutting 1.0 g of the electrospun PCL nonwovens in 1000 mL Isopropanol/water (70/30 w/w) mixture at -20 °C with the help of liquid nitrogen. The short fibers dispersion was then concentrated to 10 mg/3.6 mL.

The short PAN fiber dispersion was prepared by cutting 1.0 g of the electrospun PAN nonwovens in 1000 mL Isopropanol/water (70/30 w/w) mixture at -20 °C with the help of liquid nitrogen, until a homogenous dispersion was obtained. And the short PAN fibers were washed with water thoroughly to remove the isopropanol. Finally the short PAN fibers were redispersed in dioxane and freezing-dried under room temperature.

#### **8.3.3.3 General procedure of sponge fabrication**

The BTA-sponges were prepared according to Figure 4.3.1 in the results and discussion section (4.3). Firstly, 0.05, 0.1 wt% respectively, was dissolved in Isopropanol/H<sub>2</sub>O mixture (9/1 w/w) at elevated temperatures. Intense stirring was

applied until all the BTA are completely dissolved in the solution. Then the solution was cooled down slowly to the room temperature without any precipitation. Meanwhile, 10 mg PAN was dissolved in 20 mL water and the mixture was stirred with vortex until a homogenous short PAN fiber dispersion was obtained (0.5 mg/mL). 10 mL of 0.05 wt% or 0.1 wt% BTA solution was then added into 20 mL short PAN fiber dispersion to fabricate BTA-sponges I and II. 20 mL 0.1 wt% BTA solution was added into 40 mL short PAN fiber dispersion (0.25 mg/mL) to fabricate the BTA-sponge III. When mixed with large amount of water, the BTA supramolecular nanofibers were immediately generated by self-assembly. Afterwards, 3.6 mL (10 mg) short PCL fiber dispersion were transferred into the mixture dispersion of the short PAN fibers and BTA nanofibers, to yield the final homogenous suspension consisting of the BTA nanofibers, short PAN fibers and short PCL fibers.

Secondly, the prepared suspension in the first step was concentrated to about 1.3 g concentrated suspension under ambient condition. The concentrated suspension was then slowly cooled down to -40 °C for 1 h and was frozen at -40 °C for another 1 h. After that, in order to ensure complete freezing of the sponges, the sponges were further frozen to -55 °C for 2 h. The sponges were then freeze-dried under vacuum at room temperature for 24 h. Finally, the freeze-dried sponges were heated in the oven at 70 °C for 2 h for thermal annealing. Especially, 10 min is enough for annealing of the PAN and PCL sponge.

#### **8.3.3.4 Filtration of the AuNP**

The sponges were placed inside the syringe under ambient pressure (inner diameter of the syringe is 12.45 cm). The sponges were wetted with water before the loading of the PVP@AuNP. The PVP@AuNP powder (Formulate 2, diameter  $16.5 \pm 2.9$  nm) was from a previous work of our group.<sup>204</sup> The 3 mL PVP@AuNP (1mL containing 30  $\mu$ g Au determined by ICP-OES) solution was then filtrated through the sponges under ambient pressure. After all the solution has passed through the syringe, 3 mL Milli-Q water was passed through to remove non-adsorbed AuNP. In the end, 2 mL Milli-Q water was passed through the sponge in order to wash out all unbonded AuNP.

#### **8.3.3.5 *In Situ* formation of AuNP in the sponge**

The sponges were settled down inside the syringe under atmospheric pressure. 25  $\mu\text{L}$   $\text{HAuCl}_4 \cdot 3\text{H}_2\text{O}$  (50 mM) diluted in 5 mL water was then passed through the sponge two times. Afterwards, 4 mL water was used to wash away the unbinding gold salt. The gold-loaded sponge was immersed in 5 mL 50 mM  $\text{NaBH}_4$  solution, after being shaken at 400 rpm for 10 minutes followed by 5 mL MilliQ water washing to remove the unbinding AuNP. Finally, the AuNP-loaded sponges were immersed in 2 mL water and freeze-dried under room temperature. The amount of gold loaded was determined by ICP-OES.

#### **8.3.3.6 4-nitrophenol reduction with sponge-type AuNP carrier in batch system**

The reduction reaction of 4-nitrophenol into 4-aminophenol by sodium borohydride ( $\text{NaBH}_4$ ) was selected to determine the catalytic efficiencies and reusability of the sponge-type AuNP carriers. The catalytic reaction was carried out at the ambient temperature in the presence of AuNP-immobilized BTA-sponge I-III. In a typical procedure, 220  $\mu\text{L}$  4-nitrophenol aqueous solution (0.49 mM) was added into 2.1 mL 100mM freshly prepared  $\text{NaBH}_4$  solution. Then, AuNP-loaded sponges were explored in the mixed solution with stirring at 600 rpm. UV-Vis absorption spectra were recorded every two minutes during the reaction process.

#### **8.3.3.7 Continuous flow nitrophenol reduction with sponge-type AuNP carrier**

The sponges were placed into the syringe under ambient pressure (inner diameter of syringe is 0.94 cm). Water was passed through the sponge until the sponge is completely wetted. The syringe containing the sponge was then fixed on the syringe pump. After mixing 220  $\mu\text{L}$  4-nitrophenol aqueous solution (0.49 mM) and 2.1 mL 100 mM freshly prepared  $\text{NaBH}_4$  solution, the mixture was transferred into the syringe. The flow reaction was immediately started with a flow rate of approximately 2 mL/min. Synchronously the time was recorded with a stopwatch. The filtrate was collected until all the solution has passed through the syringe. The original mixture of nitrophenol and sodium borohydride, and the filtrate solution including the part of filtrate solution squeezed out in the very beginning were measured by UV-Vis.

### 8.3.4 Synthesis of thiolated nitrilotriacetic acid (NTA) ligand and conjugation to AuNP

#### 8.3.4.1 Synthesis of AuNP for conjugation of protein

400 mL of  $\text{HAuCl}_4$  ( $2.5 \times 10^{-4}$  M) water solution was heated to boiling. 10.4 mL trisodium citrate solution [1% (w/w)] was then added into the solution under stirring continuously. Within 5 min of boiling, the solution presented gradual colour change from yellow to white, then to grey, then to faint blue, then to violet and finally to red, which is an indication of the formation of AuNP. After another 30 min of boiling, the reaction mixture was cooled down to room temperature with mild stirring. The solution of AuNP was stable and kept at 4 °C.

#### 8.3.4.2 Synthesis of NTA ligand

The preparation of NTA ligand was performed according to method described in previous literature with modifications.<sup>199-201</sup>

##### Synthesis of 11-(acetylthio)undecanoic acid

67 mL chloroform solution of 11-mercaptoundecanoic acid (838 mg, 3.84 mmol) and 14 mL acetic acid were mixed and stirred for 15 min after the addition of 2.2 g zinc powder. Afterwards, the solution was cooled down to 0°C, treated with acetyl chloride (5.33 mL) subsequently and kept overnight under stirring. Then, zinc was filtered off with a pad of Celite, and the filtrate was washed with 30 mL 0.1 M HCl and 30 mL water two times. The organic deposit was dried using  $\text{Na}_2\text{SO}_4$ , filtered, and concentrated under vacuum. Column chromatography was used to purify the residue to yield compound **1** 650 mg (65%) as a white powder [ $^1\text{H}$  NMR (300 MHz,  $\text{CDCl}_3$ )  $\delta$  2.85 (t, 2H), 2.37 – 2.31 (m, 5H), 1.67 – 1.48 (m, 4H), 1.37-1.20 (m, 12H)]

##### Synthesis of *N*-[ $N_\alpha, N_\alpha$ -bis(carboxymethyl)-L-lysine] 11-(acetylthio)dodecanamide

9 mL anhydrous 1,2-dimethoxyethane (DME) solution of 11-(acetylthio)undecanoic acid (**1**, 164 mg, 0.63 mmol) and *N*-hydroxysuccinimide (NHS, 72.5 mg, 0.63 mmol) was cooled down to 0°C, followed by the addition of *N,N'*-dicyclohexylcarbodiimide (157 mg, 0.76 mmol). The solution was kept at 0 °C for 24 h, and the white precipitate of dicyclohexylurea was filtered off and rinsed with dry DME. The filtrate was concentrated *in vacuo* to form the white NHS ester powder, which was used with no

further purification. The NHS ester was resuspended in 0.63 mL acetone and 6.18 mL ethanol and treated with 3.15 mL water solution of  $N_{\alpha},N_{\alpha}$ -bis(carboxymethyl)-L-lysine (164.92 mg, 0.63 mmol) and  $\text{NaHCO}_3$  (211.68 mg, 2.52 mmol) under room temperature and stirred for 43 h under argon. Afterwards, the ethanol was evaporated under reduced pressure and the residue was diluted with 3.15 mL water and 1.26 mL  $\text{NaHCO}_3$  water solution (0.25 M). The white precipitate produced was filtered off. After acidify the filtrate with 1.0 M HCl to a pH of 3, the colloidal suspension was centrifuged at 4000 rpm under 25°C for 20 min, which led to the formation of crude product **3**. The resuspension/centrifugation process was repeated two times to rinse the pallet with water. The resulting residue was lyophilized to yield 156 mg (49%) of compound **3** as a pale white solid. [ $^1\text{H}$  NMR (300 MHz, DMSO)  $\delta$  3.45 (d, 4H), 3.31 (t,  $J = 7.3$  Hz, 2H), 2.98 (br, 2H), 2.81 (t,  $J = 7.2$  Hz, 2H), 2.31 (s, 3H), 2.01 (t,  $J = 7.4$  Hz, 2H), 1.64 – 1.11 (m, 22H)]

Synthesis of  $N$ -[ $N_{\alpha},N_{\alpha}$ -bis(carboxymethyl)-L-lysine] 11-mercaptododecanamide (NTA) 147 mg Hydrazine acetate (1.59 mmol) was added into 6.5 mL dimethylformamide solution of  $N$ -[ $N_{\alpha},N_{\alpha}$ -bis(carboxymethyl)-L-lysine] 11-(acetylthio)dodecanamide (compound **3**, 53 mg, 0.105 mmol) and the mixture was then bubbled with argon for 20 min at room temperature, followed by degassing and stirring for 20 h under argon. Solvent removal was carried out under reduced pressure, followed by treatment with 0.05 N HCl (20 mL). The colloidal suspension was centrifuged at 4000 rpm and 25 °C for 20 min to yield crude product **4**, denoted NTA. After the supernatant was removed, the resuspension / centrifugation steps was repeated two times to wash the residue with water. The product was lyophilized to yield 36 mg (74%) compound **4** that was a pale white solid. [ $^1\text{H}$  NMR (300 MHz, DMSO- $d_6$ )  $\delta$  3.47 (d, 4H), 3.31 (t,  $J = 7.3$  Hz, 1H), 2.98 (br, 2H), 2.44 (t,  $J = 7.2$  Hz, 2H), 2.01 (t,  $J = 7.4$  Hz, 2H), 1.66-1.10(m, 22H).  $^{13}\text{C}$  NMR (75 MHz, DMSO)  $\delta$  174.03, 173.30, 171.92, 64.34, 53.43, 38.26, 35.46, 33.46, 29.37, 28.94, 28.81, 28.54, 27.80, 25.36, 23.81, 23.15] Mass spectrometry: calculated  $(\text{M}+1)^+ = 463.247$ , observed  $(\text{M}+1)^+ = 463.2469$

#### 8.3.4.3 Preparation of $\text{Ni}^{2+}$ -NTA functionalized AuNP

1 mg NTA (**4**) was dissolved in 3 mL of 50 mM Tris, 300 mM NaCl, 10% (w/v) glycerol, pH 8. 5 mL gold nanoparticle solution was then added to the solution, and stirring was applied to the mixture overnight at room temperature. Centrifugation was performed

on the mixture at 6000 rpm for 20 min, and the supernatant was removed afterwards. The AuNP precipitated were re-dispersed in the same buffer. 3.5  $\mu\text{L}$   $\text{NiCl}_2$  (12.5 mg in 20 mL) was added to the solution of AuNP, followed by 20 min incubation at ambient temperature. The  $\text{Ni}^{2+}$ -NTA-AuNP solution was centrifuged at 6000 rpm again for 20 min. After removing the supernatant, the  $\text{Ni}^{2+}$ -NTA-AuNP were resuspended in 50 mM Tris, 300 mM NaCl, 10% (w/v) glycerol, pH 8. The particles were stored at 4°C until further use.

The gold atom molar concentration,  $c_{\text{Au}}$ , was determined by inductively coupled plasma optical emission spectrometry, see below. For the calculation of the gold nanoparticle concentrations, a spherical shape and a uniform face-centered cubic lattice (fcc) structure were assumed for the AuNP. The average number of gold atoms per nanoparticle ( $N$ ) was calculated using eq. (1), where  $\rho$  is the density for fcc gold (19.3  $\text{g cm}^{-3}$ ),  $d$  denotes the diameter of the AuNP (17.7 nm, as measured by TEM) and  $M$  represents atomic weight of gold (197  $\text{g mol}^{-1}$ ).<sup>205</sup>

$$N = \pi/6 \times (\rho d^3 / M) \quad (1)$$

eq. (2) was then used to calculate the molar concentration of the AuNP ( $c_{\text{NP}}$ ):

$$c_{\text{NP}} = c_{\text{Au}} / N \quad (2)$$

## 9 List of Abbreviations and Symbols

2D	Two dimensional
3D	Three dimensional
4-NP	4-nitrophenol
4-AP	4-aminophenol
Au	Gold
AuNP	Gold nanoparticles
ACN	Acetonitrile
BTA	Terpyridine functioned benzene-1,3,5-carboxamide
Ct	Citrate
DMF	<i>N,N</i> -dimethylformamide
DMSO	Dimethyl sulfoxide
DCCl <sub>3</sub>	Deuteriochloroform
DLS	Dynamic light scattering
DSC	Differential scanning calorimetry
D <sub>2</sub> O	Deuterium oxide
GPC	Gel permeation chromatography
H <sub>2</sub> O	Water
Hz	Hertz
HCl	Hydrochloric acid
HNO <sub>3</sub>	Nitric acid
HAuCl <sub>4</sub>	Tetrachloroauric(III) acid
IR	Infrared
iPr	Isopropyl group
ICP-OES	Inductively coupled plasma optical emission spectroscopy
Mn	Number average molar mass
MUA	11-Mercaptoundecanoic acid
NMR	Nuclear magnetic resonance spectroscopy
NaBH <sub>4</sub>	Sodium Borohydride

Ni	Nickel
NaCl	Sodium chloride
NP	Nanoparticle
PVP	Polyvinylpyrrolidone
PAN	Polyacrylonitrile
PCL	Polycaprolactone
ppm	Parts per million
SEM	Scanning electron microscopy
SAXS	Small angle X-ray scattering
SAED	Selected area electron diffraction
TEM	Transmission electron microscopy
TOF	Turnover frequency
THF	Tetrahydrofuran
TGA	Thermogravimetric analysis
UV-Vis	Ultraviolet-visible spectroscopy
XPS	X-ray photoelectron spectroscopy
%	Percentage
s	Second
cm	Centimeter
μm	Micrometer
t	Time
h	Hour
m	Mass
min	Minute
wt	Weight
<i>k</i>	Reaction rate constant

## 10 Appendix

### 10.1 The name of sample

#### 10.1.1 The first part of work

<b>Ct@AuNP/Synthesis</b>	
9.8 ± 0.9 nm	LC0311201701
16.9 ± 1.4 nm	LC0501201801
19.6 ± 1.8 nm	LC0401201802
35.2 ± 8.3 nm	LC-22
42.1 ± 7.8 nm	LC0203201801 LC04112020-2
58.1 ± 7.7 nm	LC0201201802
<b>PVP@AuNP/Synthesis</b>	
9.8 ± 0.9 nm	LC2201201801
16.9 ± 1.4 nm	LC0801201801
19.6 ± 1.8 nm	LC1201201805
35.2 ± 8.3 nm	LC2203201803
42.1 ± 7.8 nm	LC2203201801 LC06112020-1
58.1 ± 7.7 nm	LC1201201802
<b>MUA@AuNP/Synthesis</b>	
9.8 ± 0.9 nm	LC30032019-1
42.1 ± 7.8 nm	LC30032019-2
<b>Ct@AuNP/ Catalytic reaction</b>	
9.8 ± 0.9 nm	LC13112020
16.9 ± 1.4 nm	LC18052018-1
19.6 ± 1.8 nm	LC17052018

35.2 ± 8.3 nm	LC18052018-2
42.1 ± 7.8 nm	LC22052018-1
42.1 ± 7.8 nm (SAXS)	LC16112020-2
58.1 ± 7.7 nm	LC22052018-2
<b>PVP@AuNP/ Catalytic reaction</b>	
9.8 ± 0.9 nm	LC19052018PVP-4
16.9 ± 1.4 nm	LC19052018PVP-1
19.6 ± 1.8 nm	LC21052018PVP
35.2 ± 8.3 nm	LC20052018PVP-1
42.1 ± 7.8 nm	LC19052018PVP-3
42.1 ± 7.8 nm (SAXS)	LC16112020-1
58.1 ± 7.7 nm	LC20052018PVP-2

### 10.1.2 The second part of work

<b>Wet-laid Nonwoven</b>	
Reference (pure PAN nonwoven)	LC28012020-1
1	LC16122019-1
2a	LC17022020-1
2b	LC16122019-2
2c	LC28012020-2
<b>AuNP-nonwoven</b>	
AuNP-2b	LC30072020-1
AuNP-2c	LC30072020-2
<b>Catalytic reaction</b>	
AuNP-2b	LC19082020-1
AuNP-2c	LC19082020-2

### 10.1.3 The third part of work

<b>BTA-Sponge</b>	
PAN+PCL Sponge	LC26062020-1
BTA-Sponge I	LC26062020-2
BTA-Sponge II	LC26062020-3
BTA-Sponge III	LC26062020-4
<b>AuNP-BTA-Sponge</b>	
AuNP- BTA-Sponge I	LC24082020
AuNP- BTA-Sponge II	LC24082020
AuNP- BTA-Sponge III	LC24082020
<b>Catalytic reaction</b>	In Batch system
AuNP- BTA-Sponge I	LC27112020
AuNP- BTA-Sponge II	LC26112020
AuNP- BTA-Sponge III	LC25112020
<b>Catalytic reaction</b>	Continuous flow mode
AuNP- BTA-Sponge I	LC23032021

#### 10.1.4 The fourth part of work

<b>Ct@AuNP synthesis</b>	
Ct@AuNP	LC01052019
<b>NTA Ligand Synthesis</b>	
1.step	LC05022018
2.step	LC08022018
3.step	LC10022018
4.step	LC16022018
<b>NiNTA-AuNP</b>	
NiNTA-AuNP	LC05102020

## **10.2 Contribution to the figures**

Figure 4.1.13-15 were created by Jun in the frame of collaboration.

Figure 4.1.17-19 were created by Gabriel Sitaru in the frame of collaboration.

Figure 4.2.11-12 and 4.2.14-16 were shared with Markus Drummer in the frame of collaboration.

Figure 4.3.26 Figure 4.3.32 were plotted using data provided by Markus Drummer in the frame of collaboration.

Figure 4.4.1-8 were shared with Julia Dietler in the frame of collaboration.

## 11 Acknowledgements

The completion of this thesis is not possible without the direct and indirect support and help from many people. First of all, I am truly grateful to the most important person in the journey of my PhD: Prof. Dr. Andreas Greiner. I want to thank Prof. Greiner for taking me under his wings and always being very supportive and friendly. His encouragement has helped me countless times when I was facing difficulties in projects. He trained me well both to think systematically within the projects and to think out of the projects to find my own research path. When it comes to performing lab work and writing manuscripts, insightful feedback from Prof. Greiner has always come in time. Besides, Prof. Greiner also helped me to become more confident. There have of course been many ups and downs during this journey of PhD, and I feel lucky and thankful to always being supported and trusted by Prof. Greiner.

I would like to thank Prof. Dr. Agarwal for helping and supporting me numerous times during my PhD. The discussions between Prof. Agarwal and me have always been very educational and inspiring. Her dedication to take care all students in MC II group is very appreciated.

I would like also to thank Prof. Dr. Hans-Werner Schmidt, Prof. Dr. Andreas Möglich, Dr. Julia Dietler and Markus Drummer for our collaboration. It feels so nice to work with all of you and I learned a lot about protein and self-assembly BTA supramolecule from you. Special thanks go to Markus Drummer for your contribution to the AuNP separation work. We had lots of interesting scientific discussions and the teamwork was very enjoyable. Furthermore, I want to thank Prof. Dr. Stephan Gekle and Gabriel Sitaru for taking care of simulation part in my first work. Besides, I am grateful to Prof. Dr. Il-Doo Kim and Dr. Jun Young Cheong for taking care of the HR-TEM analysis in my first work. A special thanks goes to Prof. Dr. Anna Schenk and Dr. Sabina Rosenfeldt for the SAXS measurement, the scientific discussions, and contributions to my work.

I want to say thank you to Ann-Kathrin Müller for all the support in AF4 measurements. I am also thankful for all kinds of guidance and great support in TEM received from Dr. Markus Drechsler, Carmen Kunert, Dr. Ulrich Mansfeld. Also, I would like to thank Martina Heider and Dr. Ulrich Mansfeld for the kind instruction and help in SEM. In addition, I would like to thank Dr. Yu Zhong for the XPS measurements. The XPS/UPS facility

(PHI 5000 VersaProbe III system) in the Keylab Device Engineering at the Bavarian Polymer Institute at University of Bayreuth is greatly acknowledged. I'm also grateful to Christian Hils and Carmen Kunert for the help in performing ICP-OES analysis, and to Rika Schneider for GPC analysis.

It's needless to say that I owe a great deal to current and former members of the MCII Group. Thank you Dr. Pin Hu, Lothar Benker, Dr. Jian Zhu for helping me getting both my life and science started in Bayreuth. You were so kind to give a hand and cheer me up all the time. Cheers to Ann-Kathrin Müller, Felix Bretschneider, Nikola Majstorovic, Qiang Gao, Dr. Xiaojian Liao for all the nice scientific and non-scientific discussions and inspiration in the office and in the lab. My gratitude of course also goes to all nice people at the department for creating such a lovely working environment. thank you for making research life smooth and help me a lot. I would also like to thank all nice colleagues in the MC 2 group. I learn a lot from and enjoyed myself in our group.

Last but not least, I would like to thank all my friends for the laughter and shoulders to cry on. The friends that grew up together with me, my dear friends in Shanghai, the old Heidelberg crew and the even older but very active Göttingen gang, you are all greatly appreciated. Of course it goes without saying that I owe a great deal to my loving and supporting family. Thank you my dearest parents for believing in me and supporting me for all these years.

## 12 List of Publications

[1] Dietler, J.\*; **Liang, C.\***; Frank, S.; Müller A-K.; Greiner, A.; Möglich, A. Photobiologically directed assembly of gold nanoparticles. *Adv. Biology*, **2021**, *5*, 2000179.

\*Shared first authorship.

[2] Drummer, M.\*; **Liang, C.\***; Kreger, K.; Rosenfeldt, S.; Greiner, A.; Schmidt, H.W. Stable mesoscale nonwovens of electrospun polyacrylonitrile and interpenetrating supramolecular 1,3,5-benzotriazine fibers as efficient carrier for gold nanoparticles. *ACS. Appl. Mater. Interfaces*. **2021**, *13* (29), 34818-34828. \*Shared first authorship.

[3] **Liang, C.**; Cheong, J. Y.; Sitaru, G.; Rosenfeldt, S.; Schenk, A. S.; Gekle, S.; Kim, I. D.; Greiner, A. Size-Dependent Catalytic Behavior of Gold Nanoparticles. *Adv. Mater. Interfaces* **2021**, 2100867.

## 13 Reference

1. Louis, C.; Pluchery, O. *Gold nanoparticles for physics, chemistry and biology*. Imperial College Press: London, 2012.
2. Daniel, M. C.; Astruc, D. Gold nanoparticles: assembly, supramolecular chemistry, quantum-size-related properties, and applications toward biology, catalysis, and nanotechnology. *Chem. Rev.* **2004**, *104* (1), 293-346.
3. Das, M.; Shim, K. H.; An, S. S. A.; Yi, D. K. Review on gold nanoparticles and their applications. *Toxicol. Environ. Health Sci.* **2011**, *3* (4), 193-205.
4. Hutchings, G. J.; Brust, M.; Schmidbaur, H. Gold - an introductory perspective. *Chem. Soc. Rev.* **2008**, *37* (9), 1759-1765.
5. Stratakis, M.; Garcia, H. Catalysis by supported gold nanoparticles: beyond aerobic oxidative processes. *Chem. Rev.* **2012**, *112* (8), 4469-4506.
6. Pan, Y.; Neuss, S.; Leifert, A.; Fischler, M.; Wen, F.; Simon, U.; Schmid, G.; Brandau, W.; Jahnke-Dechent, W. Size-dependent cytotoxicity of gold nanoparticles. *Small* **2007**, *3* (11), 1941-1949.
7. Bansal, S. A.; Kumar, V.; Karimi, J.; Singh, A. P.; Kumar, S. Role of gold nanoparticles in advanced biomedical applications. *Nanoscale Adv.* **2020**, *2* (9), 3764-3787.
8. Boisselier, E.; Astruc, D. Gold nanoparticles in nanomedicine: preparations, imaging, diagnostics, therapies and toxicity. *Chem. Soc. Rev.* **2009**, *38* (6), 1759-1782.
9. Sonawane, A.; Mujawar, M. A.; Manickam, P.; Bhansali, S. Plasma-Induced Enhancement in Electronic Properties of Gold Nanoparticles: Application in Electrochemical Biosensing of Cortisol. *ACS Appl. Electron. Mater.* **2021**, *3* (1), 230-237.
10. Homberger, M.; Simon, U. On the application potential of gold nanoparticles in nanoelectronics and biomedicine. *Philos. Trans. R. Soc. A* **2010**, *368* (1915), 1405-1453.
11. Venditti, I. Gold Nanoparticles in Photonic Crystals Applications: A Review. *Materials* **2017**, *10* (2), 97.
12. Kim, H. J.; Hossen, M. M.; Hillier, A. C.; Vaknin, D.; Mallapragada, S. K.; Wang, W. J. Interfacial and Bulk Assembly of Anisotropic Gold Nanostructures: Implications for Photonics and Plasmonics. *ACS Appl. Nano Mater.* **2020**, *3* (8), 8216-8223.

13. Zeng, C.; Qian, H.; Li, T.; Li, G.; Rosi, N. L.; Yoon, B.; Barnett, R. N.; Whetten, R. L.; Landman, U.; Jin, R. Total structure and electronic properties of the gold nanocrystal Au<sub>36</sub>(SR)<sub>24</sub>. *Angew. Chem. Int. Ed. Engl.* **2012**, *51* (52), 13114-13118.
14. Shan, J.; Tenhu, H. Recent advances in polymer protected gold nanoparticles: synthesis, properties and applications. *Chem. Commun.* **2007**, (44), 4580-4598.
15. Armao IV, J. J.; Nyrkova, I.; Fuks, G.; Osypenko, A.; Maaloum, M.; Moulin, E.; Arenal, R.; Gavati, O.; Semenov, A.; Giuseppone, N. Anisotropic self-assembly of supramolecular polymers and plasmonic nanoparticles at the liquid–liquid interface. *J. Am. Chem. Soc.* **2017**, *139* (6), 2345-2350.
16. Krieg, E.; Weissman, H.; Shirman, E.; Shimoni, E.; Rybtchinski, B. A recyclable supramolecular membrane for size-selective separation of nanoparticles. *Nat. Nanotechnol.* **2011**, *6* (3), 141-146.
17. Xue, J.; Xie, J.; Liu, W.; Xia, Y. Electrospun nanofibers: new concepts, materials, and applications. *Acc. Chem. Res.* **2017**, *50* (8), 1976-1987.
18. Kumar, P. S.; Sundaramurthy, J.; Sundarrajan, S.; Babu, V. J.; Singh, G.; Allakhverdiev, S. I.; Ramakrishna, S. Hierarchical electrospun nanofibers for energy harvesting, production and environmental remediation. *Energy Environ. Sci.* **2014**, *7* (10), 3192-3222.
19. Sill, T. J.; Von Recum, H. A. Electrospinning: applications in drug delivery and tissue engineering. *Biomaterials* **2008**, *29* (13), 1989-2006.
20. Huang, C.; Soenen, S. J.; Rejman, J.; Lucas, B.; Braeckmans, K.; Demeester, J.; De Smedt, S. C. Stimuli-responsive electrospun fibers and their applications. *Chem. Soc. Rev.* **2011**, *40* (5), 2417-2434.
21. Langner, M.; Greiner, A. Wet-Laid Meets Electrospinning: Nonwovens for Filtration Applications from Short Electrospun Polymer Nanofiber Dispersions. *Macromol. Rapid Commun.* **2016**, *37* (4), 351-355.
22. Ofir, Y.; Samanta, B.; Rotello, V. M. Polymer and biopolymer mediated self-assembly of gold nanoparticles. *Chem. Soc. Rev.* **2008**, *37* (9), 1814-1825.
23. Lin, Q.-Y.; Mason, J. A.; Li, Z.; Zhou, W.; O'Brien, M. N.; Brown, K. A.; Jones, M. R.; Butun, S.; Lee, B.; Dravid, V. P. Building superlattices from individual nanoparticles via template-confined DNA-mediated assembly. *Science* **2018**, *359* (6376), 669-672.

24. Köhn Serrano, M. S.; König, T. A.; Haataja, J. S.; Löbbling, T. I.; Schmalz, H.; Agarwal, S.; Fery, A.; Greiner, A. Self-Organization of Gold Nanoparticle Assemblies with 3D Spatial Order and Their External Stimuli Responsiveness. *Macromol. Rapid Commun.* **2016**, *37* (3), 215-220.
25. Zhang, L.; Dai, L.; Rong, Y.; Liu, Z.; Tong, D.; Huang, Y.; Chen, T. Light-triggered reversible self-assembly of gold nanoparticle oligomers for tunable SERS. *Langmuir* **2015**, *31* (3), 1164-1171.
26. Kundu, P. K.; Samanta, D.; Leizrowice, R.; Margulis, B.; Zhao, H.; Börner, M.; Udayabhaskararao, T.; Manna, D.; Klajn, R. Light-controlled self-assembly of non-photoresponsive nanoparticles. *Nat. Chem.* **2015**, *7* (8), 646-652.
27. Kim, J.-Y.; Yeom, J.; Zhao, G.; Calcaterra, H.; Munn, J.; Zhang, P.; Kotov, N. Assembly of gold nanoparticles into chiral superstructures driven by circularly polarized light. *J. Am. Chem. Soc.* **2019**, *141* (30), 11739-11744.
28. Wang, Q.; Li, D.; Xiao, J.; Guo, F.; Qi, L. Reversible self-assembly of gold nanorods mediated by photoswitchable molecular adsorption. *Nano Res.* **2019**, *12* (7), 1563-1569.
29. Jaquay, E.; Martínez, L. J.; Huang, N.; Mejia, C. A.; Sarkar, D.; Povinelli, M. L. Light-assisted, templated self-assembly of gold nanoparticle chains. *Nano letters* **2014**, *14* (9), 5184-5188.
30. Njoki, P. N.; Lim, I. I. S.; Mott, D.; Park, H. Y.; Khan, B.; Mishra, S.; Sujakumar, R.; Luo, J.; Zhong, C. J. Size correlation of optical and spectroscopic properties for gold nanoparticles. *J. Phys. Chem. C* **2007**, *111* (40), 14664-14669.
31. Yeh, Y. C.; Czeran, B.; Rotello, V. M. Gold nanoparticles: preparation, properties, and applications in bionanotechnology. *Nanoscale* **2012**, *4* (6), 1871-1880.
32. Amendola, V.; Pilot, R.; Frascioni, M.; Marago, O. M.; Iati, M. A. Surface plasmon resonance in gold nanoparticles: a review. *J. Phys. Condens. Matter* **2017**, *29* (20), 203002.
33. Ghosh, S. K.; Pal, T. Interparticle coupling effect on the surface plasmon resonance of gold nanoparticles: from theory to applications. *Chem. Rev.* **2007**, *107* (11), 4797-4862.
34. Myroshnychenko, V.; Rodriguez-Fernandez, J.; Pastoriza-Santos, I.; Funston, A. M.; Novo, C.; Mulvaney, P.; Liz-Marzan, L. M.; Garcia de Abajo, F. J. Modelling the optical response of gold nanoparticles. *Chem. Soc. Rev.* **2008**, *37* (9), 1792-1805.

35. Fuller, M. A.; Koper, I. Biomedical applications of polyelectrolyte coated spherical gold nanoparticles. *Nano Converg.* **2019**, *6* (1), 1-10.
36. Polte, J. Fundamental growth principles of colloidal metal nanoparticles - a new perspective. *Crystengcomm* **2015**, *17* (36), 6809-6830.
37. Afrooz, A. R.; Sivalapalan, S. T.; Murphy, C. J.; Hussain, S. M.; Schlager, J. J.; Saleh, N. B. Spheres vs. rods: the shape of gold nanoparticles influences aggregation and deposition behavior. *Chemosphere* **2013**, *91* (1), 93-98.
38. Nel, A.; Xia, T.; Madler, L.; Li, N. Toxic potential of materials at the nanolevel. *Science* **2006**, *311* (5761), 622-627.
39. Limbach, L. K.; Wick, P.; Manser, P.; Grass, R. N.; Bruinink, A.; Stark, W. J. Exposure of engineered nanoparticles to human lung epithelial cells: influence of chemical composition and catalytic activity on oxidative stress. *Environ. Sci. Technol.* **2007**, *41* (11), 4158-4163.
40. Mulvihill, M. J.; Habas, S. E.; Jen-La Plante, H.; Wan, J. M.; Mokari, T. Influence of Size, Shape, and Surface Coating on the Stability of Aqueous Suspensions of CdSe Nanoparticles. *Chem. Mater.* **2010**, *22* (18), 5251-5257.
41. Zhou, D.; Ji, Z.; Jiang, X.; Dunphy, D. R.; Brinker, J.; Keller, A. A. Influence of material properties on TiO<sub>2</sub> nanoparticle agglomeration. *PloS one* **2013**, *8* (11), e81239.
42. Liu, J.; Legros, S.; Ma, G.; Veinot, J. G.; von der Kammer, F.; Hofmann, T. Influence of surface functionalization and particle size on the aggregation kinetics of engineered nanoparticles. *Chemosphere* **2012**, *87* (8), 918-924.
43. Turkevich, J.; Stevenson, P. C.; Hillier, J. A study of the nucleation and growth processes in the synthesis of colloidal gold. *Discuss. Faraday Soc.* **1951**, *11*, 55-75.
44. Gambinossi, F.; Mylon, S. E.; Ferri, J. K. Aggregation kinetics and colloidal stability of functionalized nanoparticles. *Adv. Colloid Interface Sci.* **2015**, *222*, 332-349.
45. Faraday, M. The Bakerian Lecture.—Experimental relations of gold (and other metals) to light. *Philos. Trans. R. Soc.* **1857**, (147), 145-181.
46. Zhao, P. X.; Li, N.; Astruc, D. State of the art in gold nanoparticle synthesis. *Coord. Chem. Rev.* **2013**, *257* (3-4), 638-665.
47. Herizchi, R.; Abbasi, E.; Milani, M.; Akbarzadeh, A. Current methods for synthesis of gold nanoparticles. *Artif. Cells Nanomed. Biotechnol.* **2016**, *44* (2), 596-602.

48. De Souza, C. D.; Nogueira, B. R.; Rostelato, M. E. C. M. Compounds, Review of the methodologies used in the synthesis gold nanoparticles by chemical reduction. *J. Alloys Compd.* **2019**, *798*, 714-740.
49. Frens, G. Controlled nucleation for the regulation of the particle size in monodisperse gold suspensions. *Nat. Phys. Sci.* **1973**, *241* (105), 20-22.
50. Kumar, S.; Gandhi, K. S.; Kumar, R. Modeling of formation of gold nanoparticles by citrate method. *Ind. Eng. Chem. Res.* **2007**, *46* (10), 3128-3136.
51. Thanh, N. T.; Maclean, N.; Mahiddine, S. Mechanisms of nucleation and growth of nanoparticles in solution. *Chem. Rev.* **2014**, *114* (15), 7610-7630.
52. Lopez-Sanchez, J. A.; Dimitratos, N.; Hammond, C.; Brett, G. L.; Kesavan, L.; White, S.; Miedziak, P.; Tiruvalam, R.; Jenkins, R. L.; Carley, A. F.; Knight, D.; Kiely, C. J.; Hutchings, G. J. Facile removal of stabilizer-ligands from supported gold nanoparticles. *Nat. Chem.* **2011**, *3* (7), 551-556.
53. Kimling, J.; Maier, M.; Okenve, B.; Kotaidis, V.; Ballot, H.; Plech, A. Turkevich method for gold nanoparticle synthesis revisited. *J. Phys. Chem. B* **2006**, *110* (32), 15700-15707.
54. Ji, X.; Song, X.; Li, J.; Bai, Y.; Yang, W.; Peng, X. Size control of gold nanocrystals in citrate reduction: the third role of citrate. *J. Am. Chem. Soc.* **2007**, *129* (45), 13939-13948.
55. Yao, T.; Sun, Z. H.; Li, Y. Y.; Pan, Z. Y.; Wei, H.; Xie, Y.; Nomura, M.; Niwa, Y.; Yan, W. S.; Wu, Z. Y.; Jiang, Y.; Liu, Q. H.; Wei, S. Q. Insights into Initial Kinetic Nucleation of Gold Nanocrystals. *J. Am. Chem. Soc.* **2010**, *132* (22), 7696-7701.
56. Pong, B. K.; Elim, H. I.; Chong, J. X.; Ji, W.; Trout, B. L.; Lee, J. Y. New insights on the nanoparticle growth mechanism in the citrate reduction of Gold(III) salt: Formation of the au nanowire intermediate and its nonlinear optical properties. *J. Phys. Chem. C* **2007**, *111* (17), 6281-6287.
57. Mondloch, J. E.; Bayram, E.; Finke, R. G. A review of the kinetics and mechanisms of formation of supported-nanoparticle heterogeneous catalysts. *J. Mol. Catal. A: Chem.* **2012**, *355*, 1-38.
58. Polte, J.; Ahner, T. T.; Delissen, F.; Sokolov, S.; Emmerling, F.; Thunemann, A. F.; Kraehnert, R. Mechanism of gold nanoparticle formation in the classical citrate synthesis method derived from coupled in situ XANES and SAXS evaluation. *J. Am. Chem. Soc.* **2010**, *132* (4), 1296-1301.

59. Polte, J.; Erler, R.; Thunemann, A. F.; Sokolov, S.; Ahner, T. T.; Rademann, K.; Emmerling, F.; Kraehnert, R. Nucleation and Growth of Gold Nanoparticles Studied via in situ Small Angle X-ray Scattering at Millisecond Time Resolution. *ACS Nano* **2010**, *4* (2), 1076-1082.
60. Polte, J.; Herder, M.; Erler, R.; Rolf, S.; Fischer, A.; Wurth, C.; Thunemann, A. F.; Kraehnert, R.; Emmerling, F. Mechanistic insights into seeded growth processes of gold nanoparticles. *Nanoscale* **2010**, *2* (11), 2463-2469.
61. Madras, G.; McCoy, B. J. Ostwald ripening with size-dependent rates: Similarity and power-law solutions. *J. Chem. Phys.* **2002**, *117* (17), 8042-8049.
62. Mandal, M.; Ghosh, S. K.; Kundu, S.; Esumi, K.; Pal, T. UV photoactivation for size and shape controlled synthesis and coalescence of gold nanoparticles in micelles. *Langmuir* **2002**, *18* (21), 7792-7797.
63. Brust, M.; Schiffrin, D. J.; Bethell, D.; Kiely, C. J. Novel gold-dithiol nano-networks with non-metallic electronic properties. *Adv. Mater.* **1995**, *7* (9), 795-797.
64. Perala, S. R.; Kumar, S. On the mechanism of metal nanoparticle synthesis in the Brust-Schiffrin method. *Langmuir* **2013**, *29* (31), 9863-9873.
65. Li, Y.; Zaluzhna, O.; Xu, B.; Gao, Y.; Modest, J. M.; Tong, Y. J. Mechanistic insights into the Brust-Schiffrin two-phase synthesis of organo-chalcogenate-protected metal nanoparticles. *J. Am. Chem. Soc.* **2011**, *133* (7), 2092-2095.
66. Bastus, N. G.; Comenge, J.; Puntès, V. Kinetically controlled seeded growth synthesis of citrate-stabilized gold nanoparticles of up to 200 nm: size focusing versus Ostwald ripening. *Langmuir* **2011**, *27* (17), 11098-11105.
67. Perrault, S. D.; Chan, W. C. Synthesis and surface modification of highly monodispersed, spherical gold nanoparticles of 50-200 nm. *J. Am. Chem. Soc.* **2009**, *131* (47), 17042-17043.
68. Brown, K. R.; Natan, M. J. Hydroxylamine seeding of colloidal Au nanoparticles in solution and on surfaces. *Langmuir* **1998**, *14* (4), 726-728.
69. Brown, K. R.; Lyon, L. A.; Fox, A. P.; Reiss, B. D.; Natan, M. J. Hydroxylamine seeding of colloidal Au nanoparticles. 3. Controlled formation of conductive Au films. *Chem. Mater.* **2000**, *12* (2), 314-323.
70. Narayanan, K. B.; Sakthivel, N. Phytosynthesis of gold nanoparticles using leaf extract of *Coleus amboinicus* Lour. *Mater. Charact.* **2010**, *61* (11), 1232-1238.

71. Narayanan, K. B.; Sakthivel, N. Biological synthesis of metal nanoparticles by microbes. *Adv. Colloid Interface Sci.* **2010**, *156* (1-2), 1-13.
72. Kamran, U.; Bhatti, H. N.; Iqbal, M.; Nazir, A. Green Synthesis of Metal Nanoparticles and their Applications in Different Fields: A Review. *Z. Phys. Chem.* **2019**, *233* (9), 1325-1349.
73. Su, S.; Zuo, X.; Pan, D.; Pei, H.; Wang, L.; Fan, C.; Huang, W. Design and applications of gold nanoparticle conjugates by exploiting biomolecule-gold nanoparticle interactions. *Nanoscale* **2013**, *5* (7), 2589-2599.
74. Mahato, K.; Nagpal, S.; Shah, M. A.; Srivastava, A.; Maurya, P. K.; Roy, S.; Jaiswal, A.; Singh, R.; Chandra, P. Gold nanoparticle surface engineering strategies and their applications in biomedicine and diagnostics. *3 Biotech* **2019**, *9* (2), 57.
75. Helcher, H. H. *Aurum Potabile, oder Gold-Tinctur*. 1718.
76. Mandal, T. K.; Fleming, M. S.; Walt, D. R. Preparation of polymer coated gold nanoparticles by surface-confined living radical polymerization at ambient temperature. *Nano Lett.* **2002**, *2* (1), 3-7.
77. Li, D. X.; He, Q.; Cui, Y.; Li, J. B. Fabrication of pH-responsive nanocomposites of gold nanoparticles/poly(4-vinylpyridine). *Chem. Mater.* **2007**, *19* (3), 412-417.
78. Shan, J.; Nuopponen, M.; Jiang, H.; Viitala, T.; Kauppinen, E.; Kontturi, K.; Tenhu, H. Amphiphilic gold nanoparticles grafted with poly(N-isopropylacrylamide) and polystyrene. *Macromolecules* **2005**, *38* (7), 2918-2926.
79. Krüger, C.; Agarwal, S.; Greiner, A. Stoichiometric functionalization of gold nanoparticles in solution through a free radical polymerization approach. *J. Am. Chem. Soc.* **2008**, *130* (9), 2710-2711.
80. Gao, J.; Huang, X.; Liu, H.; Zan, F.; Ren, J. Colloidal stability of gold nanoparticles modified with thiol compounds: bioconjugation and application in cancer cell imaging. *Langmuir* **2012**, *28* (9), 4464-4471.
81. Zhang, X.; Servos, M. R.; Liu, J. Ultrahigh nanoparticle stability against salt, pH, and solvent with retained surface accessibility via depletion stabilization. *J. Am. Chem. Soc.* **2012**, *134* (24), 9910-9913.
82. Ivanov, M. R.; Bednar, H. R.; Haes, A. J. Investigations of the mechanism of gold nanoparticle stability and surface functionalization in capillary electrophoresis. *ACS Nano* **2009**, *3* (2), 386-394.

83. Ong, Q.; Luo, Z.; Stellacci, F. Characterization of Ligand Shell for Mixed-Ligand Coated Gold Nanoparticles. *Acc. Chem. Res.* **2017**, *50* (8), 1911-1919.
84. Chen, Y.; Xianyu, Y.; Jiang, X. Surface Modification of Gold Nanoparticles with Small Molecules for Biochemical Analysis. *Acc. Chem. Res.* **2017**, *50* (2), 310-319.
85. Dreaden, E. C.; Alkilany, A. M.; Huang, X.; Murphy, C. J.; El-Sayed, M. A. The golden age: gold nanoparticles for biomedicine. *Chem. Soc. Rev.* **2012**, *41* (7), 2740-2779.
86. Caragheorghopol, A.; Chechik, V. Mechanistic aspects of ligand exchange in Au nanoparticles. *Phys. Chem. Chem. Phys.* **2008**, *10* (33), 5029-5041.
87. Jazayeri, M. H.; Amani, H.; Pourfatollah, A. A.; Pazoki-Toroudi, H.; Sedighimoghaddam, B. Various methods of gold nanoparticles (GNPs) conjugation to antibodies. *Sens. Biosensing Res.* **2016**, *9*, 17-22.
88. Sapsford, K. E.; Algar, W. R.; Berti, L.; Gemmill, K. B.; Casey, B. J.; Oh, E.; Stewart, M. H.; Medintz, I. L. Functionalizing Nanoparticles with Biological Molecules: Developing Chemistries that Facilitate Nanotechnology. *Chem. Rev.* **2013**, *113* (3), 1904-2074.
89. Li, F.; Lu, J.; Kong, X.; Hyeon, T.; Ling, D. Dynamic Nanoparticle Assemblies for Biomedical Applications. *Adv. Mater.* **2017**, *29* (14), 1605897.
90. Ozbay, E. Plasmonics: Merging photonics and electronics at nanoscale dimensions. *Science* **2006**, *311* (5758), 189-193.
91. Saha, K.; Agasti, S. S.; Kim, C.; Li, X.; Rotello, V. M. Gold nanoparticles in chemical and biological sensing. *Chem. Rev.* **2012**, *112* (5), 2739-2779.
92. Zhang, Q.; Xu, T. Y.; Zhao, C. X.; Jin, W. H.; Wang, Q.; Qu, D. H. Dynamic Self-Assembly of Gold/Polymer Nanocomposites: pH-Encoded Switching between 1D Nanowires and 3D Nanosponges. *Chem. Asian J.* **2017**, *12* (19), 2549-2553.
93. Sun, C.; Lee, J. S.; Zhang, M. Magnetic nanoparticles in MR imaging and drug delivery. *Adv. Drug Deliv. Rev.* **2008**, *60* (11), 1252-1265.
94. Grzelczak, M.; Liz-Marzán, L. M.; Klajn, R. Stimuli-responsive self-assembly of nanoparticles. *Chem. Soc. Rev.* **2019**, *48* (5), 1342-1361.
95. Cheng, Y.; Dong, J.; Li, X. Light-Switchable Self-Assembly of Non-Photoresponsive Gold Nanoparticles. *Langmuir* **2018**, *34* (21), 6117-6124.
96. Klajn, R. Spiropyran-based dynamic materials. *Chem. Soc. Rev.* **2014**, *43* (1), 148-184.

97. Klajn, R.; Stoddart, J. F.; Grzybowski, B. A. Nanoparticles functionalised with reversible molecular and supramolecular switches. *Chem. Soc. Rev.* **2010**, *39* (6), 2203-2237.
98. Klajn, R. Immobilized azobenzenes for the construction of photoresponsive materials. *Pure and Appl. Chem.* **2010**, *82* (12), 2247-2279.
99. Grzybowski, B. A.; Fitzner, K.; Paczesny, J.; Granick, S. From dynamic self-assembly to networked chemical systems. *Chem. Soc. Rev.* **2017**, *46* (18), 5647-5678.
100. Kohntopp, A.; Dabrowski, A.; Malicki, M.; Temps, F. Photoisomerisation and ligand-controlled reversible aggregation of azobenzene-functionalised gold nanoparticles. *Chem. Commun.* **2014**, *50* (70), 10105-10107.
101. Shiraishi, Y.; Shirakawa, E.; Tanaka, K.; Sakamoto, H.; Ichikawa, S.; Hirai, T. Spiropyran-modified gold nanoparticles: reversible size control of aggregates by UV and visible light irradiations. *ACS Appl. Mater. Interfaces* **2014**, *6* (10), 7554-7562.
102. Bell, N. S.; Piech, M. Photophysical Effects between Spirobenzopyran– Methyl methacrylate-Functionalized Colloidal Particles. *Langmuir* **2006**, *22* (4), 1420-1427.
103. Du, Y.; Sheng, H.; Astruc, D.; Zhu, M. Atomically precise noble metal nanoclusters as efficient catalysts: A bridge between structure and properties. *Chem. Rev.* **2019**, *120* (2), 526-622.
104. Corma, A.; Garcia, H. Supported gold nanoparticles as catalysts for organic reactions. *Chem. Soc. Rev.* **2008**, *37* (9), 2096-2126.
105. Zhang, Y.; Cui, X.; Shi, F.; Deng, Y. Nano-gold catalysis in fine chemical synthesis. *Chem. Rev.* **2012**, *112* (4), 2467-2505.
106. Ishida, T.; Murayama, T.; Taketoshi, A.; Haruta, M. Importance of Size and Contact Structure of Gold Nanoparticles for the Genesis of Unique Catalytic Processes. *Chem. Rev.* **2020**, *120* (2), 464-525.
107. Wunder, S.; Polzer, F.; Lu, Y.; Mei, Y.; Ballauff, M. Kinetic Analysis of Catalytic Reduction of 4-Nitrophenol by Metallic Nanoparticles Immobilized in Spherical Polyelectrolyte Brushes. *J. Phys. Chem. C* **2010**, *114* (19), 8814-8820.
108. Zhao, P. X.; Feng, X. W.; Huang, D. S.; Yang, G. Y.; Astruc, D. Basic concepts and recent advances in nitrophenol reduction by gold- and other transition metal nanoparticles. *Coord. Chem. Rev.* **2015**, *287*, 114-136.
109. Pradhan, N.; Pal, A.; Pal, T. Catalytic reduction of aromatic nitro compounds by coinage metal nanoparticles. *Langmuir* **2001**, *17* (5), 1800-1802.

110. Noh, J.; Meijboom, R. Reduction of 4-nitrophenol as a model reaction for nanocatalysis. in *Application of Nanotechnology in water research* **2014**, 333-405.
111. Herves, P.; Perez-Lorenzo, M.; Liz-Marzan, L. M.; Dzubiella, J.; Lu, Y.; Ballauff, M. Catalysis by metallic nanoparticles in aqueous solution: model reactions. *Chem. Soc. Rev.* **2012**, *41* (17), 5577-5587.
112. Wunder, S.; Lu, Y.; Albrecht, M.; Ballauff, M. Catalytic Activity of Faceted Gold Nanoparticles Studied by a Model Reaction: Evidence for Substrate-Induced Surface Restructuring. *ACS Catal.* **2011**, *1* (8), 908-916.
113. Menumarov, E.; Hughes, R. A.; Neretina, S. Catalytic Reduction of 4-Nitrophenol: A Quantitative Assessment of the Role of Dissolved Oxygen in Determining the Induction Time. *Nano Lett.* **2016**, *16* (12), 7791-7797.
114. Strachan, J.; Barnett, C.; Masters, A. F.; Maschmeyer, T. 4-Nitrophenol Reduction: Probing the Putative Mechanism of the Model Reaction. *ACS Catal.* **2020**, *10* (10), 5516-5521.
115. Gu, S.; Wunder, S.; Lu, Y.; Ballauff, M.; Fenger, R.; Rademann, K.; Jaquet, B.; Zaccone, A. Kinetic Analysis of the Catalytic Reduction of 4-Nitrophenol by Metallic Nanoparticles. *J. Phys. Chem. C* **2014**, *118* (32), 18618-18625.
116. Ma, T.; Yang, W. S.; Liu, S. M.; Zhang, H. J.; Liang, F. A Comparison Reduction of 4-Nitrophenol by Gold Nanospheres and Gold Nanostars. *Catalysts* **2017**, *7* (2), 38.
117. Ni, B.; Wang, X. Face the Edges: Catalytic Active Sites of Nanomaterials. *Adv. Sci.* **2015**, *2* (7), 1500085.
118. Mikami, Y.; Dhakshinamoorthy, A.; Alvaro, M.; Garcia, H. Catalytic activity of unsupported gold nanoparticles. *Catal. Sci. Technol.* **2013**, *3* (1), 58-69.
119. Shifrina, Z. B.; Matveeva, V. G.; Bronstein, L. M. Role of Polymer Structures in Catalysis by Transition Metal and Metal Oxide Nanoparticle Composites. *Chem. Rev.* **2020**, *120* (2), 1350-1396.
120. Xue, J.; Wu, T.; Dai, Y.; Xia, Y. Electrospinning and Electrospun Nanofibers: Methods, Materials, and Applications. *Chem. Rev.* **2019**, *119* (8), 5298-5415.
121. Greiner, A.; Wendorff, J. H. Electrospinning: a fascinating method for the preparation of ultrathin fibers. *Angew. Chem. Int. Ed.* **2007**, *46* (30), 5670-5703.
122. Reneker, D. H.; Fong, H. *Polymeric nanofibers*. *ACS Symp. Ser.* **2006**, *918*, 1-6.

123. Huang, Z. M.; Zhang, Y. Z.; Kotaki, M.; Ramakrishna, S. A review on polymer nanofibers by electrospinning and their applications in nanocomposites. *Compos. Sci. Technol.* **2003**, *63* (15), 2223-2253.
124. Bognitzki, M.; Czado, W.; Frese, T.; Schaper, A.; Hellwig, M.; Steinhart, M.; Greiner, A.; Wendorff, J. H. Nanostructured fibers via electrospinning. *Adv. Mater.* **2001**, *13* (1), 70-72.
125. Zhang, C. L.; Yu, S. H. Nanoparticles meet electrospinning: recent advances and future prospects. *Chem. Soc. Rev.* **2014**, *43* (13), 4423-4448.
126. Yang, G.; Li, X.; He, Y.; Ma, J.; Ni, G.; Zhou, S. From nano to micro to macro: Electrospun hierarchically structured polymeric fibers for biomedical applications. *Prog. Polym. Sci.* **2018**, *81*, 80-113.
127. Russell, S. J. *Handbook of nonwovens*. Woodhead Publishing: 2006.
128. Latifi, M.; Tafreshi, H. V.; Pourdeyhimi, B. A note on an optical method to evaluate fiber dispersion in wet-laid nonwoven process. *Text. Res. J.* **2008**, *78* (6), 518-523.
129. Das, D.; Butola, B. S.; Renuka, S. An Investigation into Fiber Dispersion Behavior in Water with Reference to Wet-Lay Nonwoven Technology. *J. Dispers. Sci. Technol.* **2012**, *33* (8), 1225-1232.
130. Yi, W.; Huaiyu, Z.; Jian, H.; Yun, L.; Shushu, Z. Wet-laid non-woven fabric for separator of lithium-ion battery. *J. Power Sources.* **2009**, *189* (1), 616-619.
131. Yeole, P.; Ning, H. B.; Hassen, A. A.; Vaidya, U. K. The Effect of Flocculent, Dispersants, and Binder on Wet-laid Process for Recycled Glass Fiber/PA6 Composite. *Polym. Polym. Compos.* **2018**, *26* (3), 259-269.
132. Ghossein, H.; Hassen, A. A.; Paquit, V.; Love, L. J.; Vaidya, U. K. Innovative Method for Enhancing Carbon Fibers Dispersion in Wet-Laid Nonwovens. *Mater. Today Commun.* **2018**, *17*, 100-108.
133. Ghossein, H.; Hassen, A. A.; Kim, S.; Ault, J.; Vaidya, U. K. Characterization of Mechanical Performance of Composites Fabricated Using Innovative Carbon Fiber Wet Laid Process. *J. Compos. Sci.* **2020**, *4* (3), 124.
134. Pakdel, E.; Kashi, S.; Varley, R.; Wang, X. J. R. Conservation; Recycling, Recent progress in recycling carbon fibre reinforced composites and dry carbon fibre wastes. *Resour. Conserv. Recycl.* **2020**, 105340.

135. Reich, S.; Burgard, M.; Langner, M.; Jiang, S. H.; Wang, X. Q.; Agarwal, S.; Ding, B.; Yu, J. Y.; Greiner, A. Polymer nanofibre composite nonwovens with metal-like electrical conductivity. *Npj Flex. Electron.* **2018**, *2* (1), 1-6.
136. Langner, M.; Greiner, A. Wet-Laid Meets Electrospinning: Nonwovens for Filtration Applications from Short Electrospun Polymer Nanofiber Dispersions. *Macromol. Rapid Commun.* **2016**, *37* (4), 351-355.
137. Duan, G.; Jiang, S.; Jérôme, V.; Wendorff, J. H.; Fathi, A.; Uhm, J.; Altstädt, V.; Herling, M.; Breu, J.; Freitag, R.; Agarwal, S.; Greiner, A. Ultralight, soft polymer sponges by self-assembly of short electrospun fibers in colloidal dispersions. *Adv. Funct. Mater.* **2015**, *25* (19), 2850-2856.
138. Qian, Z. C.; Wang, Z.; Zhao, N.; Xu, J. Aerogels Derived from Polymer Nanofibers and Their Applications. *Macromol. Rapid Commun.* **2018**, *39* (14), 1700724.
139. Jiang, S.; Agarwal, S.; Greiner, A. Low-Density Open Cellular Sponges as Functional Materials. *Angew. Chem. Int. Ed.* **2017**, *56* (49), 15520-15538.
140. Hartlieb, M.; Mansfield, E. D. H.; Perrier, S. A guide to supramolecular polymerizations. *Polym. Chem.* **2020**, *11* (6), 1083-1110.
141. Cantekin, S.; de Greef, T. F.; Palmans, A. R. Benzene-1,3,5-tricarboxamide: a versatile ordering moiety for supramolecular chemistry. *Chem. Soc. Rev.* **2012**, *41* (18), 6125-6137.
142. Curtius, T. Hydrazide und Azide organischer Säuren. XXX. Abhandlung. Bildung von Hydrazihydraziden und Hydraziaziden dreibasischer Säuren. *J. Prakt. Chem.* **1915**, *91* (1), 39-102.
143. Lee, S.; Oh, S.; Lee, J.; Malpani, Y.; Jung, Y. S.; Kang, B.; Lee, J. Y.; Ozasa, K.; Isoshima, T.; Lee, S. Y.; Hara, M.; Hashizume, D.; Kim, J. M. Stimulus-responsive azobenzene supramolecules: fibers, gels, and hollow spheres. *Langmuir* **2013**, *29* (19), 5869-5877.
144. Smulders, M. M.; Schenning, A. P.; Meijer, E. W. Insight into the mechanisms of cooperative self-assembly: The “sergeants-and-soldiers” principle of chiral and achiral C<sub>3</sub>-symmetrical discotic triamides. *J. Am. Chem. Soc.* **2008**, *130* (2), 606-611.
145. Rest, C.; Kandanelli, R.; Fernández, G. Strategies to create hierarchical self-assembled structures via cooperative non-covalent interactions. *Chem. Soc. Rev.* **2015**, *44* (8), 2543-2572.

146. Yashima, E.; Ousaka, N.; Taura, D.; Shimomura, K.; Ikai, T.; Maeda, K. Supramolecular Helical Systems: Helical Assemblies of Small Molecules, Foldamers, and Polymers with Chiral Amplification and Their Functions. *Chem. Rev.* **2016**, *116* (22), 13752-13990.
147. Kulkarni, C.; Meijer, E. W.; Palmans, A. R. A. Cooperativity Scale: A Structure-Mechanism Correlation in the Self-Assembly of Benzene-1,3,5-tricarboxamides. *Acc. Chem. Res.* **2017**, *50* (8), 1928-1936.
148. Krieg, E.; Bastings, M. M.; Besenius, P.; Rybtchinski, B. Supramolecular Polymers in Aqueous Media. *Chem. Rev.* **2016**, *116* (4), 2414-2477.
149. Savyasachi, A. J.; Kotova, O.; Shanmugaraju, S.; Bradberry, S. J.; O'Maille, G. M.; Gunnlaugsson, T. Supramolecular Chemistry: A Toolkit for Soft Functional Materials and Organic Particles. *Chem* **2017**, *3* (5), 764-811.
150. Cantekin, S.; de Greef, T. F.; Palmans, A. R. Benzene-1, 3, 5-tricarboxamide: a versatile ordering moiety for supramolecular chemistry. *Chem. Soc.Rev.* **2012**, *41* (18), 6125-6137.
151. Wang, Y.; Chou, J.; Sun, Y.; Wen, S.; Vasilescu, S.; Zhang, H. Supramolecular-based nanofibers. *Mater. Sci. Eng. C* **2019**, *101*, 650-659.
152. Kluge, D.; Singer, J. C.; Neugirg, B. R.; Neubauer, J. W.; Schmidt, H. W.; Fery, A. Top-down meets bottom-up: A comparison of the mechanical properties of melt electrospun and self-assembled 1,3,5-benzenetrisamide fibers. *Polymer* **2012**, *53* (25), 5754-5759.
153. Bernet, A.; Behr, M.; Schmidt, H. W. Supramolecular nanotube-based fiber mats by self-assembly of a tailored amphiphilic low molecular weight hydrogelator. *Soft Matter* **2011**, *7* (3), 1058-1065.
154. Weiss, D.; Kreger, K.; Schmidt, H. W. Engineering, Self-assembly of alkoxy-substituted 1, 3, 5-benzenetrisamides under controlled conditions. *Macromol. Mater. Eng.* **2017**, *302* (1), 1600390.
155. Misslitz, H.; Kreger, K.; Schmidt, H. W. Supramolecular Nanofiber Webs in Nonwoven Scaffolds as Potential Filter Media. *Small* **2013**, *9* (12), 2053-2058.
156. Panigrahi, S.; Basu, S.; Praharaj, S.; Pande, S.; Jana, S.; Pal, A.; Ghosh, S. K.; Pal, T. Synthesis and size-selective catalysis by supported gold nanoparticles: study on heterogeneous and homogeneous catalytic process. *J. Phys. Chem. C* **2007**, *111* (12), 4596-4605.

157. Fenger, R.; Fertitta, E.; Kirmse, H.; Thünemann, A. F.; Rademann, K. Size dependent catalysis with CTAB-stabilized gold nanoparticles. *Phys. Chem. Chem. Phys.* **2012**, *14* (26), 9343-9349.
158. Sau, T. K.; Pal, A.; Pal, T. Size regime dependent catalysis by gold nanoparticles for the reduction of eosin. *J. Phys. Chem. B* **2001**, *105* (38), 9266-9272.
159. Piella, J.; Merkoçi, F.; Genç, A.; Arbiol, J.; Bastús, N. G.; Puntès, V. Probing the surface reactivity of nanocrystals by the catalytic degradation of organic dyes: the effect of size, surface chemistry and composition. *J. Mater. Chem. A* **2017**, *5* (23), 11917-11929.
160. Liang, C.; Cheong, J. Y.; Sitaru, G.; Rosenfeldt, S.; Schenk, A. S.; Gekle, S.; Kim, I. D.; Greiner, A. Size-Dependent Catalytic Behavior of Gold Nanoparticles. *Adv. Mater. Interfaces* **2021**, 2100867.
161. Avellan, A.; Yun, J.; Zhang, Y.; Spielman-Sun, E.; Unrine, J. M.; Thieme, J.; Li, J.; Lombi, E.; Bland, G.; Lowry, G. V. Nanoparticle size and coating chemistry control foliar uptake pathways, translocation, and leaf-to-rhizosphere transport in wheat. *ACS Nano* **2019**, *13* (5), 5291-5305.
162. Vanzha, E.; Pylaev, T.; Khanadeev, V.; Konnova, S.; Fedorova, V.; Khlebtsov, N. Gold nanoparticle-assisted polymerase chain reaction: effects of surface ligands, nanoparticle shape and material. *RSC adv.* **2016**, *6* (111), 110146-110154.
163. Menon, S. V. G.; Manohar, C.; Rao, K. S. A New Interpretation of the Sticky Hard-Sphere Model. *J. Chem. Phys.* **1991**, *95* (12), 9186-9190.
164. De, S. K.; Mondal, S.; Sen, P.; Pal, U.; Pathak, B.; Bardhan, M.; Bhattacharya, M.; Satpati, B.; De, A.; Senapati, D. Crystal-defect-induced facet-dependent electrocatalytic activity of 3D gold nanoflowers for the selective nanomolar detection of ascorbic acid. *Nanoscale* **2018**, *10* (23), 11091-11102.
165. Xie, C.; Yan, D.; Li, H.; Du, S.; Chen, W.; Wang, Y.; Zou, Y.; Chen, R.; Wang, S. Defect Chemistry in Heterogeneous Catalysis: Recognition, Understanding, and Utilization. *ACS Catal.* **2020**, *10* (19), 11082-11098.
166. Pal, P.; Singha, R. K.; Saha, A.; Bal, R.; Panda, A. B. Defect-induced efficient partial oxidation of methane over nonstoichiometric Ni/CeO<sub>2</sub> nanocrystals. *J. Phys. Chem. C* **2015**, *119* (24), 13610-13618.

167. Ma, Y.; Wang, R.; Wang, H.; Linkov, V.; Ji, S. Evolution of nanoscale amorphous, crystalline and phase-segregated PtNiP nanoparticles and their electrocatalytic effect on methanol oxidation reaction. *Phys. Chem. Chem. Phys.* **2014**, *16* (8), 3593-3602.
168. Goldman, A. J.; Cox, R. G.; Brenner, H. Slow viscous motion of a sphere parallel to a plane wall—I Motion through a quiescent fluid. *Chem. Eng. Sci.* **1967**, *22* (4), 637-651.
169. Daddi-Moussa-Ider, A.; Guckenberger, A.; Gekle, S. Long-lived anomalous thermal diffusion induced by elastic cell membranes on nearby particles. *Phys. Rev. E* **2016**, *93* (1), 012612.
170. Smith, A. M.; Marbella, L. E.; Johnston, K. A.; Hartmann, M. J.; Crawford, S. E.; Kozycz, L. M.; Seferos, D. S.; Millstone, J. E. Quantitative analysis of thiolated ligand exchange on gold nanoparticles monitored by <sup>1</sup>H NMR spectroscopy. *Anal. Chem.* **2015**, *87* (5), 2771-2778.
171. Drummer, M.; Liang, C.; Kreger, K.; Rosenfeldt, S.; Greiner, A.; Schmidt, H. W. Stable Mesoscale Nonwovens of Electrospun Polyacrylonitrile and Interpenetrating Supramolecular 1, 3, 5-Benzenetrisamide Fibers as Efficient Carriers for Gold Nanoparticles. *ACS Appl. Mater. Interfaces* **2021**, *13* (29), 34818-34828.
172. Wei, C.; He, Y.; Shi, X.; Song, Z. Terpyridine-metal complexes: Applications in catalysis and supramolecular chemistry. *Coord. Chem. Rev.* **2019**, *385*, 1-19.
173. Winter, A.; Newkome, G. R.; Schubert, U. S. Catalytic Applications of Terpyridines and their Transition Metal Complexes. *Chemcatchem* **2011**, *3* (9), 1384-1406.
174. Jung, S. H.; Jeon, J.; Kim, H.; Jaworski, J.; Jung, J. H. Chiral arrangement of achiral Au nanoparticles by supramolecular assembly of helical nanofiber templates. *J. Am. Chem. Soc.* **2014**, *136* (17), 6446-6452.
175. Kotova, O.; Daly, R.; dos Santos, C. M.; Boese, M.; Kruger, P. E.; Boland, J. J.; Gunnlaugsson, T. Europium-directed self-assembly of a luminescent supramolecular gel from a tripodal terpyridine-based ligand. *Angew. Chem. Int. Ed. Engl.* **2012**, *51* (29), 7208-7212.
176. Hu, D.; Xiao, Y.; Liu, H.; Wang, H.; Li, J.; Zhou, B.; Liu, P.; Shen, M.; Shi, X. Loading of Au/Ag bimetallic nanoparticles within electrospun PVA/PEI nanofibers for catalytic applications. *Colloids Surf. A Physicochem. Eng. Asp.* **2018**, *552*, 9-15.

177. Wang, C.; Sun, S.; Zhang, L.; Yin, J.; Jiao, T.; Zhang, L.; Xu, Y.; Zhou, J.; Peng, Q. Facile preparation and catalytic performance characterization of AuNPs-loaded hierarchical electrospun composite fibers by solvent vapor annealing treatment. *Colloids Surf. A Physicochem. Eng. Asp.* **2019**, *561*, 283-291.
178. Liu, Z.; Yan, Z.; Bai, L. Electrospun nanofiber templated assembly of hybrid nanoparticles. *RSC adv.* **2018**, *8* (17), 9344-9352.
179. Cabreira, C. R.; Camilo, F. F. Evaluation of catalytic activity of cellulose films decorated with gold nanoparticles in the reduction of 4-nitrophenol. *Cellulose* **2020**, 1-11.
180. Nechikkattu, R.; Ha, C.-S. Tunable catalytic activity of gold nanoparticle decorated SBA-15/PDMAEMA hybrid system. *J. Porous Mater.* **2020**, *27* (2), 611-620.
181. Shanmugaraj, K.; Bustamante, T. M.; Torres, C. C.; Campos, C. H. Gold nanoparticles supported on mesostructured oxides for the enhanced catalytic reduction of 4-nitrophenol in water. *Catal. Today* **2020**.
182. Qin, L.; Huang, D.; Xu, P.; Zeng, G.; Lai, C.; Fu, Y.; Yi, H.; Li, B.; Zhang, C.; Cheng, M. In-situ deposition of gold nanoparticles onto polydopamine-decorated g-C<sub>3</sub>N<sub>4</sub> for highly efficient reduction of nitroaromatics in environmental water purification. *J. colloid interface sci.* **2019**, *534*, 357-369.
183. Zhou, X.-J.; Lu, H.-P.; Kong, L.-L.; Zhang, D.; Zhang, W.; Nie, J.-J.; Yuan, J.-Y.; Du, B.-Y.; Wang, X.-P. Thermo-sensitive microgels supported gold nanoparticles as temperature-mediated catalyst. *Chin. J. Polym. Sci.* **2019**, *37* (3), 235-242.
184. Zhang, M.; Lu, X.; Wang, H.-Y.; Liu, X.; Qin, Y.; Zhang, P.; Guo, Z.-X. Porous gold nanoparticle/graphene oxide composite as efficient catalysts for reduction of 4-nitrophenol. *RSC adv.* **2016**, *6* (42), 35945-35951.
185. Duan, G.; Koehn-Serrano, M.; Greiner, A. Highly Efficient Reusable Sponge-Type Catalyst Carriers Based on Short Electrospun Fibers. *Macromol. Rapid Commun.* **2017**, *38* (3), 1600511.
186. Yu, Y.; Xiao, W.; Zhou, T.; Zhang, P.; Yan, C.; Zheng, Z. Monolithic hierarchical gold sponges for efficient and stable catalysis in a continuous-flow microreactor. *Mater. Chem. Front.* **2017**, *1* (3), 482-486.
187. Ye, Y.; Jin, M.; Wan, D. One-pot synthesis of porous monolith-supported gold nanoparticles as an effective recyclable catalyst. *J. Mater. Chem. A* **2015**, *3* (25), 13519-13525.

188. He, J.; Razzaque, S.; Jin, S.; Hussain, I.; Tan, B. Efficient synthesis of ultrafine gold nanoparticles with tunable sizes in a hyper-cross-linked polymer for nitrophenol reduction. *ACS Appl. Nano Mater.* **2018**, *2* (1), 546-553.
189. Liao, X.; Dulle, M.; de Souza e Silva, J. M.; Wehrspohn, R. B.; Agarwal, S.; Förster, S.; Hou, H.; Smith, P.; Greiner, A. High strength in combination with high 195 toughness in robust and sustainable polymeric materials. *Science* **2019**, *366* (6471), 1376-1379.
190. Mader, M.; Jérôme, V. r.; Freitag, R.; Agarwal, S.; Greiner, A. Ultraporous, compressible, wettable polylactide/polycaprolactone sponges for tissue engineering. *Biomacromolecules* **2018**, *19* (5), 1663-1673.
191. Si, Y.; Fu, Q.; Wang, X.; Zhu, J.; Yu, J.; Sun, G.; Ding, B. Superelastic and superhydrophobic nanofiber-assembled cellular aerogels for effective separation of oil/water emulsions. *ACS Nano* **2015**, *9* (4), 3791-3799.
192. Majouga, A. G.; Beloglazkina, E. K.; Manzheliy, E. A.; Denisov, D. A.; Evtushenko, E. G.; Maslakov, K. I.; Golubina, E. V.; Zyk, N. V. New type of organic/gold nanohybrid material: Preparation, properties and application in catalysis. *Appl. Surf. Sci.* **2015**, *325*, 73-78.
193. Kondratowicz, I.; Zelechowska, K.; Nadolska, M.; Jazdzewska, A.; Gazda, M. Comprehensive study on graphene hydrogels and aerogels synthesis and their ability of gold nanoparticles adsorption. *Colloids Surf. A Physicochem. Eng. Asp.* **2017**, *528*, 65-73.
194. Kotova, O.; Daly, R.; dos Santos, C. M.; Kruger, P. E.; Boland, J. J.; Gunnlaugsson, T. Cross-Linking the Fibers of Supramolecular Gels Formed from a Tripodal Terpyridine Derived Ligand with d-Block Metal Ions. *Inorg. Chem.* **2015**, *54* (16), 7735-7741.
195. Christie, J. M.; Reymond, P.; Powell, G. K.; Bernasconi, P.; Raibekas, A. A.; Liscum, E.; Briggs, W. R. Arabidopsis NPH1: a flavoprotein with the properties of a photoreceptor for phototropism. *Science* **1998**, *282* (5394), 1698-1701.
196. Losi, A.; Gardner, K. H.; Moglich, A. Blue-Light Receptors for Optogenetics. *Chem. Rev.* **2018**, *118* (21), 10659-10709.
197. Christau, S.; Moeller, T.; Genzer, J.; Koehler, R.; von Klitzing, R. Salt-Induced Aggregation of Negatively Charged Gold Nanoparticles Confined in a Polymer Brush Matrix. *Macromolecules* **2017**, *50* (18), 7333-7343.

198. Pamies, R.; Cifre, J. G. H.; Espin, V. F.; Collado-Gonzalez, M.; Banos, F. G. D.; de la Torre, J. G. Aggregation behaviour of gold nanoparticles in saline aqueous media. *J. Nanopart Res.* **2014**, *16* (4), 1-11.
199. Xu, C. J.; Xu, K. M.; Gu, H. W.; Zhong, X. F.; Guo, Z. H.; Zheng, R. K.; Zhang, X. X.; Xu, B. Nitrilotriacetic acid-modified magnetic nanoparticles as a general agent to bind histidine-tagged proteins. *J. Am. Chem. Soc.* **2004**, *126* (11), 3392-3393.
200. Abad, J. M.; Mertens, S. F.; Pita, M.; Fernández, V. M.; Schiffrin, D. J. Functionalization of thioctic acid-capped gold nanoparticles for specific immobilization of histidine-tagged proteins. *J. Am. Chem. Soc.* **2005**, *127* (15), 5689-5694.
201. Park, H. Y.; Kim, K.; Hong, S.; Kim, H.; Choi, Y.; Ryu, J.; Kwon, D.; Grailhe, R.; Song, R. Compact and versatile nickel-nitrilotriacetate-modified quantum dots for protein imaging and Forster resonance energy transfer based assay. *Langmuir* **2010**, *26* (10), 7327-7333.
202. Dietler, J.; Liang, C.; Frank, S.; Müller, A. K.; Greiner, A.; Möglich, A. Photobiologically Directed Assembly of Gold Nanoparticles. *Adv. Biology*, **2021**, *5*, 2000179.
203. Satapathy, S.; Mohanta, J.; Si, S. Modulating the catalytic activity of gold nanoparticles through surface tailoring. *ChemistrySelect* **2016**, *1* (15), 4940-4948.
204. Kronawitt, J.; Fan, Z.; Schöttle, M.; Agarwal, S.; Greiner, A. Redispersible Gold Nanoparticle/Polymer Composite Powders Ready for Ligand Exchange Reactions. *ChemNanoMat* **2019**, *5* (2), 181-186.
205. Liu, X.; Atwater, M.; Wang, J.; Huo, Q. Extinction coefficient of gold nanoparticles with different sizes and different capping ligands. *Colloids Surf. B Biointerfaces* **2007**, *58* (1), 3-7.

## 14 (Eidesstattliche) Versicherungen und Erklärungen

(§ 9 Satz 2 Nr. 3 PromO BayNAT)

*Hiermit versichere ich eidesstattlich, dass ich die Arbeit selbstständig verfasst und keine anderen als die von mir angegebenen Quellen und Hilfsmittel benutzt habe (vgl. Art. 64 Abs. 1 Satz 6 BayHSchG).*

(§ 9 Satz 2 Nr. 3 PromO BayNAT)

*Hiermit erkläre ich, dass ich die Dissertation nicht bereits zur Erlangung eines akademischen Grades eingereicht habe und dass ich nicht bereits diese oder eine gleichartige Doktorprüfung endgültig nicht bestanden habe.*

(§ 9 Satz 2 Nr. 4 PromO BayNAT)

*Hiermit erkläre ich, dass ich Hilfe von gewerblichen Promotionsberatern bzw. -vermittlern oder ähnlichen Dienstleistern weder bisher in Anspruch genommen habe noch künftig in Anspruch nehmen werde.*

(§ 9 Satz 2 Nr. 7 PromO BayNAT)

*Hiermit erkläre ich mein Einverständnis, dass die elektronische Fassung meiner Dissertation unter Wahrung meiner Urheberrechte und des Datenschutzes einer gesonderten Überprüfung unterzogen werden kann.*

(§ 9 Satz 2 Nr. 8 PromO BayNAT)

*Hiermit erkläre ich mein Einverständnis, dass bei Verdacht wissenschaftlichen Fehlverhaltens Ermittlungen durch universitätsinterne Organe der wissenschaftlichen Selbstkontrolle stattfinden können.*

.....  
Ort, Datum, Unterschrift